INSIGHTS IN APPLIED NEUROIMAGING: 2021

EDITED BY: Jan Kassubek
PUBLISHED IN: Frontiers in Neurology

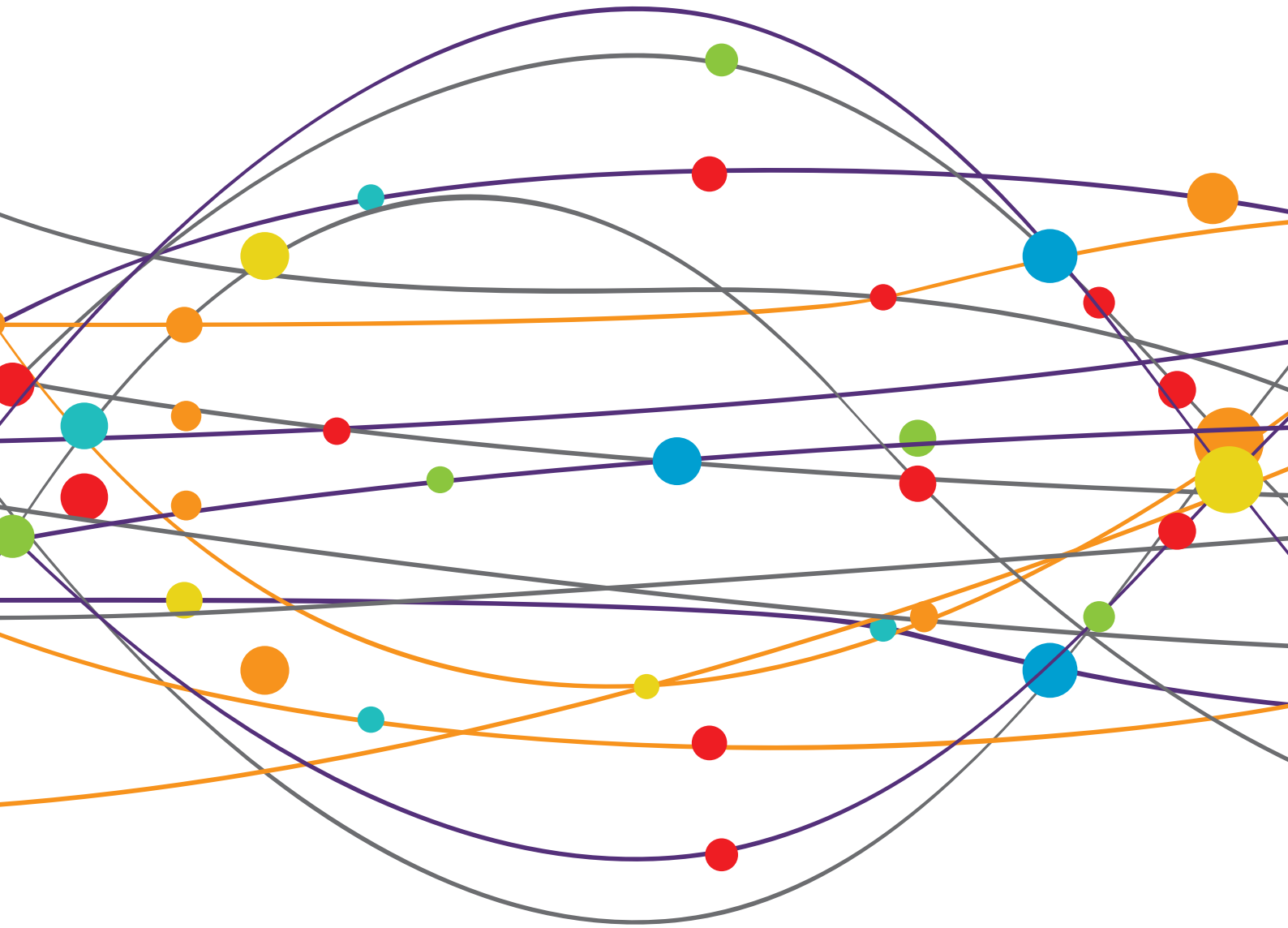

frontiers Research Topics

frontiers

ISSN 1664-8714
ISBN 978-2-83250-802-2
DOI 10.3389/978-2-83250-802-2

About Frontiers

Frontiers is more than just an open-access publisher of scholarly articles: it is a pioneering approach to the world of academia, radically improving the way scholarly research is managed. The grand vision of Frontiers is a world where all people have an equal opportunity to seek, share and generate knowledge. Frontiers provides immediate and permanent online open access to all its publications, but this alone is not enough to realize our grand goals.

Frontiers Journal Series

The Frontiers Journal Series is a multi-tier and interdisciplinary set of open-access, online journals, promising a paradigm shift from the current review, selection and dissemination processes in academic publishing. All Frontiers journals are driven by researchers for researchers; therefore, they constitute a service to the scholarly community. At the same time, the Frontiers Journal Series operates on a revolutionary invention, the tiered publishing system, initially addressing specific communities of scholars, and gradually climbing up to broader public understanding, thus serving the interests of the lay society, too.

Dedication to Quality

Each Frontiers article is a landmark of the highest quality, thanks to genuinely collaborative interactions between authors and review editors, who include some of the world's best academicians. Research must be certified by peers before entering a stream of knowledge that may eventually reach the public - and shape society; therefore, Frontiers only applies the most rigorous and unbiased reviews.
Frontiers revolutionizes research publishing by freely delivering the most outstanding research, evaluated with no bias from both the academic and social point of view. By applying the most advanced information technologies, Frontiers is catapulting scholarly publishing into a new generation.

What are Frontiers Research Topics?

Frontiers Research Topics are very popular trademarks of the Frontiers Journals Series: they are collections of at least ten articles, all centered on a particular subject. With their unique mix of varied contributions from Original Research to Review Articles, Frontiers Research Topics unify the most influential researchers, the latest key findings and historical advances in a hot research area! Find out more on how to host your own Frontiers Research Topic or contribute to one as an author by contacting the Frontiers Editorial Office: frontiersin.org/about/contact

INSIGHTS IN APPLIED NEUROIMAGING: 2021

Topic Editor:
Jan Kassubek, University of Ulm, Germany

Citation: Kassubek, J., ed. (2022). Insights in Applied Neuroimaging: 2021. Lausanne: Frontiers Media SA. doi: 10.3389/978-2-83250-802-2

Table of Contents

frontiers | Frontiers in Neurology

TYPE Editorial
PUBLISHED 02 November 2022
DOI 10.3389/fneur.2022.1048674

OPEN ACCESS

EDITED AND REVIEWED BY
Jussi Tohka,
University of Eastern Finland, Finland

*CORRESPONDENCE
Jan Kassubek
jan.kassubek@uni-ulm.de

SPECIALTY SECTION
This article was submitted to Applied Neuroimaging, a section of the journal Frontiers in Neurology

RECEIVED 19 September 2022
ACCEPTED 18 October 2022
PUBLISHED 02 November 2022

CITATION
Kassubek J (2022) Editorial: Insights in applied neuroimaging: 2021. *Front. Neurol.* 13:1048674. doi: 10.3389/fneur.2022.1048674

Editorial: Insights in applied neuroimaging: 2021

Jan Kassubek*

Department of Neurology, University of Ulm, Ulm, Germany

KEYWORDS

neuroimaging (anatomic and functional), brain disease and dynamics, multimodality, brain age, technical development

Editorial on the Research Topic
Insights in applied neuroimaging: 2021

The annual "Insights in" Research Topic series in *Frontiers in Neurology* aims to collect studies that represent current challenges and discoveries, recent advances, and future perspectives in the respective field, i.e., in Applied Neuroimaging for this Research Topic. Contributions are considered to mirror the state of the art and to address major accomplishments that have been achieved. In the field of neuroimaging applications, both technical novelties, especially with respect to both data acquisition protocols including multimodal combinations and data analysis with innovation in novel (unbiased) algorithms and data integration, exploring the contribution of neuroimaging to complex clinical challenges. This Research Topic aims to specifically support the aim of the section to report clinical and neuroscientific research with all imaging modalities, providing a forum for the promising and rapidly advancing field of neuroimaging applications to the advanced structural and functional mapping of the nervous system (1).

In the Research Topic „Insights in Applied Neuroimaging 2021", the multifaceted advances of current neuroimaging applications are represented in the publications according to this outline. Kenda et al. address the challenge of the prognostication of neurological outcome after cardiac arrest by CT and to this end, assessed the gray white matter ratio in the head CTs of 95 cardiac arrest patients both by human raters and by a recently published computer algorithm. They observed a very good interrater agreement between human raters with different levels of expertise and the computer algorithm, however, with considerable interrater variability in individual patients. The authors conclude that the results emphasize the need for strategies to standardize quantitative head CT analysis and for multimodal prognostication in general. In a study in 247 healthy subjects targeting to set up a reference data set, Sun Z., et al. used automatic vessel segmentation, centerline tracking, and phase mapping on MR angiography to investigate age and gender effects on brain-supplying neck arteries regarding tortuosity and flow changes. By this approach, quantifiable age-related morphological and hemodynamic alterations in the investigated arteries could be demonstrated, including the differences between female and male patients. Also in healthy subjects, Boban et al. studied physiological brain aging by a correlation analysis of four white matter diffusivity measures in diffusion tensor imaging (DTI) data with

chronological age and education levels. All DTI metrics showed significant correlations with the advancing age of the participants, however, this involved largely different regional patterns and the authors concluded that different patterns of degradation during aging are true for different brain fiber tracts and that not one single of the currently available theories can globally explain age-related changes in the brain. In another study taking advantage of a fully automated MRI analysis technology, i.e., AccuBrain^{TM} for segmentation and quantitative volumetry, Sun W., et al. investigated 242 patients with cerebral small vessel disease and observed that the disease was associated with widespread cerebral atrophy including the lobes and that the volumes of periventricular white matter hyperintensities and medial temporal atrophy were independent predictors of cognitive decline. Ioachim et al. investigated the clinical challenge of chronic pain associated with fibromyalgia by task-based functional MRI with a pain-related paradigm; they observed differences in pain processing between people with fibromyalgia and healthy controls and that this altered pain processing may be linked to changes in both descending pain regulation and autonomic regulation, even while the participants are only anticipating the pain, thus advancing the understanding of fibromyalgia. By use of resting state functional MRI (rsfMRI) within a multiparametric protocol at ultra-high field of 7T, Morrison et al. analyzed the dorsal attention, salience, and frontoparietal networks in young patients after cranial radiation therapy for a brain tumor. Compared to controls, patients exhibited widespread hyperconnectivity, similar modularity, and significantly increased efficiency and network variability, correlated with memory performance, suggesting that these rsfMRI metrics might be promising imaging-based markers for monitoring the cognitive side effects of radiation therapy. An MRI-based study on brain changes associated with COVID-19 neurological manifestations was contributed by Napolitano et al., who investigated cerebral microbleeds by susceptibility-weighted imaging (including a semi-automatic processing procedure) in 63 patients during the first wave in Italy. Cerebral microbleeds were a frequent finding in hospitalized patients with COVID-19 and neurological manifestations, with a specific pattern of distribution (i.e., prominent callosal and juxtacortical involvement) and seemed to be related to pro-inflammatory status. In a technical report by a multi-national study group, Bouget et al. investigated standardized and automatic methods (i.e., Raidionics and Raidionics-Slicer within the AGU-Net architecture) for tumor detection and assessment of tumor characteristics in MRI in the most occurring brain tumor types (glioblastomas, lower grade gliomas, meningiomas, metastases) in up to 4,000 patients' data. The detailed performance assessment enabled the identification of the most relevant metrics from a large panel, and for clinical practice, tumor segmentation could be performed in less than a minute. The generation of a standardized clinical report took less than 15 min — *nota bene*, all trained models have been made publicly available (open-access) together with the source code for the software solutions and validation metrics computation. In the perspective article by Juengling et al., an international group of authors reviewed the current state of the art in the application of simultaneous PET/MRI to motor neuron disease (like amyotrophic lateral sclerosis) and how this combination of advanced neuroimaging modalities can guide in characterizing this neurodegenerative disease *in vivo* by the complementary information on disease pathology. Yeo et al. address the relationship between white matter hyperintensities in MRI and right-to-left shunt in migraine patients by a systematic review and meta-analysis (of 8 observational studies comprising 1,125 patients), and they reported that in migraine, the right-to-left shunt was significantly associated with the presence of white matter hyperintensities. Finally, in a case report (comparative case study) by Golden et al., two patients with fibrous dysplasia and similar craniofacial lesion burden were investigated by ^{18}F-sodium fluoride PET/CT and multiparametric MRI, and the detailed phenotypic characterization incorporating the advanced imaging approach guided the understanding of the variable experiences with pain in craniofacial fibrous dysplasia.

These contributions demonstrate both technical and clinical "insights" on the application of advanced neuroimaging, comprising, on the one hand, various technical approaches with computed tomography, and multiparametric MRI including structural imaging (atrophy assessment, white matter alterations/lesions, tumor lesion, and susceptibility imaging), microstructural diffusion-based imaging, and functional imaging (both task-based and resting-state intrinsic connectivity-based), and multimodality approaches (PET/MRI and PET/CT). On the other hand, studies in healthy ($N = 2$) and diseased brains ($N = 9$) are included, the latter covering a very broad pathological spectrum from vascular diseases and neurodegeneration, COVID-19, and pain disorders to multi-organ orphan diseases. Finally, single-center cohort studies and multi-site collaborations of researchers are represented, together with meta-analysis data. Although heterogeneous in their approaches, the contributions to this Research Topic all target the integration of research on clinical and neuroscientific grounds with all modalities of neuroimaging and advanced postprocessing.

Author contributions

The author confirms being the sole contributor of this work and has approved it for publication.

Conflict of interest

The author declares that the research was conducted in the absence of any commercial or financial relationships that could be construed as a potential conflict of interest.

Publisher's note

References

1. Kassubek J. The application of neuroimaging to healthy and diseased brains: present and future. *Front Neurol.* (2017) 8:61. doi: 10.3389/fneur.2017.00061

frontiers in Neurology

CASE REPORT
published: 16 March 2022
doi: 10.3389/fneur.2022.855157

Case Report: The Imperfect Association Between Craniofacial Lesion Burden and Pain in Fibrous Dysplasia

*Emma Golden[1], Fan Zhang[2], Daryl J. Selen[3,4], David Ebb[5], Laura Romo[6], Laura A. Drubach[7], Nehal Shah[2], Lauren J. O'Donnell[2], Jordan D. Lemme[1], Rachel Myers[1], Mariesa Cay[1], Henry M. Kronenberg[3,4], Carl-Fredrik Westin[2], Alison M. Boyce[8], Leonard B. Kaban[9] and Jaymin Upadhyay[1,10]**

[1] Department of Anesthesiology, Critical Care and Pain Medicine, Boston Children's Hospital and Harvard Medical School, Boston, MA, United States, [2] Department of Radiology, Brigham and Women's Hospital and Harvard Medical School, Boston, MA, United States, [3] Endocrine Unit, Department of Medicine, Massachusetts General Hospital, Boston, MA, United States, [4] Harvard Medical School, Boston, MA, United States, [5] Department of Pediatric Hematology Oncology, Massachusetts General Hospital and Harvard Medical School, Boston, MA, United States, [6] Head and Neck Imaging, Department of Radiology, Massachusetts Eye and Ear, Harvard Medical School, Boston, MA, United States, [7] Department of Radiology, Boston Children's Hospital and Harvard Medical School, Boston, MA, United States, [8] Metabolic Bone Disorders Unit, National Institute of Dental and Craniofacial Research, National Institutes of Health, Bethesda, MD, United States, [9] Department of Oral and Maxillofacial Surgery, Massachusetts General Hospital and Harvard School of Dental Medicine, Boston, MA, United States, [10] Department of Psychiatry, McLean Hospital and Harvard Medical School, Belmont, MA, United States

OPEN ACCESS

Edited by:
Jan Kassubek,
University of Ulm, Germany

Reviewed by:
Anne-Marie Heegaard,
University of Copenhagen, Denmark
Alessandro Vittori,
Bambino Gesù Children's Hospital (IRCCS), Italy

***Correspondence:**
Jaymin Upadhyay
jaymin.upadhyay@childrens.harvard.edu

Specialty section:
This article was submitted to Applied Neuroimaging, a section of the journal Frontiers in Neurology

Received: *14 January 2022*
Accepted: *08 February 2022*
Published: *16 March 2022*

Citation:
Golden E, Zhang F, Selen DJ, Ebb D, Romo L, Drubach LA, Shah N, O'Donnell LJ, Lemme JD, Myers R, Cay M, Kronenberg HM, Westin C-F, Boyce AM, Kaban LB and Upadhyay J (2022) Case Report: The Imperfect Association Between Craniofacial Lesion Burden and Pain in Fibrous Dysplasia. Front. Neurol. 13:855157. doi: 10.3389/fneur.2022.855157

Patients with fibrous dysplasia (FD) often present with craniofacial lesions that affect the trigeminal nerve system. Debilitating pain, headache, and migraine are frequently experienced by FD patients with poor prognosis, while some individuals with similar bone lesions are asymptomatic. The clinical and biological factors that contribute to the etiopathogenesis of pain in craniofacial FD are largely unknown. We present two adult females with comparable craniofacial FD lesion size and location, as measured by ^{18}F-sodium fluoride positron emission tomography/computed tomography (PET/CT), yet their respective pain phenotypes differed significantly. Over 4 weeks, the average pain reported by Patient A was 0.4/0–10 scale. Patient B reported average pain of 7.8/0–10 scale distributed across the entire skull and left facial region. Patient B did not experience pain relief from analgesics or more aggressive treatments (denosumab). In both patients, evaluation of trigeminal nerve divisions (V1, V2, and V3) with CT and magnetic resonance imaging (MRI) revealed nerve compression and displacement with more involvement of the left trigeminal branches relative to the right. First-time employment of diffusion MRI and tractography suggested reduced apparent fiber density within the cisternal segment of the trigeminal nerve, particularly for Patient B and in the left hemisphere. These cases highlight heterogeneous clinical presentation and neurobiological properties in craniofacial FD and also, the disconnect between peripheral pathology and pain severity. We hypothesize that a detailed phenotypic characterization of patients that incorporates an advanced imaging approach probing the trigeminal system may provide enhanced insights into the variable experiences with pain in craniofacial FD.

Keywords: fibrous dysplasia, craniofacial lesions, trigeminal nerve system, pain, headache, migraine

INTRODUCTION

Fibrous dysplasia (FD, OMIM 174800) is a rare bone disease arising from an R201 missense mutation of the *GNAS* gene (1–3). FD may be complicated by co-existing pigmented skin lesions, precocious puberty, and other endocrinopathies resulting in the diagnosis of McCune Albright Syndrome (MAS) (4). Pain remains a complex, inadequately understood and poorly managed feature of FD (5–7). Craniofacial skeletal lesions in FD are the probable and inciting cause of atypical facial pain, headaches, or migraines (8–10). However, the severity or type of pain reported by patients with FD is highly variable. Further complicating the understanding of pain in FD or its treatment is the weak correlation between patient-reported pain intensity and skeletal disease burden (11). This dissociation points to the need to uncover both clinical and active biological mechanisms that cause pain in individual patients with FD.

In the current comparative case report, two adult (22 years of age) female patients with similar craniofacial FD lesion burden, but who presented with contrasting pain experiences are described. However, the patients contrasted tremendously in terms of their respective experiences with pain. Over a period of many years, Patient A reported little to no pain, while Patient B has had an unfortunately long history of suffering from craniofacial pain in the trigeminal distribution, headaches, and migraines. A multidisciplinary approach was taken to investigate potential factors associated with the divergent pain profiles specific to Patients A and B. Our strategy involved phenotyping pain and related symptoms (i.e., altered mood) using several clinical instruments. In parallel, molecular imaging techniques were employed to define craniofacial lesion burden and FD's impact on trigeminal nerves and branches. Examination and comparison between the two FD patient datasets indicate the importance of the need for a closer psychological and neurological assessment of pain in FD.

CLINICAL OVERVIEW

This study was approved by the Boston Children's Hospital (BCH) and the Massachusetts General Brigham, Institutional Review Boards. Patient A and Patient B provided informed consent and underwent study evaluation in January 2021 and February 2021, respectively.

Patient A, Craniofacial FD Without Pain

Patient A is a 22-year-old woman with polyostotic FD of the left zygomaticomaxillary complex (maxilla, zygoma and sphenoid bones) and parasymphyseal regions of the mandible. Her disease was first identified at age 11 when she presented with a painless swelling of the left maxilla during a routine dental examination. Panoramic radiograph at that time demonstrated a radio-opaque lesion, particularly of the left zygomaticomaxillary complex and filling the left maxillary sinus. She was subsequently referred to oral and maxillofacial surgery (OMS) at Massachusetts General Hospital (MGH) where a computed tomographic (CT) scan of the facial bones revealed marked expansion of the left maxilla, zygoma, and sphenoid bones with a ground glass appearance, consistent with a diagnosis of FD. This was confirmed by histologic evaluation of a biopsy specimen in August 2010.

Following this initial consultation in OMS, further evaluations were undertaken by Ophthalmology, Endocrinology, Pediatric Orthopedic Surgery, and Neuro-ophthalmology to document the presence of additional osseous pathology and/or functional deficits. A Tc-99m-methylene diphosphonate technetium single-photon emission computerized tomography (SPECT) scan in August 2010 revealed no other foci of FD. Skin examination demonstrated a small hyperpigmented lesion over the lower back measuring 1 × 2 cm. Serial endocrine evaluations have demonstrated no evidence of precocious puberty or other endocrinopathies that might be present in MAS. Despite narrowing of the optic canal and displacement of her left globe by growth of the bone lesions in the left sphenoid wing, zygoma, and maxilla, her visual acuity has remained normal during serial examinations, with no evidence of visual field defects or optic nerve pathology.

During 11 years of follow-up, the patient has undergone multiple contour resections of the left facial skeleton to manage progressive expansile changes in the left maxilla, zygoma, and sphenoid bones with associated exophthalmos. The first procedure was performed in August 2012, at 13.5 years of age, when she presented with expansile changes in the left zygomaticomaxillary complex, proptosis and intermittent mild tenderness over the corresponding left side of the face. Since the initial operation, she has not had pain or tenderness despite intermittent growth of the FD warranting 3 additional contour resections: June 2012, December 2015, and May 2018. During the 3-year period since 2018, the disease has been quiescent with only slow, minor growth. Based on this history, finishing college and entering the workforce, she had, what is hoped will be, a final contour resection of the zygomaticomaxillary lesion in June 2021.

Patient B, Craniofacial FD With Pain

Patient B was first diagnosed with polyostotic craniofacial FD in November 2019 at age 21. She initially presented at that time with worsening of her chronic headaches, vision changes, amnesia, and gait imbalance. She reported fatigue for the prior month, worsening headaches for 2–3 weeks, blurry vision for 2–3 days, and a week of forgetfulness that culminated in her getting lost while driving, prompting presentation to an emergency department (ED). In retrospect, she had noticed severe headaches for the past 5 years and had a history of four concussions from 2014 to 2017 from motor vehicle accidents and playing soccer. At the outside hospital, she had a cranial CT that revealed a sclerotic left skull lesion involving the left sphenoid wing, anterior clivus, left pterygoid plate, and left temporal bone, so she was transferred to the MGH ED for further evaluation. Imaging was repeated at MGH and CT revealed ground glass marrow expansion of the sphenoid bone and left temporal bone consistent with FD with narrowing of the skull base foramina, fissures, and middle cranial fossa. Endocrinology was consulted while the patient was in the ED due to new diagnosis of FD, as well as concern for pituitary compression and need for a hormonal evaluation.

During her initial evaluation in the ED, her calcium, phosphate, magnesium, parathyroid hormone, albumin, and

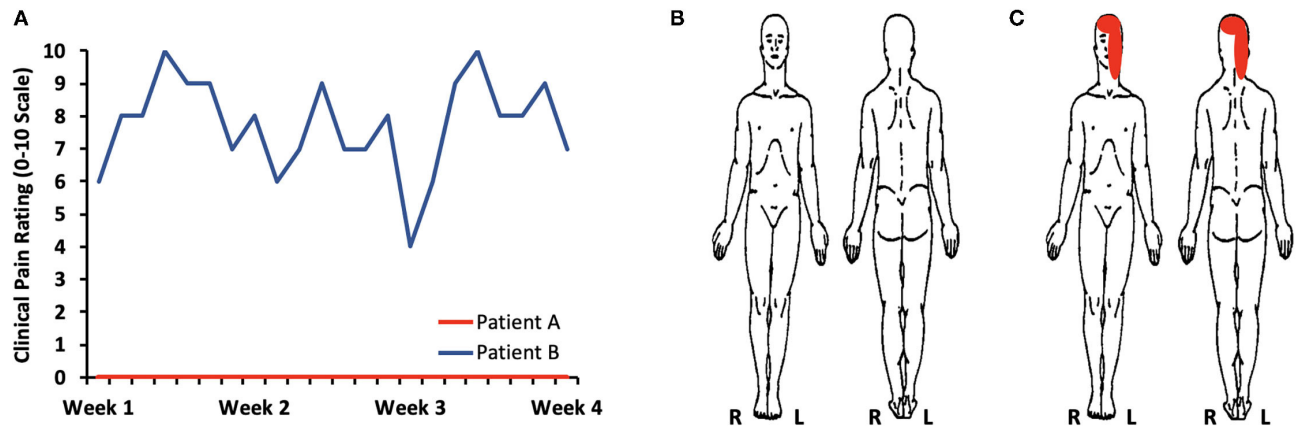

FIGURE 1 | Clinical pain levels. **(A)** Self-reported daily pain levels over 4 weeks confirms the presence of little to no pain for Patients A (average pain: 0.4/0–10 scale) and moderate to severe pain for Patient B (average pain: 7.8/0–10 scale). **(B)** A body map further defined an absence of pain in Patient A. **(C)** Patient B described pain primarily on the left side of her face and over the majority of the skull.

25-OH vitamin D labs were normal. On exam, she had no café-au-lait skin lesions or history of precocious puberty or hyperfunctioning endocrinopathies, so the clinical suspicion for MAS was low. Additional endocrine evaluation revealed normal thyroid function, no evidence of adrenal insufficiency, and otherwise normal gonadal and insulin-like growth factor-I hormonal axes. OMS and Neuro-ophthalmology recommended no surgical treatment due to normal visual exam and auditory testing. For her daily severe, debilitating headaches, the patient was further evaluated by Neurology, and her headaches were attributed to the FD of the skull, with an additional component of intractable migraine without aura. Patient B was also diagnosed with trigeminal neuralgia. For headaches, she achieved no symptomatic relief with magnesium, riboflavin, sumatriptan, topiramate, or ibuprofen. She was treated with On abotulinumtoxinA injections for migraines in August 2020, July 2021, and November 2021, and she did experience temporary symptomatic relief for a few weeks after each treatment.

Due to her desire for pregnancy within a few years after diagnosis, treatment with denosumab was recommended instead of bisphosphonates due to concerns of long-lasting retention of bisphosphonates in the bones and possible future fetal exposure (12). Denosumab, a monoclonal antibody to RANK ligand that directly inhibits osteoclastogenesis, was used off-label to attempt to reduce pain associated with FD as well as lesion expansion (13–18). She received two 120 mg doses of denosumab in total spaced by 6 months in 2020 but did not notice any improvement in her pain. This was in contrast to prior reports noting fast analgesic action following treatment induction with denosumab. Notably, there has not been expansion of her FD lesions in the year since her last dose of denosumab. The patient was further discussed with Neurosurgery and Radiation Oncology who thought that neither debulking nor radiation to the areas of FD were easy or safe options due to the risk of significant complications. She continues to receive Botox injections for headache and migraine relief, but otherwise has not achieved symptomatic control of her headaches or migraines.

CLINICAL PAIN

Patient A not only reported a minimal amount of clinical pain, but also showed low levels of psychological symptoms or distress (**Supplementary Table 1**). Self-reported daily pain levels monitored over 4 weeks confirmed the absence or minimal amount of pain for Patient A (**Figure 1**). In contrast, Patient B harbored severe pain, consistent with her experience of daily headaches with superimposed migraines in addition to intermittent trigeminal neuralgia. High levels of craniofacial and headache-type pain were present at the time of imaging evaluation (**Supplementary Table 1**) as well as over the course of 4 weeks (**Figure 1**). In conjunction with experiencing severe pain, Patient B presented with a clinically relevant level of pain catastrophizing–a maladaptive cognitive and emotional response to pain (19, 20). The presence of pain catastrophizing was in line with the occurrence psychological stress with mild levels of depressive symptoms. Patients A and B reported similar levels of sleep quality.

CRANIOFACIAL LESION BURDEN AND SEVERITY

Whole-body ^{18}F-sodium fluoride positron emission tomography/computed tomography [^{18}F-NaF PET/CT; Injected dose = 4.0 millicurie (mCi) of ^{18}F-NaF] was performed at BCH and on a Siemens Biograph Vision system (Siemens, Erlangen, Germany). In Patient A, whole-body ^{18}F-NaF PET/CT showed intense radiotracer uptake corresponding to ground glass and expansile appearance of the left inferolateral frontal bone involving the ipsilateral zygoma and zygomatic arch (**Figure 2**). Uptake of ^{18}F-NaF was evident in the sphenoid bone (involving both clinoid processes) and clivus extending across midline, as well as the left pterygoid plates and the left maxilla extending to the midline alveolar ridge and surrounding the left-sided maxillary incisors, bicuspids, and molars. There was a

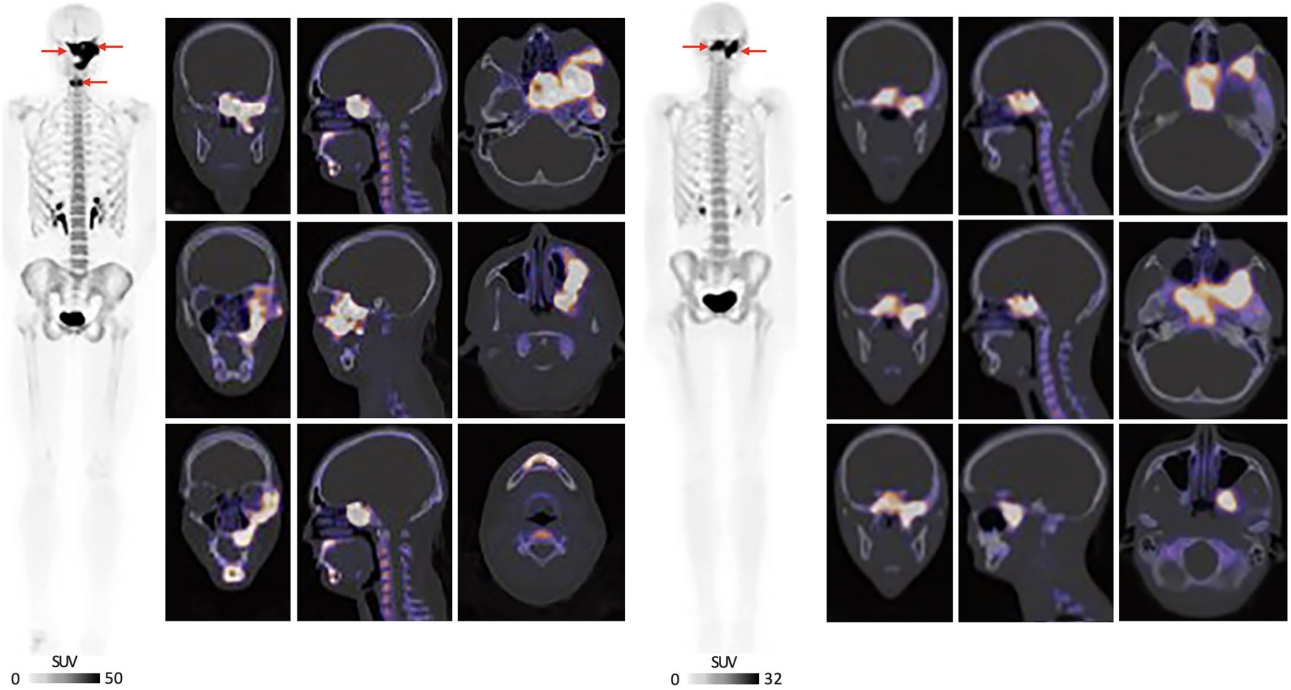

FIGURE 2 | Craniofacial FD burden and severity. **(A)** Patient A: ^{18}F-NaF PET/CT showed intense radiotracer uptake in the left frontal bone and zygomatic arch, left maxilla, left sphenoid bone, and livus. There was also involvement of the anterior mandible. **(B)** Patient B: ^{18}F-NaF PET/CT showed intense uptake involving the base of the skull, clivus, sella and left sphenoid bone. The patient also had scattered areas of increased uptake in the left temporal bone with $SUV_{max} = 13$. All ^{18}F-NaF PET/CT data were read by a board-certified nuclear medicine physician (Dr. Drubach).

separate but discrete area of intense radiotracer uptake along the parasymphyseal mandible along the anterior aspect. Scattered areas of lytic-appearing bone were noted in the maxilla and left sphenoid wing.

Whole-body ^{18}F-NaF PET/CT (Injected dose = 4.0 mCi of ^{18}F-NaF) performed in Patient B showed overlapping craniofacial FD burden relative to Patient A. Several regions of increased ^{18}F-NaF uptake in the skull were consistent with FD involvement in Patient B (**Figure 2**). There was intense uptake in the midline of the base of the skull involving the clivus and sella, left sphenoid bone, and most medial regions of the right sphenoid bone. There were a few scattered areas of increased uptake in the left temporal bone. The areas of increased uptake were associated with expanded ground glass appearance of the bone on CT. ^{18}F-NaF uptake outside of the craniofacial regions was not observed for either Patients A or B.

THE IMPACT OF CRANIOFACIAL FD ON TRIGEMINAL NERVES

Non-contrast magnetic resonance imaging (MRI) was performed on a 3T Siemens Prisma with a 64-channel head coil (Siemens, Erlangen) at McLean Hospital. For both Patients A and B, involvement of the sphenoid bone by FD resulted in a mass effect as well as narrowing and displacement of the left superior fissure, which transmits the first (V1) division of the left trigeminal nerve (CNV), the left foramen rotundum (FR) transmitting the second (V2) division of CNV, and the left foramen ovale (FO) transmitting the third (V3) division of CNV (**Figure 3**). In addition, there was narrowing of the left superior orbital fissure (SOF). Overall and for both patients, the narrowing and displacement was more prominent for left hemisphere cranial structures relative to the right. Patient A additionally showed structural alterations of the left inferior orbital fissure and the left infraorbital canal, both of which transmit the infra-orbital nerve, a branch of V2. More proximally, FR and FO were narrowed and superolaterally displaced on the left compared to the right.

Using a combination of diffusion MRI and tractography, the apparent axonal fiber density of the cisternal segment of CNV (brainstem to trigeminal ganglion) was investigated with previously described procedures (21, 22) (**Figure 4**). Although the caliber and symmetry of CNV on T2-SPACE MRI and STIR MRI appeared normal for Patients A and B, both individuals appeared to have a of loss apparent fiber density in the left CNV relative to the right. However, Patient B appeared to differentiate from Patient A based on a comparatively lower level of bilateral fiber density (defined as the number of streamlines/voxel). The latter novel finding suggests modulation of trigeminal system function and structure, and possibly involvement of central pain processing pathways in FD. Further investigation may demonstrate the utility of diffusion MRI to more directly document nerve pathology in patients with craniofacial FD.

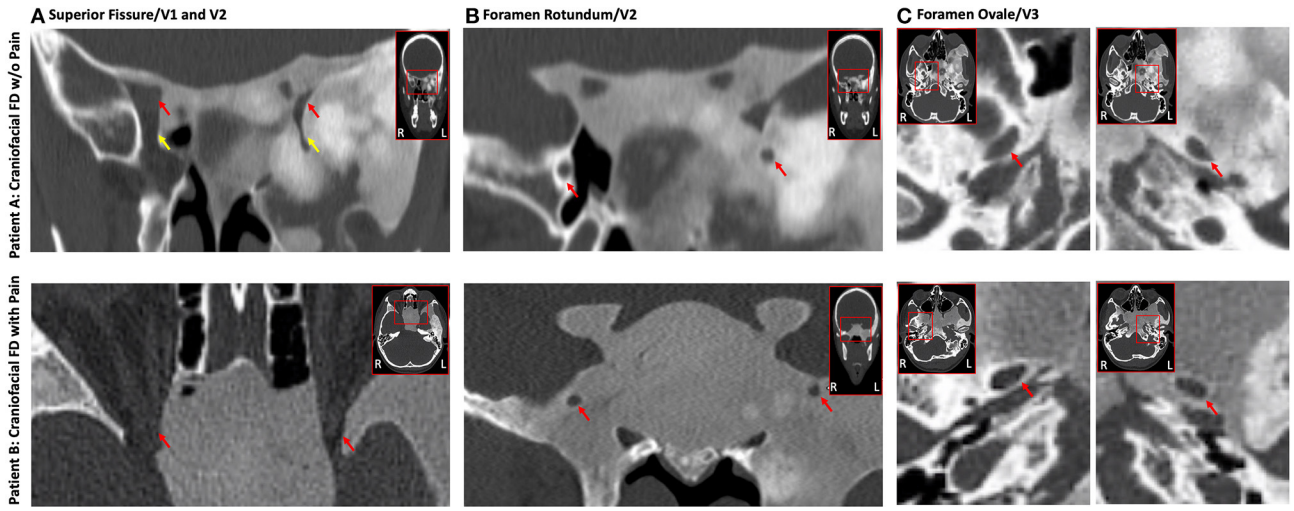

FIGURE 3 | Impact of FD on the trigeminal nerve system. Craniofacial FD lesions caused a highly similar impact on conduits carrying trigeminal nerves in both Patients A and B. Displacement and narrowing of the V1 **(A)**, V2 **(B)**, and V3 **(C)** divisions of the trigeminal nerves was evident on CT for both FD patients with generally a greater impact on left hemisphere structures relative to the right. The top (Patient A) and bottom (Patient B) rows show coronal or axial cross-sections from CT. **(A)** Constriction of the superior orbital fissure (red arrow) and inferior orbital fissure (yellow arrow; Patient A only). **(B)** Narrowing and displacement of the left foramen rotundum (red arrows). **(C)** Narrowing and displacement of the left foramen ovale (red arrows). **(C)** All data were read by a board-certified neuroradiologist (Dr. Romo).

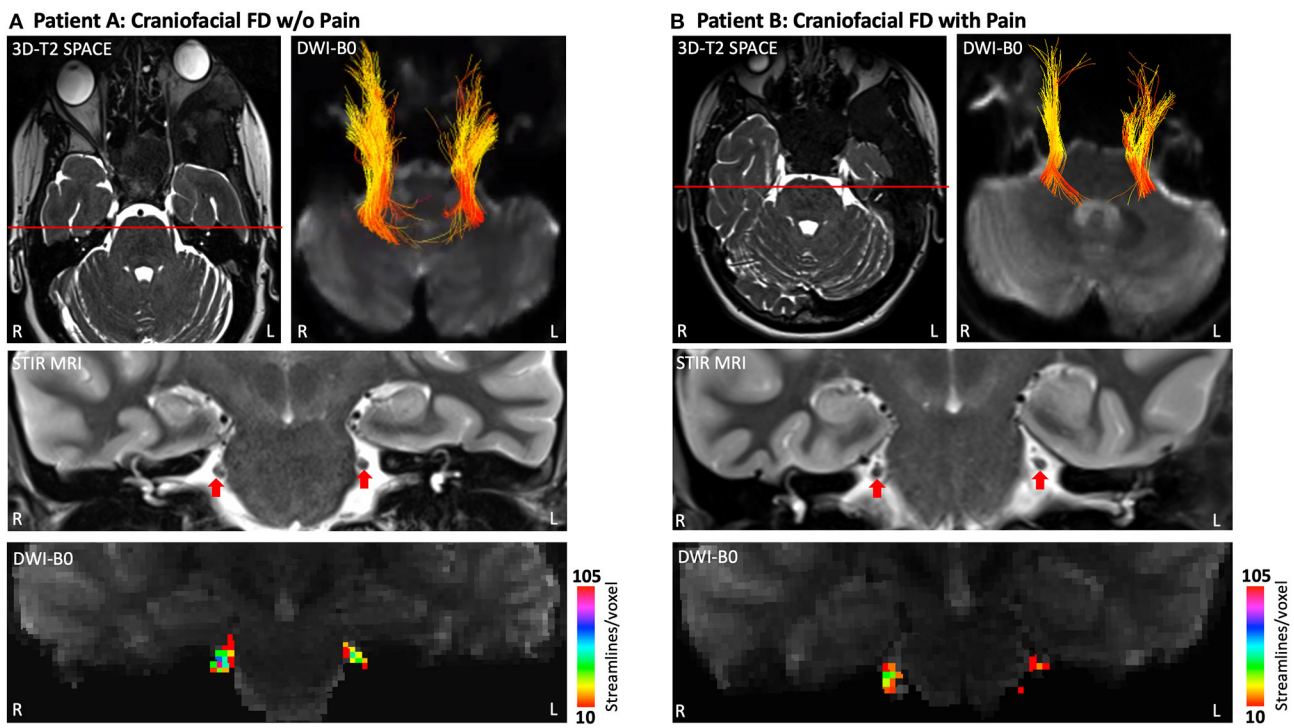

FIGURE 4 | Apparent fiber loss in the CNV (cisternal segment). Patient A **(A)** and Patient B **(B)** each demonstrated a lower level of apparent fiber density in left hemisphere CNV at the cisternal level as determined by diffusion MRI and tractography. Fiber streamlines projecting between the brainstem and trigeminal ganglion are shown colored by fractional anisotropy (FA). Coronal cross-sections of T2-SPACE MRI show normal caliber and symmetry of CNV for both patients. However, heat maps derived from diffusion tractography indicate a lower magnitude of streamlines per voxel (apparent fiber density) for the left hemisphere CNV, particularly for Patient B. Heat maps for the right hemisphere CNV indicate a lower level of streamlines per voxel in Patient B compared to Patient A. DTI data were collected using Human Connectome Project protocols (29). 3D-T2-SPACE, 3D-T2 Sampling Perfection with Application-Optimized Contrasts by Using Flip Angle Evolution; FA, Fractional Anisotropy; STIR MRI, Short Tau Inversion Recovery Magnetic Resonance Imaging; DWI, Diffusion Weighted Imaging.

DISCUSSION

The two cases described in the current report point to the remarkable spectrum of pain phenotypes present in FD. On one hand, the heterogeneous nature of FD likely contributes to the variability of both the pain severity reported across patients, as well as the responses to palliative treatments that aim to manage FD lesions or mitigate pain (e.g., reconstructive surgery, On abotulinumtoxinA injections, bisphosphonate, denosumab, and analgesics) (13–17, 23–26). Yet Patients A and B possessed a number of similarities from demographic (i.e., age and gender) and biological (i.e., anatomical distribution plus severity of craniofacial lesions and non-MAS status) perspectives. Considering the many parallels between the two FD patients, the extreme differences regarding pain is perplexing, but also highlights the challenge in identifying how best clinically to approach pain treatment in FD. Moreover, adding to the complexity in providing effective pain treatment to patients with FD is the high probability of many unknown clinical and biological drivers of pain active in individual patients or possibly, FD subtypes.

Patients A and B did in fact differentiate in multiple domains, which may suggest why Patient B currently experiences craniofacial pain and migraines headaches. Diagnosis of FD for Patients A and B occurred at ages 11 and 21, respectively. Thus, the implementation of surgical care and other treatments in Patient A much earlier in the course of disease as well as (neuro-) development may have provided the foundation necessary to limit, for example, maladaptive neurological process associated with peripheral or central pain sensitization. It is noted, however, that many patients with FD/MAS have an even earlier diagnosis and receive treatment shortly after yet still suffer from pain, headaches or migraine. Patient B not only had a much later FD diagnosis, but also experienced multiple concussions, which collectively may have contributed to or worsened her chronic craniofacial pain and migraine phenotype (27, 28). Further insights into why Patient B has not experienced pain relief despite the use of multiple modes of therapy may be garnered by considering her feelings of helplessness or constant rumination of pain as defined by the pain catastrophizing scale. An additional possibility is that long-term suffering from almost constant headaches and migraines may have caused her to catastrophize about pain and become psychologically distressed. Importantly, such a robust emotional state may solidify the presence of pain and drive some patients with FD to become resistant to various analgesic treatment strategies. Finally, Patients A and B also differed according to how their respective craniofacial lesions structurally impacted trigeminal nerves and branches. In both patients, CT and MRI demonstrated narrowing and displacement of V1, V2, and V3; an effect that appeared more notable on left hemisphere craniofacial structures compared to the right. Diffusion tractography revealed abnormalities in the cisternal segment of the trigeminal nerve, where the loss of apparent fiber density was more notable for Patient B.

Based on the current comparative case study, we project that in a sub-population of patients with craniofacial FD, a combination of neurological abnormalities, particularly those more proximal to the central nervous system, together with the psychological aspects of pain facilitate a complex and difficult to treat pain state. Whether and how peripheral and central features drive pain in FD should be the focus of future prospective studies, which may result in identification of biomarkers in FD/MAS that can predict pain trajectories, prognosis, or treatment response.

DATA AVAILABILITY STATEMENT

The data that support the findings of this study are available upon reasonable request.

ETHICS STATEMENT

The studies involving human participants were reviewed and approved by Boston Children's Hospital IRB. The patients/participants provided their written informed consent to participate in this study. Written informed consent was obtained from the individual(s) for the publication of any potentially identifiable images or data included in this article.

AUTHOR CONTRIBUTIONS

EG, FZ, LR, LD, LO'D, and C-FW analyzed data, drafted the initial manuscript, and reviewed and revised the manuscript. DS, DE, HK, and LK provided patient care, acquired and analyzed data, drafted the initial manuscript, and reviewed and revised the manuscript. NS, JL, RM, and MC designed the study and acquired and analyzed data. AB designed the study and drafted the initial manuscript. AB and JU acquired funding in support of this case report. JU designed the study, acquired and analyzed data, drafted the initial manuscript, and reviewed and revised the manuscript. All authors approved the final manuscript as submitted and agree to be accountable for all aspects of the work.

FUNDING

This research was funded by the MAYDAY Fund (PI: JU). DS was supported by NIH T32 grant (T32DK007028).

ACKNOWLEDGMENTS

The authors thank the FD/MAS Alliance and FD/MAS Patient Registry for their support with patient outreach throughout the course of this study. The authors would also like to thank Kathleen Thangaraj, Blaise Frederick, and Ivan Kane of the McLean Imaging Center for their assistance during the course of this study.

SUPPLEMENTARY MATERIAL

The Supplementary Material for this article can be found online at: https://www.frontiersin.org/articles/10.3389/fneur.2022.855157/full#supplementary-material

REFERENCES

1. Boyce AM, Florenzano P, de Castro LF, Collins MT. Fibrous dysplasia/mccune-albright syndrome. In: Adam MP, Ardinger HH, Pagon RA, Wallace SE, Bean LJH, Stephens K, Amemiya A, editors. *GeneReviews((R))*. Seattle (WA): University of Washington (1993).
2. Riminucci M, Liu B, Corsi A, Shenker A, Spiegel AM, Robey PG, et al. The histopathology of fibrous dysplasia of bone in patients with activating mutations of the Gs alpha gene: site-specific patterns and recurrent histological hallmarks. *J Pathol.* (1999) 187:249-58.
3. Ramaswamy G, Kim H, Zhang D, Lounev V, Wu JY, Choi Y, et al. Shore gsalpha controls cortical bone quality by regulating osteoclast differentiation *via* cAMP/PKA and beta-catenin pathways. *Sci Rep.* (2017) 7:45140. doi: 10.1038/srep45140
4. Florenzano P, Pan KS, Brown SM, Paul SM, Kushner H, Guthrie LC, et al. Age-related changes and effects of bisphosphonates on bone turnover and disease progression in fibrous dysplasia of bone. *J Bone Miner Res.* (2019) 34:653–60. doi: 10.1002/jbmr.3649
5. Chapurlat RD, Gensburger D, Jimenez-Andrade JM, Ghilardi JR, Kelly M, Mantyh P. Pathophysiology and medical treatment of pain in fibrous dysplasia of bone. *Orphanet J Rare Dis.* (2012) 7:S3. doi: 10.1186/1750-1172-7-S1-S3
6. Kelly MH, Brillante B, Collins MT. Pain in fibrous dysplasia of bone: age-related changes and the anatomical distribution of skeletal lesions *Osteoporos Int.* (2008) 19:57–63. doi: 10.1007/s00198-007-0425-x
7. Majoor BCJ, Andela CD, Bruggemann J, van de Sande MAJ, Kaptein AA, Hamdy NAT, et al. Determinants of impaired quality of life in patients with fibrous dysplasia. *Orphanet J Rare Dis.* (2017) 12:80. doi: 10.1186/s13023-017-0629-x
8. Couturier A, Aumaitre O, Gilain L, Jean B, Mom T, Andre M. Craniofacial fibrous dysplasia: a 10-case series. *Eur Ann Otorhinolaryngol Head Neck Dis.* (2017) 134:229–35. doi: 10.1016/j.anorl.2017.02.004
9. Frisch CD, Carlson ML, Kahue CN, Pelosi S, Haynes DS, Lane JI, et al. Driscoll fibrous dysplasia of the temporal bone: a review of 66 cases. *Laryngoscope.* (2015) 125:1438–43. doi: 10.1002/lary.25078
10. Kim KS. Headache attributed to fibrous dysplasia of the ethmoid bone mimicking menstrual migraine without aura. *J Craniofac Surg.* (2016) 27:e417–9. doi: 10.1097/SCS.0000000000002685
11. Majoor BCJ, Traunmueller E, Maurer-Ertl W, Appelman-Dijkstra NM, Fink A, Liegl B, et al. Pain in fibrous dysplasia: relationship with anatomical and clinical features. *Acta Orthop.* (2019) 90:401–5. doi: 10.1080/17453674.2019.1608117
12. Stathopoulos IP, Liakou CG, Katsalira A, Trovas G, Lyritis GG, Papaioannou NA, et al. The use of bisphosphonates in women prior to or during pregnancy and lactation. *Hormones.* (2011) 10:280–91. doi: 10.14310/horm.2002.1319
13. Eller-Vainicher C, Rossi DS, Guglielmi G, Beltramini GA, Cairoli E, Russillo A, et al. Prompt clinical and biochemical response to denosumab in a young adult patient with craniofacial fibrous dysplasia. *Clin Cases Miner Bone Metab.* (2016) 13:253–6. doi: 10.11138/ccmbm/2016.13.3.253
14. Wang HD, Boyce AM, Tsai JY, Gafni RI, Farley FA, Kasa-Vubu JZ, et al. Effects of denosumab treatment and discontinuation on human growth plates. *J Clin Endocrinol Metab.* (2014) 99:891–7. doi: 10.1210/jc.2013-3081
15. Ganda K, Seibel MJ. Rapid biochemical response to denosumab in fibrous dysplasia of bone: report of two cases. *Osteoporos Int.* (2014) 25:777–82. doi: 10.1007/s00198-013-2585-1
16. Benhamou J, Gensburger D, Chapurlat R. Transient improvement of severe pain from fibrous dysplasia of bone with denosumab treatment. *Joint Bone Spine.* (2014) 81:549–50. doi: 10.1016/j.jbspin.2014.04.013
17. Majoor BCJ, Papapoulos SE, Dijkstra PDS, Fiocco M, Hamdy NAT, Appelman-Dijkstra NM. Denosumab in patients with fibrous dysplasia previously treated with bisphosphonates. *J Clin Endocrinol Metab.* (2019) 104:6069–78. doi: 10.1210/jc.2018-02543
18. Raborn LN, Burke AB, Ebb DH, Collins MT, Kaban LB, Boyce AM. Denosumab for craniofacial fibrous dysplasia: duration of efficacy and post-treatment effects. *Osteoporos Int.* (2021) 32:1889–93. doi: 10.1007/s00198-021-05895-6
19. Darnall BD, Sturgeon JA, Cook KF, Taub CJ, Roy A, Burns JW, et al. Development and validation of a daily pain catastrophizing scale. *J Pain.* (2017) 18:1139–49. doi: 10.1016/j.jpain.2017.05.003
20. Quartana PJ, Campbell CM, Edwards RR. Pain catastrophizing: a critical review. *Expert Rev Neurother.* (2009) 9:745–58. doi: 10.1586/ern.09.34
21. Zhang F, Xie G, Leung L, Mooney MA, Epprecht L, Norton I, et al. Creation of a novel trigeminal tractography atlas for automated trigeminal nerve identification. *Neuroimage.* (2020) 220:117063. doi: 10.1016/j.neuroimage.2020.117063
22. Xie G, Zhang F, Leung L, Mooney MA, Epprecht L, Norton I, et al. Anatomical assessment of trigeminal nerve tractography using diffusion MRI: a comparison of acquisition b-values and single- and multi-fiber tracking strategies. *Neuroimage Clin.* (2020) 25:102160. doi: 10.1016/j.nicl.2019.102160
23. Boyce AM, Kelly MH, Brillante BA, Kushner H, Wientroub S, Riminucci M, et al. A randomized, double blind, placebo-controlled trial of alendronate treatment for fibrous dysplasia of bone. *J Clin Endocrinol Metab.* (2014) 99:4133–40. doi: 10.1210/jc.2014-1371
24. Sweeney K, Kaban LB. Natural history and progression of craniofacial fibrous dysplasia: a retrospective evaluation of 114 patients from massachusetts general hospital. *J Oral Maxillofac Surg.* (2020) 78:1966–80. doi: 10.1016/j.joms.2020.05.036
25. Lee JS, FitzGibbon EJ, Chen YR, Kim HJ, Lustig LR, Akintoye SO, et al. Clinical guidelines for the management of craniofacial fibrous dysplasia. *Orphanet J Rare Dis.* (2012) 7:S2. doi: 10.1186/1750-1172-7-S1-S2
26. Tucker-Bartley A, Lemme J, Gomez-Morad A, Shah N, Veliu M, Birklein F, et al. Pain phenotypes in rare musculoskeletal and neuromuscular diseases. *Neurosci Biobehav Rev.* (2021) 124:267–90. doi: 10.1016/j.neubiorev.2021.02.009
27. Seifert T. The relationship of migraine and other headache disorders to concussion. *Handb Clin Neurol.* (2018) 158:119–26. doi: 10.1016/B978-0-444-63954-7.00012-4
28. Ishii R, Schwedt TJ, Trivedi M, Dumkrieger G, Cortez MM, Brennan KC, et al. Mild traumatic brain injury affects the features of migraine. *J Headache Pain.* (2021) 22:80. doi: 10.1186/s10194-021-01291-x
29. Glasser MF, Smith SM, Marcus DS, Andersson JL, Auerbach EJ, Behrens TE, et al. The human connectome project's neuroimaging approach. *Nat Neurosci.* (2016) 19:1175–87. doi: 10.1038/nn.4361

Conflict of Interest: AB through the National Institute of Dental and Craniofacial Research, receives support from Amgen, Inc., for an investigator sponsored study of denosumab treatment for fibrous dysplasia.

The remaining authors declare that the research was conducted in the absence of any commercial or financial relationships that could be construed as a potential conflict of interest.

The reviewer A-MH declared a past co-authorship with one of the authors AB to the handling Editor.

frontiers | Frontiers in Neurology

ORIGINAL RESEARCH
published: 29 April 2022
doi: 10.3389/fneur.2022.858805

Age-Related Tortuosity of Carotid and Vertebral Arteries: Quantitative Evaluation With MR Angiography

*Zhe Sun[1,2], Dengrong Jiang[3], Peiying Liu[3], Marco Muccio[1], Chenyang Li[1,2], Yan Cao[4], Thomas M. Wisniewski[5,6,7,8], Hanzhang Lu[3] and Yulin Ge[1]**

[1] Department of Radiology, NYU Grossman School of Medicine, New York, NY, United States, [2] Vilcek Institute of Biomedical Science, NYU Grossman School of Medicine, New York, NY, United States, [3] Department of Radiology and Radiological Science, Johns Hopkins University School of Medicine, Baltimore, MD, United States, [4] Department of Mathematical Sciences, University of Texas at Dallas, Richardson, TX, United States, [5] Department of Neurology, NYU Grossman School of Medicine, New York, NY, United States, [6] Department of Pathology, NYU Grossman School of Medicine, New York, NY, United States, [7] Department of Psychiatry, NYU Grossman School of Medicine, New York, NY, United States, [8] Center for Cognitive Neurology, NYU Grossman School of Medicine, New York, NY, United States

Background and Purpose: The vascular tortuosity (VT) of the internal carotid artery (ICA), and vertebral artery (VA) can impact blood flow and neuronal function. However, few studies involved quantitative investigation of VT based on magnetic resonance imaging (MRI). The main purpose of our study was to evaluate the age and gender effects on ICA and VA regarding the tortuosity and flow changes by applying automatic vessel segmentation, centerline tracking, and phase mapping on MR angiography.

Methods: A total of 247 subjects (86 males and 161 females) without neurological diseases participated in this study. All subjects obtained T1-weighted MRI, 3D time-of-flight MR angiography, and 2D phase-contrast (PC) MRI scans. To generate quantitative tortuosity metrics from TOF images, the vessel segmentation and centerline tracking were implemented based on Otsu thresholding and fast marching algorithms, respectively. Blood flow and velocity were measured using PC MRI. Among the 247 subjects, 144 subjects (≤60 years, 49 males/95 females) were categorized as the young group; 103 subjects (>60 years, 37 males/66 females) were categorized as the old group.

Results: Independent *t*-test showed that older subjects had higher tortuosity metrics, whereas lower blood flow and velocity than young subjects ($p < 0.0025$, Bonferroni-corrected). Cerebral blood flow calculated using the sum flux of four target arteries normalized by the brain mass also showed significantly lower values in older subjects ($p < 0.001$). The age was observed to be positively correlated with the VT metrics. Compared to the males, the females demonstrated higher geometric indices within VAs as well as faster age-related vascular profile changes. After adjusting age and gender as covariates, maximum blood velocity is negatively correlated with geometric measurements. No association was observed between blood flux and geometric measures.

Conclusions: Vascular auto-segmentation, centerline tracking, and phase mapping provide promising quantitative assessments of tortuosity and its effects on blood flow. The neck arteries demonstrate quantifiable and significant age-related morphological and

OPEN ACCESS

Edited by:
Chengcheng Zhu, University of Washington, United States

Reviewed by:
Zhang Shi, Fudan University, China
Ruiting Zhang, Zhejiang University, China

***Correspondence:**
Yulin Ge
yulin.Ge@nyulangone.org

Specialty section:
This article was submitted to Applied Neuroimaging, a section of the journal Frontiers in Neurology

Received: *20 January 2022*
Accepted: *30 March 2022*
Published: *29 April 2022*

Citation:
Sun Z, Jiang D, Liu P, Muccio M, Li C, Cao Y, Wisniewski TM, Lu H and Ge Y (2022) Age-Related Tortuosity of Carotid and Vertebral Arteries: Quantitative Evaluation With MR Angiography. Front. Neurol. 13:858805. doi: 10.3389/fneur.2022.858805

hemodynamic alterations. Moreover, females showed more distinct vascular changes with age. Our work is built upon a comprehensive quantitative investigation of a large cohort of populations covering adult lifespan using MRI, the results can serve as reference ranges of each decade in the general population.

Keywords: aging, carotid artery, vascular tortuosity, blood flow, magnetic resonance angiography

INTRODUCTION

The internal carotid artery (ICA) and vertebral artery (VA) are main feeding arteries of the brain and play critical roles in supplying energy and maintaining normal neuronal function. It has been widely reported in the literatures that extracranial arteries are prone to demonstrate geometric and morphological variants with normal aging (1–3). Due to the long courses of extracranial arteries in the neck region, the age-related morphological variations represent distinctly as abnormal twisting, turns, and loops found in the elderly in contrast to the normal anatomical turns. These vascular morphological changes can limit the blood flow, which may lead to stroke and other ischemic events, such as the transit ischemic attack and vertigo (4–8). Thus, it is clinically important to assess vascular tortuosity (VT) for a better understanding how VT can affect the blood flow. Non-invasive clinical imaging techniques, particularly ultrasound and MRI, stand at the epicenter of VT and flow assessment in the elderly population. Compared to ultrasound, MRI is operator-independent with higher fidelity, larger field of view (FOV), and greater capacity of deep vessel detection (e.g., VA). While these age-related tortuosity changes raise the awareness of their etiology, pathophysiological mechanisms, and clinical monitoring, few published studies have quantified the VT and its correlation with blood flow using MRI.

The aging and the mechanical injury of vessel wall were proposed as the two important pathological processes of VT. With aging, degenerative changes of extracellular matrix and endothelium result in arterial wall remodeling, stiffness, and tortuosity (9). The mechanical factors also increase the incidence of VT secondary to the repetitive cardiac pulsatile flow effects accumulated over the lifespan in the elderly. Responding to constantly imposed forces of blood flow, the vessels become tortuous associated with elastin degradation and proinflammatory signaling activation (10, 11), Conversely, VT impedes flow effects and affect vascular wall shear stress (WSS) associated with platelets activation and thrombosis (12). These have been observed clinically with decreased cerebral blood flow (CBF) in the elderly with more tortuosity vessels (13, 14). Ultrasound studies have shown that blood velocities in ICAs were stable up to the age of 40–45 years and decreased afterward associated with increased tortuosity appearances (15, 16). However, the clear associations between tortuosity and flow changes in normal aging have not been established.

Time-of-flight (TOF) and phase-contrast (PC) imaging are two MR angiographic (MRA) techniques commonly used in the routine clinical settings for vascular characteristic inspection (17–20). The present study aims to comprehensively quantify the age-related VT of ICAs, and VAs and their blood flow by applying automated vessel segmentation, centerline tracking, and phase mapping on MRA. The methods developed in this study can potentially be implemented in clinical scans for grading the vessel integrity of major brain feeding arteries by referring to quantitative metrics of vascular characteristics.

MATERIALS AND METHODS

Study Population

After the institutional review board's approval, 251 subjects were initially recruited, and four of them were excluded due to the abnormal arteries on TOF–MRA or missing unilateral VA, which is a type of variant anatomy. Finally, 247 individuals (86 males and 161 females) were enrolled with age ranging from 20 to 88 years in this retrospective study. Among the 247 subjects, 144 participants younger than and including 60 years old were classified as the young group; 103 participants older than 60 years old were classified as the old group. The participants of our study were subset of the Dallas Lifespan Brain Study (DLBS) designed to understand the preservation and decline of cognitive function. All participants underwent screening and had no contraindications to MRI scan (pacemaker, implanted metallic objects, and claustrophobia) and were generally of good health, without serious medical conditions such as neurological disease, brain injury, shaking, or medications affecting cognitive functions (7). All participants were right-handed native English speaker with Mini-Mental State Exam (MMSE) score of 26 or greater. Among the 247 participants, 232 had blood pressure (BP) (i.e., systolic and diastolic) that was measured 5 times around the time of MRI scan. The mean systolic and diastolic BP of the five measurements was then used for the further analyses related to tortuosity (21). Among them, 33 participants with a diagnosis of hypertension were taking antihypertensive medications, most of which were angiotensin covering enzyme inhibitors, beta-blockers, and angiotensin II receptor antagonists (7).

The MR Imaging Acquisition

The MR imaging was performed using a 3T MRI system with an 8-channel head coil. Also, T1-weighted magnetization-prepared-rapid-acquisition-of-gradient-echo (MPRAGE), 3D-TOF, and 2D non-gated PC–MRI scans were acquired for each subject. The MPRAGE sequence used the following imaging parameters: Repetition time (TR)/echo time (TE)/flip angle (FA) = 8.1 ms/3.7 ms/12°, voxel size = 1 mm × 1 mm × 1 mm. For the purpose of the vessel segmentation and PC–MRI positioning, the TOF was acquired with the following parameters: TR/TE/FA = 23 ms/3.45 ms/18°, voxel size = 1.0 mm × 1.0 mm × 1.5 mm, number

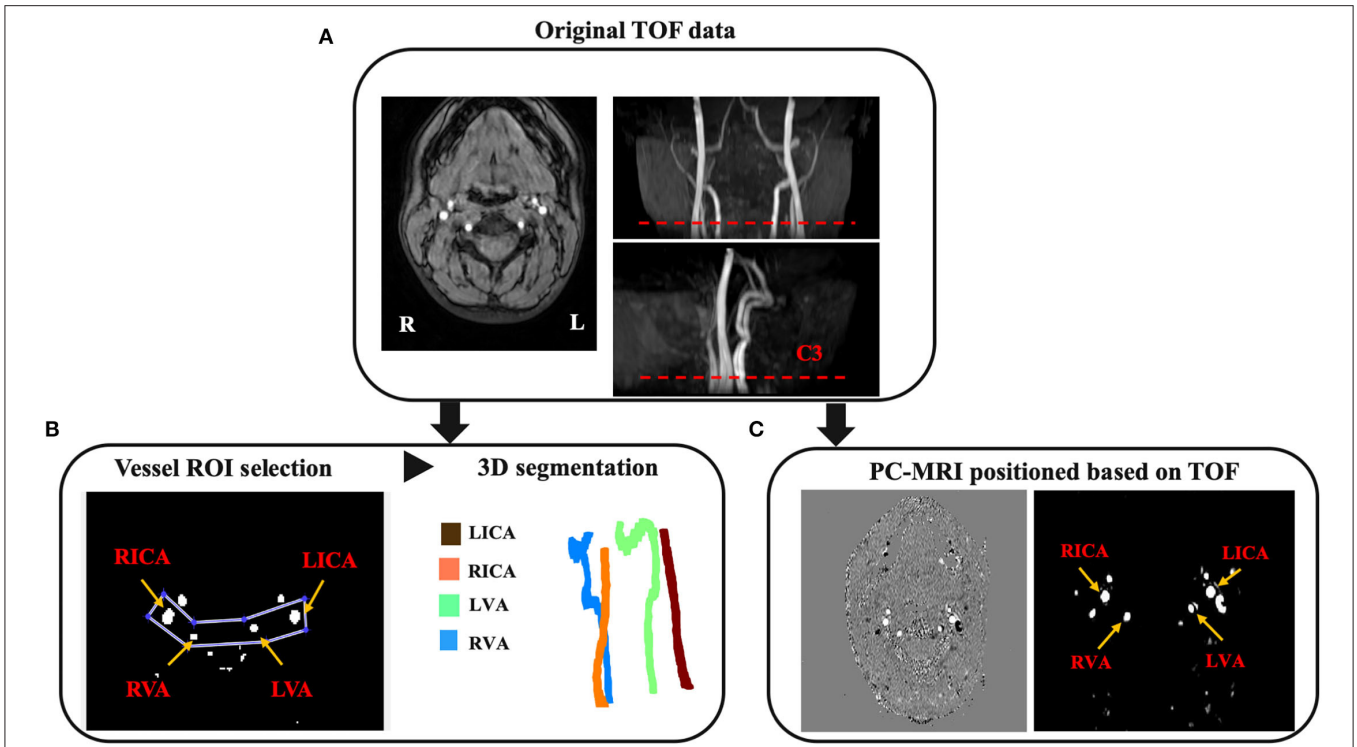

FIGURE 1 | Image postprocessing workflow. **(A)** The TOF magnetic resonance angiography (MRA) including raw axial images, coronal and sagittal MIP images are acquired for the purpose of vessel segmentation and PC-MRI positioning. The PC-MRI scan plane is positioned around the level of cervical vertebrate C3 (red dash line), where above the carotid bifurcations. **(B)** The ROI enclosing target arteries and surrounding tissues are selected for the purpose of vessel segmentation and tortuosity measurement. Arteries can be detected based on the mean and standard deviation of the object region. **(C)** Corresponding phase image (left) and magnitude image (right) from the feeding arteries positioned at the level around C3 [red dash line in **(A)**].

of slices = 47, a 60-mm saturation band positioned above the imaging slab, scan time = 1 min 26 s. The top of the angiographic imaging slab was positioned at the level of the bottom of pons, with the bottom FOV margin at the level around cervical spine C4, covering the cervical segment of ICA. Based on the coronal maximum intensity projection (MIP) images from TOF, the non-gated PC–MRI scan covering the four feeding arteries was conducted around the level of cervical spine C3 above the carotid bifurcations with following parameters: TR/TE/FA = 20 ms/7 ms/15°, voxel size = 0.45 mm × 0.45 mm × 5 mm, velocity encoding (VENC) = 80 cm/s, scan duration = 30 s.

Segmentation, Centerline Tracking and Quantitative Tortuosity Measurements of Neck Vessels

We segmented and tracked the centerline of the vessels from 3D-TOF angiogram using the in-house code run on MATLAB 2020a (MATLAB and statistics Toolbox Release 2020a, MathWorks, Inc. Natick, MA). **Figure 1** shows the image postprocessing workflow. A preliminary ROI enclosing the targeting arteries was drawn. The artery region $T(x)$ consisting pixels x was determined using the following equation:

$$T(x) = I(x) - \mu - j \cdot \sigma,$$

where $I(x)$ is the intensity of the object region (Ω) consisting of both the arteries and the surrounding tissues; μ and σ are the mean and standard deviation intensities of Ω, respectively. Since the signal intensities of the arteries are inhomogeneous, we need to start with a high value of j and decrease it gradually until an optimal value was reached. The optimal value of j, which varied between subjects, should be high enough to exclude surrounding tissue meanwhile low enough to include the arteries (22). Although j was determined subject-by-subject basis, we found an empirical search range of 6–4 in descending order was applicable for most cases. After the artery pixels were determined for each slice, they were connected if their faces or edges touched so as to get the 3D segmentation of arteries.

Based on the arterial surface derived from 3D segmentation, the arterial centerline was acquired using multi-stencils fast marching algorithm, which calculates the shortest distance from a source point to all other pixels in an image volume by solving the Eikonal equation along stencils that cover neighboring points entirely (23). The centers of these level curves formed the skeleton representing the artery. The coordinates of the extracted arterial skeleton can be acquired to quantitatively assess the VT. We proposed to use tortuosity index (TI), bending length (BL), and inflection count metric (ICM) as quantitative VT indices (**Figure 2**). The TI is the ratio between the actual length (AL) and the direct length (DL). The BL is the maximum perpendicular

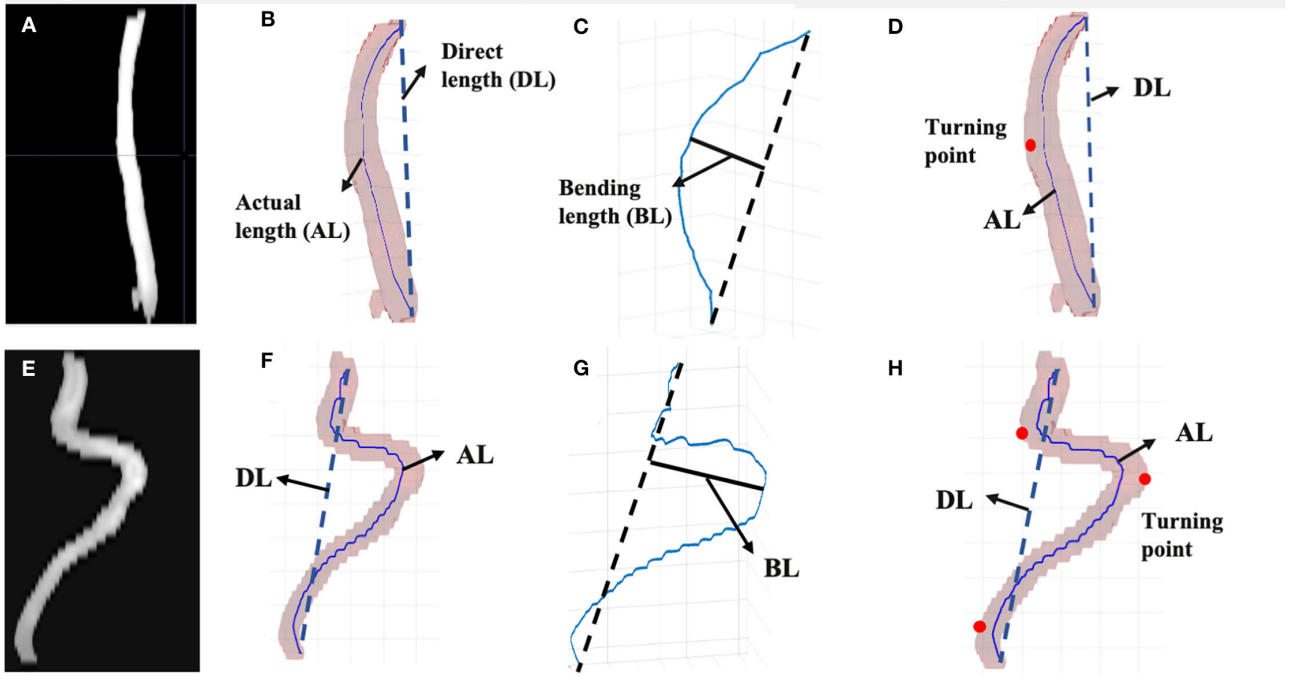

FIGURE 2 | Segmentation and the centerline of the vessel were acquired. The measurements included TI, BL, and ICM. **(A)** Left ICA vessel segmentation of a young subject (≤ 60 years old). **(B)** The TI is the ratio between AL and DL. **(C)** The BL is the distance between the foremost points on the vessel path and the start-end points link. **(D)** The ICM is the product of turning points number (red dots) and TI. Corresponding vessel segmentation and measurements of an old subject (>60 years old) are shown in parts **(E–H)**.

distance between the AL and the DL, reflecting the extent of curving. The ICM is the product of turning points number (N) and TI, which takes turning frequency into consideration. Here, N was determined by visually checking the centerline skeleton.

Postprocessing of PC-MRI

Each PC–MRI scan generated a phase image and a magnitude image. The data processing of PC–MRI followed previously reported method (24). Briefly, the region of interests (ROIs) were manually drawn on the magnitude images by circling the targeted artery (bilateral ICAs and VAs) based on the brightness of the voxels (25). A signal intensity threshold set to be 5 times the background noise was then applied to the magnitude image to get vessel mask. The mask was then applied to the phase image to calculate blood flux and maximum blood velocity (MaxV). The unit volume CBF (in ml/min/100 g) was calculated as the sum of blood flux of the four arteries normalized to the brain's parenchyma mass obtained from T1WI.

Evaluation of Accuracy and Reproducibility

We used maximal intensity projection (MIP) images (both coronal and sagittal planes) generated from TOF–MR angiogram as a reference to evaluate the accuracy of arterial vessel segmentation. After overlaying the acquired centerline on the arterial segment, it would be easy to identify false branches and tell the tracking accuracy. All the segmented arteries and centerline images were visually inspected and the arteries with incomplete processing or aborted algorithms were excluded.

In addition, a scan–rescan study was performed to evaluate the reproducibility of 3D-TOF vessel tortuosity measurements. Seven young, healthy subjects (4 males, 3 females, 26.4 ± 3.7 years) underwent two MRI sessions with a 5-min break in between. During each session, 3D-TOF angiogram and PC-MRI scan were acquired. Inter-session coefficient of variation (CoV) of tortuosity measurements was calculated as follows:

$$CoV_{intersession} = \frac{|measument_1 - measurement_2|}{\sqrt{2} \cdot Mean(measurement_1, measurement_2)}$$

where $measurement_1$ and $measurement_2$ represent the TI, BL, or ICM from two scan and rescan sessions, respectively. These two separate scans are supposed to consist of repositioning error, and TOF–MRA noise.

Statistical Analysis

Two-tailed t-test was applied to identify VT and flow differences between young and old groups. Since 20 analyses on the same dependent variable were being performed, Bonferroni-corrected alpha ($\alpha_{corrected} = 0.0025$) was calculated to control the Type I error and a value of $p \leq 0.0025$ was considered

TABLE 1 | The ICA VT and flow measurements of each age decade.

Age group		20–30 ($n = 42$)	31–40 ($n = 32$)	41–50 ($n = 36$)	51–60 ($n = 34$)	61–70 ($n = 46$)	71–80 ($n = 32$)	>80 ($n = 25$)
Demographic data								
Age		24.31 ± 2.97	34.88 ± 2.73	45.58 ± 3.02	54.91 ± 3.03	66.24 ± 3.16	73.4 ± 2.60	83.67 ± 2.46
Gender		14 M/ 28 F	10 M/ 22 F	15 M/ 21 F	10 M/ 24 F	17 M/ 29 F	10 M/ 22 F	10 M/ 15 F
Hypertension		0	1	2	4	11	9	7
BP		111/75	111/77	119/80	127/83	136/84	139/84	141/81
The VT measurements								
TI	LICA	1.70 ± 0.37	1.72 ± 0.30	1.83 ± 0.43	2.09 ± 0.70	2.36 ± 0.69	2.59 ± 0.76	2.87 ± 1.04
	RICA	1.74 ± 0.43	1.89 ± 0.53	1.92 ± 0.53	2.22 ± 0.61	2.64 ± 0.98	2.57 ± 0.61	3.00 ± 0.79
BL	LICA	19.84 ± 7.37	21.77 ± 6.71	22.69 ± 7.01	28.44 ± 10.4	31.44 ± 10.45	36.26 ± 12.97	39.24 ± 13.48
	RICA	19.49± 7.44	24.54 ± 8.05	24.30 ± 6.37	31.1 ± 10.45	34.56 ± 12.93	35.05 ± 8.51	43.05 ± 10.6
ICM	LICA	2.37 ± 1.22	2.38 ± 1.01	3.18 ± 2.22	4.53 ± 2.69	5.25 ± 2.49	5.70 ± 2.74	6.22 ± 3.78
	RICA	2.73± 2.12	3.17± 1.87	3.51 ± 2.56	4.8 ± 2.79	6.02 ± 3.98	6.14 ± 3.03	6.68 ± 4.11
Flow measurements								
Blood flux	LICA	286.37 ± 59.09	269.90 ± 46.10	246.26 ± 51.93	245.42 ± 56.47	222.71 ± 56.12	196.01 ± 62.71	191.82 ± 54.8
	RICA	275.43 ± 56.67	265.6 ± 49.56	258.88 ± 51.98	222.88 ± 56.54	213.47 ± 59.95	200.86 ± 52.16	199.06 ± 45.4
MaxV	LICA	36.17 ± 8.20	34.69 ± 9.33	34.7 ± 8.31	31.26 ± 8.4	25.93 ± 8.05	25.54 ± 6.88	22.07 ± 6.0
	RICA	36.61 ± 8.18	36.18 ± 8.04	37.22 ± 8.81	32.21 ± 9.42	26.81 ± 9.1	26.18 ± 5.86	25.19 ± 6.58

BP, blood pressure presenting as systolic/diastolic with 15 subjects' measurements missing. LICA, left internal carotid artery; RICA, right carotid artery; TI, tortuosity index; BL, bending length (mm); ICM, inflection count metric; Blood flux in ml/min; MaxV, maximum blood velocity, in cm/s.

statistically significant for multiple comparisons and correlation studies. The Pearson correlation coefficients (r) were calculated to reveal the relationship between age and each vascular feature respectively. The multivariate linear regression was also performed using age as independent variable, VT and flow measurements as dependent variables, and BP (mean systolic and diastolic) measurements as covariates. Since the previous study showed hypertension might be associated with arteriosclerotic and vessel wall changes, we included these analyses to remove the hypertension effects from aging. To determine whether there is a statistically significant difference of VT and flow measurements between hypertension and normotension, 33 age/gender-matched non-hypertensive subjects (age: 67.91 ± 11.85; 24 females/9 males) were chosen to compare with the 33 hypertensive subjects (age: 69.53 ± 12.4; 24 females/9 males) using Student's t-test. We further split the cohort into females and males. Two-tailed t-test was applied to identify VT and flow differences between male and female groups. Univariate linear regression analyses were performed to investigate relationship and coefficients between age and vascular features for different genders. The association between tortuosity and blood flow was calculated using multivariate linear regression, treating age, gender, and each VT measurement as regressors. GraphPad Prism 8 was used for the statistical analysis.

RESULTS

Demographic Characteristics

The descriptive statistics associated with blood pressure, and vascular profiles of ICA across the seven age decade groups are reported in **Table 1**. A detailed information of females and males in each decade group are reported in **Supplementary Tables 1** and **2**, respectively. Among 247 subjects (aged 53.23 ± 19.62 years, 86 males/161 females), we identified 144 younger subjects with age less than and including 60 years (aged 39.20 ± 12.11, 49 males/95 females) and 103 older subjects with age more than 60 years (aged 72.86 ± 7.5, 37 males/66 females). The mean systolic (137.8 ± 16.5 mm Hg) and diastolic (83.2 ± 9.6 mm Hg) BP of participants in old group was significantly higher than that of young subjects (116.7 ± 13.6 and 78.7 ± 9.6, respectively) ($p < 0.001$). Chi-square analysis did not reveal a statistically significant difference in gender for each age group.

Group Comparison of VT and Blood Flow

As shown in **Figure 3**, VTs were widely observed in the older subject group. Quantitatively, ICAs of older subjects demonstrated significantly higher TI (left = 2.56 ± 0.83, right = 2.70 ± 0.84), BL (left = 34.78 ± 12.3, right = 36.92 ± 11.7), and ICM (left = 5.65 ± 2.92, right = 6.28 ± 3.76) than younger subjects' TI (left = 1.83 ± 0.49, right = 1.93 ± 0.55), BL (left = 22.96 ± 8.6, right = 24.49 ± 9.11), and ICM values (left = 3.09 ± 2.08, right = 3.52 ± 2.46) ($p < 0.001$ for all; details can be found in **Table 1**); significantly higher ICM of left vertebral artery (LVA) ($p < 0.001$) and BL of right vertebral artery (RVA) ($p < 0.001$) could be observed in older subjects. The TI, BL values of LVA and TI, ICM of RVA did not show significant difference. The old subjects demonstrated significantly lower blood flux, and MaxV for all arteries compared to young subjects. Compared to global-wise reports, unit mass CBF was significantly lower in old (49.15 ± 10.56 ml/min/100 g) as compared to young participants (55.77 ± 9.89 ml/min/100 g) ($p < 0.001$). A detailed descriptive statistics and p-values can be found in **Table 2**.

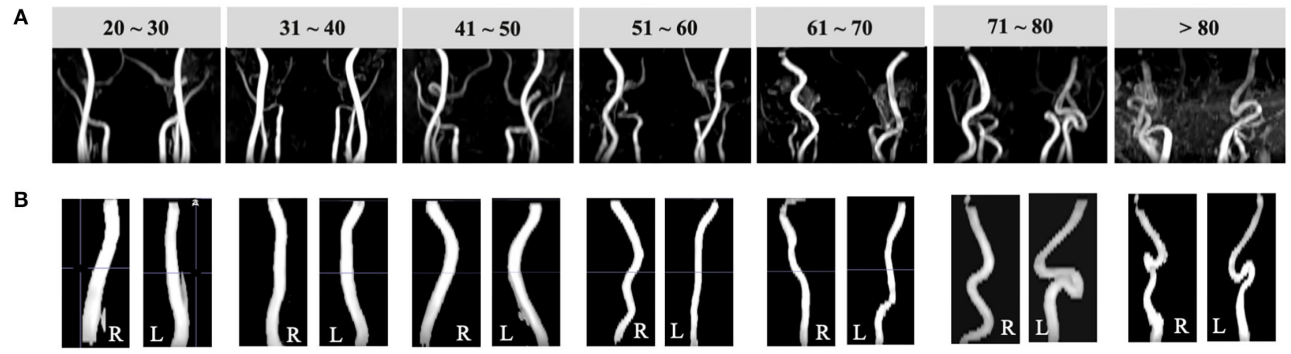

FIGURE 3 | Illustrations of vessel segmentation for each decade over the adult lifespan. **(A)** Coronal TOF images (radiological view) of subjects from each decade demonstrate arteries become more tortuous with aging. **(B)** Left and right ICA segmentation results of subjects of age from 20 to 80 years.

TABLE 2 | Comparison of VT and flow measurements between young ($n = 144$) and old ($n = 103$) groups.

	LICA			RICA		
	Young	**Old**	***p***	**Young**	**Old**	***p***
The VT measurements						
TI	1.83 ± 0.49	2.56 ± 0.83	<0.001	1.93 ± 0.55	2.70 ± 0.84	<0.001
BL	22.96 ± 8.6	34.78 ± 12.33	<0.001	24.49 ± 9.11	36.92 ± 11.7	<0.001
ICM	3.09 ± 2.08	5.65 ± 2.92	<0.001	3.52 ± 2.46	6.28 ± 3.76	<0.001
Flow measurements						
Blood flux	263.01 ± 56.3	206.08 ± 59.1	<0.001	256.70 ± 56.7	206.05 ± 54.0	<0.001
MaxV	34.31 ± 8.6	24.91 ± 7.4	<0.001	35.63 ± 8.7	26.22 ± 7.6	<0.001
	LVA			**RVA**		
The VT measurements						
TI	1.24 ± 0.2	1.32 ± 0.26	0.01*	1.3 ± 0.4	1.36 ± 0.27	0.18*
BL	4.77 ± 2.52	5.83 ± 2.94	0.003*	5.07 ± 2.79	6.44 ± 3.18	<0.001
ICM	1.54 ± 0.76	2.14 ± 1.27	<0.001	1.78 ± 1.75	2.28 ± 1.29	0.01*
Flow measurements						
Blood flux	102.54 ± 43.3	84.38 ± 38.0	<0.001	86.83 ± 39.7	68.34 ± 32.8	<0.001
MaxV	22.99 ± 6.7	17.67 ± 5.3	<0.001	20.09 ± 6.0	15.75 ± 4.8	<0.001

LICA, left internal carotid artery; RICA, right carotid artery; LVA, left vertebral artery; RVA, right vertebral artery; TI, tortuosity index; BL, bending length (mm); ICM, inflection count metric; Blood flux is in ml/min; MaxV, maximum blood velocity, is in cm/s. Adjusted $p \leq 0.0025$ is the threshold for significance.
**There is no significant difference ($p > 0.0025$).*

Age Effects on VT and Flow Measurements

According to the Pearson correlation results, TI (r of left: 0.52 and right: 0.52), BL (r of left: 0.55 and right: 0.61), and ICM (r of left: 0.52 and right: 0.43) were positively correlated with age for bilateral ICAs ($p < 0.001$). The ICM of bilateral VAs (r of left: 0.29 and right: 0.19, $p < 0.001$ and $p = 0.002$, respectively) and BL of RVA ($r = 0.2$, $p = 0.002$) were positively correlated with age. Significantly, the negative correlations were identified between the flow measurements and age for all arteries ($p < 0.001$). A detailed r and p-values were summarized in **Table 3**. Separate multivariate linear regression was performed and showed statistical significance for tortuosity measurements of bilateral ICAs, as well as ICM of bilateral VAs in relation with age after adjusting mean systolic and diastolic BP as covariates ($p < 0.0025$ for all measurements). Similarly, the multivariate linear regression result showed significant associations for blood flux and maximum velocity of all four arteries ($p < 0.001$) in relation with age.

Hypertension Effects on VT and Flow Measurements

Student's t-test did not show statistically significant difference in VT and flow measurements for all vessels between hypertensive subjects and age- and gender-matched non-hypertensive subjects ($p > 0.05$ for all measurements). The multivariate linear regression showed systolic and diastolic BP measured before MRI did not significantly associated with VT and blood flow

TABLE 3 | Age in relation to the VT and blood flow measurements.

	LICA		RICA		LVA		RVA	
	r	*p*	*r*	*p*	*r*	*p*	*r*	*p*
The VT measurements								
TI	0.52	<0.001	0.52	<0.001	0.13	0.04*	0.07	0.26*
BL	0.55	<0.001	0.61	<0.001	0.15	0.02*	0.20	0.002
ICM	0.52	<0.001	0.43	<0.001	0.29	<0.001	0.19	0.002
Flow measurements								
Blood flux	−0.52	<0.001	−0.48	<0.001	−0.27	<0.001	−0.29	<0.001
MaxV	−0.52	<0.001	−0.49	<0.001	−0.44	<0.001	−0.41	<0.001

r: Pearson correlation coefficient; Adjusted p ≤ 0.0025 is the threshold for significance.
**There is no significant difference (p > 0.0025).*

TABLE 4 | Comparison of VT and flow measurements between males ($n = 86$) and females ($n = 161$) regardless of age.

	LICA			RICA		
	Male	**Female**	***p***	**Male**	**Female**	***p***
The VT measurements						
TI	2.08 ± 0.73	2.16 ± 0.76	0.46*	2.13 ± 0.76	2.31 ± 0.79	0.08*
BL	28.5 ± 12.12	27.57 ± 11.71	0.56*	29.67 ± 11.5	29.68 ± 12.2	0.99*
ICM	3.68 ± 2.87	4.41 ± 2.68	0.05*	3.99 ± 3.32	5.03 ± 3.35	0.02*
Flow measurements						
Blood flux	230.06 ± 60.3	244.18 ± 65.1	0.02*	223.55 ± 58.3	242 ± 61.6	0.02*
MaxV	28.62 ± 7.9	31.33 ± 9.95	0.02*	29.8 ± 8.39	32.72 ± 9.89	0.02*
	LVA			**RVA**		
The VT measurements						
TI	1.22 ± 0.21	1.30 ± 0.24	0.006*	1.23 ± 0.25	1.37 ± 0.39	<0.001
BL	4.34 ± 2.28	5.67 ± 2.87	<0.001	4.43 ± 2.40	6.30 ± 3.13	<0.001
ICM	1.50 ± 0.64	1.94 ± 1.18	<0.001	1.44 ± 0.68	2.28 ± 1.84	<0.001
Flow measurements						
Blood flux	89.33 ± 40.1	97.98 ± 42.9	0.11*	70.99 ± 33.8	83.46 ± 39.5	0.01*
MaxV	19.11 ± 7.0	21.66 ± 5.72	0.002	16.69 ± 5.99	19.13 ± 4.57	0.001

Adjusted p ≤ 0.0025 is the threshold for significance.
**There is no significant difference (p > 0.0025).*

measurements ($p > 0.05$ for all measurements) after adjusting for age as a covariate.

Gender Effects on VT and Flow Measurements

To further investigate the gender effects, we then compared VT and flow measurements between males (age: 53.62 ± 20.07) and females (age: 53.04 ± 19.45) regardless of age. The VT and the flow of bilateral ICAs did not show any significant difference ($p > 0.0025$) between males and females. However, within the VA system, females showed significantly higher values of RVA TI (right = 1.37 ± 0.39), BL (left = 5.67 ± 2.87, right = 6.30 ± 3.13), and ICM (left = 1.94 ± 1.18, right = 2.28 ± 1.84) than those of males (TI: right = 1.22 ± 0.21; BL: left = 4.34 ± 2.28, right = 4.43 ± 2.28; ICM: left = 1.50 ± 0.64, right: 1.44 ± 0.68) ($p < 0.001$). Among flow measurements, males had lower MaxV for bilateral VAs ($p < 0.0025$). A detailed descriptive statistics and *p*-values can be found in **Table 4**.

We then applied linear regression model on four vessels to reveal the relationship between age and vascular characteristics in females and males separately. A detailed r^2 and coefficients were summarized in **Table 5**. Females had higher absolute values of coefficients, reflecting faster changing patterns associated with age, excluding blood flux of ICAs. We then chose LICA as the representative vessel to show the different changing trends of vascular profiles in relation to the age for different genders (**Figure 4**). Although *t*-test did not reveal significant gender difference for bilateral ICAs tortuosity, the general trend still could be observed that females have relatively higher values at elder stage than males.

TABLE 5 | The r^2 and coefficients of univariate linear regression analysis between age and vascular characteristics for males ($n = 86$) and females ($n = 161$).

	LICA						RICA					
	Male			Female			Male			Female		
	r^2	coeff	p	r^2	Coeff	p	r^2	coeff	p	r^2	coeff	p
TI	0.15	0.014	<0.001	0.35	0.023	<1e−4	0.27	0.019	<1e−4	0.28	0.022	<1e−4
BL	0.17	0.24	<0.01	0.40	0.38	<1e−4	0.33	0.33	<1e−4	0.40	0.40	<1e−4
ICM	0.11	0.05	0.002	0.40	0.09	<1e−4	0.19	0.06	<1e−4	0.20	0.08	<1e−4
Blood flux	0.34	−1.75	<1e−4	0.25	−1.66	<1e−4	0.27	−1.51	<1e−4	0.22	−1.47	<1e−4
MaxV	0.21	−0.18	<1e−4	0.30	−0.28	<1e−4	0.14	−0.15	<0.001	0.30	−0.28	<1e−4
	LVA						RVA					
TI	6e−3	8e−4	0.47*	0.03	2e−3	0.04*	4e−3	8e−4	0.55*	7e−3	2e−3	0.31*
BL	0.02	0.017	0.17*	0.02	0.02	0.05*	0.04	0.02	0.07*	0.05	0.04	0.005*
ICM	0.13	0.01	<0.001	0.10	0.02	<1e−4	0.05	7e−3	0.03*	0.05	0.02	0.005*
Blood flux	0.08	−0.58	<0.001	0.07	−0.60	<0.001	0.05	−0.39	0.03*	0.11	−0.65	<1e−4
MaxV	0.14	−0.10	<0.001	0.23	−0.17	<1e−4	0.13	−0.10	<0.001	0.20	−0.14	<1e−4

r^2: r squared; coeff: coefficients of linear regression; Adjusted $p \leq 0.0025$ is the threshold for significance.
**There is no significant difference ($p > 0.0025$).*

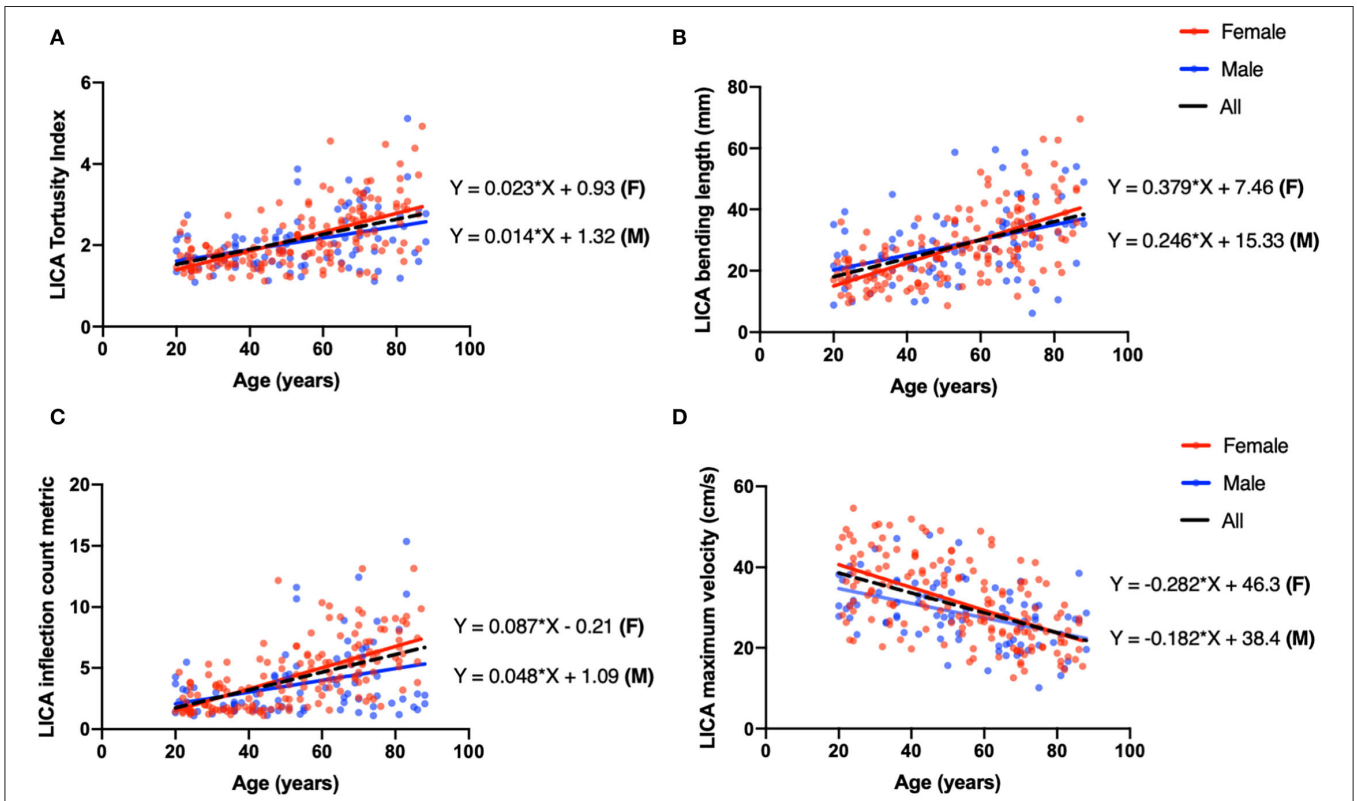

FIGURE 4 | Univariate linear regression plot of left ICA (LICA) as a representative vessel to show the coefficient difference between males (blue) and females (red). **(A)** The TI of LICA has a positive correlation with age (coeff = 0.018, $P < 0.001$, black dash line), and the linear correlation coefficients for males and females are 0.014 and 0.023, respectively. **(B)** Bending length (BL) of LICA is negatively correlated with age (coeff = 0.30, $p < 0.001$, black dash line), and the linear correlation coefficients for males and females are 0.246 and 0.379, respectively. **(C)** The ICM of LICA has significantly positive correlation with age (coeff = 0.072, $p < 0.001$, black dash line). The coefficients for males and females are 0.048 and 0.087. **(D)** The MaxV of LICA is negatively correlated with age (coeff = −0.247, $p < 0.001$, black dash line), and coefficients for males and females are −0.182 and −0.282.

TABLE 6 | The VT measurements in relation to the MaxV within ICAs.

Tortuosity measurements	*Coeff* (95% CI)	Adjusted r^2	*p*
TI			
LICA	−3.20 (−4.72 to −1.68)	0.32	<0.001
RICA	−3.60 (−5.09 to −2.11)	0.31	<0.001
BL			
LICA	−0.21 (−0.31 to −0.11)	0.32	<0.001
RICA	−0.16 (−0.27 to −0.05)	0.27	<0.001
ICM			
LICA	−0.69 (−1.18 to −0.35)	0.31	<0.001
RICA	−0.60 (−0.94 to −0.26)	0.28	<0.001

Coeff, coefficients of linear regression; Adjusted p ≤ 0.0025 is the threshold for significance.
**There is no significant difference (p > 0.0025).*

Association Between VT and Flow

Multivariate linear regression was performed to predict flow properties using age, gender and each tortuosity measurement as independent predictors. The VT had no significant contribution to the blood flow predictions ($p > 0.05$). Significant regression equations were found for MaxV within bilateral ICAs ($p < 0.001$). We then calculated the correlation coefficients between tortuosity and flow measurements. All tortuosity measurements of ICAs showed significantly negative correlation results. A detailed coefficients with 95% CI, adjusted r^2, and *p*-values are summarized in **Table 6**.

Accuracy and Reproducibility Evaluation

Regarding the accuracy evaluation in the large dataset of 247 subjects, the algorithm successfully extracted vascular skeleton for 204 subjects of all four arteries, with a subject-based successful rate of 82.6%. Artery-wise, the algorithm successfully provided the vascular skeleton for 941 arteries out of a total of 988 (i.e., 247 × 4) arteries with a success rate of 95.2%. Further investigation showed that we can get satisfied arterial segmentation if appropriate threshold was chosen using multi-level algorithms. However, in cases that the centerline tracking algorithm was failed are likely due to the following reasons: (1) The artery has complicated geometry such as coiling where two segments overlapped with each other; (2) the target vessel (i.e., ICA) was very close to the external carotid artery (ECA) and the algorithm falsely identified the ECA as part of ICA. The aforementioned failed vascular tracking can be improved by increasing the signal threshold so that the signals from unwanted vessels can be excluded and the overlapping between two segments or two vessels can be eliminated.

Among these seven subjects with test–retest scans, the algorithm successfully provided the vascular skeleton for all arteries with no failure. The mean and standard error of inter-session CoV for TI, BL, and ICM measurements were 3.0% ± 0.76%, 7.70% ± 2.27%, and 3.0% ± 0.76%, respectively, across all 28 arteries.

The details of the reproducibility of PC–MRI blood flow quantification have been reported by Liu and Peng et al. (25–27). It has been reported that the inter-session CoV for the blood flux across all 28 arteries was 5.25 ± 2.93% and the inter-session CoV for the unit CBF was reported as 7.41 ± 2.99%.

DISCUSSION

We applied MRA techniques to neck major brain feeding arteries to reveal the VT and flow changes in a large cohort across the adult lifespan. Older subjects demonstrated higher values of tortuosity measurements. Tortuosity of bilateral VAs are less evident than ICAs, which might be due to the anatomical restriction from the transverse foramina of the cervical spine. Age-related higher VT measurements correlate with lower blood flux and velocity in extracranial arteries, suggesting tortuosity changes in the elderly may limit the efficient blood supply and influence neuronal functions, particularly when neural activity is increased with high energy demand. Further, the results in this study provide quantitative VT measurements in each decade, which can be used as reference values for future clinical studies of patients.

Previous studies suggested that the hypertension was associated with damage of arterial walls, which potentially lead to vessel morphological alterations (6, 28). In this study, we did not find the significant effect of hypertension on VT or flow measurements in our cohort. This discrepancy might be attributable to the following factors. First, the pathophysiological effects of hypertension are dependent on the size of vessels where the resistance and BP will be higher for small vessels with narrow lumen (29). The vessels that, when relaxed, measured lesser than 400 μm in lumen diameter are the major site of vascular resistance, which included a network of small arteries (lumen ≈ 100 to 400 μm) and arterioles (<100 μm). The ICAs and VAs, however, are large arteries with relatively low resistance, and this may be why the tortuosity measurements were less affected by the hypertension. Second, the participants in this normal lifespan study are all healthy subjects from DLBS cohort without history of neurological disorders, such as stroke, transient ischemic attack (TIA), cognitive disorders or MMSE lower than 26. Those pathological conditions potentially complicated the interactions between blood pressure, blood flow, and vasculature topology. Third, the number of hypertensive subjects is relatively small, only 13% had diagnosed hypertension whose symptoms were controlled by taking antihypertensive medication; some of them had normal BP at the time of MRI. They are expected to be part of the normal aging process. Last, the mechanisms of vessel wall remodeling from elevated pulse wave velocity associated with hypertension may be different from that of normal aging. Hypertensive-related changes in large elastic arteries, i.e., ICA, represent as thickening of the vascular wall and increased intima-media thickness (IMT) instead of elastin fracture and collagen deposition seen in normal aging (9, 30). Finally, few studies applied quantitative VT assessment method as used in this study; and most of the previous studies revealed the effects of hypertension purely based on categorical data. However, more studies with larger and chronic hypertensive population are necessary to better understand how hypertension affects the vascular topology.

Gender is another important factor affecting vascular properties. It has been suggested that females are prone to have VT, stiffer large arteries and higher pulse pressure (31–33). While our study did not observe significant difference between females and males in bilateral ICAs, more evident age-related changing patterns can be observed in females. Underlying mechanisms may include variations in sex steroid levels and less stable intervertebral joints in females (34). After menopause, females are prone to stiffer and more tortuous large arteries, resulting from declining female sex steroids secretion associated with decreased elastin/collagen ratios (35). Consequently, the arterial wall remodeling can alter the profile of blood flow.

We hypothesized that vessel morphological changes (e.g., twists and turns) may cause a reduction of arterial pressure and flow velocity in the vessel. Therefore, we analyzed the relationship between VT changes characterized on TOF-MRI and blood flow characterized on PC-MRI. Tortuosity measurements were negatively correlated with blood velocity after adjusting age and gender as covariance, whereas, no association was observed between VT and blood flow. It suggested that age contributes the most to the flow reduction instead of tortuous change based on the multiple regression model. We speculated it was sufficient for the vascular elasticity to regulate the vascular resistance induced by VT aiming to maintain sufficient blood flow under resting conditions (36), whereas this regulatory capacity decreases with aging. The reduced blood velocity is attributable to an elevated resistance and reduced pulse pressure induced by VT. The alteration of flow velocity consequently affects WSS, an indicator of atherogenesis and cognitive function impairment (37, 38), which is determined by the velocity gradient from the vessel wall toward the vessel center. The WSS reduction induced by VT increases the risk of plaque formation mediated by inflammatory factors (39). Several *in vitro* numerical simulation studies have validated that VT results in pressure and flow drops in the distal vessel segments regardless of the bending angles (40, 41). These consequences could further lead to intracranial hypoperfusion and ischemic status.

Extracranial VT changes were investigated extensively with different imaging modalities and our findings are in agreement with most reports, which are largely based on qualitative visual inspection (8, 42–44). There is still an unmet clinical need for quantitative assessment of major brain feeding arteries using clinical imaging. Unlike the most geometric data derived from 2D planar analysis (45–47), our study established an automatic algorithm for 3D vessel segmentation, centerline tracking and VT quantification. While there are several advanced segmentation algorithms developed for complicated vasculature, we applied simplicity multilevel threshold-based segmentation by taking advantage of its fast process and high accuracy (26). Averaged processing time of segmentation, centerline tracking combined with VT computation for a single vessel is within 2 min. In this study, we characterized VT objectively using three rational indices, which addressed the urgency to overcome subjective visual assessment and establish a quantitative tortuosity measurement scheme in clinical settings.

Since our work is built upon a comprehensive quantitative investigation of a large cohort of healthy populations using MRI, the results can potentially serve as normal reference values of each decade in healthy aging. While many studies have been conducted using ultrasound, the accuracy might be limited due to ultrasound's inability and inefficiency to detect thin vessels deep in the tissue or partially hidden behind the bone structures, such as VAs. Meanwhile, the operative-dependent variabilities including the angle of insonation and anatomic location might be introduced. The advantages of MRI over ultrasound include larger coverage, deep vessel detection, and smaller measurement variability (48). Owing to the clinical accessibility and fast acquisition (<5 min), it is practical to perform TOF and PC-MRI as routine scans for quick evaluation of neck vessels regarding intracranial health. The fast and user-interaction algorithm developed in this study makes it feasible to be implemented in MRI scan workstation in the future and provide real-time quantitative measurements of vascular tortuosity.

Some potential limitations of our study should be acknowledged. First, we do not have clinical data regarding some cardiovascular risk factors such as family history of vascular disease, smoking, alcohol use, and hyperlipidemia. Although these risk factors may also be associated with the vessel tortuosity measurements, it is worth noting that the participants in this DLBS study were healthier and more educated than the general population by pre-study screening. Therefore, they were considered as "best-case-scenario" model representing the normal aging effect in the general population with less unwanted noise that potentially confound the biological process (7). Second, in this cohort, there were more female than male participants with the gender ratio almost 2:1, which is primarily due to the reason that females are more willing to participate for this study. However, the detailed tortuosity measurements based on gender were provided in **Supplementary Material**, and we did not find any gender distribution differences between young and old groups. Third, the vessel diameter or the vessel size was not measured in this study primarily due to the lack of robustness of the techniques used in this study. Last, the tortuosity evaluation for intracranial arteries was not included in this study although morphological variations can present in both intracranial and extracranial arterial segments. This is because the age-related changes of extracranial carotid and vertebral arteries are more common and distinguished due to their eminent anatomical course (no branches) and long length in the neck region. The intracranial segments are often obscured by their complicated route and branches with variable spatial relation with cranial nerve and cavernous sinus (49, 50), which are difficult to be reliably segmented with the methods of this study. The assessment of age-related intracranial VT should be assessed in future studies with specific techniques that are more robust to intracranial segments.

In summary, the levels of age-related VT changes can be quantitatively assessed with the developed vessel segmentation and centerline tracking methods based on fast and non-invasive MRA clinical imaging. Increased tortuosity and decreased

blood flow measurements were observed with aging. The blood flow velocity showed an inverse relationship with the tortuosity measurements. The quantitative evaluation of changes of these extracranial major feeding arteries can provide potential indicators of neurological disorders, which would both increase our general understanding of aging and improve clinical treatment and prevention through quantitative analysis of tortuosity levels.

DATA AVAILABILITY STATEMENT

The original contributions presented in the study are included in the article/**Supplementary Material**, further inquiries can be directed to the corresponding author.

ETHICS STATEMENT

The studies involving human participants were reviewed and approved by UT Southwestern Institutional Review Board. The patients/participants provided their written informed consent to participate in this study.

AUTHOR CONTRIBUTIONS

YG and HL contributed to the conceptualization and design of the study. ZS, DJ, PL, and YC contributed to the methodology and algorithms. ZS, DJ, and PL organized the database. ZS performed the statistical analysis. ZS and YG wrote the first draft of the manuscript. All authors contributed to manuscript revision, read, and approved the submitted version.

FUNDING

This study was funded by the National Institutes of Health Grants (RF1 NS11041, R56 AG060822, R01 NS108491, R13 AG067684, P30 AG066512, and P01 AG060882). This study is also supported by Alzheimer's Association (AARG-17-533484).

SUPPLEMENTARY MATERIAL

The Supplementary Material for this article can be found online at: https://www.frontiersin.org/articles/10.3389/fneur.2022.858805/full#supplementary-material

REFERENCES

1. Kamenskiy AV. Pipinos, II, Carson JS, MacTaggart JN, Baxter BT. Age and disease-related geometric and structural remodeling of the carotid artery. *J Vasc Surg.* (2015) 62:1521–8. doi: 10.1016/j.jvs.2014.10.041
2. Wen W, Luo R, Tang X, Tang L, Huang HX, Wen X, et al. Age-related progression of arterial stiffness and its elevated positive association with blood pressure in healthy people. *Atherosclerosis.* (2015) 238:147–52. doi: 10.1016/j.atherosclerosis.2014.10.089
3. Kotsis V, Stabouli S, Karafillis I, Nilsson P. Early vascular aging and the role of central blood pressure. *J Hypertens.* (2011) 29:1847–53. doi: 10.1097/HJH.0b013e32834a4d9f
4. El Assar M, Angulo J, Vallejo S, Peiro C, Sanchez-Ferrer CF, Rodriguez-Manas L. Mechanisms involved in the aging-induced vascular dysfunction. *Front Physiol.* (2012) 3:132. doi: 10.3389/fphys.2012.00132
5. Han HC. Twisted blood vessels: symptoms, etiology and biomechanical mechanisms. *J Vasc Res.* (2012) 49:185–97. doi: 10.1159/000335123
6. Pancera P, Ribul M, Presciuttini B, Lechi A. Prevalence of carotid artery kinking in 590 consecutive subjects evaluated by Echocolordoppler. Is there a correlation with arterial hypertension? *J Intern Med.* (2000) 248:7–12. doi: 10.1046/j.1365-2796.2000.00611.x
7. Lu H, Xu F, Rodrigue KM, Kennedy KM, Cheng Y, Flicker B, et al. Alterations in cerebral metabolic rate and blood supply across the adult lifespan. *Cereb Cortex.* (2011) 21:1426–34. doi: 10.1093/cercor/bhq224
8. Del Corso L, Moruzzo D, Conte B, Agelli M, Romanelli AM, Pastine F, et al. Tortuosity, kinking, and coiling of the carotid artery: expression of atherosclerosis or aging? *Angiology.* (1998) 49:361–71. doi: 10.1177/000331979804900505
9. Xu X, Wang B, Ren C, Hu J, Greenberg DA, Chen T, et al. Age-related impairment of vascular structure and functions. *Aging Dis.* (2017) 8:590–610. doi: 10.14336/AD.2017.0430
10. Langille BL. Arterial remodeling: relation to hemodynamics. *Can J Physiol Pharmacol.* (1996) 74:834–41. doi: 10.1139/y96-082
11. Frosen J, Cebral J, Robertson AM, Aoki T. Flow-induced, inflammation-mediated arterial wall remodeling in the formation and progression of intracranial aneurysms. *Neurosurg Focus.* (2019) 47:E21. doi: 10.3171/2019.5.FOCUS19234
12. Chesnutt JK, Han HC. Tortuosity triggers platelet activation and thrombus formation in microvessels. *J Biomech Eng.* (2011) 133:121004. doi: 10.1115/1.4005478
13. Chen JJ, Rosas HD, Salat DH. Age-associated reductions in cerebral blood flow are independent from regional atrophy. *Neuroimage.* (2011) 55:468–78. doi: 10.1016/j.neuroimage.2010.12.032
14. Tarumi T, Zhang R. Cerebral blood flow in normal aging adults: cardiovascular determinants, clinical implications, and aerobic fitness. *J Neurochem.* (2018) 144:595–608. doi: 10.1111/jnc.14234
15. Kochanowicz J, Mariak Z, Rutkowski R, Turek G, Lyson T, Krejza J. Age and sex dependency of blood flow velocity in the internal carotid artery. *Neurol Neurochir Pol.* (2009) 43:3–8. Retrieved from: https://journals.viamedica.pl/neurologia_neurochirurgia_polska/index
16. Krejza J, Szydlik P, Liebeskind DS, Kochanowicz J, Bronov O, Mariak Z, et al. Age and sex variability and normal reference values for the V(MCA)/V(ICA) index. *AJNR Am J Neuroradiol.* (2005) 26:730–5. Retrieved from: http://www.ajnr.org/
17. Platzek I, Sieron D, Wiggermann P, Laniado M. Carotid artery stenosis: comparison of 3D time-of-flight MR angiography and contrast-enhanced MR angiography at 3T. *Radiol Res Pract.* (2014) 2014:508715. doi: 10.1155/2014/508715
18. Zhang J, Ding S, Zhao H, Sun B, Li X, Zhou Y, et al. Evaluation of chronic carotid artery occlusion by non-contrast 3D-MERGE MR vessel wall imaging: comparison with 3D-TOF-MRA, contrast-enhanced MRA, and DSA. *Eur Radiol.* (2020) 30:5805–14. doi: 10.1007/s00330-020-06989-1
19. Tanaka H, Watanabe Y, Nakamura H, Takahashi H, Arisawa A, Fujiwara T, et al. Multiple blood flow measurements before and after carotid artery stenting via phase-contrast magnetic resonance imaging: an observational study. *PLoS ONE.* (2018) 13:e0195099. doi: 10.1371/journal.pone.0195099
20. Yim PJ, Tilara A, Nosher JL. The paradoxical flow hypothesis of the carotid artery: supporting evidence from phase-contrast magnetic resonance imaging. *J Stroke Cerebrovasc Dis.* (2008) 17:101–8. doi: 10.1016/j.jstrokecerebrovasdis.2007.10.004
21. De Vis JB, Peng SL, Chen X, Li Y, Liu P, Sur S, et al. Arterial-spin-labeling (ASL) perfusion MRI predicts cognitive function in elderly individuals: a 4-year longitudinal study. *J Magn Reson Imaging.* (2018) 48:449–58. doi: 10.1002/jmri.25938

22. Otsu NA. Threshold selection method from gray-level histograms. *IEEE Trans Syst Man Cybern.* (1979) 9:62–6. doi: 10.1109/TSMC.1979.4310076
23. Hassouna MS, Farag AA. Multi-stencils fast marching methods: a highly accurate solution to the eikonal equation on cartesian domains. *IEEE Trans Pattern Anal Mach Intell.* (2007) 29:1563–74. doi: 10.1109/TPAMI.2007.1154
24. Xu F, Ge Y, Lu H. Noninvasive quantification of whole-brain cerebral metabolic rate of oxygen ($CMRO_2$) by MRI. *Magn Reson Med.* (2009) 62:141–8. doi: 10.1002/mrm.21994
25. Peng SL, Su P, Wang FN, Cao Y, Zhang R, Lu H, et al. Optimization of phase-contrast MRI for the quantification of whole-brain cerebral blood flow. *J Magn Reson Imaging.* (2015) 42:1126–33. doi: 10.1002/jmri.24866
26. Liu P, Lu H, Filbey FM, Pinkham AE, McAdams CJ, Adinoff B, et al. Automatic and reproducible positioning of phase-contrast MRI for the quantification of global cerebral blood flow. *PLoS ONE.* (2014) 9:e95721. doi: 10.1371/journal.pone.0095721
27. Liu P, Xu F, Lu H. Test-retest reproducibility of a rapid method to measure brain oxygen metabolism. *Magn Reson Med.* (2013) 69:675–81. doi: 10.1002/mrm.24295
28. Spangler KM, Challa VR, Moody DM, Bell MA. Arteriolar tortuosity of the white matter in aging and hypertension. A microradiographic study. *J Neuropathol Exp Neurol.* (1994) 53:22–6. doi: 10.1097/00005072-199401000-00003
29. Intengan HD, Schiffrin EL. Structure and mechanical properties of resistance arteries in hypertension: role of adhesion molecules and extracellular matrix determinants. *Hypertension.* (2000) 36:312–8. doi: 10.1161/01.HYP.36.3.312
30. Laurent S, Boutouyrie P. The structural factor of hypertension: large and small artery alterations. *Circ Res.* (2015) 116:1007–21. doi: 10.1161/CIRCRESAHA.116.303596
31. Martins HFG, Mayer A, Batista P, Soares F, Almeida V, Pedro AJ, et al. Morphological changes of the internal carotid artery: prevalence and characteristics. A clinical and ultrasonographic study in a series of 19 804 patients over 25 years old. *Eur J Neurol.* (2018) 25:171–7. doi: 10.1111/ene.13491
32. Chiha J, Mitchell P, Gopinath B, Burlutsky G, Kovoor P, Thiagalingam A. Gender differences in the prevalence of coronary artery tortuosity and its association with coronary artery disease. *Int J Cardiol Heart Vasc.* (2017) 14:23–7. doi: 10.1016/j.ijcha.2016.11.005
33. Waddell TK, Dart AM, Gatzka CD, Cameron JD, Kingwell BA. Women exhibit a greater age-related increase in proximal aortic stiffness than men. *J Hypertens.* (2001) 19:2205–12. doi: 10.1097/00004872-200112000-00014
34. Stemper BD, Yoganandan N, Pintar FA, Maiman DJ, Meyer MA, DeRosia J, et al. *Anatomical gender differences in cervical vertebrae of size-matched volunteers.* Spine (2008) 33(2):E44–9. doi: 10.1097/BRS.0b013e318160462a
35. Natoli AK, Medley TL, Ahimastos AA, Drew BG, Thearle DJ, Dilley RJ, et al. Sex steroids modulate human aortic smooth muscle cell matrix protein deposition and matrix metalloproteinase expression. *Hypertension.* (2005) 46:1129–34. doi: 10.1161/01.HYP.0000187016.06549.96
36. Wacker CM, Bauer WR. Myocardial microcirculation in humans—new approaches using MRI. *Herz.* (2003) 28:74–81. doi: 10.1007/s00059-003-2451-6
37. van Es AC, van der Flier WM, Box FM, Middelkoop HA, Westendorp RG, van Buchem MA, et al. Carotid and basilar artery wall shear stress in Alzheimer's disease and mild cognitive impairment. *Dement Geriatr Cogn Disord.* (2009) 28:220–4. doi: 10.1159/000237740
38. Han D, Starikov A, Gransar H, Kolli KK, Lee JH, et al. Relationship between endothelial wall shear stress and high-risk atherosclerotic plaque characteristics for identification of coronary lesions that cause ischemia: a direct comparison with fractional flow reserve. *J Am Heart Assoc.* (2016) 5:4186. doi: 10.1161/JAHA.116.004186
39. Markl M, Wegent F, Zech T, Bauer S, Strecker C, Schumacher M, et al. In vivo wall shear stress distribution in the carotid artery: effect of bifurcation geometry, internal carotid artery stenosis, and recanalization therapy. *Circ Cardiovasc Imaging.* (2010) 3:647–55. doi: 10.1161/CIRCIMAGING.110.958504
40. Wang L, Zhao F, Wang D, Hu S, Liu J, Zhou Z, et al. Pressure drop in tortuosity/kinking of the internal carotid artery: simulation and clinical investigation. *Biomed Res Int.* (2016) 2016:2428970. doi: 10.1155/2016/2428970
41. Li Y, Shi Z, Cai Y, Feng Y, Ma G, Shen C, et al. Impact of coronary tortuosity on coronary pressure: numerical simulation study. *PLoS ONE.* (2012) 7:e42558. doi: 10.1371/journal.pone.0042558
42. Choudhry FA, Grantham JT, Rai AT, Hogg JP. Vascular geometry of the extracranial carotid arteries: an analysis of length, diameter, and tortuosity. *J Neurointerv Surg.* (2016) 8:536–40. doi: 10.1136/neurintsurg-2015-011671
43. Thomas JB, Antiga L, Che SL, Milner JS, Steinman DA, Spence JD, et al. Variation in the carotid bifurcation geometry of young versus older adults: implications for geometric risk of atherosclerosis. *Stroke.* (2005) 36:2450–6. doi: 10.1161/01.STR.0000185679.62634.0a
44. Lam RC, Lin SC, DeRubertis B, Hynecek R, Kent KC, Faries PL. The impact of increasing age on anatomic factors affecting carotid angioplasty and stenting. *J Vasc Surg.* (2007) 45:875–80. doi: 10.1016/j.jvs.2006.12.059
45. Togay-Isikay C, Kim J, Betterman K, Andrews C, Meads D, Tesh P, et al. Carotid artery tortuosity, kinking, coiling: stroke risk factor, marker, or curiosity? *Acta Neurol Belg.* (2005) 105:68–72.
46. Khasiyev F, Rundek T, Di Tullio MR, Wright CB, Sacco RL, Elkind MSV, et al. Systemic arterial correlates of cervical carotid artery tortuosity: the Northern Manhattan study. *Clin Neuroradiol.* (2021). doi: 10.1007/s00062-021-01044-y
47. Welby JP, Kim ST, Carr CM, Lehman VT, Rydberg CH, Wald JT, et al. Carotid artery tortuosity is associated with connective tissue diseases. *AJNR Am J Neuroradiol.* (2019) 40:1738–43. doi: 10.3174/ajnr.A6218
48. Duivenvoorden R, de Groot E, Elsen BM, Lameris JS, van der Geest RJ, Stroes ES, et al. In vivo quantification of carotid artery wall dimensions: 3.0-Tesla MRI versus B-mode ultrasound imaging. *Circ Cardiovasc Imaging.* (2009) 2:235–42. doi: 10.1161/CIRCIMAGING.108.788059
49. Metgudmath RB, Metgudmath AR, Metgudmath VV, Jainkeri V. Variations of the cervical internal carotid artery. *Indian J Otolaryngol Head Neck Surg.* (2013) 65:210–3. doi: 10.1007/s12070-011-0408-2
50. Nuza AB, Taner D. Anatomical variations of the intracavernous branches of the internal carotid artery with reference to the relationship of the internal carotid artery and sixth cranial nerve. A microsurgical study. *Acta Anat.* (1990) 138:238–45. doi: 10.1159/000146946

Conflict of Interest: The authors declare that the research was conducted in the absence of any commercial or financial relationships that could be construed as a potential conflict of interest.

Publisher's Note: All claims expressed in this article are solely those of the authors and do not necessarily represent those of their affiliated organizations, or those of the publisher, the editors and the reviewers. Any product that may be evaluated in this article, or claim that may be made by its manufacturer, is not guaranteed or endorsed by the publisher.

frontiers | Frontiers in Neurology

ORIGINAL RESEARCH
published: 06 May 2022
doi: 10.3389/fneur.2022.862976

Altered Pain in the Brainstem and Spinal Cord of Fibromyalgia Patients During the Anticipation and Experience of Experimental Pain

Gabriela Ioachim[1], *Howard J. M. Warren*[1], *Jocelyn M. Powers*[1], *Roland Staud*[2], *Caroline F. Pukall*[1,3] *and Patrick W. Stroman*[1,4,5]*

[1] Center for Neuroscience Studies, Queen's University, Kingston, ON, Canada, [2] Department of Medicine, University of Florida, Seffner, FL, United States, [3] Department of Psychology, Queen's University, Kingston, ON, Canada, [4] Department of Biomedical and Molecular Sciences, Queen's University, Kingston, ON, Canada, [5] Department of Physics, Queen's University, Kingston, ON, Canada

Chronic pain associated with fibromyalgia (FM) affects a large portion of the population but the underlying mechanisms leading to this altered pain are still poorly understood. Evidence suggests that FM involves altered neural processes in the central nervous system and neuroimaging methods such as functional magnetic resonance imaging (fMRI) are used to reveal these underlying alterations. While many fMRI studies of FM have been conducted in the brain, recent evidence shows that the changes in pain processing in FM may be linked to autonomic and homeostatic dysregulation, thus requiring further investigation in the brainstem and spinal cord. Functional magnetic resonance imaging data from 15 women with FM and 15 healthy controls were obtained in the cervical spinal cord and brainstem at 3 tesla using previously established methods. In order to investigate differences in pain processing in these groups, participants underwent trials in which they anticipated and received a predictable painful stimulus, randomly interleaved with trials with no stimulus. Differences in functional connectivity between the groups were investigated by means of structural equation modeling. The results demonstrate significant differences in brainstem/spinal cord network connectivity between the FM and control groups which also correlated with individual differences in pain responses. The regions involved in these differences in connectivity included the LC, hypothalamus, PAG, and PBN, which are known to be associated with autonomic homeostatic regulation, including fight or flight responses. This study extends our understanding of altered neural processes associated with FM and the important link between sensory and autonomic regulation systems in this disorder.

Keywords: fMRI, brainstem, spinal cord, pain, human, chronic, fibromyalgia

OPEN ACCESS

Edited by:
Jaymin Upadhyay, Boston Children's Hospital and Harvard Medical School, United States

Reviewed by:
Catherine R. Jutzeler, ETH Zürich, Switzerland
Wen Wu, Southern Medical University, China

***Correspondence:**
Patrick W. Stroman
stromanp@queensu.ca

Specialty section:
This article was submitted to Applied Neuroimaging, a section of the journal Frontiers in Neurology

Received: *26 January 2022*
Accepted: *07 April 2022*
Published: *06 May 2022*

Citation:
Ioachim G, Warren HJM, Powers JM, Staud R, Pukall CF and Stroman PW (2022) Altered Pain in the Brainstem and Spinal Cord of Fibromyalgia Patients During the Anticipation and Experience of Experimental Pain. Front. Neurol. 13:862976. doi: 10.3389/fneur.2022.862976

INTRODUCTION

Fibromyalgia (FM) is a chronic pain condition that is characterized by both hyperalgesia (heightened pain sensitivity) and allodynia (disproportionate pain or sensitivity from sensory stimuli that would not normally be painful) (1–3). Most evidence to date suggests that the abnormal pain responses in FM may be the result of central sensitization (4–11), which has prompted

functional magnetic resonance imaging (fMRI) studies of the central nervous system. However, the majority of these studies focus on the brain (8, 12–20) and a large proportion used model-driven analyses, which we have recently shown may provide an incomplete picture when investigating pain processing with fMRI (21, 22). Importantly, additional studies examining the brainstem and spinal cord, which include regions that are known to play key roles in descending pain modulation (23), can advance knowledge of pain processing in FM.

Most prior MRI studies of FM in the brainstem and spinal cord included structural studies (24, 25) and studies of resting-state function which did not involve a painful stimulus (26). However, functional studies that involved noxious stimuli have also been carried out, and have provided crucial evidence of altered pain processing. The results have demonstrated differences in BOLD signal changes associated with temporal summation of pain and descending modulation in women with fibromyalgia compared to healthy controls (7, 11). These studies, however, modeled the time course of neuronal activation only during and after noxious stimulation.

Our recent study has demonstrated that pain modulation in the brainstem and spinal cord includes both a reactive component and a continuous component of pain modulation related to cognitive and emotional influences on pain, which are present before, during, and after a painful stimulus (27). Brainstem and spinal cord network connectivity variations have been described both before and during stimulation in healthy volunteers, and they appear to be related to pain expectation or pain relief in (28, 29). Some of these effects related to pain expectations may also be linked in part to autonomic homeostatic regulation in a subset of brainstem regions (28, 30). Previous evidence shows that functional differences in FM exist in brain regions linked to motivational-affective components of pain processing (12–15). Therefore it is possible that similar important differences in pain modulation may also exist in brainstem and spinal cord regions. Some behavioral studies have linked changes in autonomic regulation to changes in pain sensitivity in FM (31–33), but this has not been investigated with functional neuroimaging studies.

The objective of the present study was to advance our understanding of the neural processes underlying heighted pain sensitivity in FM, by means of fMRI in the brainstem and spinal cord, to investigate function during both the anticipation and experience of pain. We used structural equation modeling to investigate a network of brainstem and spinal cord regions associated with descending pain modulation (23), motivational-affective components of pain (28, 29) and autonomic homeostatic regulation (34). We hypothesized that during the anticipation and experience of pain, the connectivity in spinal cord and brainstem networks was altered in FM compared to healthy controls.

METHODS

All study methods were reviewed and approved by our institutional research ethics board, and participants provided fully informed written consent before participating. The study protocol conformed to the ethical guidelines of the 2013 Declaration of Helsinki.

Participant Recruitment

Participants with and without FM were recruited through online advertisements as well as physical flyers posted in the general community and in chronic pain support groups. Participation involved two fMRI sessions as part of a larger study, one imaging the brain and the other imaging the brainstem and spinal cord, although not all participants completed both sessions. The current study of the brainstem and spinal cord involved 15 women with FM (mean age 46 ±13 years) who fulfilled the 1990 and 2016 FM criteria, and 15 healthy women (mean age 39 ±10 years). All participants were free of any contraindications for MR imaging (e.g., metallic implants, claustrophobia, pregnancy, etc.), were not taking any centrally-acting medications. They were allowed to continue on other medications if they were taking them for at least 3 months prior to the study. The participants were not asked to stop medication they were already taking, as reports suggest that conventional treatments do not alleviate fibromyalgia pain, and stopping medications may pose a risk to a participant's health. Participants taking centrally-acting pain medication, however, were still excluded from the study.

Questionnaires

In addition to the imaging data, participants completed a series of questionnaires related to demographic information, mental health, pain symptoms, and autonomic functioning. All participants completed the 2016 Fibromyalgia Survey Questionnaire (FSQ) (35) to assess whether they met the most recent classification criteria for FM, as some participants had been diagnosed over a decade previously by their physicians. Some studies have also found discrepancies between physician diagnoses of FM and classification based on the most recent diagnostic criteria (36). Participants also completed the State-Trait Anxiety Inventory (STAI) (37), and Beck Depression Inventory (BDI) (38), because FM has been associated with high anxiety and depression (1). The Social Desirability Scale (SDS) (39) and the Pain Catastrophizing Scale (PCS) (40) were also included to assess whether individual reports of pain ratings were associated with the desire to perform well for the study or the tendency to catastrophize painful sensations. The Composite Autonomic Symptom Score 31 (COMPASS-31) (41) was used to assess autonomic health. This questionnaire includes subscales for 6 domains of autonomic symptom severity, namely orthostatic intolerance, vasomotor, secretomotor, gastrointestinal, bladder, and pupillomotor symptoms. To assess pain and pain symptoms, we also included the Revised Fibromyalgia Impact Questionnaire (FIQR) (42) and the Short-Form McGill Pain Questionnaire-2 (SF-MPQ-2) (43). Participants in the HC group were still given the FIQR but the word "fibromyalgia" was omitted (questions referred to how pain impacted their lives) as these participants did not have any experience of fibromyalgia. The SF-MPQ-2 included four subscales of pain quality, namely affective descriptors, continuous, intermittent, and

predominantly neuropathic pain. These questionnaire scores were used to compute group means for the FM and HC participants, which were then compared using *t*-tests. Group means for each subscale (in inventories that included subscales) were also computed and tested. Significant differences in average scores were inferred at a threshold of $p < 0.05$.

Participant Training

All participants completed a 1-h sham training session before their imaging session. This time was used to familiarize the participant with the study paradigm, complete the algometry testing portion of the study, ease any anxiety about the imaging session by practicing in a sham MRI, and introduce them to the pain stimulus used in the study. This training session was the first time the participants were exposed to the numerical pain rating scale used in the study and the heat stimulus used. All sessions were carried out by two examiners to facilitate the training, one male and one female researcher. First, participants underwent tender point test according to the 1,190 ACR FM criteria (35, 44, 45). For simplicity and participant comfort, only 12 points above the waist were examined for pain (bilateral occiput, bilateral epicondyle, bilateral low cervical, bilateral supraspinatus, bilateral trapezius, and bilateral second rib) alongside a control point on the forehead (44, 45). For each point, a researcher applied pressure in even increments of 1 kg/s (to a maximum of 4 kg) with an algometer (FPK 10 pain test algometer, Wagner Instruments, Greenwich, Connecticut). Participants were instructed to say "stop" as soon as the sensation became painful, and the pressure needed to reach this point was recorded. If a participant did not report pain for a point even after the maximum pressure was reached, "no pain" was recorded. Each point was probed only once, and all pressure-point exams were conducted by the same researcher (male) for consistency in application.

Next, participants were introduced to the numerical pain intensity scale (NPS) they would use to rate their pain (46), as well as the stimulus used during the study. This scale ranges from 0 to 100 in increments of 10, with descriptors at each increment (0 = no sensation, 10 = warm, 20 = a barely painful sensation, 30 = very weak pain, 40 = weak pain, 50 = moderate pain, 60 = slightly strong pain, 70 = strong pain, 80 = very strong pain, 90 = nearly intolerable pain, 100 = intolerable pain). Participants were told they would not be experiencing temperatures that could cause harm to their skin, and that the study did not aim to induce pain above a rating of moderately severe (70) on the NPS.

This study used a MRI-compatible Robotic Contact-Heat Thermal Heat Stimulator (RTS-2) to deliver the noxious stimulus. A heat stimulus was chosen in order to compare these results to recent pain research in the spinal cord (7, 28, 47–49), as well as the fact that fibromyalgia has been associated with higher heat pain sensitivity (1). The RTS-2's plexiglass casing houses a heated aluminum thermode which can be advanced to exit the casing and touch the skin of a participant or retracted into the casing. The movement and temperature of the thermode are precisely controlled by custom written software in MATLAB (Mathworks Inc., Natick, MA). Participants were instructed to place their right hand on the casing so the thermode would make contact with the thenar eminence of their right hand. This placement was chosen because that area of the skin corresponds to the C6 dermatome and would allow these results to be compared to previous spinal cord studies of pain (27, 28, 48, 49). A number of calibration tests were performed to allow the participant to become familiar with the stimulus and determine the temperature needed to elicit moderate pain in each participant. Each test consisted of 10 heat contacts, 1.5 second duration, with onsets every 3 seconds over the span of 30 s with the thermode temperatures ranging between 40 and 52 °C (the temperature was constant during each test). This stimulation paradigm can cause wind-up, and the time interval between the contacts produces a robust BOLD response without receptor adaptation. We chose this paradigm because FM is believed to involve central sensitization, which is exacerbated by a wind-up paradigm. Prior studies using a thermal stimulus have shown that participants with FM have altered responses to this paradigm compared to pain-free participants (7, 8, 10). In addition, the choice of a thermal stimulus allows for the calibration of pain intensity for each participant's level of sensitivity and can be easily applied in an MRI environment.

Each participant received the same stimulus intensities in the same order, consisting of trials of 46, 50, 44, and 48°C respectively. During each test, participants verbally rated each of the 10 contacts out loud using the NPS. They were encouraged to rate in increments of 5 but were not corrected if they used other numbers. The temperatures used never exceeded 52°C to prevent tissue damage. Participants were kept blinded to this objective as well as to the temperatures used during the tests to avoid any response bias. They were informed that if the sensation was ever intolerable they could remove their hand from the device at any time during the study. This served both to relieve their anxiety as well as avoid causing high levels of subjective pain.

The training session concluded with a practice run of the experimental protocol in the sham MRI scanner. To prevent motion artifacts, participants cannot verbalize their ratings during the imaging, therefore they were instructed to rate each contact mentally and remember the ratings they gave for the first and last contact. The sham tests also allowed participants to practice laying as still and relaxed as possible to avoid movement during imaging, and they were reassured that the NPS would be displayed, requiring no memorization of the scale. The sham MRI provides an environment similar to the MRI to allow participants to familiarize themselves with how imaging will feel and ease anxiety. Participants lay supine on a mobile bed and were provided with a mirror over their eyes to view a rear-projection screen and listen to recorded sounds from MRI scans that were played for them on a speaker. The practice scan for this study used the same stimulation paradigm as the subsequent imaging session, allowing participants to practice mentally rating their pain and recalling the first and last ratings.

FMRI Paradigm

This study employed a "threat vs. safety" paradigm to allow us to examine periods of anticipation of pain, periods of painful stimulation, and periods of rest. The imaging session consisted of 10 fMRI runs of 4.5 min each, separated into five

"Pain" runs in which participants experienced the noxious heat stimulus, interleaved in a randomized order with five 'No-Pain' runs in which participants did not feel the stimulus. While the majority of participants completed this session, some participants only underwent four "Pain" runs due to time constraints or participants being unable to comfortably lie still for the amount of time needed to complete all five runs. During each run, at the 1-minute mark, they were informed via a rear-projection screen whether they would feel the stimulus or not that run. If it was a "Pain" run, participants were told at the 2-min mark that the stimulation would begin. During stimulation, they experienced 10 heat contacts over a span of 30 seconds at the calibrated temperature. During the stimulation, the NPS was displayed and participants were instructed to mentally rate each contact on the scale. After the stimulation, imaging continued for another 2 min before ending. After each "Pain" run, participants were asked over an intercom to give their ratings for the first and last contact, and were told that another run would begin soon. Imaging was conducted over the same amount of time in the No Pain condition, but participants were told they would not receive the stimulus. This paradigm has been previously employed in several pain studies (22, 27, 28, 49).

FMRI Data Acquisition

This study included data from a larger research program that included both brainstem/spinal cord and brain imaging sessions. Only the brainstem/spinal cord imaging data are discussed here. Functional MRI scans were carried out on a Siemens 3 tesla MRI system (Siemens Magnetom, Erlangen, Germany). During the data collection phase of this study, the MR system underwent an upgrade from a Siemens Magnetom Trio to a Siemens Magnetom Prisma. Efforts were made to keep scan quality equivalent pre- and post-upgrade, and checks were performed with data from the FM and HC groups before and after the upgrade as well as additional volunteer data to compare the quality of the data and the signal to noise ratio in each. No significant differences were found in scan quality or signal-to-noise ratio before and after the upgrade.

Localizer images were acquired in three planes to provide a reference for the subsequent slice positions. Functional images were acquired using a half-Fourier single-shot fast spin-echo (HASTE) sequence with BOLD contrast, spanning the full brainstem and cervical spinal cord (first thoracic vertebra to above the thalamus). This method has been shown to provide optimal image quality and BOLD sensitivity in the brainstem and spinal cord (48). The 3D volume was imaged in 9 contiguous sagittal slices, 2 mm wide, with a 28 × 21 cm field-of-view and a 1.5 × 1.5 mm in-plane resolution. Imaging parameters included an echo time (TE) of 76 ms and a repetition time (TR) of 6.75 s/volume for optimal T2-weighted BOLD sensitivity. Each imaging run consisted of 40 volumes (equivalent to a 4.5 min run). In total, 10 runs were acquired for each participant, 5 Pain and 5 No Pain, therefore each condition consisted of 200 volumes per individual.

FMRI Data Preprocessing and Analysis

Data Preprocessing

Preprocessing was carried out using custom-written software (48), "spinalfmri9" (https://www.queensu.ca/academia/stromanlab/home/fmri-analysis-software) in MATLAB (MathWorks, Natick, MA, USA). Image data were first converted from DICOM to NIfTI format, after which they were co-registered to correct for bulk body motion using the non-rigid 3D registration tool in the MIRT package (Medical Image Registration Toolbox) (50, 51). Images were then resized to 1 mm^3 voxels and spatially normalized to a pre-defined anatomical template, as described previously (27, 47). Physiological noise estimates were obtained from the recording of the peripheral pulse (synchronized to each fMRI time series), estimates of global noise were obtained from regions of white matter, and motion parameters obtained from the co-registration procedures were used as models of bulk movement. These noise models were fit to the data using a general linear model (GLM) and subtracted from the data. This method has been shown to be highly effective for removing physiological noise in this region (52).

Data Analysis

The threat/safety paradigm enables comparisons of periods with and without the anticipation, and experience, of the noxious heat stimulus. For this study we focused the analysis on two time periods; the second minute of the baseline period preceding the noxious stimulus, and the stimulation period. Two epochs were analyzed, consisting of 45 s blocks. The first epoch is centered around the 1 min 30 s mark and is termed the "Expectation" period. This is the time after participants were told to expect pain, but before they had experienced any stimulus. The second epoch is centered around the 2 min 15 sec mark and is termed the "Stimulation" period, and is the time when participants were experiencing a painful stimulus. This also allowed us to compare these results to our previous studies (28, 30).

Analyses consisted of characterizations of BOLD responses, and connectivity analyses. As it is not practical to apply these analyses on a voxel-by-voxel basis, we selected 10 regions of interest (ROIs) in the brainstem and spinal cord which were identified using a previously-established anatomical region map (7, 47, 53). These regions and their expected locations were compiled from several anatomical atlases and published articles (54–58). The regions included the thalamus, hypothalamus (Hyp), periaqueductal gray matter (PAG), parabrachial nucleus (PBN), locus coeruleus (LC), nucleus tractus solitarius (NTS), nucleus raphe magnus (NRM), nucleus gigantocellularis (NGc), dorsal reticular nucleus of the medulla (DRt), and the pontine reticular formation (PRF). As the noxious stimulus was applied to the palm of the right hand, which corresponds to the C6 dermatome, we also included the right dorsal quadrant of the 6^{th} cervical spinal cord segment (C6RD). However, because entire anatomical regions are not expected to be uniformly involved with pain responses (28, 30, 34, 59, 60), regions were divided into sub-regions based on fMRI time-course properties. Each ROI was divided into 5 clusters of voxels (i.e., sub-regions) by means of k-means clustering. This method provides greater

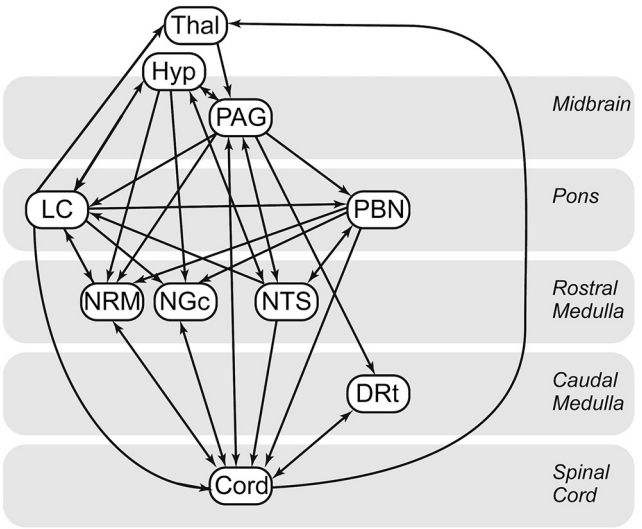

FIGURE 1 | Anatomical model of the regions and connections used for the structural equation modeling (SEM) analysis.

spatial precision by dividing the voxels into clusters based on their functional characteristics.

Structural Equation Modeling

Cluster-to-cluster correlations may not always be sufficient to explain complex coordination between regions (28, 30, 59). As in previous studies (27, 28, 30, 49, 59), we used structural equation modeling to examine coordinated networks. These methods have been validated for use in the brainstem and spinal cord (61), and in previous studies they have been used to identify and characterize robust networks in the brain, brainstem and spinal cord (30, 59), as well as characterize connectivity networks during pain processing (60) and the expectation of pain (28). SEM requires a pre-defined model of anatomical regions and connections between these regions. We have chosen a previously-described model based on known pain related neuroanatomy (23, 62–64) (**Figure 1**), which includes the brainstem regions described above, the C6RD quadrant of the spinal cord, as well as information about the anatomical directionality of connections.

Connectivity analyses (SEM) were carried out separately for the Expectation and Stimulation periods by means of a general linear model (GLM) fitting method which was used to calculate the linear weighting factors (β) which describe the relative contribution of each "source" input to a "target" region. These β values reflect the connectivity strength between regions, and are calculated as follows: if a region A receives inputs from two other regions, B and C, and the BOLD signal time series in these responses are S_A, S_B, and S_C respectively, then $S_A = \beta_{AB}S_B + \beta_{AC}S_C + e_A$ where e_A is the residual signal variation that is not explained by the fit. Within the model are several network components that consist of a target region (e.g., S_A) and the multiple source regions providing input to that target region (e.g., S_B and S_C). The weighting factors (beta, β) were calculated separately for each network component, and networks were investigated for every combination of clusters of each region in order to identify the clusters that resulted in the best fits to the data measured. The beta value for each connection is therefore calculated several times with different combinations of "source" and "target" clusters. The amount of variance in each target region that can be explained by the fit was calculated and expressed as an R^2 value, and the significance of the fit was estimated by converting R values to a Z-score by means of a Fisher's Z-transform. This fitting was repeated with one source region at a time omitted from the network, and an F-test was used to identify terms that did not uniquely account for a significant component of the variance in each target region. Any terms that did not account for a significant component of the target region variance were not included in the results. A threshold of $F(1,\infty) > 3.845$ was used to determine significance (corresponding with $p < 0.05$).

Analyses and Comparisons of Connectivity Networks

Connectivity networks were compared between and within the FM and HC groups, for each time period, by means of analyses of covariance (ANCOVA). The ANCOVA included the Group (FM vs. HC) as a discrete variable, and the participants' normalized pain scores, as a continuous variable. Normalized pain scores were calculated for each individual by taking the ratio of their average pain rating during the "Pain" runs to the average temperature applied to the hand (i.e., pain rating/temperature). A higher ratio reflects higher pain sensitivity. The results thus demonstrate significant group differences, significant dependences on pain ratings, and interactions between the group and pain ratings. Significance was inferred at a multiple-comparison corrected probability threshold of $p < 0.05$, using a Bonferroni family-wise error-rate correction to account for the number of independent connections tested. ANCOVA analyses were applied separately using data in the "Expectation" and "Stimulation" periods.

RESULTS

Participant Characteristics

Questionnaire scores were compared between study groups (FM vs. HC) by means of Student's *T*-tests, and are summarized in **Tables 1**, **2**. Fibromyalgia participants were observed to have a significantly higher normalized pain scores than healthy controls, $t(28) = -3.303$, $p = 0.003$. They also scored significantly higher on measures of depression (BDI), measures of pain catastrophizing (total and sub-scores of rumination, magnification, and helplessness), measures of pain symptomatology (total FIQR and function, impact and symptom subscales), measures of autonomic function (total COMPASS and all subscales), and pain inventory scores (total MPQ and continuous, intermittent, neuropathic, and affective subscales). No demographic information such as age, smoking habits, or drinking, was significantly different between the groups.

To examine the relationship between traits such as pain catastrophizing, anxiety, depression, autonomic function, and pain symptomatology and experience, Spearman's rank correlations of all scale and subscale scores with normalized pain

TABLE 1 | Demographic information for the healthy control (HC) and fibromyalgia (FM) groups. Where applicable the mean score is given, followed by the standard deviation in parentheses. The normalized pain score was calculated by dividing each individual's average pain rating by the average stimulus temperature needed to elicit that rating. A higher number indicates higher pain sensitivity. The participant groups had significantly different scores on all four measures.

Demographic information	HC (SD)	FM (SD)
Age	39.2 (10.3)	46.7 (13.5)
BMI	27.6 (3.8)	25.8 (5.1)
Normalized pain score	0.72 (0.2)	1.01 (0.2)
Initial pain score	2.3 (5.62)	33.9 (23.7)

scores was also conducted (**Table 3**). This was done separately for FM and HC participants. In the FM group, age was significantly correlated with pain scores, with older participants having higher pain scores, $rho(13) = 0.567$, $p = 0.02$. No other correlations were found to be significant.

Network Comparisons

SEM analyses identified extensive networks in the brainstem and spinal cord for both participant groups, in the Expectation and Stimulation periods. **Table 4** summarizes the significant connectivity values in both groups during both periods of interest. While expecting pain, SEM results from both groups included significant connectivity from the LC to the PBN and from the PAG to the LC. Significant network connectivity was also observed from the LC and the PAG to the NGC in the HC group, while significant hypothalamus to LC and PAG to PBN connectivity was observed in the FM group. During the stimulation period, both groups had significant PAG to LC network connectivity. The connectivity network observed in the healthy control group also included connections from the LC to the PBN and thalamus, from the hypothalamus to the NTS, from the thalamus to the PAG, and from the NTS to the LC. In contrast, the network connectivity observed in the FM group during the painful stimulation also included connections from the PAG to the PBN and DRt, and from the hypothalamus to the NRM.

The results of ANCOVA analyses to compare connectivity values between groups, and in relation to pain scores, are listed in **Table 5**. The results show significant main effects of the study group and pain scores as well as significant interaction effects in both the Expectation and Stimulation time periods. During the Expectation time period, there were significant main effects of the study group in connections from the hypothalamus to the NRM and NGc, from the PAG to the NGc, and from the spinal cord to the thalamus. During the Stimulation period, these effects were observed in connections from the LC to the NRM, from the PAG to the LC, NGc, and hypothalamus, from the spinal cord to the NGc and PAG, and from the PBN to the NGc. Connectivity between regions also varied significantly with normalized pain scores in both time periods. In the Expectation period, this connectivity was localized within brainstem regions (from the hypothalamus to the LC, and from the PAG to the LC, and NGc). In the Stimulation period, these effects were relatively similar in terms of brainstem-to-brainstem connectivity, but also included additional connections from the PBN and spinal cord to the NGc, and from the hypothalamus and LC to the NRM. Interaction effects were more pronounced in the Expectation time period, and involved connectivity from the spinal cord to the thalamus, from the PAG and LC to the NGc, from the PAG and hypothalamus to the NRM, and from the NTS to the LC.

TABLE 2 | Significant differences in group means (FM vs. HC) of questionnaire scores. Group means, standard error, t value, and p value are given for each comparison. All comparisons listed show significant differences between the groups. Other differences that were tested but were not significant were state-trait anxiety and social desirability. Acronyms, in order given in the table, represent questionnaire scores for depression (BDI), pain catastrophizing (PC) including total questionnaire scores and subscales, fibromyalgia impact (FIQR) including total scores and subscales, autonomic symptoms (COMPASS) including total scores and subscales for various symptom categories, normalized pain score (calculated as the ratio of the average pain rating given to the average temperature of the stimulus), and pain symptoms (MPQ) including total scores and subscale scores. The initial pain rating refers to the rating participants gave for their overall bodily pain before starting the study, using the same 100 point scale they were trained to use during the sham MRI session.

Questionnaire	HC (SE)	FM (SE)	t	*p*
BDI	7.13 (2.45)	16.26 (2.77)	−2.462	0.02
PC total	6.71 (1.7)	21.28 (3.29)	−3.930	0.001
PC rumination	3.57 (0.91)	7.64 (1.25)	−2.629	0.014
PC magnification	1.0 (0.31)	4.21 (0.68)	−4.286	0.001
PC helplessness	2.14 (0.67)	9.42 (1.71)	−3.963	0.001
FIQR total	10.31 (3.18)	50.26 (3.66)	−8.223	0.001
FIQR function with FM	1.11 (0.67)	11.22 (1.53)	−6.040	0.000
FIQR impact of FM	1.26 (0.78)	10.0 (1.02)	−6.756	0.000
FIQR symptoms of FM	7.93 (1.92)	29.03 (1.63)	−8.370	0.000
COMPASS total	12.96 (2.36)	39.53 (4.31)	−5.395	0.000
COMPASS orthostatic intolerance	5.6 (1.78)	14.94 (2.74)	−2.855	0.008
COMPASS vasomotor	0.0 (0.0)	1.93 (0.37)	−5.263	0.000
COMPASS secretomotor	1.28 (0.54)	7.02 (0.94)	−5.246	0.000
COMPASS gastrointestinal	4.7 (0.80)	10.58 (1.21)	−4.047	0.000
COMPASS bladder	0.44 (0.23)	2.44 (0.77)	−2.461	0.02
COMPASS pupillomotor	0.94 (0.24)	2.56 (0.26)	−4.554	0.000
Normalized pain score	0.71 (0.59)	1.01 (0.06)	−3.303	0.003
Initial pain	2.33 (5.62)	33.92 (23.77)	−4.848	0.000
MPQ total	12.8 (3.66)	87.13 (12.1)	−5.88	0.00
MPQ continuous	5.5 (1.36)	28.93 (3.26)	−6.614	0.00
MPQ intermittent	2.0 (1.18)	21.67 (4.32)	−4.383	0.000
MPQ neuropathic	3.4 (1.9)	22.80 (3.81)	−4.551	0.000
MPQ affective descriptors	1.9 (1.17)	13.73 (2.16)	−4.796	0.000

Shaded cells represent overall questionnaire scores, while unshaded cells represent subscales of the questionnaires.

TABLE 3 | Pearson's correlations of group questionnaire scores (FM or HC) with individual normalized pain score (calculated as mean pain intensity/mean stimulus temperature for each individual).

	Healthy controls	Fibromyalgia
Questionnaires	**Normalized pain score (rho)**	**Normalized pain score (rho)**
Age	−0.084	**0.567**
BMI	−0.038	−0.347
Anxiety (STAI)	0.028	−0.426
Depression (BDI)	−0.020	−0.347
PC total	−0.063	0.425
PC rumination	−0.128	0.172
PC magnification	−0.034	0.426
PC helplessness	−0.025	0.513
FIQR total	−0.260	0.195
FIQR function with FM	−0.110	0.220
FIQR impact of FM	−0.110	0.074
FIQR symptoms of FM	−0.246	0.081
COMPASS total	−0.055	0.093
COMPASS orthostatic intolerance	−0.122	−0.128
COMPASS vasomotor	NA	0.078
COMPASS secretomotor	0.170	0.072
COMPASS gastrointestinal	−0.027	0.318
COMPASS bladder	−0.485	0.314
COMPASS pupillomotor	−0.154	0.245
MPQ total	−0.280	0.257
MPQ continuous	0.055	0.272
MPQ intermittent	−0.270	0.094
MPQ neuropathic	−0.311	0.277
MPQ affective descriptors	−0.216	0.183

Spearman's rank rho values are given for each comparison, with any values significant at $p < 0.05$ given in bold font. Acronyms, in order given in the table, represent questionnaire scores for depression (BDI), pain catastrophizing (PC) including total questionnaire scores and subscales, fibromyalgia impact (FIQR) including total scores and subscales, autonomic symptoms (COMPASS) including total scores and subscales for various symptom categories, normalized pain score (calculated as the ratio of the average pain rating given to the average temperature of the stimulus), and pain symptoms (MPQ) including total scores and subscale scores. Shaded cells represent overall questionnaire scores, while unshaded cells represent subscales of the questionnaires. Note that the COMPASS Vasomotor cell in the healthy control group has no rho value. This is because all healthy controls scored zero points on this COMPASS subscale (no impairment) and a correlation could therefore not be computed with one variable being a constant.

In contrast, interaction effects in the Stimulation period involved only brainstem to brainstem connectivity, namely from the PAG to the PBN and hypothalamus, and from the PBN to the NGc.

DISCUSSION

The results of this study demonstrate important differences in pain processing between people with FM and a healthy control group. The differences exist across participant characteristics, pain behavioral responses, and coordinated brainstem/spinal cord function identified by means of fMRI, and they demonstrate that altered pain processing in FM may be linked to changes in both descending pain regulation and autonomic regulation. This study is also the first to show that these differences in FM are present *before* a noxious stimulus is applied, while the participants are anticipating the pain.

TABLE 4 | Summary of significant spinal cord/brainstem connectivity in the healthy control (first column) and fibromyalgia (second column) groups, analyzed with SEM. The upper section of the table summarizes connectivity during the Expectation period, and the lower section summarizes the Stimulation period.

Healthy controls		Fibromyalgia	
Region Source→Target	**β ± SE**	**Region Source→Target**	**β ± SE**
Expecting pain		**Expecting pain**	
LC → PBN	0.13 ± 0.03	LC → PBN	0.13 ± 0.02
LC → PBN	0.17 ± 0.04	LC → PBN	0.10 ± 0.02
PAG→ LC	0.42 ± 0.03	PAG → LC	0.39 ± 0.05
LC → NGC	0.27 ± 0.05	Hypothalamus → LC	0.32 ± 0.05
PAG → NGC	0.22 ± 0.05	PAG → PBN	0.18 ± 0.04
Experiencing pain		**Experiencing pain**	
PAG→ LC	0.29 ± 0.07	PAG → LC	0.39 ± 0.04
LC → PBN	0.18 ± 0.04	PAG → PBN	0.25 ± 0.05
LC → Thalamus	0.09 ± 0.02	PAG → PBN	0.19 ± 0.05
Hypothalamus → NTS	0.27 ± 0.06	Hypothalamus → NRM	0.44 ± 0.09
Thalamus → PAG	0.42 ± 0.09	PAG → DRt	0.30 ± 0.09
NTS→ LC	0.28 ± 0.06	PAG → PBN	0.25 ± 0.04

For each connection, the β value and standard error calculated with SEM are given. All connections listed have statistically significant β values. Repeated connections between the same regions indicate that different clusters within the regions had significant connectivity. Abbreviations: dorsal reticular nucleus (DRt), locus coeruleus (LC), nucleus raphe magnus (NRM), nucleus gigantocellularis (NGc), nucleus tractus solitarius (NTS), periaqueductal gray (PAG), parabrachial nucleus (PBN), and the right dorsal region of the 6th cervical cord segment (C6RD).

Our SEM analyses confirm that extensive brainstem and spinal cord network connectivity exists during the expectation and experience of pain in both control participants and women with fibromyalgia (**Table 4**). Both groups showed extensive connectivity between the LC, PAG, and PBN brainstem regions both while expecting and experiencing pain. The PAG is a key brainstem region associated with descending modulation of pain (23), while the LC and PBN have functions associated with pain modulation, motivational affective aspects of pain, as well as autonomic homeostatic regulation (28, 60, 65). Connectivity between these regions has been previously identified in other studies both during the expectation and experience of pain in healthy controls (28, 49). Importantly, these regions were also part of key elements identified as part of the brainstem networks associated with the expectation of pain specifically (28).

Comparisons between the groups (ANCOVA) also revealed significant differences in pain processing between fibromyalgia participants and healthy control women, both before and

TABLE 5 | ANCOVA results for both the Expectation and Stimulation epochs, comparing main effects of group (FM vs. HC), main effects of normalized pain scores, and group x pain score interaction effects.

Expecting pain	Experiencing pain
Region Source→ Target	**Region Source→ Target**
Main effect of Group (FM vs. HC)	**Main effect of Group (FM vs. HC)**
PAG → NGC	LC → NRM
C6RD → Thalamus	C6RD → PAG
Hypothalamus → NGC	PAG → LC
Hypothalamus → NRM	PBN → NGC
	C6RD → NGC
	PAG → Hypothalamus
	PAG → NGC
Main effect of Pain Score	**Main effect of Pain Score**
PAG → NGC	PAG → LC
Hypothalamus → LC	PBN → NGC
PAG → LC	Hypothalamus → NRM
	LC → NRM
	C6RD → NGC
	PAG → NGC
Interaction effect (Group x Pain Score)	**Interaction effect (Group x Pain Score)**
C6RD→ Thalamus	PAG → PBN
PAG → NGC	PBN → NGC
LC → NGC	PAG → Hypothalamus
PAG → NRM	
Hypothalamus → NRM	
PAG→ NGC	
NTS → LC	

The table summarizes all statistically significant effects.

during painful stimulation (**Table 5**). **Figure 2** shows details of relationships between connectivity strengths and pain scores for selected connections with significant main effects of group, normalized pain scores, and interaction effects. The selected connections include an example of a main effect of the Group (FM vs. HC) in the PAG to the NGc connection, in the Expectation period. The connectivity values varied with pain scores in both groups, but had consistently higher values in FM. These results support previous evidence that FM may involve altered descending regulation (11), and show that this is the case even when differences in individual pain scores are taken into account.

Furthermore, we were able to demonstrate that such differences in brainstem and spinal cord connectivity exist between fibromyalgia and healthy control participants both before and during the painful stimulation (**Table 5**). In the Expectation period, group differences in connectivity involved mainly signaling from the hypothalamus to brainstem areas such as the NGc and NRM, and feedback signaling from the spinal cord to the thalamus. This may indicate that a component of fibromyalgia pain is altered pain modulation during the anticipation of pain. As we demonstrated in our previous study, pain modulation includes a continuous component which is present before a painful stimulus is applied and may contribute to readying spinal cord areas to receive incoming nociceptive signals (49). If this process is altered in fibromyalgia, it may explain why these participants often have disproportionate pain responses to similar stimuli as given to healthy controls, or why they require stimuli of lower intensity to elicit similar pain responses to healthy controls (including in the current study) (7, 8, 11–20).

In contrast, differences in the Stimulation period involve more extensive brainstem to brainstem signaling as well as some feedback signaling from the spinal cord to brainstem areas such as the PAG and NGc. These results support our expectations that descending pain regulation is altered in fibromyalgia during noxious stimulation, as the primary differences in connectivity involve the PAG-RVM-spinal cord descending pain modulation pathway (23). However, there are additional connectivity differences involving areas such as the LC, the hypothalamus and the PBN, whose function is associated in part with arousal and autonomic regulation (34). The areas involved in these differences may therefore indicate that this altered descending regulation may have a contribution from altered autonomic signaling. While FM pain has been associated with autonomic dysfunction in previous behavioral studies (31–33), this is the first study to show evidence of this link that is supported by fMRI data.

The ANCOVA analysis also showed a significant main effect of normalized pain scores in both the Expectation and Stimulation time periods, indicating that pain scores are linked to connectivity strengths in these networks regardless of which participant group the participants were in (**Figure 2**). During the Expectation period these differences were exclusively signaling to and from brainstem areas including the PAG and LC, and did not involve any significant connectivity to/from the spinal cord. In a previous study, we demonstrated that several components of these brainstem and spinal cord networks may be specific to expecting pain (28), and many of these components are seen here in this brainstem-to-brainstem signaling as varying with individual pain scores. These connections were also part of significant group x pain score interaction effects, where the observed connectivity strengths depended on a combination of the participants' normalized pain scores as well as which group they belonged to. These results indicate that the activity changes in these regions and the differences in pain scores in fibromyalgia are closely linked.

One review of chronic pain studies suggests a link between certain types of emotional regulation and altered pain responses (66). The authors showed that maladaptive emotional regulation in response to acute pain may contribute to depressed mood and enhanced pain catastrophizing (but not anxiousness), and in turn mediate altered pain responses. Our results align with this idea as we found that women with fibromyalgia had higher BDI and PCS scores than the controls but not STAI scores (**Table 2**), even though both anxiety and depression are

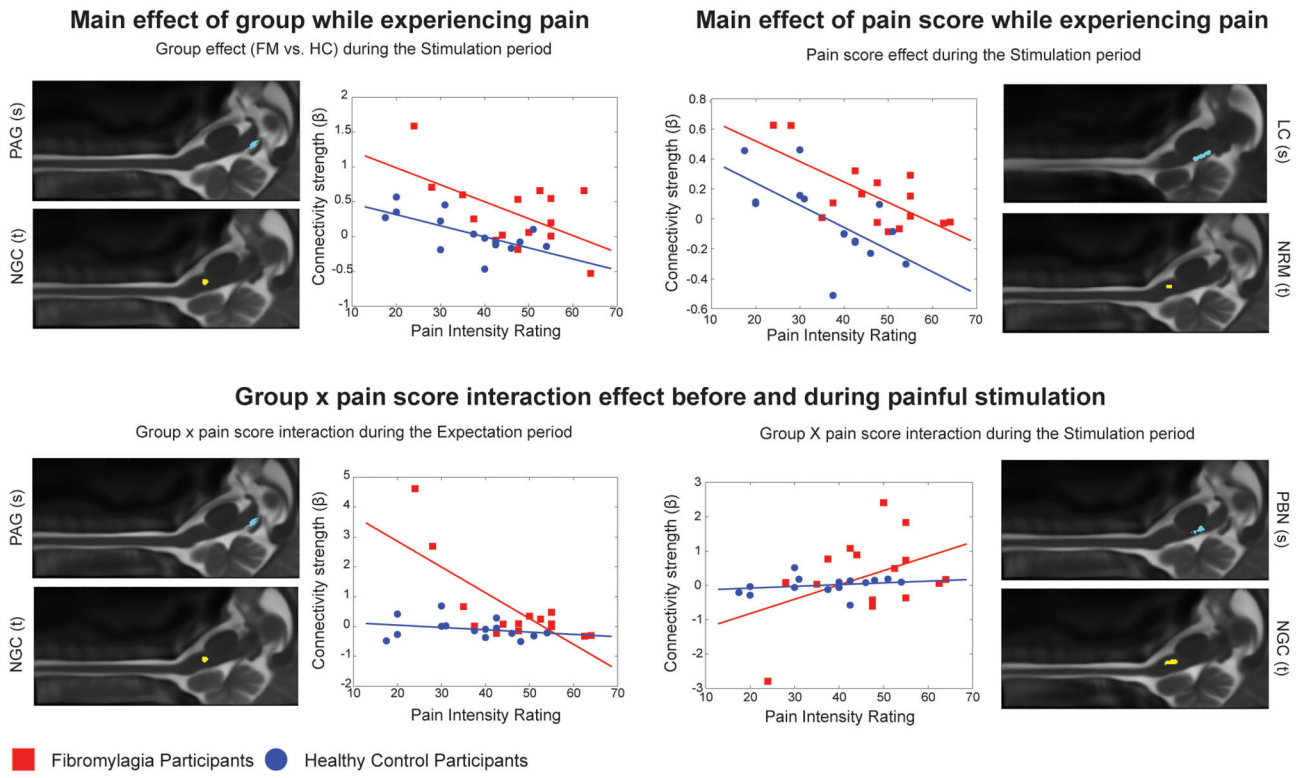

FIGURE 2 | Connection details for 4 example connections obtained from ANCOVA results for both the Expectation and Stimulation periods, comparing main effects of group (FM vs. HC), main effects of normalized pain score, and group x pain score interaction effects. Source regions are denoted with (s) while target regions are denoted with (t). Red points represent individual participants with fibromyalgia while blue points represent the healthy controls. For each figure, the x axis shows the individual average pain intensity ratings for the stimulus while the y axis shows the individual connectivity strengths (calculated and represented as a β value).

known to be comorbid with the condition (1, 67–69). A recent study also showed that people with fibromyalgia have more difficulty regulating emotions, and this predicted heightened pain responses depending on their coping strategies (70). Some brain fMRI studies in pain-free people identified that connectivity changes between the PAG and some cortical areas were associated with a participant's tendency to disengage their attention from the pain and obtain pain relief through distraction (71, 72). Our fibromyalgia group had significantly higher pain catastrophizing scores than the healthy control group, a measure which takes into account in part how people think about and attend to their pain (40). It is possible that a similar process is occurring here with connectivity between the PAG and other brainstem areas.

While we have no direct measures of emotional regulation and coping strategies in the current study, we do have evidence that the altered pain experienced by the fibromyalgia participants is likely due to alterations in a convergence of autonomic regulation and pain modulation systems. Women with fibromyalgia also scored higher on the COMPASS-31 questionnaire which measures symptoms of autonomic system dysfunction. These symptoms may be related to the increased pain sensitivity that is a characteristic of fibromyalgia (1, 2, 73–75), as previous studies have also noted that HPA axis dysregulation may be a part of chronic pain symptomatology and manifestation (33, 76–79). As our results show that connectivity between the PAG and other brainstem areas varies with a participant's pain score, it is possible that this link may be driving some of the differences in pain processing we observed in the fibromyalgia group (who, on average, have higher normalized pain scores than the healthy controls). Motivational-affective components of pain processing and autonomic control are closely interlinked and have been shown to contribute to altered pain responses in the brain (12–15). Based on this and the evidence that maladaptive emotional regulation (an affective component of pain processing) can lead to altered pain in fibromyalgia (66, 70), it is possible that our results show the underlying neural basis of these effects at the level of the brainstem and spinal cord.

Limitations

This article uses SEM as a hypothesis-driven and data-driven analytical approach to fMRI pain data. Structural equation modeling requires a pre-defined anatomical model and can therefore not give information on other regions present in the spinal cord and brainstem that were not included in the original network. Our network was chosen to include regions known to be associated with pain and pain modulation, homeostatic regulation, and arousal. While we are confident in the results presented, we cannot guarantee that other effects are not present in other regions which may influence the

connectivity changes in the given network. There were also unintended differences in the age of participants although efforts were made to age-match participants wherever possible. Lastly, it must be noted that FM is a heterogenous condition with a spectrum of possible symptoms and presentations. Our results are an important step for exploring overall pain processing differences between FM and healthy controls, but more studies are needed to expand on this and explore how these results generalize to different FM populations with different symptom presentations.

Conclusions

These results are an important step in advancing our understanding of fibromyalgia. Women with fibromyalgia have altered descending pain modulation compared to healthy controls. Furthermore, these differences can exist without a noxious stimulus, as network connectivity in the brainstem and spinal cord is altered during both the expectation and the experience of pain. Importantly, many of these changes in network connectivity in FM were related at least in part to individual normalized pain scores. While many brainstem areas carry out several different functions, the areas involved in these connectivity differences seem to indicate that altered pain in fibromyalgia may be the result of changes in a convergence of systems involved with pain regulation, arousal, and autonomic homeostatic regulation. The latter is especially interesting, as links of fibromyalgia pain with changes in autonomic system function have been demonstrated previously by some important behavioral research, which can now be in part supported with novel findings from brainstem and spinal cord fMRI data. Our evidence supports the conclusion that fibromyalgia may involve changes in how autonomic regulation is integrated with descending pain regulation in the brainstem and spinal cord.

DATA AVAILABILITY STATEMENT

The data that support the findings of this study are available from the corresponding author upon reasonable request.

ETHICS STATEMENT

The studies involving human participants were reviewed and approved by Queen's University Research Ethics Board. The patients/participants provided their written informed consent to participate in this study.

AUTHOR CONTRIBUTIONS

GI: participant recruitment, data collection, data analysis, data interpretation, first manuscript preparation, and manuscript review. HW and JP: participant recruitment, data collection, data analysis, data interpretation, and manuscript review. RS and CP: data interpretation and manuscript review and editing. PS: study design, data collection, data analysis, data interpretation, and manuscript review and editing. All authors contributed to the article and approved the submitted version.

FUNDING

This research was funded by the National Sciences and Engineering Research Council (NSERC), RGPIN/06221-2015. This work was also supported by Spectrum Therapeutics through MITACS.

ACKNOWLEDGMENTS

We would like to thank Don Brien and Janet Mirtle-Stroman for their help with data collection.

REFERENCES

1. Plesner KB, Vaegter HB. Symptoms of fibromyalgia according to the 2016 revised fibromyalgia criteria in chronic pain patients referred to multidisciplinary pain rehabilitation: influence on clinical and experimental pain sensitivity. *J Pain.* (2018) 19:777–86. doi: 10.1016/j.jpain.2018.02.009
2. Fitzcharles MA, Ste-Marie PvA, Goldenbers DL, Pereira JX, Abbey S, Choiniere M, et al. Narional Fibromyalgia Guidline Advisory, Panel. 2012 Canadian Guidelines for the diagnosis and management of fibromyalgia syndrome: executive summary. *Pain Res Manag.* (2013) 18:119–26. doi: 10.1155/2013/918216
3. Staud R, Godfrey MM, Robinson ME. Fibromyalgia patients are not only hypersensitive to painful stimuli but also to acoustic stimuli. *J Pain.* (2021) 22:914–25. doi: 10.1016/j.jpain.2021.02.009
4. Bazzichi L, Giacomelli C, Consensi A, Giorgi V, Batticciotto A, Di Franco M, et al. One year in review 2020: fibromyalgia. *Clin Exp Rheumatol.* (2020) 38 (Suppl 123):3–8.
5. Cagnie B, Coppieters I, Denecker S, Six J, Danneels L, Meeus M. Central sensitization in fibromyalgia? A systematic review on structural and functional brain. *MRI Semin Arthritis Rheum.* (2014) 44:68–75. doi: 10.1016/j.semarthrit.2014.01.001
6. Boomershine CS. Fibromyalgia: the prototypical central sensitivity syndrome. *Curr Rheumatol Rev.* (2015) 11:131–45. doi: 10.2174/1573397111666150619095007
7. Bosma RL, Mojarad EA, Leung L, Pukall C, Staud R, Stroman PW, et al. of spinal and supra-spinal correlates of temporal pain summation in fibromyalgia patients. *Hum Brain Mapp.* (2016) 37:1349–60. doi: 10.1002/hbm.23106
8. Staud R, Craggs G, Perlstein WM, Robinson ME, Price DD. Brain activity associated with slow temporal summation of C-fiber evoked pain in fibromyalgia patients and healthy controls. *Eur J Pain.* (2008) 12:1078–89. doi: 10.1016/j.ejpain.2008.02.002
9. Staud R, Robinson ME, Price DD. Temporal summation of second pain and its maintenance are useful for characterizing widespread central sensitization of fibromyalgia patients. *J Pain.* (2007) 8:893–901. doi: 10.1016/j.jpain.2007.06.006
10. Staud R, Vierck CJ, Cannon RL, Mauderli AP, Price DD. Abnormal sensitization and temporal summation of second pain (wind-up) in patients with fibromyalgia syndrome. *Pain.* (2001) 91:165–75. doi: 10.1016/S0304-3959(00)00432-2
11. Staud R, Boissoneault J, Lai S, Mejia MS, Ramanlal R, Godfrey MM, et al. Spinal cord neural activity of fibromyalgia patients and healthy controls during temporal summation of pain: an fMRI study. *J Neurophysiol.* (2021). doi: 10.1152/jn.00276.2021
12. Jensen KB, Loitoile R, Kosek E, Petzke F, Carville S, Fransson P, et al. Patients with fibromyalgia display less functional connectivity in the brain's pain inhibitory network. *Mol Pain.* (2012) 8:32. doi: 10.1186/1744-8069-8-32

13. Jensen KB, Loitoile R, Kosek E, Petzke F, Carville S, Fransson P, et al. Overlapping structural and functional brain changes in patients with long-term exposure to fibromyalgia pain. *Arthritis Rheum.* (2013) 65:3293–303. doi: 10.1002/art.38170
14. Kim J, Loggia ML, Cahalan CM, Harris RE, Beissner DPN F, Garcia RG, et al. The somatosensory link in fibromyalgia: functional connectivity of the primary somatosensory cortex is altered by sustained pain and is associated with clinical/autonomic dysfunction. *Arthritis Rheumatol.* (2015) 67:1395–405. doi: 10.1002/art.39043
15. Pujol J, Lopez-Sola M, Ortiz H, Vilanova JC, Harrison BJ, Yucel M, et al. Mapping brain response to pain in fibromyalgia patients using temporal analysis of FMRI. *PLoS ONE.* (2009) 4:e5224. doi: 10.1371/journal.pone.0005224
16. Cook DB, Lange G, Ciccone DS, Liu WC, Steffener J, Natelson BH. Functional imaging of pain in patients with primary fibromyalgia. *J Rheumatol.* (2004) 31:364–78.
17. Gracely RH, Petzke F, Wolf JM, Clauw DJ. Functional magnetic resonance imaging evidence of augmented pain processing in fibromyalgia. *Arthritis Rheum.* (2002) 46:1333–43. doi: 10.1002/art.10225
18. Kim SH, Chang Y, Kim JH, Song HJ, Seo J, Kim SH, et al. Insular cortex is a trait marker for pain processing in fibromyalgia syndrome–blood oxygenation level-dependent functional magnetic resonance imaging study in Korea. *Clin Exp Rheumatol.* (2011) 29(6 Suppl 69):S19–27.
19. Loggia ML, Berna C, Kim J, Cahalan CM, Gollub RL, Wasan AD, et al. Disrupted brain circuitry for pain-related reward/punishment in fibromyalgia. *Arthritis Rheumatol.* (2014) 66:203–12. doi: 10.1002/art.38191
20. Lopez-Sola M, Woo CW, Pujol J, Deus J, Harrison BJ, Monfort J, et al. Towards a neurophysiological signature for fibromyalgia. *Pain.* (2017) 158:34–47. doi: 10.1097/j.pain.0000000000000707
21. Stroman PW, Warren HJM, Ioachim G, Powers JM, McNeil K. A comparison of the effectiveness of functional MRI analysis methods for pain research: The new normal. *PLoS ONE.* (2020) 15:e0243723. doi: 10.1371/journal.pone.0243723
22. Warren HJM, Ioachim G, Powers JM, Stroman PW. How fMRI Analysis Using Structural Equation Modeling Techniques Can Improve Our Understanding of Pain Processing in Fibromyalgia. *J Pain Res.* (2021) 14:381–98. doi: 10.2147/JPR.S290795
23. Millan MJ. Descending control of pain. *Prog Neurobiol.* (2002) 66:355–474. doi: 10.1016/S0301-0082(02)00009-6
24. Sundermann B, Dehghan Nayyeri M, Pfleiderer B, Stahlberg K, Junke L, Baie L, et al. Subtle changes of gray matter volume in fibromyalgia reflect chronic musculoskeletal pain rather than disease-specific effects. *Eur J Neurosci.* (2019) 50:3958–67. doi: 10.1111/ejn.14558
25. McCrae CS, O'Shea AM, Boissoneault J, Vatthauer KE, Robinson ME, Staud R, et al. Fibromyalgia patients have reduced hippocampal volume compared with healthy controls. *J Pain Res.* (2015) 8:47–52. doi: 10.2147/JPR.S71959
26. Martucci KT, Weber KA. 2nd, Mackey SC. Altered cervical spinal cord resting-state activity in fibromyalgia. *Arthritis Rheumatol.* (2019) 71:441–50. doi: 10.1002/art.40746
27. Stroman PW, Bosma RL, Cotoi AI, Leung RH, Kornelsen J, Lawrence-Dewar JM, et al. Continuous Descending Modulation of the Spinal Cord Revealed by Functional MRI. *PLoS One.* (2016) 11:e0167317. doi: 10.1371/journal.pone.0167317
28. Ioachim G, Powers JM, Warren HJM, Stroman PW. Coordinated Human Brainstem and Spinal Cord Networks during the Expectation of Pain Have Elements Unique from Resting-State Effects. *Brain Sci.* (2020) 10:568. doi: 10.3390/brainsci10090568
29. Stroman PW, Powers JM, Ioachim G, Warren HJM, McNeil K. Investigation of the neural basis of expectation-based analgesia in the human brainstem and spinal cord by means of functional magnetic resonance imaging. *Neurobiol Pain.* (2021) 10:100068. doi: 10.1016/j.ynpai.2021.100068
30. Ioachim G, Powers JM, Stroman PW. Comparing coordinated networks across the brainstem and spinal cord in the resting state and altered cognitive state. *Brain Connect.* (2019) 9:415–24. doi: 10.1089/brain.2018.0659
31. Kulshreshtha P, Gupta R, Yadav RK, Bijlani RL, Deepak KK. A comprehensive study of autonomic dysfunction in the fibromyalgia patients. *Clin Auton Res.* (2012) 22:117–22. doi: 10.1007/s10286-011-0150-6
32. Schmidt-Wilcke T, Diers M. New Insights into the Pathophysiology and Treatment of Fibromyalgia. *Biomedicines.* (2017) 5:22. doi: 10.3390/biomedicines5020022
33. Casale R, Sarzi-Puttini P, Botto R, Alciati A, Batticciotto A, Marotto D, et al. Fibromyalgia and the concept of resilience. *Clin Exp Rheumatol.* (2019) 37 (Suppl 116):105–13.
34. Craig AD. How do you feel? Interoception: the sense of the physiological condition of the body. *Nat Rev Neurosci.* (2002) 3:655–66. doi: 10.1038/nrn894
35. Wolfe F, Clauw DJ, Fitzcharles MA, Goldenberg DL, Hauser W, Katz RL, et al. 2016 Revisions to the 2010/2011 fibromyalgia diagnostic criteria. *Semin Arthritis Rheum.* (2016) 46:319–29. doi: 10.1016/j.semarthrit.2016.08.012
36. Wolfe F, Walitt B, Perrot S, Rasker JJ, Hauser W. Fibromyalgia diagnosis and biased assessment: Sex, prevalence and bias. *PLoS ONE.* (2018) 13:e0203755. doi: 10.1371/journal.pone.0203755
37. Spielberger CD. State-trait anxiety inventory. *Corsini Encyclopedia Psychol.* (2010). doi: 10.1002/9780470479216.corpsy0943
38. Beck AT, Ward CH, Mendelson M, Mock J, Erbaugh J. An inventory for measuring depression. *Arch Gen Psychiatry.* (1961) 4:561–71. doi: 10.1001/archpsyc.1961.01710120031004
39. Crowne DP, Marlowe D. A new scale of social desirability independent of psychopathology. *J Consult Psychol.* (1960) 24:349–54. doi: 10.1037/h0047358
40. Sullivan MJL, Bishop SR, Pivik J. The pain catastrophizing scale: development and validation. *Psychol Assess.* (1995) 7:524–32. doi: 10.1037/1040-3590.7.4.524
41. Sletten DM, Suarez GA, Low PA, Mandrekar J, Singer W, COMPASS. 31: a refined and abbreviated Composite Autonomic Symptom Score. *Mayo Clin Proc.* (2012) 87:1196–201. doi: 10.1016/j.mayocp.2012.10.013
42. Bennett RM, Friend R, Jones KD, Ward R, Han BK, Ross RL. The Revised Fibromyalgia Impact Questionnaire (FIQR): validation and psychometric properties. *Arthritis Res Ther.* (2009) 11:R120. doi: 10.1186/ar2830
43. Dworkin RH, Turk DC, Revicki DA, Harding G, Coyne KS, Peirce-Sandner S, et al. Development and initial validation of an expanded and revised version of the Short-form McGill Pain Questionnaire (SF-MPQ-2). *Pain.* (2009) 144:35–42. doi: 10.1016/j.pain.2009.02.007
44. Wolfe F, Hauser W. Fibromyalgia diagnosis and diagnostic criteria. *Ann Med.* (2011) 43:495–502. doi: 10.3109/07853890.2011.595734
45. Wolfe F, Clauw DJ, Fitzcharles MA, Goldenberg DL, Katz RS, Mease P, et al. The American College of Rheumatology preliminary diagnostic criteria for fibromyalgia and measurement of symptom severity. *Arthritis Care Res (Hoboken).* (2010) 62:600–10. doi: 10.1002/acr.20140
46. Vierck CJ Jr, Cannon RL, Fry G, Maixner W, Whitsel BL. Characteristics of temporal summation of second pain sensations elicited by brief contact of glabrous skin by a preheated thermode. *J Neurophysiol.* (1997) 78:992–1002. doi: 10.1152/jn.1997.78.2.992
47. Bosma RL, Ameli Mojarad E, Leung L, Pukall C, Staud R, Stroman PW. Neural correlates of temporal summation of second pain in the human brainstem and spinal cord. *Hum Brain Mapp.* (2015) 36:5038–50. doi: 10.1002/hbm.22993
48. Powers JM, Ioachim G, Stroman PW. Ten Key Insights into the Use of Spinal Cord fMRI. *Brain Sci.* (2018) 8:173. doi: 10.3390/brainsci8090173
49. Stroman PW, Ioachim G, Powers JM, Staud R, Pukall C. Pain processing in the human brainstem and spinal cord before, during, and after the application of noxious heat stimuli. *Pain.* (2018) 159:2012–20. doi: 10.1097/j.pain.0000000000001302
50. Myronenko A, Song XB. Intensity-based image registration by minimizing residual complexity. *IEEE Trans Med Imaging.* (2010) 29:1882–91. doi: 10.1109/TMI.2010.2053043
51. Myronenko A, Song XB. Image Registration by Minimization of Residual Complexity. In: *Cvpr: 2009 Ieee Conference on Computer Vision and Pattern Recognition* (Miami, FL). (2009):49–56.
52. Harita S, Stroman PW. Confirmation of resting-state BOLD fluctuations in the human brainstem and spinal cord after identification and removal of physiological noise. *Magn Reson Med.* (2017). doi: 10.1002/mrm.26606
53. Khan HS, Stroman PW. Inter-individual differences in pain processing investigated by functional magnetic resonance imaging of the brainstem and spinal cord. *Neuroscience.* (2015) 307:231–41. doi: 10.1016/j.neuroscience.2015.08.059

54. Talairach J, Tournoux P. *Co-Planar Stereotaxic Atlas of the Human Brain*. New York: Thieme Medical Publishers, Inc (1988).
55. Williams PL, Bannister LH, Berry MM, Colins P, Dyson M, Dussek JE, et al. *Gray's Anatomy: The Anatomical Basis of Medicine and Surgery*. New York: Churchill-Livingstone (1995). pp. 975–1011.
56. Naidich TP, Duvernoy HM, Delman BN, Sorensen AG, Kollias S, Haacke EM. Internal architechture of the brain stem with key axial sections: duvernoy's atlas of the human brain stem and cerebellum. New York: Springer-Verlag/Wien (2009). pp. 79-82.
57. Lang J, Bartran CT. Fila radicularia of the ventral and dorsal radices of the human spinal cord. *Gegenbaurs Morphol Jahrb.* (1982) 128:417–62.
58. Lang, J. Clinical anatomy of the cervical spine. New York: Thieme medical publishers. (1993). p. 192.
59. Harita S, Ioachim G, Powers J, Stroman PW. Investigation of Resting-State BOLD Networks in the Human Brainstem and Spinal Cord. *Neuroscience.* (2019) 404:71–81. doi: 10.1016/j.neuroscience.2019.02.009
60. Stroman PW, Ioachim G, Powers JM, Staud R, Pukall C. Pain processing in the human brainstem and spinal cord before, during and after the application of noxious heat stimuli. *Pain.* (2018) 159:2012–20. doi: 10.1080/24740527.2019.1591821
61. Stroman PW. Validation of structural equation modeling methods for functional MRI data acquired in the human brainstem and spinal cord. *Crit Rev Biomed Eng.* (2016) 44:227–41. doi: 10.1615/CritRevBiomedEng.2017020438
62. Samuels ER, Szabadi E. Functional neuroanatomy of the noradrenergic locus coeruleus: its roles in the regulation of arousal and autonomic function part II: physiological and pharmacological manipulations and pathological alterations of locus coeruleus activity in humans. *Curr Neuropharmacol.* (2008) 6:254–85. doi: 10.2174/157015908785777193
63. Llorca-Torralba, Borges G, Neto F, Mico JA, Berrocoso E. Noradrenergic Locus Coeruleus pathways in pain modulation. *Neuroscience*. (2016) 338:93–113. doi: 10.1016/j.neuroscience.2016.05.057
64. Schwarz LA, Luo L. Organization of the locus coeruleus-norepinephrine system. *Curr Biol.* (2015) 25:R1051–6. doi: 10.1016/j.cub.2015.09.039
65. Craig AD. Interoception: the sense of the physiological condition of the body. *Curr Opin Neurobiol.* (2003) 13:500–5. doi: 10.1016/S0959-4388(03)00090-4
66. Koechlin H, Coakley R, Schechter N, Werner C, Kossowsky J. The role of emotion regulation in chronic pain: A systematic literature review. *J Psychosom Res.* (2018) 107:38–45. doi: 10.1016/j.jpsychores.2018.02.002
67. Arnold LM, Choy E, Clauw DJ, Goldenberg DL, Harris RE, Helfenstein M. Jr, et al. Fibromyalgia and chronic pain syndromes: a white paper detailing current challenges in the field. *Clin J Pain.* (2016) 32:737–46. doi: 10.1097/AJP.0000000000000354
68. Fitzcharles MA, Perrot S, Hauser W. Comorbid fibromyalgia: a qualitative review of prevalence and importance. *Eur J Pain.* (2018) 22:1565–76. doi: 10.1002/ejp.1252
69. Lichtenstein A, Tiosano S, Amital H. The complexities of fibromyalgia and its comorbidities. *Curr Opin Rheumatol.* (2018) 30:94–100. doi: 10.1097/BOR.0000000000000464
70. Trucharte A, Leon L, Castillo-Parra G, Magan I, Freites D, Redondo M. Emotional regulation processes: influence on pain and disability in fibromyalgia patients. *Clin Exp Rheumatol.* (2020) 38 (Suppl 123):40–6.
71. Sprenger C, Eippert F, Finsterbusch J, Bingel U, Rose M, Buchel C. Attention modulates spinal cord responses to pain. *Curr Biol.* (2012) 22:1019–22. doi: 10.1016/j.cub.2012.04.006
72. Kucyi A, Salomons TV, Davis KD. Mind wandering away from pain dynamically engages antinociceptive and default mode brain networks. *Proc Natl Acad Sci U S A.* (2013) 110:18692–7. doi: 10.1073/pnas.1312902110
73. Hohenschurz-Schmidt DJ, Calcagnini G, Dipasquale O, Jackson JB, Medina S, O'Daly O, et al. Linking pain sensation to the autonomic nervous system: the role of the anterior cingulate and periaqueductal gray resting-state networks. *Front Neurosci.* (2020) 14:147. doi: 10.3389/fnins.2020.00147
74. Kyle BN, McNeil DW. Autonomic arousal and experimentally induced pain: a critical review of the literature. *Pain Res Manag.* (2014) 19:159–67. doi: 10.1155/2014/536859
75. Terkelsen AJ, Andersen OK, Molgaard H, Hansen J, Jensen TS. Mental stress inhibits pain perception and heart rate variability but not a nociceptive withdrawal reflex. *Acta Physiol Scand.* (2004) 180:405–14. doi: 10.1111/j.1365-201X.2004.01263.x
76. Timmers I, Kaas AL, Quaedflieg C, Biggs EE, Smeets T, de Jong JR. Fear of pain and cortisol reactivity predict the strength of stress-induced hypoalgesia. *Eur J Pain.* (2018) 22:1291–303. doi: 10.1002/ejp.1217
77. Eller-Smith OC, Nicol AL, Christianson JA. Potential Mechanisms Underlying Centralized Pain and Emerging Therapeutic Interventions. *Front Cell Neurosci.* (2018) 12:35. doi: 10.3389/fncel.2018.00035
78. Russo R, Cristiano C, Avagliano C, De Caro C, La Rana G, Raso GM, et al. Gut-brain axis: role of lipids in the regulation of inflammation, pain and CNS diseases. *Curr Med Chem.* (2018) 25:3930–52. doi: 10.2174/0929867324666170216113756
79. Tsigos C, Chrousos GP. Hypothalamic-pituitary-adrenal axis, neuroendocrine factors and stress. *J Psychosom Res.* (2002) 53:865–71. doi: 10.1016/S0022-3999(02)00429-4

Conflict of Interest: The authors declare that the research was conducted in the absence of any commercial or financial relationships that could be construed as a potential conflict of interest.

Publisher's Note: All claims expressed in this article are solely those of the authors and do not necessarily represent those of their affiliated organizations, or those of the publisher, the editors and the reviewers. Any product that may be evaluated in this article, or claim that may be made by its manufacturer, is not guaranteed or endorsed by the publisher.

frontiers | Frontiers in Neurology

ORIGINAL RESEARCH
published: 18 May 2022
doi: 10.3389/fneur.2022.858171

Medial Temporal Atrophy Contributes to Cognitive Impairment in Cerebral Small Vessel Disease

Wenshan Sun[1,2,3†], *Lili Huang*[2†], *Yue Cheng*[2], *Ruomeng Qin*[2], *Hengheng Xu*[2], *Pengfei Shao*[2], *Junyi Ma*[2], *Zhelv Yao*[2], *Lin Shi*[4,5] *and Yun Xu*[1,2*]

[1] Department of Neurology, Nanjing Drum Tower Hospital, Clinical College of Nanjing Medical University, Nanjing, China, [2] Department of Neurology, Nanjing Drum Tower Hospital, Medical School and The State Key Laboratory of Pharmaceutical Biotechnology, Institute of Brain Science, Jiangsu Key Laboratory for Molecular Medicine, Nanjing University, Nanjing, China, [3] Department of Neurology, Affiliated Jiangning Hospital of Nanjing Medical University, Nanjing, China, [4] Department of Imaging and Interventional Radiology, The Chinese University of Hong Kong, Hong Kong, Hong Kong SAR, China, [5] BrainNow Research Institute, Hong Kong Science and Technology Park, Hong Kong, Hong Kong SAR, China

Background: The role of brain atrophy in cognitive decline related to cerebral small vessel disease (CSVD) remains unclear. This study used AccuBrain™ to identify major CSVD-related brain changes and verified the relationship between brain atrophy and different cognition domains in CSVD patients.

Methods: All enrolled 242 CSVD patients and 76 healthy participants underwent magnetic resonance imaging examinations and detailed neuropsychological scale assessments were collected at the same time. The AccuBrain™ technology was applied to fully automated image segmentation, measurement, and calculation of the acquired imaging results to obtain the volumes of different brain partitions and the volume of WMH for quantitative analysis. Correlation analyses were used to estimate the relationship between MRI features and different cognitive domains. Multifactor linear regression models were performed to analyze independent predictors of MTA and cognitive decline.

Results: CSVD patients exhibited multiple gray matter nucleus volume decreases in the basal ganglia regions and brain lobes, including the temporal lobe ($P = 0.019$), especially in the medial temporal lobe ($p < 0.001$), parietal lobe ($p = 0.013$), and cingulate lobe ($p = 0.036$) compare to HC. The volume of PWMH was an independent predictor of MTA for CSVD patients. Both medial temporal atrophy (MTA) and PWMH were associated with cognition impairment in CSVD-CI patients. MTA mediated the effect of PWMH on executive function in CSVD-CI patients.

Conclusions: Our results showed that MTA was related to cognition impairment in CSVD patients, which might become a potential imaging marker for CSVD-CI.

Keywords: brain atrophy, medial temporal atrophy, cerebral small vessel disease, white matter hyperintensities, cognitive impairment

OPEN ACCESS

Edited by:
Mario Mascalchi,
University of Florence, Italy

Reviewed by:
Edith Hofer,
Medical University of Graz, Austria
Francesco Arba,
Careggi University Hospital, Italy
Cristiano Capurso,
University of Foggia, Italy

***Correspondence:**
Yun Xu
xuyun20042001@aliyun.com

†These authors have contributed equally to this work

Specialty section:
This article was submitted to Applied Neuroimaging, a section of the journal Frontiers in Neurology

Received: *21 January 2022*
Accepted: *14 April 2022*
Published: *18 May 2022*

Citation:
Sun W, Huang L, Cheng Y, Qin R, Xu H, Shao P, Ma J, Yao Z, Shi L and Xu Y (2022) Medial Temporal Atrophy Contributes to Cognitive Impairment in Cerebral Small Vessel Disease. Front. Neurol. 13:858171. doi: 10.3389/fneur.2022.858171

INTRODUCTION

Cerebral small vessel disease (CSVD) is one of the main causes of vascular cognitive impairment and vascular dementia (VD). The neuroimaging features of CSVD include small subcortical infarcts, lacunes, white matter hyperintensities (WMHs), enlarged perivascular spaces, cerebral microbleeds (CMBs), and brain atrophy (1).

Brain atrophy, especially hippocampal atrophy and medial temporal lobe atrophy (MTA), has been proven to be closely related to Alzheimer's disease (AD) while increasing evidence has shown that it has also been associated with cognitive performance in cerebrovascular diseases alone or in combination with other factors (2–4). The mechanisms of the relationship between brain atrophy and vascular dementia are still unknown, evidence showed that individuals with cognitive dysfunction develop microstructure damage and BBB breakdown in the hippocampus irrespective of Alzheimer's biomarker changes, suggesting that neurovascular dysfunction may represent a factor contributing to cognitive decline, independent of the classic pathophysiological hallmarks of AD (5). Previous studies have reported that the strongest predictor of cognitive performance in patients with CSVD was the volume of WMH (6, 7) which may have a direct effect on cognition by disrupting brain networks sub-serving cognitive processes. Vascular risk factors are strongly associated with WMH, suggesting that the etiology of WMH is more likely related to vascular diseases (8). However, WMH contributes to cognitive decline and neuronal loss not only in VD but also in AD (9, 10). Although the relationship between WMH with cognitive functioning and AD has been described consistently, the mechanisms of this relationship are poorly understood. Therefore, it is important to examine CSVD markers in addition to AD markers in older adults presenting with CSVD. Additionally, the progression of WMH, especially periventricular WMH (PWMH), has a crucial impact on brain atrophy (11). The intermediary role of brain atrophy in cognition decline has been proposed but needs to be further confirmed.

Computer-generated magnetic resonance imaging (MRI) segmentation has been available for different types of CSVD changes. AccuBrain™ is a multi-atlas-based anatomical segmentation tool that has good accuracy in the segmentation of subcortical structures and has been used for the quantification of brain volumetry and volumetric structural covariance. It has been validated for AD to have a better performance among the existing automatic brain segmentation tools (12). This study aimed to use AccuBrain™ to identify major CSVD-related brain imaging features and verify the relationship between brain atrophy and different cognition domain in CSVD patients.

METHODS

Participants

Two hundred and forty two CSVD patients and 76 healthy individuals among the outpatients and inpatients in the Department of Neurology between January 2017 and January 2019 were consecutively recruited. Ethical approval was provided by the ethics committee of Nanjing Drum Tower Hospital and written informed consent was received from all participants. Based on the established research criteria, CSVD in this study was defined as lesions of moderate-to-severe WMH (Fazekas score of 2 or higher) and/or lacunar infarction (LI) on neuroimaging, with or without perivascular spaces, microbleeds, and brain atrophy (1, 13, 14). WMHs are hyperintense on T2-weighted or FLAIR sequences, appearing as isointense or hypointense on T1-weighted sequences, depending on the sequence parameters and severity of the pathological changes, LI is a small subcortical infarct with a diameter ranging from 3 to 15 mm on axial sections (1).

The inclusion criteria were as follows: (a) age of 45–84 years; (b) CSVD diagnosis; and (c) agreement to sign an informed consent form. The exclusion criteria were as follows: (a) cerebral infarctions >20 mm in diameter; (b) leukoencephalopathy of non-vascular origin (e.g., multiple sclerosis, immunological demyelination, and metabolic, toxic, or infectious diseases); (c) intracranial or extracranial large artery stenosis of >50%; (d) intracranial hemorrhage; (e) other diseases interfering with neuropsychological tests, such as AD, Parkinson's disease, or severe psychiatric disorders; (f) inability or refusal to undergo cerebral MRI, and (g) left-handedness. All control participants underwent a brain MRI scan and had no territorial infarctions or other structural brain lesions on brain MRI.

MRI Protocol and Image Processing

All participants were studied using MRI following a standard protocol. Scans were obtained using a 3T Philips Intera scanner (Achieva 3.0 T TX, Philips Medical Systems, the Netherlands) at the Imaging Department of Drum Tower Hospital. The protocol included the following sequences: Three-dimensional, high-resolution T1 weighted turbo gradient echo sequence was performed with the following parameters: repetition time (TR) = 9.8 ms, echo time (TE) = 4.6 ms, flip angle (FA) = 8°, slices = 192, the field of view (FOV) = 250 × 250 mm2, acquisition matrix = 256 × 256, thickness = 1.0 mm. The fluid-attenuated inversion recovery (FLAIR) images were performed with TR/TE/inversion time (TI) at 4,500/333/1,600 ms, slices = 200, voxel size = 0.95 × 0.95 × 0.95 mm3, acquisition matrix = 270 × 260. In addition, axial T2-weighted, diffusion-weighted imaging (DWI) sequence, and susceptibility-weighted imaging (SWI) were collected to detect acute or subacute infarctions, and cerebral microbleeds. At baseline, participants underwent brain MRI and clinical assessments, including a standard neurological examination, functional status evaluation, and a neuropsychological examination.

The number of LIs (on T1-weighted and FLAIR images) and CMBs (on susceptibility-weighted imaging) was counted by two expert neurologists separately. Volumetry of anatomical regions was obtained from T1-weighted MRI scans automatically segmented using AccuBrain™. The WMH volume segmentation and quantification were based on additional T2-FLAIR MRI images, which were standardized by dividing the volume of different brain regions and WMH volume by the intracranial volume (ICV) for each participant (brain volume/ICV × 100%) **Figure 1**. MTA is defined as the ratio of the ipsilateral lateral subventricular horn to hippocampal volume.

Neuropsychological Evaluation

All participants completed neuropsychological measures on the same day as the MRI scan, and overall cognitive function scores were assessed using the Mini-Mental State Examination (MMSE)

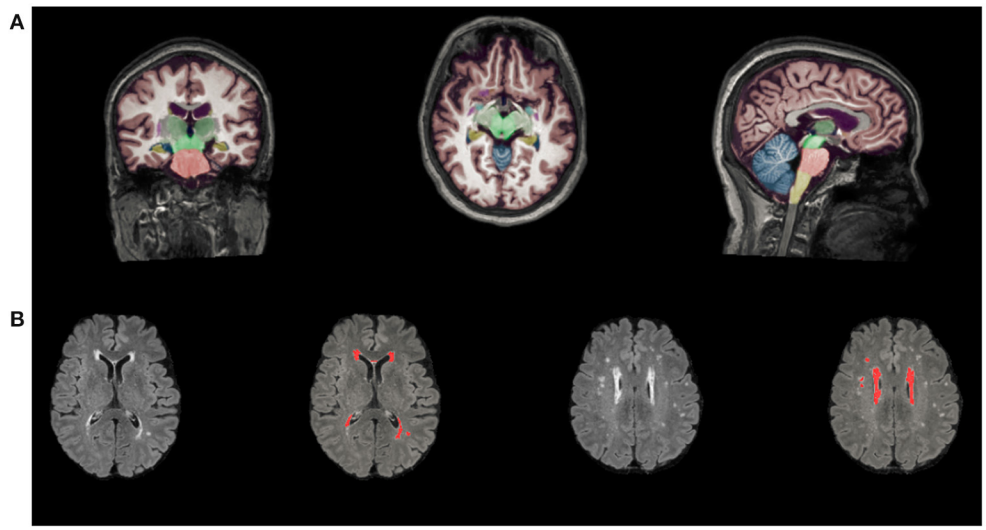

FIGURE 1 | Automated segmentation and quantitative using AccuBrain™. **(A)** Volume segmentation and quantification of anatomical regions based on T1-weighted MRI scans. **(B)** WMH volume segmentation and quantification were based on FLAIR images. WMH, white matter hyperintensities.

and Montreal Cognitive Assessment (MoCA). CSVD patients were classified into CSVD-non-CI (CSVD patients without cognitive impairment) and CSVD-CI (CSVD patients with cognitive impairment) groups according to different educational levels, which were presented in our published paper (15). For the evaluation of cognitive subdomains, information processing speed scores were assessed using Stroop Color and Word Tests B (Stroop-B) and Trail Making Test-A (TMT-A). Executive function was obtained via Stroop-C and TMT-B. Contextual memory scores were assessed using the visual reproduction-long-delayed recall portion of the Wechsler Memory Scale (WMS-VR-DR), and the auditory verbal learning test-delayed recall (AVLT-DR) assessment was available. Language scores were obtained through category verbal fluency (CVF) and Boston Naming Test (BNT) assessments. Visuospatial function scores were obtained using the clock drawing test (CDT) and visual reproduction-copy (VR-C) assessments. All raw data were transformed into standard scores (z-score), which were averaged to assess general cognitive function and other cognitive domains.

Statistical Analyses

Continuous variables with normal distribution were presented as mean ± standard deviation (SD), variables with non-normal distribution are presented as median (interquartile ranges), and categorical as frequencies (percentages). One-way ANOVA was applied for the comparison of normally distributed data, Kruskal–Wallis test was used for the comparisons of non-normal distributed data, and χ^2 test was applied for the ranked data. A *post hoc* analysis was performed to investigate group differences between any two groups, additionally correcting for multiple comparisons with Bonferroni correction.

Spearman correlation analyses were applied in the CSVD group to assess the relationships between MTA and all other variables of interest, including age, sex, years of education, history of hypertension, history of LI/TIA, LI count, and CMB count, the volume of WMH, PWMH, DWMH. Stepwise multiple linear regression models with MTA as dependent variable and significant factors in the correlation analysis as independent variables controlling for age, sex, years of education, hypertension, and history of TIA were built to determine the relationship between MTA and other conventional MRI markers of CSVD patients. Partial correlation analyses controlling for age, sex, years of education, history of hypertension, and history of LI/TIA were performed in the CSVD-CI group to assess the relationships between cognitive decline and other MRI variables, including LI count, CMB count, WMH volumes, PWMH volumes, DWMH volumes, MTA and regional brain volume. To build predictive models of cognitive functions, a stepwise multiple linear regression analysis was performed in the CSVD-CI patients. The cognitive domain function was taken as the dependent variable, and the significant factors in the correlation analysis were taken as the independent variables.

The PROCESS module (V2.16.3) written by Andrew F. Hayes (www.afhayes.com) was used for the intermediate analysis to explore whether MTA is involved in the relationship between PWMH volume and cognition controlling. First, we tested the direct effects of the primary predictor (PWMH volume) on the mediator (MTA) and the direct relationship between the mediator (MTA) and the outcome (cognitive functioning). Next, we tested the indirect mediating effect on the relationship between PWMH volume and cognitive functioning operating statistically through MTA. We considered PWMH volume, MTA, and cognitive functioning (global and each of the cognitive domains) as predictors, mediators, and outcomes, respectively. We computed bias corrected 95% confidence intervals for the size of the mediating effects with bootstrapping ($k = 5{,}000$ samples). All data were analyzed using SPSS 23.0 statistical

TABLE 1 | Demographic, clinical, volume, and neuropsychological data.

Item	HC ($n = 76$)	CSVD			$F/\chi^2/H$	p	*Post hoc* analyses		
		CSVD-nonCI ($n = 107$)	CSVD-CI ($n = 135$)	Total ($n = 318$)			HC vs. CSVD-non-CI	HC vs. CSVD-CI	CSVD-non-CI vs. CSVD-CI
Demographics									
Age, years	63 (58, 67.5)	65 (59, 72)	65 (60, 73)	65 (59, 71)	6.36	0.042*	0.230	0.037*	1.000
Male, *n* (%)	39 (51.3)	59 (55.1)	75 (55.6)	173 (54.4)	0.39	0.824	-	-	-
Education, years	12 (9, 15)	12 (9, 16)	9 (9, 12)	12 (9, 15)	7.07	0.029*	1.000	0.240	0.034*
Clinical characteristics									
Hypertension, *n* (%)	39 (52.3)	75 (70.1)	92 (68.1)	206 (64.8)	8.03	0.018*	0.013*	0.018*	0.781
Diabetes mellitus, *n* (%)	15 (19.7)	28 (26.2)	33 (24.4)	76 (23.9)	1.05	0.592	-	-	-
Hyperlipidemia, *n* (%)	13 (17.1)	23 (21.5)	28 (20.7)	64 (20.1)	0.59	0.745	-	-	-
Coronary heart disease, *n* (%)	6 (7.9)	7 (6.5)	6 (4.4)	19 (6.0)	1.12	0.570	-	-	-
History of LI/TIA, *n* (%)	10 (13.2)	27 (25.2)	49 (36.3)	87 (2.4)	13.21	0.001*	0.042*	<0.001*	0.098*
History of smoking, *n* (%)	12 (15.8%)	24 (22.4%)	36 (26.7%)	72 (22.6)	3.29	0.193	-	-	-
History of drinking, *n* (%)	9 (11.8%)	22 (20.6%)	26 (19.3%)	57 (17.9)	2.58	0.275	-	-	-
LI count, *n*	0 (0, 0)	1 (0, 2)	1 (0, 3)	0 (0, 2)	56.50	<0.001*	<0.001*	<0.001*	1.000
CMB count, *n*	0 (0, 0)	0 (0–2)	0.5 (0, 2)	0 (0, 2)	36.51	<0.001*	<0.001*	<0.001*	0.284
Volume data									
ICV (mL)	1425.85 ± 116.40	1435.29 ± 124.84	1425.55 ± 129.62	1428.90 ± 124.66	0.21	0.810	-	-	-
Brain parenchyma (mL)	1065.90 ± 88.57	1064.17 ± 95.20	1045.69 ± 102.11	1056.74 ± 96.88	1.54	0.217	-	-	-
Hippocampus (mL)	6.87 ± 0.65	6.94 ± 0.72	6.72 ± 0.79	6.84 ± 0.74	2.77	0.064	-	-	-
Amygdala (mL)	3.62 ± 0.39	3.70 ± 0.45	3.63 (3.35, 3.87)	3.64 (3.35, 3.89)	1.69	0.430	-	-	-
Thalamus-Proper (mL)	12.12 ± 1.01	11.98 ± 1.09	11.72 ± 1.14	11.91 ± 1.10	3.87	0.022*	0.998	0.025*	0.210
Caudate (mL)	6.55 ± 0.72	6.93 ± 0.82	6.96 (6.41, 7.60)	6.81 (6.29, 7.43)	16.27	<0.001*	0.004*	<0.001*	1.000
Putamen (mL)	10.61 ± 1.01	10.84 ± 0.99	10.80 ± 1.29	10.77 ± 1.13	1.01	0.364	-	-	-
Pallidum (mL)	3.06 ± 0.35	3.04 (2.74, 3.23)	2.97 ± 0.34	2.99 ± 0.35	2.24	0.327	-	-	-
Hypothalamus (mL)	0.64 (0.60, 0.71)	0.66 ± 0.07	0.65 ± 0.07	0.65 ± 0.07	0.84	0.660	-	-	-
MTA	0.35 ± 0.06	0.38 (0.33, 0.48)	0.43 (0.35, 0.54)	0.3 (0.33, 0.48)	38.89	<0.001*	0.001*	<0.001*	0.014*
White matter (mL)	486.07 ± 47.70	485.41 ± 52.58	480.30 ± 53.38	483.40 ± 5,172	0.42	0.655	-	-	-
WMH (mL)	1.57 ± 0.64	3.87 (1.74, 7.62)	4.9 (2.65, 11.86)	3.15 (1.60, 6.62)	88.45	<0.001*	<0.001*	<0.001*	0.046*
PWMH (mL)	1.18 ± 0.61	2.97 (1.41, 6.3)	4.33 (2.10, 10.82)	2.51 (1.18, 5.96)	91.28	<0.001*	<0.001*	<0.001*	0.025*
DWMH (mL)	0.35 (0.18, 0.55)	0.49 (0.25, 0.96)	0.53 (2.63, 1.05)	0.44 (0.25, 0.86)	17.13	<0.001*	0.004*	<0.001*	1.000
Gray matter (mL)	579.82 ± 46.57	578.75 ± 48.61	565.39 ± 54.02	573.34 ±50.83	2.91	0.056	-	-	-
Frontal lobe (mL)	151.10 ± 13.48	150.47 ± 15.08	147.36 ± 15.83	149.30 ± 15.09	1.99	0.138	-	-	-
Occipital lobe (mL)	63.43 ± 6.77	62.38 ± 6.90	61.09 ± 8.16	62.08 ± 7.47	2.54	0.080	-	-	-
Temporal lobe (mL)	97.31 ± 9.05	98.07±10.71	94.53 ± 10.43	96.39 ± 10.3	3.99	0.019*	1.000	0.178	0.023*
Parietal lobe (mL)	82.13 ± 7.69	81.85 ± 7.28	79.30 ± 8.64	80.83 ± 8.06	4.37	0.013*	1.000	0.042*	0.042*
Cingulate lobe	23.77 ± 2.39	23.80 ± 2.56	23.03 ± 2.64	23.47 ± 2.57	3.37	0.036*	0.939	0.046*	0.022*
Insular (mL)	12.39 ± 1.28	12.34 ± 1.44	12.12 ± 1.48	12.26 ± 1.42	1.10	0.335	-	-	-

(Continued)

TABLE 1 | Continued

Item	HC (n = 76)	CSVD			$F/\chi2/H$	p	*Post hoc* analyses		
		CSVD-nonCI (n = 107)	CSVD-CI (n = 135)	Total (n = 318)			HC vs. CSVD-non-CI	HC vs. CSVD-CI	CSVD-non-CI vs. CSVD-CI
Neuropsychological data									
General cognitive function	0.59(0.27, 0.85)	0.59 (0.27,0.76)	−0.35 (−1.07,0.00)	0.14(-0.31,0.63)	150.03	<0.001*	1.000	<0.001*	<0.001*
Episodic memory	0.38±0.74	0.27±0.88	−0.34 ± 0.79	0.03 ± 0.80	29.91	<0.001*	1.000	<0.001*	<0.001*
Language	0.24±0.72	0.27±0.70	−0.37±0.74	0.00 ± 0.86	19.01	<0.001*	1.000	<0.001*	<0.001*
Information processing speed (inverse)	−0.33 (−0.49, −0.11)	−0.35 (−0.49, −0.10)	0.06 (−0.24, 0.50)	−0.21 (−0.42,1.58)	67.97	<0.001*	1.000	<0.001*	<0.001*
Executive function (inverse)	−0.33 (−0.49, −0.11)	−0.34 (−0.52, −0.08)	0.02 (−0.27, 0.55)	−0.20 (−0.43,1.12)	58.27	<0.001*	1.000	<0.001*	<0.001*
Visuospatial function	0.41 (0.41, 0.41)	0.41 (0.41,0.41)	0.41 (−0.41, 0.41)	0.41 (0.00,0.41)	18.47	<0.001*	1.000	0.015*	<0.001*

Values are presented as the mean ± standard deviation (SD), median (interquartile ranges) or number (percentage). One-way ANOVA was applied for the comparison of normally distributed data, χ2 test was applied for the ranked data, and the Kruskal–Wallis test was used for the comparisons of non-normally distributed data.

**Indicates a statistical difference between groups, $p < 0.05$.*

HC, health control; CSVD, cerebral small vessel disease; CSVD-nonCI, CSVD patients without cognitive impairment; CSVD-CI, CSVD patients with cognitive impairment; n, number; TIA, transient ischemic attack; ICV, intracranial volume; MTA, medial temporal atrophy, the ratio of the ipsilateral lateral subventricular horn to hippocampal volume. WMH, white matter hyperintensities; WMH, total white matter hyperintensities; PWMH, periventricular white matter hyperintensities; DWMH, deep white matter hyperintensities; LI, lacunar infarction; CMB cerebral microbleed.

software (Chicago, IL, USA). A *P*-value of <0.05 was considered statistically significant.

RESULTS

Demographic, Clinical, and Neuropsychological Characteristics

The demographic and clinical data of the HC and CSVD groups are presented in **Table 1**. There was no significant difference in gender or prevalence of diabetes mellitus, dyslipidemia, history of coronary heart disease, smoking, and drinking. The CSVD group showed a significantly increased age ($p = 0.042$), history of hypertension ($p = 0.018$), and LI/TIA ($p = 0.001$). One hundred and seven CSVD patients were without cognitive impairment (CSVD-non-CI) and 135 with cognitive impairment (CSVD-CI). WMH, PWMH, DWMH volumes, LI count, and CMB count in CSVD-non-CI and CSVD-CI were significantly higher than those in HCs. The CSVD-CI subgroup showed poorer performances on general cognitive function, episodic memory, language, information processing, executive function, and visuospatial function than other subgroups. Compared to CSVD-non-CI group, patients in CSVD-CI group were less educated ($p = 0.034$). No significant differences in the cognitive tests were shown between the CSVD-non-CI group and the HC group.

Group Comparisons of Brain Regional Volumetry Quantified Using AccuBrain™

The group comparisons of brain volumetric differences quantified using AccuBrain^{TM} are also summarized in **Table 1**. The volume of the thalamus-proper, caudate, temporal lobe, parietal lobe, cingulate lobe, and MTA were statistically significant among groups. As the *post-hoc* analysis showed, compared with the CSVD-non-CI group, the CSVD-CI had severer atrophy in the temporal lobe ($p = 0.023$), parietal lobe ($P = 0.042$), and cingulate lobe ($p = 0.022$). Notably, MTA exhibited significant differences between HC vs. CSVD-non-CI ($p = 0.001$), HC vs. CSVD-CI ($p < 0.001$), and CSVD-non-CI vs. CSVD-CI ($p = 0.014$).

Association Between MTA and Conventional MRI Markers of CSVD Patients

In CSVD patients, Spearman correlation analyses showed MTA were significantly correlated to age ($r = 0.524$, $p < 0.001$), WMH volume ($r = 0.436$, $p = p<0.001$), PWMH volume ($r = 0.472$, $p < 0.001$), LI count ($r = 0.138$, $p = 0.035$), and CMB count ($r = 0.230$, $p < 0.001$). No significant correlation was found between MTA and DWMH volume ($r = 0.046$, $p = 0.475$). Age, sex, education and hypertension and history of TIA, LI count, and CMB count, PWMH volume was further included in the stepwise multiple linear regression models with MTA as dependent variable. Multiple linear regression analysis revealed that the volume of PWMH was an independent predictor of MTA for CSVD patients ($\beta = 0.478$, 95%CI: 0.377–0.581).

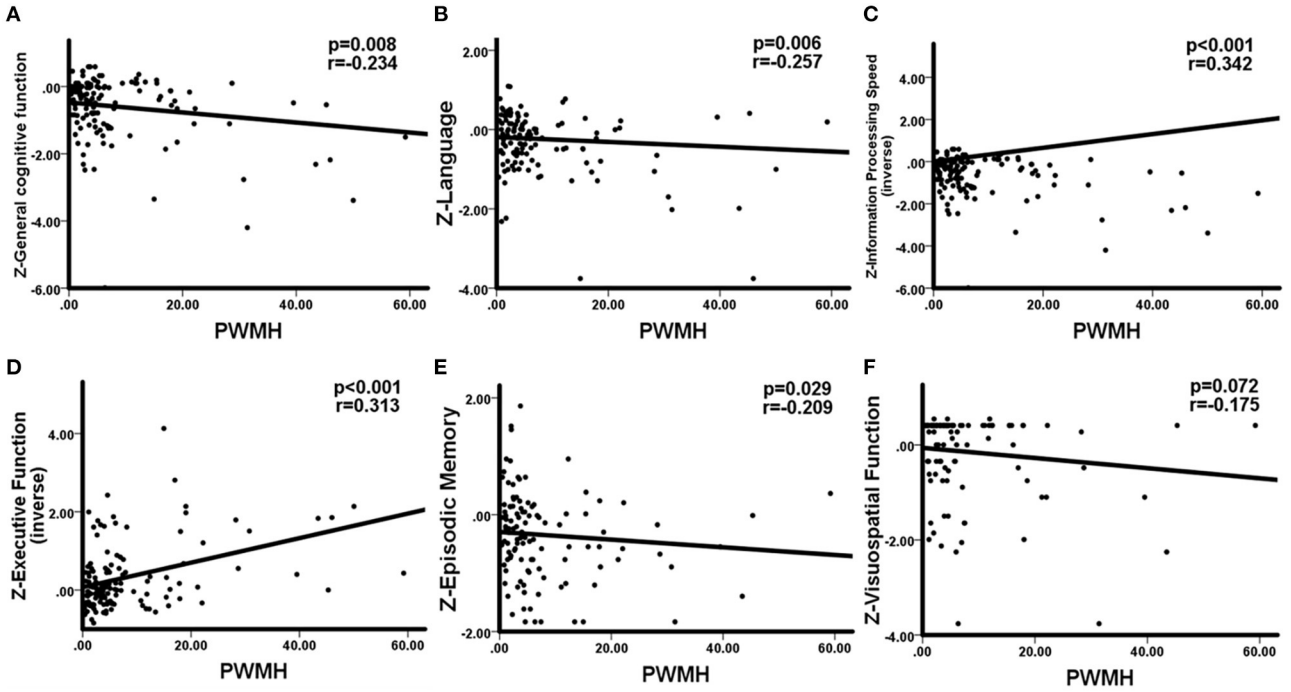

FIGURE 2 | Correlations between PWMH and cognitive function in CSVD-CI patients. Partial correlation was conducted by controlling for age, gender, years of education, history of hypertension, and history of LI/TIA in CSVD-CI group. **(A)** Increased PWMH volume was associated with worse general cognitive function. **(B)** Larger PWMH volume showed significant impairment in the language domain. **(C)** Information processing speed was negatively associated with increased PWMH volume. **(D)** PWMH volume had a negative correlation with executive function. **(E)** PWMH volume correlated negatively with episodic memory. **(F)** No significant correlation was observed between PWMH volume and visuospatial function. PWMH, periventricular white matter hyperintensities; CSVD-CI, cerebral small vessel disease patients with cognitive impairment; TIA, transient ischemic attack; LI, lacunar infarction.

Associations Between Brain Atrophy and Cognition in CSVD-CI Patients

For 135 CSVD-CI patients, partial correlation analyses revealed that volume of WMH and PWMH, MTA, CMB count, volume of the temporal lobe, parietal lobe, and cingulate lobe were significantly associated with impairment in various cognitive domains controlling for age, sex, years of education, history of hypertension, and history of LI/TIA.

WHM volume was negatively correlation with general cognitive function ($r = -0.224$, $p = 0.011$), language ($r = -0.266$, $p = 0.004$), information processing speed ($r = -0.353$, $p < 0.001$), executive function ($r = -0.310$, $p < 0.001$), and memory ($r = -0.191$, $p = 0.046$). No significant correlations between DWMH and cognition were observed. The correlations between PWMH volume and cognitive function are presented in **Figure 2**, correlations between MTA and cognitive function are presented in **Figure 3**. In summary, PWMH and MTA extensively affected various cognitive domains in CSVD-CI patients. Particularly, PWMH volume was associated with impairment in all cognitive domains except visual space. MTA had a more prominent effect on executive function and information processing speed, and memory than on language and visuospatial function.

We found the CMB count was significantly related to language ($r = -0.188$, $p = 0.046$), information processing speed ($r = -0.224$, $p = 0.011$), executive function ($r = -0.201$, $p = 0.023$) but not general cognitive function ($r = 0.071$, $p = 0.429$), memory ($r = -0.047$, $p = 0.629$) and visuospatial function ($r = -0.070$, $p = 0.478$). No significant correlations existed between LI count and cognition. Both temporal lobe volume and parietal lobe volume was positively correlated with information processing speed ($r = 0.233$, $p = 0.008$; $r = 0.192$, $p = 0.028$) and executive function ($r = 0.258$, $p = 0.003$; $r = 0.252$, $p = 0.004$). Positive association was also observed between cingulate lobe volume and information processing speed ($r = 0.175$, $p = 0.046$).

In multiple linear regression analysis, general and each cognitive domain was set as dependent variables separately, the volume of PWMH, temporal lobe, parietal lobe, and cingulate lobe, CMB count, and MTA as independent variables, with age, sex, years of education, history of hypertension, history of stroke/TIA as covariant. MTA was significantly associated with worse overall performance in all cognitive domains (**Table 2**). The volume of PWMH was an independent predictor of decline in executive function. Years of education predicted overall cognitive function, language, memory, executive function, and visuospatial function but not information processing speed. Gender differences were the predictors of overall cognitive and language function. Age was a risk factor for visuospatial deficits. Additionally, cingulate atrophy was predictive of overall

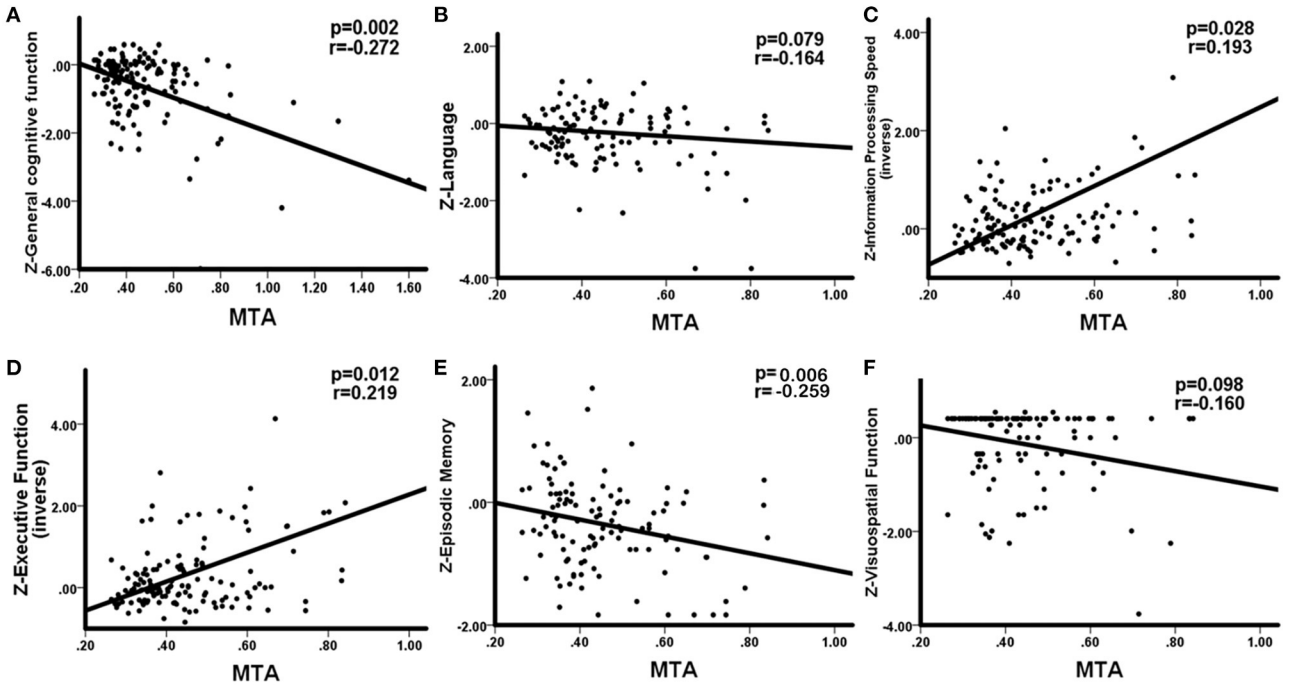

FIGURE 3 | Correlations between MTA and cognitive function in CSVD-CI patients. Partial correlation was conducted by controlling for age, gender, years of education, history of hypertension, and history of LI/TIA in CSVD-CI group. **(A)** MTA correlated negatively with general cognitive function. **(B)** No significant correlation was observed between MTA and the language domain. **(C)** MTA had a negative correlation with information processing speed. **(D)** MTA had a negative correlation with executive function. **(E)** MTA correlated negatively with episodic memory. **(F)** No significant correlation was observed between MTA and visuospatial function. MTA, medial temporal atrophy, the ratio of the ipsilateral lateral subventricular horn to hippocampal volume; CSVD-CI, cerebral small vessel disease patients with cognitive impairment; TIA, transient ischemic attack; LI, lacunar infarction.

cognitive decline; however, no correlation was found with other cognitive domains.

Direct and mediated effects of periventricular WMH on executive function are presented in **Figure 4**. The PWMH had a direct effect on the impairment of executive function (direct effect: −0.019, 95%CI: −0.036∼-0.002); a larger PWMH volume was associated with lower executive function performance and more serious MTA. In mediation analyses, the associations of PWMH with executive functioning were significantly mediated by MTA (indirect effect: −0.010, 95%: −0.0428 to−0.0039).

DISCUSSION

In our study, segmentation and detection of the volumes of brain regions revealed that CVSD showed cerebral atrophy not only in the basal ganglia region but also in the lobes. We further analyzed the factors associated with cognitive decline, and our results revealed that the volume of PWMH and MTA were independent predictors of cognitive decline in CSVD. Previous studies have suggested that WMH is the most common cause of vascular cognitive impairment, from mild cognitive impairment to VD (16), and significantly affects executive function and processing speed (17). Moreover, different areas of WMH distribution contribute to each cognitive domain; the periventricular WMH is more correlated with patients' executive function decline than DWMH, and WMH in the parietal temporal lobe is more correlated with memory decline (18).

Notably, compared with the HC group, the CSVD group showed more WHM volume, both in PWMH and DWMH volumes, while in CSVD subgroup, no significant difference was detected between CSVD-CI and CSVD-non-CI in DWMH volumes. Furthermore, the following correlation analysis also failed to find the association between different cognitive domains and DWMH volumes. PWMH and DWMH were reported to be associated with different histopathological, and aetiological features. From the aspect of histopathologic correlates, peri-WMH mostly reflects non-ischemic damages whereas DWMH is associated with ischemic tissue damages (19). Previous studies found that the elderly with PWMH, rather than DWMH, is associated with impaired cognitive function, especially executive function. A possible explanation was that PWMH lesions interfere with long connections, leading to worse performance in mostly cognitive domains whereas DWMH damage is responsible for short connections that are less associated with cognitive performance but may play an important role in motor dysfunction (20).

Our most important findings are that MTA is an independent risk factor for cognitive decline in CSVD and that the effect of PWMH on cognitive decline is either directly or indirectly mediated by MTA. MTA and hippocampal atrophy have been

TABLE 2 | Multiple linear regression analysis for cognitive function in CSVD-CI group ($n = 135$).

	β	95%CI	*p*
General cognitive function			
MTA	−0.558	−0.672 to −0.401	<0.001
Education	0.428	0.290 to 0.555	<0.001
Gender	−0.252	−0.387 to −0.104	0.001
Cingulate lobe	−0.163	−0.309 to −0.014	0.032
Episodic memory			
MTA	−0.335	−0.512 to −0.159	<0.001
Education	0.184	0.006 to 0.297	0.041
Language			
MTA	−0.325	−0.417 to −0.135	<0.001
Education	0.282	0.100 to 0.390	0.001
Gender	−0.196	−0.288 to −0.023	0.020
Information processing speed (inverse)			
MTA	0.448	0.339 to 0.702	<0.001
Executive function (inverse)			
MTA	0.350	0.180 to 0.582	<0.001
Education	−0.221	−0.413 to −0.079	0.004
PWMH volume	0.207	0.025 to 0.426	0.025
Visuospatial function			
Education	0.210	0.032 to 0.383	0.021
MTA	−0.347	−0.660 to −0.196	<0.001
Age	0.263	0.071 to 0.449	0.007

CSVD, cerebral small vessel disease; CSVD-CI, CSVD patients with cognitive impairment; MTA, medial temporal atrophy, the ratio of the ipsilateral lateral subventricular horn to hippocampal volume; PWMH, periventricular white matter hyperintensities; **β**, *standardized coefficients.*

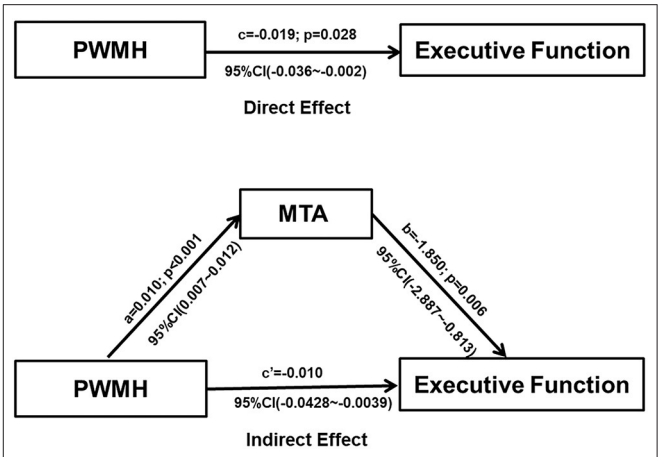

FIGURE 4 | Graphical illustration of the direct and indirect effects of PWMH volume and MTA on cognitive functioning. Each path of the connection, standard coefficient (a, b, c, c'), and *p*-value were shown. Mediation analysis revealed that the association between PWMH and executive function was mediated by MTA (Indirect effect: −0.01, 95% CI: −0.0428 to −0.0039). PWMH, periventricular white matter hyperintensities; MTA, medial temporal atrophy, the ratio of the ipsilateral lateral subventricular horn to hippocampal volume.

implicated in age-related cognitive decline and as important imaging markers of AD (21). While it has been also reported that MTA correlates with VD, Arba et al. assessed the relationship between cognition and imaging features in patients with stroke or TIA over a 1-year period and found that moderate to severe MTA was present in 44% of the patients, confirming that VD features are independently associated with MTA (22). In the case of patients with cerebral autosomal dominant arteriopathy with subcortical infarcts and leukoencephalopathy, hippocampal atrophy is significantly associated with dementia (23), and animal models of long-term hypoperfusion have shown that neurodegenerative changes are not a prerequisite for hippocampal atrophy (24). All these findings suggest that MTA is not only an important alteration in neurodegenerative disease but also an important pathway for the development of vascular cognitive dysfunction.

Although the specific mechanisms of cognitive decline in VD remain unclear, MTA and WMH are common morphological features of AD and CSVD. Our study found strong direct effects and indirect effects of WMH on cognition through MTA in CSVD-CI patients, suggesting that some of the consistently observed associations of WMH with cognition are at least partially attributable to their effect on brain atrophy. This finding has implications for understanding why WMH are strong predictors of cognitive decline and AD. Indeed, previous work has shown that in individuals with higher levels of WMH, the coupling of structural and functional connections is disrupted, with subsequent effects on executive function and memory (25). The observed indirect effects of WMH on cognition through cortical thinning may reflect axonal damage associated with CSVD (26), which promotes neurodegenerative changes in the cerebral cortex that in turn drives cognitive loss. This process may be dependent on hyper-phosphorylated tau, suggesting a direct causal link between CSVD and AD pathology (27).

Our study features a combination of big data applications and neuroimaging studies and the quantitative analysis of brain atrophy by applying AccuBrain^{TM} technology, which is an application of machine/deep learning strategy for cerebrovascular disease risk assessment. Further development of the technology will have a greater potential in research related to imaging for CSVD. However, this study had some limitations. First, this is a cross-sectional study, the conclusions will be more convincing if they can be replicated in future longitudinal studies, especially in the exploration of the regional brain atrophy progression with the development of CSVD. Second, due to the small sample size, statistical power might be insufficient. the results need to be further validated with a larger sample. Third, the study had a single assessment method and did not incorporate other functional brain imaging tools, for example, magnetic resonance-based diffusion tensor imaging (DTI) is not involved in this study, which is a powerful non-invasive imaging technique and a very advanced quantitative measurement that can be used to trace white matter microstructures and abnormal white matter connectivity *in vivo*. Last but not the least, we mainly focused on superficial imaging characteristics, the volume of WHM, and brain region, other factors like white matter

microstructural, enlarged perivascular spaces on cognition were not analyzed, the potential pathogenesis needs to be further explored in subsequent studies.

In conclusion, brain atrophy in patients with CSVD was mainly characterized by alterations of multiple gray matter nuclei in the basal ganglia regions, including the thalamus and caudate nucleus. Atrophy of the lobes was concentrated in the temporal lobes, especially in the medial temporal lobe. The PWMH was an independent predictor of MTA that independently influences cognitive decline in patients with CSVD. The effect of PWMH on executive function was mediated by MTA.

DATA AVAILABILITY STATEMENT

The raw data supporting the conclusions of this article will be made available by the authors, without undue reservation.

ETHICS STATEMENT

The studies involving human participants were reviewed and approved by Ethics Committee of Nanjing Drum Tower Hospital. The patients/participants provided their written informed consent to participate in this study. Written informed consent was obtained from the individual(s) for the publication of any potentially identifiable images or data included in this article.

AUTHOR CONTRIBUTIONS

YX conceived and designed the analysis. WS performed the analysis and wrote the paper. LH collected and evaluated the brain MRI and also conducted the statistical analysis. YC and RQ evaluated all neuropsychological scales. PS, JM, and ZY collected the clinical characteristics data. LS contributed the analysis tool of segmentation and detection of the volumes of brain structure by AccuBrainTM. All authors contributed to the article and approved the submitted version.

ACKNOWLEDGMENTS

We thank Department of Imaging and Interventional Radiology, the Chinese University of Hong Kong for providing the anatomical segmentation tool. We also thank Penglei Pan for his assistance in proofreading the manuscript.

REFERENCES

1. Wardlaw JM, Smith EE, Biessels GJ, Cordonnier C, Fazekas F, Frayne R, et al. Neuroimaging standards for research into small vessel disease and its contribution to ageing and neurodegeneration. *Lancet Neurol.* (2013) 128:822–38. doi: 10.1016/S1474-4422(13)70124-8
2. Habes M, Erus G, Toledo JB, Bryan N, Janowitz D, Doshi J, et al. Regional tract-specific white matter hyperintensities are associated with patterns of aging-related brain atrophy via vascular risk factors, but also independently. *Alzheimers Dement.* (2018) 10:278–84. doi: 10.1016/j.dadm.2018.02.002
3. Bastos-Leite AJ, van der Flier WM, van Straaten EC, Staekenborg SS, Scheltens P, Barkhof F. The contribution of medial temporal lobe atrophy and vascular pathology to cognitive impairment in vascular dementia. *Stroke.* (2007) 38:3182–5. doi: 10.1161/STROKEAHA.107.490102
4. Chen L, Song J, Cheng R, Wang K, Liu X, He M, et al. Cortical thinning in the medial temporal lobe and precuneus is related to cognitive deficits in patients with subcortical ischemic vascular disease. *Front Aging. Neurosci.* (2020) 12:614833. doi: 10.3389/fnagi.2020.614833
5. Nation DA, Sweeney MD, Montagne A, Sagare AP, D'Orazio LM, Pachicano M, et al. Blood-brain barrier breakdown is an early biomarker of human cognitive dysfunction. *Nat Med.* (2019) 25:270–6. doi: 10.1038/s41591-018-0297-y
6. Jokinen H, Koikkalainen J, Laakso HM, Melkas S, Nieminen T, Brander A, et al. Global burden of small vessel disease–related brain changes on MRI predicts cognitive and functional decline. *Stroke.* (2020) 51:170–8. doi: 10.1161/STROKEAHA.119.026170
7. Cannistraro RJ, Badi M, Eidelman BH, Dickson DW, Middlebrooks EH, Meschia JF. CNS small vessel disease. *Neurology.* (2019) 92:1146–56. doi: 10.1212/WNL.0000000000007654
8. Jiménez-Balado J, Riba-Llena I, Abril O, Garde E, Penalba A, Ostos E, et al. Cognitive impact of cerebral small vessel disease changes in patients with hypertension. *Hypertension.* (2019) 73:342–9. doi: 10.1161/HYPERTENSIONAHA.118.12090
9. Hachinski V. Stroke and potentially preventable dementias proclamation. *Stroke.* (2015) 46:3039–40. doi: 10.1161/STROKEAHA.115.011237
10. Huynh K, Piguet O, Kwok J, Dobson-Stone C, Halliday GM, Hodges JR, et al. Clinical and biological correlates of white matter hyperintensities in patients with behavioral-variant frontotemporal dementia and Alzheimer Disease. *Neurology.* (2021) 30:e1743–e1754. doi: 10.1212/WNL.0000000000011638
11. Rizvi B, Narkhede A, Last BS, Budge M, Tosto G, Manly JJ, et al. The effect of white matter hyperintensities on cognition is mediated by cortical atrophy. *Neurobiol Aging.* (2018) 64:25–32. doi: 10.1016/j.neurobiolaging.2017.12.006
12. Yu Q, Mai Y, Ruan Y, Luo Y, Zhao L, Fang W, et al. An MRI-based strategy for differentiation of frontotemporal dementia and Alzheimer's disease. *Alzheimers Res Ther.* (2021) 13:23. doi: 10.1186/s13195-020-00757-5
13. Liu R, Chen H, Qin R, Gu Y, Chen X, Zou J, et al. The altered reconfiguration pattern of brain modular architecture regulates cognitive function in cerebral small vessel disease. *Front Neurol.* (2019) 10:324. doi: 10.3389/fneur.2019.00324
14. Huang L, Chen X, Sun W, Chen H, Ye Q, Yang D, et al. Early segmental white matter fascicle microstructural damage predicts the corresponding cognitive domain impairment in cerebral small vessel disease patients by automated fiber quantification. *Front Aging Neurosci.* (2021) 12:598242. doi: 10.3389/fnagi.2020.598242
15. Gu Y, Liu R, Qin R, Chen X, Zou J, Jiang Y, et al. Characteristic changes in the default mode network in hypertensive patients with cognitive impairment. *Hypertens Res.* (2019) 42:530–40. doi: 10.1038/s41440-018-0176-4
16. Iadecola C, Duering M, Hachinski V, Joutel A, Pendlebury ST, Schneider JA, et al. Vascular cognitive impairment and dementia. *J Am Coll Cardiol.* (2019) 73:3326–44. doi: 10.1016/j.jacc.2019.04.034
17. Lampe L, Kharabian-Masouleh S, Kynast J, Arelin K, Steele CJ, Löffler M, et al. The relationships between white matter hyperintensities on cognition in the healthy elderly. *J Cereb Blood Flow Metab.* (2019) 39:36–43. doi: 10.1177/0271678X17740501
18. Ten Kate M, Barkhof F, Boccardi M, Visser PJ, Jack CR Jr, Lovblad KO, et al. Clinical validity of medial temporal atrophy as a biomarker for Alzheimer's disease in the context of a structured 5-phase development framework. *Neurobiol Aging.* (2017) 52:167–82. doi: 10.1016/j.neurobiolaging.2016.05.024
19. Bolandzadeh N, Davis JC, Tam R, Handy TC, Liu-Ambrose T. The association between cognitive function and white matter lesion location in older adults: a systematic review. *BMC Neurol.* (2012) 12:126. doi: 10.1186/1471-2377-12-126
20. Griffanti L, Jenkinson M, Suri S, Zsoldos E, Mahmood A, Filippini N, et al. Classification and characterization of periventricular and deep white matter

hyperintensities on MRI: a study in older adults. *Neuroimage*. (2018) 170:174–81. doi: 10.1016/j.neuroimage.2017.03.024
21. de Flores R, Wisse LEM, Das SR, Xie L, McMillan CT, Trojanowski JQ, et al. Contribution of mixed pathology to medial temporal lobe atrophy in Alzheimer's disease. *Alzheimers Dement.* (2020) 16:843–52. doi: 10.1002/alz.12079
22. Arba F, Quinn T, Hankey GJ, Ali M, Lees KR, Inzitari D, et al. Cerebral small vessel disease, medial temporal lobe atrophy and cognitive status in patients with ischemic stroke and transient ischemic attack. *Eur J Neurol.* (2017) 24:276–82. doi: 10.1111/ene.13191
23. O'Sullivan M, Ngo E, Viswanathan A, Jouvent E, Gschwendtner A, Saemann PG, et al. Hippocampal volume is an independent predictor of cognitive performance in CADASIL. *Neurobiol Aging.* (2009) 30:890–7. doi: 10.1016/j.neurobiolaging.2007.09.002
24. Nishio K, Ihara M, Yamasaki N, Kalaria RN, Maki T, Fujita Y, et al. A mouse model characterizing features of vascular dementia with hippocampal Atrophy. *Stroke.* (2010) 41:1278–84. doi: 10.1161/STROKEAHA.110.581686
25. Reijmer YD, Schultz AP, Leemans A, O'Sullivan MJ, Gurol ME, Sperling R, et al. Decoupling of structural and functional brain connectivity in older adults with white matter hyperintensities. *Neuroimage.* (2015) 117:222–9. doi: 10.1016/j.neuroimage.2015.05.054
26. Koike MA, Green KN, Blurton-Jones M, Laferla FM. Oligemic Hypoperfusion differentially affects tau and amyloid-β. *Am J Pathol.* (2010) 177:300–10. doi: 10.2353/ajpath.2010.090750
27. Uiterwijk R, Huijts M, Staals J, Duits A, Gronenschild E, Kroon AA, et al. Subjective cognitive failures in patients with hypertension are related to cognitive performance and cerebral microbleeds. *Hypertension.* (2014) 64:653–7. doi: 10.1161/HYPERTENSIONAHA.114.03621

Conflict of Interest: LS is the director of BrainNow Research Institute.

The remaining authors declare that the research was conducted in the absence of any commercial or financial relationships that could be construed as a potential conflict of interest.

Publisher's Note: All claims expressed in this article are solely those of the authors and do not necessarily represent those of their affiliated organizations, or those of the publisher, the editors and the reviewers. Any product that may be evaluated in this article, or claim that may be made by its manufacturer, is not guaranteed or endorsed by the publisher.

frontiers | Frontiers in Neurology

ORIGINAL RESEARCH
published: 23 May 2022
doi: 10.3389/fneur.2022.884449

Cerebral Microbleeds Assessment and Quantification in COVID-19 Patients With Neurological Manifestations

Angela Napolitano[1†], Alberto Arrigoni[2†], Anna Caroli[2†], Mariangela Cava[3], Andrea Remuzzi[4†], Luca Giovanni Longhi[5], Antonino Barletta[1], Rosalia Zangari[6], Ferdinando Luca Lorini[7†], Maria Sessa[8†] and Simonetta Gerevini[1†]*

[1] Department of Neuroradiology, ASST Papa Giovanni XXIII, Bergamo, Italy, [2] Bioengineering Department, Istituto di Ricerche Farmacologiche Mario Negri IRCCS, Bergamo, Italy, [3] Radiology Unit, S. Giacomo Hospital, Novi Ligure, Italy, [4] Department of Management, Information and Production Engineering, University of Bergamo, Bergamo, Italy, [5] Neurosurgical Intensive Care Unit, Department of Anesthesia and Critical Care Medicine, ASST Papa Giovanni XXIII, Bergamo, Italy, [6] Research Foundation, ASST Papa Giovanni XXIII, Bergamo, Italy, [7] Department of Emergency and Critical Care Area, ASST Papa Giovanni XXIII, Bergamo, Italy, [8] Department of Neurology, ASST Papa Giovanni XXIII, Bergamo, Italy

It is increasingly acknowledged that Coronavirus Disease 2019 (COVID-19) can have neurological manifestations, and cerebral microbleeds (CMBs) have been observed in this setting. The aim of this study was to characterize CMBs patterns on susceptibility-weighted imaging (SWI) in hospitalized patients with COVID-19 with neurological manifestations. CMBs volume was quantified and correlated with clinical and laboratory parameters. The study included patients who were hospitalized due to COVID-19, exhibited neurological manifestations, and underwent a brain MRI between March and May 2020. Neurological, clinical, and biochemical variables were reported. The MRI was acquired using a 3T scanner, with a standardized protocol including SWI. Patients were divided based on radiological evidence of CMBs or their absence. The CMBs burden was also assessed with a semi-automatic SWI processing procedure specifically developed for the purpose of this study. Odds ratios (OR) for CMBs were calculated using age, sex, clinical, and laboratory data by logistic regression analysis. Of the 1,760 patients with COVID-19 admitted to the ASST Papa Giovanni XXIII Hospital between 1 March and 31 May 2020, 116 exhibited neurological symptoms requiring neuroimaging evaluation. Of these, 63 patients underwent brain MRI and were therefore included in the study. A total of 14 patients had radiological evidence of CMBs (CMBs+ group). CMBs+ patients had a higher prevalence of CSF inflammation ($p = 0.020$), a higher white blood cell count ($p = 0.020$), and lower lymphocytes ($p = 0.010$); the D-dimer ($p = 0.026$), LDH ($p = 0.004$), procalcitonin ($p = 0.002$), and CRP concentration ($p < 0.001$) were higher than in the CMBs- group. In multivariable logistic regression analysis, CRP (OR $= 1.16$, $p = 0.011$) indicated an association with CMBs. Estimated CMBs volume was higher in females than in males and decreased with age (Rho $= -0.38$; $p = 0.18$); it

Edited by:
Jean Chen,
University of Toronto, Canada

Reviewed by:
Marialuisa Zedde,
IRCCS Local Health Authority of Reggio Emilia, Italy
Lina Palaiodimou,
University General Hospital Attikon, Greece

***Correspondence:**
Angela Napolitano
anapolitano@asst-pg23.it

†ORCID:
Anna Caroli
orcid.org/0000-0002-4130-4663
Alberto Arrigoni
orcid.org/0000-0002-1914-6582
Simonetta Gerevini
orcid.org/0000-0002-2374-194X
Maria Sessa
orcid.org/0000-0002-9589-0290
Angela Napolitano
orcid.org/0000-0001-8423-4485
Andrea Remuzzi
orcid.org/0000-0002-4301-8927
Ferdinando Luca Lorini
orcid.org/0000-0002-2711-3377

Specialty section:
This article was submitted to Applied Neuroimaging, a section of the journal Frontiers in Neurology

Received: 26 February 2022
Accepted: 07 April 2022
Published: 23 May 2022

Citation:
Napolitano A, Arrigoni A, Caroli A, Cava M, Remuzzi A, Longhi LG, Barletta A, Zangari R, Lorini FL, Sessa M and Gerevini S (2022) Cerebral Microbleeds Assessment and Quantification in COVID-19 Patients With Neurological Manifestations. Front. Neurol. 13:884449. doi: 10.3389/fneur.2022.884449

was positively associated with CRP (Rho = 0.36; $p = 0.22$), and negatively associated with lymphocytes (Rho = −0.52; $p = 0.07$). CMBs are a frequent imaging finding in hospitalized patients with COVID-19 with neurological manifestations and seem to be related to pro-inflammatory status.

Keywords: susceptibility-weighted imaging (SWI), neuro-COVID, inflammation, MRI, cerebral microbleeds (CMBs)

INTRODUCTION

In December 2019, the new severe acute respiratory syndrome coronavirus 2 (SARS-CoV-2) caused an outbreak of severe pneumonia and coronavirus-related diseases (COVID-19) in China, which rapidly spread globally. Italy and the Lombardy region, in particular, were severely affected (1).

Although the predominant symptoms are respiratory, associated neurological manifestations—such as stroke, headache, altered mental status, epileptic seizures, movement disorders, and hyposmia/ageusia—have increasingly been acknowledged, with a rising number of studies detecting central nervous system abnormalities in patients affected by COVID-19 (2–4).

Concurrently, microhemorrhages (cerebral microbleeds, CMBs) have been observed radiologically in the brain. Whether these reported alterations are coincidental occurrences, non-specific implications of a systemic disorder, common complications of a severe infectious disease, or a direct consequence of the viral infection, remains open. It is fully acknowledged that SARS-CoV-2 can enter and damage endothelial cells in the lungs, heart, and kidneys by binding angiotensin-converting enzyme 2 (ACE2) and activating inflammatory and thrombotic pathways. A similar cascade could be involved in cerebral damage observed in COVID-19 patients (5–7). In particular, slow blood flow in cerebral microvessels allows the viral spike protein to interact with ACE2 receptors in capillaries in the endothelium. A damaged endothelial lining would favor viral access to the brain, where the virus can damage neuronal cells expressing ACE2, even in the absence of substantial inflammation. The endothelial ruptures in cerebral capillaries may lead to cerebral hemorrhage (5). CMBs appear on susceptibility-weighted imaging (SWI) as parenchymal punctate hypointensities, potentially unrelated to ischemia and macro hemorrhage (8) and this can be observed in a variety of conditions, especially in patients with acute respiratory distress syndrome (9) or widespread intravascular coagulation (10). CMBs can be observed in the subcortical white matter (WM) and splenium of the corpus callosum (CC) in critically ill patients who have experienced prolonged respiratory failure and periods of hypoxemia (11–13).

In this context, the aim of the study was to characterize CMBs patterns on SWI and investigate possible associations between the incidence of CMBs and potential risk factors, neurological symptoms and clinical and laboratory data from patients hospitalized due to COVID-19 with neurological manifestations. In addition, CMBs volume was quantified and correlated with clinical and laboratory parameters.

MATERIALS AND METHODS

Study Design and Patient Selection

Patients who were hospitalized due to COVID-19, who exhibited neurological manifestations and underwent a brain MRI between March and May 2020 were eligible for inclusion. Patients included in the study were divided into groups based on radiological evidence of CMBs (CMBs+ group) or the absence of CMBs (CMBs-). The local ethics committee approved the collection and scientific use of the patients' data as part of a larger observational study protocol (reg 2020-144). Informed consent was obtained from patients or provided by their next of kin or legal guardians.

COVID-19 Diagnosis

The COVID-19 diagnosis was confirmed using an algorithm based on local guidelines that included: (1) real-time reverse-transcriptase polymerase-chain-reaction (RT-PCR) on at least 1 nasopharyngeal swab; or (2) RT-PCR on bronchoalveolar lavage in case of high clinical suspicion of SARS-CoV-2 infection in spite of negative test results from at least two nasopharyngeal swabs performed at least 24 h apart; or (3) in the case of negative RT-PCR for SARS-COV-2, typical clinical presentation during the epidemic phase (fever, dry cough, and dyspnea) with radiological evidence of interstitial pneumonia.

Clinical and Laboratory Data

Clinical and laboratory data were extracted from patients' electronic medical records in the Hospital Information System. Clinical data included demographic information, past medical history, presenting symptoms and neurological symptoms, and the need for ventilatory support. The laboratory data considered were levels of white blood cells, lymphocytes, hemoglobin (Hb), platelet maximum and minimum counts, C-reactive protein (PCR), procalcitonin, creatinine, lactate dehydrogenase (LDH), prothrombin time (PT), activated partial thromboplastin time (aPTT), D-dimer, fibrinogen and, when available, cerebrospinal fluid (CSF) analysis. Inflammatory CSF was defined as pleocytosis and elevated protein concentration. Only data from laboratory tests performed within 3 days of the brain MRI were considered.

MRI Acquisition and Visual Assessment

All brain MRI scans were acquired at the ASST Papa Giovanni XXIII hospital in Bergamo, Italy, using a General Electric 3 Tesla MRI scanner (Discovery MR 750w GEM).

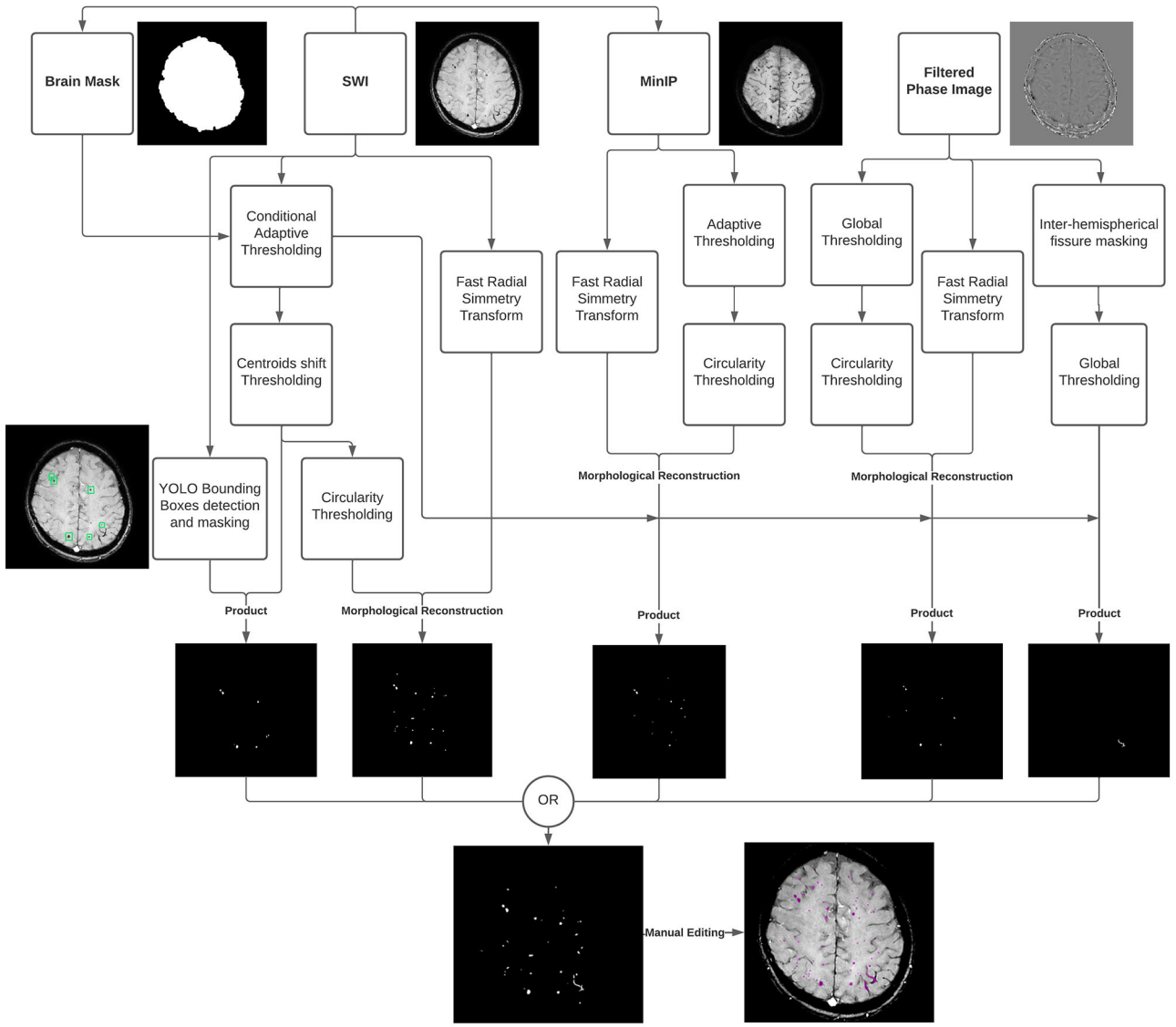

FIGURE 1 | Diagram summarizing the cerebral microbleeds (CMBs) segmentation algorithm developed and used in the study. The algorithm uses the susceptibility-weighted imaging (SWI) sequence along with the Filtered Phase sequence and a brain mask, as input, followed by a Minimum Intensity Projection (MinIP) generated from the SWI scans. A Fast Radial Symmetry Transform (FRST) technique is used to detect regions of interest based on local radial symmetry. Likewise, a deep learning (YOLO) detection algorithm is used to identify CMBs bounding boxes on SWI scans. The resulting binary masks are combined with the output of intensity thresholding and geometric feature extraction techniques to provide possible CMBs segmentations. Different intensity thresholding approaches are used according to the different input images and pathways. Specifically, a global approach is used for the flat gray Filtered Phase images; adaptive thresholding is used on the MinIP images to deal with the presence of different brightness regions picking the locally darkest particles, associated with the lesions; and the Conditional Adaptive Thresholding method is applied to the SWI scans to compute local thresholds inside the previously defined brain mask. A centroid criterion is additionally applied to consecutive slices to avoid the segmentation of the vessels' orthogonal sections resembling dot-shaped and spheric CMBs. An optional step based on global thresholding and inter-hemispherical fissure masking of the Filtered Phase stack makes it possible to segment tubular-shaped CMBs in addition to the round lesions. The resulting segmentations results are finally combined via the OR operator, and the outcome can be manually refined to fix possible segmentation inaccuracies.

The brain MRI acquisition protocol included pre-contrast coronal T2-weighted, pre-contrast axial T1-weighted and post-contrast 3D T1-weighted, pre- and post-contrast sagittal FLAIR, diffusion-weighted and tensor imaging, susceptibility-weighted imaging (SWI) and perfusion imaging. SWI acquisition was performed axially, with the following parameters: TR = 38 ms, TE = 26 ms, matrix size = 512 × 512, slice thickness = 1.3 mm.

All anonymized MRI scans were evaluated independently by two experienced neuroradiologists (SG, MC) while two more junior colleagues who were blinded to the clinical data (AB, AN) reviewed the abnormalities to classify the

findings. When their assessments diverged the cases were reviewed by a third person, and decisions were based on consensus in all cases. SWI scans were reviewed to assess and quantify microbleeds. CMBs were described in terms of number and location, and the involvement of specific brain areas, such as the corpus callosum (CC), internal capsules (IC), and cerebellar peduncles was considered. CC microbleeds were further classified as involving all of the segments or only the splenium. The shape of CMBs could be defined as dot-like or linear, the latter resembling a vascular structure. Superficial siderosis was also noted. In the presence of CMBs on SWI, the FLAIR and DWI sequences were analyzed to detect white matter abnormalities or restricted diffusion lesions. Leukoencephalopathy was defined as diffuse confluent white matter FLAIR hyperintensities, more than expected for age-related microangiopathy on the basis of visual qualitative assessment.

MRI Processing and CMBs Quantification

The CMBs burden was assessed on SWI scans using an in-house semi-automatic processing procedure (**Figure 1**), using: ImageJ/Fiji, version 1.53c (https://imagej.nih.gov/ij), Python, version 3.7 (http://www.python.org) and MATLAB, version R2019a (Natick, MA, USA).

A brain mask was first created using SWI scans with an intensity-based region-growing approach, and the Minimum Intensity Projection (MinIP) was generated to differentiate between CMBs and circular vessel sections.

Secondly, a pre-trained YOLO deep learning model was used to detect and mask CMBs bounding boxes. Taking CMBs morphology into account and based on previous findings (14), the actual segmentation procedure relied on the Fast Radial Symmetry Transform (FRST) technique (15).

FRST was combined with an intensity-based adaptive thresholding approach, so-called "Conditional Adaptive Thresholding" (16), which made it possible to compute pixel-specific thresholds inside the brain mask. An optional step based on thresholding of the Filtered Phase stack made it possible to identify and also include linear-shaped lesions.

The resulting segmentation could be manually edited using 3D Slicer software to fix possible inaccuracies in concordance with a neuroradiologist (AN) and CMBs quantification was finally performed by multiplying the total segmented area by the space between slices and the number of slices.

Statistical Analysis

Comparisons between CMBs+ and CMBs- patients were performed using the Mann–Whitney or Fisher tests as appropriate. Odds ratios (OR) for CMBs were identified in age, sex, clinical and laboratory data using logistic regression analysis. Univariate analyses were performed first; all variables with nearly significant contributions ($p < 0.1$) at univariate analysis were included in the multivariate analysis, alongside age and sex. The model was subsequently reduced using an AIC stepwise model selection technique. In patients with CMBs, the distribution of CMBs total volume by each binary variable (sex, intensive care, CSF findings, comorbidities, and clinical symptoms) was displayed using boxplots. The correlation between CMBs total volume and age, time to MRI, duration of hospitalization or invasive mechanical ventilation and each clinical and laboratory variable was assessed using Spearman correlation. Statistical significance was set at $p < 0.05$. All statistical analyses were performed using R software (R Core Team, Vienna, Austria), version 4.0.5.

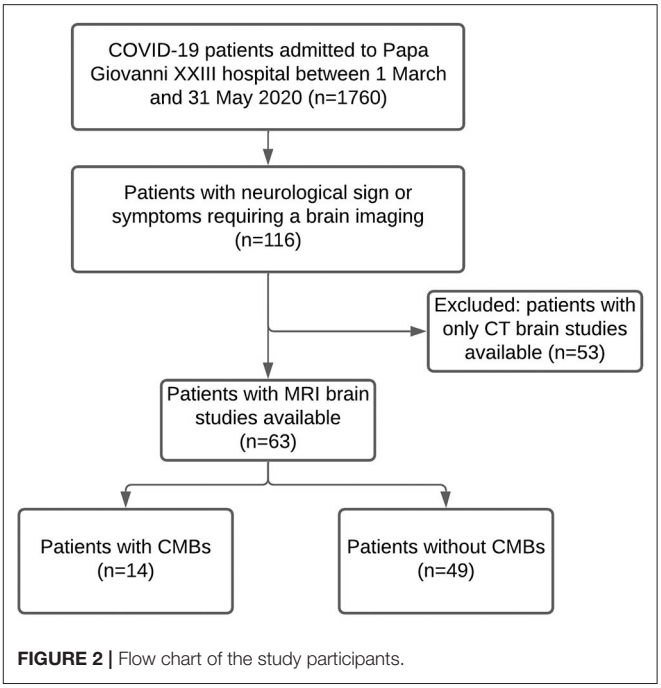

FIGURE 2 | Flow chart of the study participants.

RESULTS

Out of 1,760 patients hospitalized due to COVID-19, 116 exhibited neurological symptoms and required brain imaging. Fifty-three of them underwent a brain CT scan, while the remaining 63 underwent a brain MRI scan and were therefore eligible for the study. Of these patients, 14 had radiological evidence of CMBs (CMBs+ group), while 49 did not (CMBs- group). **Figure 2** is a flow chart that describes the study participants.

CMBs Subgroups Characterization and Risk Factors

Socio-demographic features and clinical and laboratory data for the two subgroups are summarized in **Table 1**.

Both CMBs+ and CMBs- patients were predominantly male, and there were no significant differences between the two groups regarding age. Leukoencephalopathy was reported in three CMBs+ and in none of the patients with no CMBs (21 vs. 0%; $p = 0.009$). CMBs+ were hospitalized for longer than—patients with no CMBs- (median of 41 vs. 20 days; $p = 0.028$) and also required more frequent invasive mechanical ventilation (64 vs. 24%; $p = 0.009$). CMBs+ underwent MRI significantly

TABLE 1 | Demographic and clinical characteristics of 63 patients hospitalized due to COVID-19 and exhibiting neurological symptoms.

		Total ($N = 63$)	CMBs+ ($n = 14$)	CMBs- ($n = 49$)	*p*-value
Sex (M)		39 (62%)	10 (71%)	29 (59%)	0.538
Age (years)		64 (56–73)	62 (56–73)	64 (56–72)	0.741
Comorbidities					
Dyslipidemia		4 (6%)	1 (7%)	3 (6%)	1.000
Heart disease		18 (29%)	5 (36%)	13 (27%)	0.517
Diabetes		12 (19%)	0 (0%)	12 (24%)	0.053
Hypertension		27 (43%)	7 (50%)	20 (41%)	0.557
COPD		5 (8%)	1 (7%)	4 (8%)	1.000
Cancer		4 (6%)	2 (14%)	2 (4%)	0.211
Past CVA or TIA		5 (8%)	3 (21%)	2 (4%)	0.068
Clinical presentation					
Dyspnea		27 (43%)	8 (57%)	19 (39%)	0.239
Head trauma		4 (6%)	1 (7%)	3 (6%)	1.000
Cough		22 (35%)	6 (43%)	16 (33%)	0.534
Fever		34 (54%)	10 (71%)	24 (49%)	0.224
Confusion		24 (38%)	8 (57%)	16 (33%)	0.124
Visual impairment		3 (5%)	0 (0%)	3 (6%)	1.000
Headache		8 (13%)	0 (0%)	8 (16%)	0.182
Stroke		9 (14%)	1 (7%)	8 (16%)	0.669
Ataxia		3 (5%)	0 (0%)	3 (6%)	1.000
Seizure		10 (16%)	2 (14%)	8 (16%)	1.000
Anosmia or ageusia		2 (3%)	1 (7%)	1 (2%)	0.398
Neuropathy		5 (8%)	1 (7%)	4 (8%)	1.000
Focal deficit		18 (29%)	1(7%)	17 (35%)	0.051
Coma		7 (11%)	2 (14%)	5 (10%)	0.646
Laboratory tests					
Inflammatory CSF		9 (14%)	5 (36%)	4 (8%)	**0.020**
White blood cells ($10^3/\mu l$)	no. with data	60	13	47	
	Median [IQR]	11.1 (8.3–15.8)	14.7 (12.7–19.4)	10.4 (7.8–14.8)	**0.020**
Lymphocytes ($10^3/\mu l$)	no. with data	59	13	46	
	Median [IQR]	0.7 (0.5–1.1)	0.5 (0.3–0.7)	0.8 (0.6–1.3)	**0.010**
Hemoglobin (g/dl)	no. with data	60	13	47	
	Median [IQR]	10.6 (8.1–13.1)	8.1 (7.7–10.0)	11.4 (8.8–13.5)	**0.013**
Platelet (min) ($10^3/\mu l$)	no. with data	58	13	45	
	Median [IQR]	174 (124–239)	136 (110–174)	188 (144–244)	0.086
Platelet (max) ($10^3/\mu l$)	no. with data	60	13	47	
	Median [IQR]	332 (278–451)	329 (300–427)	334 (274–452)	0.907
C-reactive protein (mg/dL)	no. with data	59	13	46	
	Median [IQR]	12.0 (3.7–26.6)	27.1 (18.3–36.5)	7.8 (3.2–17.9)	**<0.001**
Procalcitonin (ng/ml)	no. with data	32	8	24	
	Median [IQR]	0.85 (0.19–1.33)	1.7 (1.28–12.20)	0.5 (0.10–1.04)	**0.002**
Creatinine (mg/dL)	no. with data	55	13	42	
	Median [IQR]	1.0 (0.8–1.4)	1.2 (0.8–1.8)	0.9 (0.8–1.2)	0.146
LDH (IU/l)	no. with data	56	13	43	
	Median [IQR]	404 (250–601)	583 (468–715)	384 (234–540)	**0.004**
PT (s)	no. with data	56	13	43	
	Median [IQR]	1.1 (1.0–1.3)	1.1 (1.0–1.3)	1.1 (1.0–1.3)	0.806
aPTT (s)	no. with data	58	13	45	

(Continued)

TABLE 1 | Continued

		Total ($N = 63$)	CMBs+ ($n = 14$)	CMBs- ($n = 49$)	*p*-value
	Median [IQR]	1.1 (1.0–1.3)	1.1 (1.0–1.3)	1.0 (1.0–1.3)	*0.540*
D-dimer (ng/ml)	no. with data	52	12	40	
	Median [IQR]	1,590 (578–4,345)	5,135 (1,023–8,910)	1,211 (520–3,565)	**0.026**
Fibrinogen (mg/dL)	no. with data	43	11	32	
	Median [IQR]	730 (485–960)	704 (496–932)	762 (489–952)	0.900
Invasive mechanical ventilation		21 (33%)	9 (64%)	12 (24%)	**0.009**
/ duration		16 (9–26)	19 (12–26)	15 (9–24)	0.749
Chest X-ray COVID-19 positivity		29/40 (73%)	9/14(64%)	20/26 (77%)	0.469
Chest CT COVID-19 positivity		41/55 (75%)	9/13 (69%)	32/42 (76%)	0.719
Pulmonary embolism		3/18 (17%)	1/5 (20%)	2/13 (15%)	1.000
Hospitalizations (days)	no. with data	60	14	46	
	Median [IQR]	23 (11–42)	41 (24–54)	20 (9–35)	**0.028**
Time to MRI (days)	no. with data	61	14	47	
	Median [IQR]	7 (3–22)	31 (14–55)	6 (3–13)	**0.002**
FAZEKAS					
	- 0	39 (62%)	6 (43%)	33 (67%)	0.205
	- 1	16 (25%)	6 (43%)	10 (20%)	
	- 2	6 (10%)	2 (14%)	4 (8%)	
	- 3	2 (3%)	0 (0%)	2 (4%)	
Leukoencephalopathy		3 (5%)	3 (21%)	0 (0%)	**0.009**
Exitus (Death)		4/61 (7%)	1/14 (7%)	3/47 (6%)	1

Patients were divided into groups based on the presence or absence of cerebral microbleeds on MRI scans (CMBs+ and CMBs-, respectively).
Data are reported as median (IQR; continuous/numerical variables) or number (%; binary/categorical variables). p-values are computed using the Mann-Whitney test (continuous variables) or Fisher's exact test (binary or categorical variables).
aPTT, activated partial thromboplastin time; COPD, Chronic obstructive pulmonary disease; CRP, C-reactive protein; CSF, cerebrospinal fluid; CT, computed tomography; CVA, cerebrovascular accident; LDH, lactate dehydrogenase; MRI, magnetic resonance imaging; PT, prothrombin time; TIA, transient ischemic attack.
Bold means statistically significant.

later than CMBs- patients (31 vs. 6 days after admission; $p = 0.002$). The two groups also exhibited significant differences in laboratory parameters: CMBs+ patients had a higher prevalence of CSF inflammation (36 vs. 8%; $p = 0.020$), higher white blood cell concentration (14.7 vs. 10.4 $10^3/\mu l$; $p = 0.020$), and a lower lymphocyte concentration than CMBs- patients (0.5 vs. 0.8 $10^3/\mu l$; $p = 0.010$).

In the CMBs+ group, hemoglobin was significantly lower (8.1 vs. 11.4 $10^3/\mu l$; $p = 0.013$), while the D-dimer (5,135 vs. 1,211; $p = 0.026$), LDH (583 vs. 384; $p = 0.004$), procalcitonin (1.7 vs. 0.5; $p = 0.002$), and CRP concentration (27.1 vs. 7.8; $p < 0.001$) were significantly higher than in the CMBs- group. On the other hand, the two groups were not significantly different in terms of symptoms at presentation and comorbidities (**Table 1**).

Invasive mechanical ventilation, duration of hospitalization, the time between admission and MRI acquisition**,** inflammatory CSF, lymphocytes, Hb, CRP, and LDH were found to be significant OR for the radiological evidence of CMBs in the univariate logistic regression analysis (**Table 2**). Among those parameters, the main risk factors included in the reduced multivariate model were age, sex, past CVA or TIA, focal deficit, positive CSF, LDH, and CRP. The only OR that remained significant in multivariate analysis was CRP concentration [OR = 1.16 (95% CI, 1.05–1.34), $p = 0.011$] (**Table 2**).

CMBs Qualitative Assessment

The distribution of CMBs is shown in **Table 3** and some examples are shown in **Figure 3**. CMBs presented as punctuated in all patients; in four patients linear hypointensities were also detected in association with dot-like hypointensities. CMBs mainly involved the juxtacortical white matter and corpus callosum, particularly the splenium. Supratentorial and infratentorial involvement, both in the subcortical and deep WM, was labeled as diffuse. CMBs were observed in all the segments of the CC in 9 (64%) patients, whereas two patients had CMBs involving only the splenium. The infratentorial location was involved in 7/14 patients (50%) with lesions seen in the pons and cerebellar peduncles. The gray matter was mostly spared.

CMBs were associated with leukoencephalopathy in three patients, without evidence of WM cytotoxic edema on the DWI sequence; in three cases, small foci of restricted diffusion indicating small ischemic lesions in the "border zone" areas were detectable; in eight cases, microbleeds were the sole imaging pathological finding. No major bleeding was found in CMBs+

TABLE 2 | Demographic, clinical, and laboratory risk factors for cerebral microbleeds MRI finding in 63 patients hospitalized due to COVID-19 and exhibiting neurological symptoms.

	Univariable		Multivariable	
	OR (95% CI)	***p*-value**	**OR (95% CI)**	***p*-value**
Sex (M)	1.72 (0.50–7.00)	*0.409*	7.01 (0.76–139)	0.1261
Age (per year)	1.00 (0.93–1.05)	*0.807*	1.09 (0.96–1.30)	*0.260*
Comorbidities				
Dyslipidemia	1.18 (0.06–10.10)	*0.890*		
Heart disease	1.54 (0.41–5.36)	*0.504*		
Diabetes	-			
Hypertension	1.45 (0.43–4.87)	*0.541*		
COPD	0.86 (0.04–6.51)	*0.901*		
Cancer	3.92 (0.43–35.50)	*0.194*		
Past CVA or TIA	6.41 (0.96–53.30)	*0.056*	52.2 (1.63–7,158)	*0.050*
Clinical presentation				
Dyspnea	2.11 (0.64–7.32)	*0.226*		
Head trauma	1.18 (0.06–10.10)	*0.890*		
Cough	1.55 (0.44–5.22)	*0.482*		
Fever	2.60 (0.76–10.50)	*0.145*		
Confusion	2.75 (0.82–9.68)	*0.103*		
Visual impairment	-			
Headache	-			
Stroke	0.39 (0.02–2.45)	*0.401*		
Ataxia	-			
Seizure	0.85 (0.19–4.00)	*0.854*		
Anosmia or ageusia	3.69 (0.14– 97.70)	*0.367*		
Neuropathy	0.87 (0.04–6.51)	*0.901*		
Focal deficit	0.145 (0.01–0.82)	*0.074*	0.13 (0.01–1.43)	*0.144*
Coma	1.47 (0.19–7.80)	*0.670*		
Laboratory tests				
Inflammatory CSF	6.25 (1.40–30.00)	***0.016***	26.7 (0.97–2,547)	*0.081*
White blood cells ($10^3/\mu l$)	1.06 (0.99–1.13)	*0.080*		
Lymphocytes ($10^3/\mu l$)	0.05 (0.00– 0.39)	***0.017***		
Hemoglobin (g/dl)	0.70 (0.50–0.93)	***0.020***		
Platelet (min) ($10^3/\mu l$)	0.99 (0.98–1.00)	*0.145*		
Platelet (max) ($10^3/\mu l$)	0.99 (0.99–1.00)	*0.712*		
C-reactive protein (mg/dl)	1.11 (1.05–1.19)	***0.001***	1.16 (1.05–1.34)	***0.011***
Procalcitonin (ng/ml)	1.03 (1.00–1.10)	*0.245*		
Creatinine (mg/dl)	1.31 (0.90–2.05)	*0.160*		
LDH (IU/l)	1.00 (1.00–1.01)	***0.018***	1.00 (1.00–1.01)	*0.200*
PT (s)	1.04 (0.33–2.48)	*0.936*		
aPTT (s)	1.10 (0.51–1.95)	*0.751*		
D-dimer (ng/ml)	1.00 (0.99–1.00)	*0.389*		
Fibrinogen (mg/dl)	0.99 (0.99–1.00)	*0.466*		
Invasive mechanical ventilation	5.55 (1.61– 21.30)	***0.008***		
/ duration	1.00 (0.95–1.05)	*0.941*		
Chest X-ray COVID-19 positivity	0.54 (0.13–2.30)	*0.396*		
Chest CT COVID-19 positivity	0.70 (0.18–3.03)	*0.616*		
Pulmonary embolism	1.38 (0.05–18.9)	*0.814*		
Hospitalizations (days)	1.03 (1.00–1.05)	***0.037***		
Time to MRI (days)	1.04 (1.01–1.06)	***0.005***		

(Continued)

TABLE 2 | Continued

	Univariable		Multivariable	
	OR (95% CI)	***p*-value**	**OR (95% CI)**	***p*-value**
FAZEKAS				
- 1	3.30 (0.86–12.9)	*0.080*		
- 2	2.75 (0.33–17.9)	*0.299*		
Exitus (Death)	1.13 (0.05–9.69)	0.920		

Odds ratios, 95% CI, and p-values were first computed for each variable using univariate logistic regression models (left). All variables with significant contributions in univariate analysis were included in the multivariate analysis alongside age and gender, and main risk factors (right) were finally identified by reducing the multivariate model using an AIC stepwise model selection technique. The number of missing data for each variable included in the univariate analysis is reported in ***Table 1****. Only patients with no missing data (n = 56) were included in the multivariate analysis.*

aPTT, activated partial thromboplastin time; COPD, Chronic obstructive pulmonary disease; CRP, C-reactive protein; CSF, cerebrospinal fluid; CT, computed tomography; CVA, cerebrovascular accident; LDH, lactate dehydrogenase; MRI, magnetic resonance imaging; PT, prothrombin time; TIA, transient ischemic attack.

Bold means statistically significant.

TABLE 3 | Distribution of CMBs and leukoencephalopathy.

	N. of Patients (%)
Distribution of leukoencephalopathy, *n* = 3	
Diffuse	3 (100%)
Distribution of cerebral microbleeds, *n* = 14	
Diffuse	8 (57%)
Lobar	11 (79%)
Pons/cerebellum	7 (50%)
Corpus callosum including splenium	9 (64%)
Splenium only	2 (14%)
Subcortical white matter	12 (86%)
Deep white matter	7 (50%)

patients. All patients with CMBs presented a negative CT concomitant evaluation, no focal or extensive hyperdense lesions were found.

CMBs Quantitative Assessment

The procedure designed in-house identified and quantified CMBs total volume on the SWI scans (**Figure 3**).

Estimated CMBs volume was higher in females than in males and decreased with age (Rho = −0.38; $p = 0.18$); it was positively associated with CRP (Rho = 0.36; $p = 0.22$), and negatively associated with lymphocytes (Rho = −0.52; $p = 0.07$) and fibrinogen concentration (Rho = −0.68; $p = 0.025$; **Figure 4**).

DISCUSSION

Cerebral microbleeds are an emerging and singular imaging finding in patients with COVID-19 (17–19). CMBs may be secondary to endothelial dysfunction, causing the focal extravasation of red blood cells into the brain. The pathophysiological basis of this in COVID-19 remains a matter of debate, and several hypotheses have been proposed. In the setting of severe COVID-19 infection, hypoxemia-induced brain changes have been postulated as the cause of both leukoencephalopathy and CMBs (20).

We observed a specific pattern of distribution of CMBs in COVID-19, characterized by prominent callosal and juxtacortical involvement, as reported in the literature. This pattern, only detected by blood-sensitive MRI sequences, has been described extensively in critical illness associated-CMBs, a rare condition reported in patients with acute respiratory failure that requires mechanical ventilation, and sometimes ECMO (21, 22). Severe hypoxemia is common in such conditions and could account for CMBs formation but may not be the only cause. In our study, the CMBs-positive group had a higher rate of invasive mechanical ventilation (IMV) compared to patients without this imaging finding. As described by other groups (20, 23, 24), patients with CMBs had critical COVID-19 (i.e., need for IMV in the ICU setting and longer hospitalization).

It is well-documented that SARS-CoV-2 can cause damage to endothelial cells in several organs, such as the lungs, heart, and kidneys, activating inflammatory and thrombotic pathways (6). Endothelial cell infection or monocyte activation, the upregulation of tissue factors, and the release of microparticles, which activate the thrombotic pathway, might occur in SARS-CoV-2, like in other viruses (25, 26).

This phenomenon may explain the high number of acute coronary syndromes or acute myocardial dysfunction without clear culprits, such as lesions observed through angiography, which were considered to be related to myocarditis (27) or acute extensive pulmonary failure with no evidence of acute pulmonary emboli that had dilated peripheral vessels, with 100% of the patients exhibiting perfusion defects in a dual-energy CT (28).

In our study the presence of CMBs was associated with a CSF inflammatory profile; reduced concentrations of Hb and lymphocytes; higher levels of white blood cells, procalcitonin, and LDH and CRP, which correlated positively with CMBS total volume. In the adjusted regression multivariable analysis, the association with CRP levels is confirmed, thus suggesting that inflammation plays a predominant role. The RECOVERY

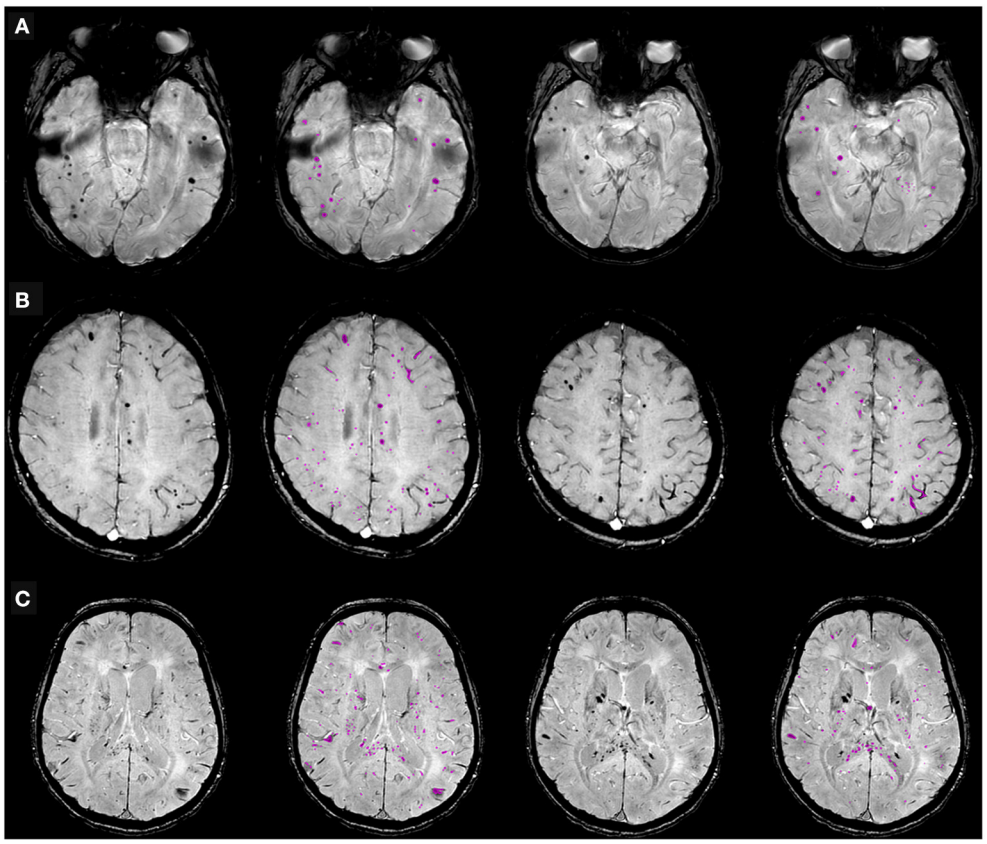

FIGURE 3 | Cerebral microbleeds (CMBs) segmentation on susceptibility-weighted imaging (SWI) in representative patients hospitalized due to COVID-19, with neurological symptoms. **(A)** 68-year old man with typical dot-shaped and spherical CMBs; **(B)** 48-year old woman with the less common ovoid and tubular-shaped lesions in addition to the conventional appearance; **(C)** 55-year old man with CMBs also located in the corpus callosum. Two SWI slices per patient are shown, along with pertinent CMBs segmentation results.

trial has also provided solid evidence of the importance of inflammation in body due to COVID-19 (29).

It is probable that the inflammatory response plays the most important role in inducing damage to the blood-brain barrier (BBB). In a large autopsy cohort study performed in the Netherlands (30), like in other smaller pathology studies, the authors report increased blood-brain barrier (BBB) permeability and rupture and blood red cell extravasation.

The burden of CMBs, as well as their presence, may be important. In our study, the estimated volume of CMBs seems to correlate with the inflammatory status and severity of the disease, as represented by lymphopenia (31). It remains unknown whether this pattern of brain involvement has a similar pathophysiology as neurological symptoms of the long-COVID syndrome.

The limitations of this retrospective single-center study include the limited number of COVID-19 patients with a brain MRI, especially those with radiological evidence of CMBs, and the design of the study, so that caution is required in interpreting the results. Because of the state of the epidemic (32) many steps were limited by the astonishing number of patients treated for COVID-19 pneumonia. Only a fraction of patients were hospitalized, and it is likely that some neurological manifestations were underrecognized in these patients. Lastly, gold standard procedures like brain autopsy were not available.

Furthermore, to our knowledge, this is one of the largest single-center cohorts of consecutive patients with COVID-19 with neurological manifestations. The study period corresponds to the first wave in Italy, one of the first in the world, so no previous exposure to the virus or vaccination could reduce the effect of the disease. MRI studies were performed with a standardized acquisition protocol, which made comparisons more reliable. Finally, this customized semi-automatic segmentation procedure made it possible to quantify CMBs total volume. The implemented solution combined state-of-the-art methods previously used to detect CMBs on SWI scans (14, 33, 34) with the deep learning detection approach (35–37), and an optimized thresholding method, with the techniques supporting each other and providing accurate CMBs segmentation and volume quantification. Since CMBs have been reported in a variety of clinical conditions (38), our CMBs segmentation technique could also be useful in other settings, apart from COVID-19 (e.g., amyloid angiopathy).

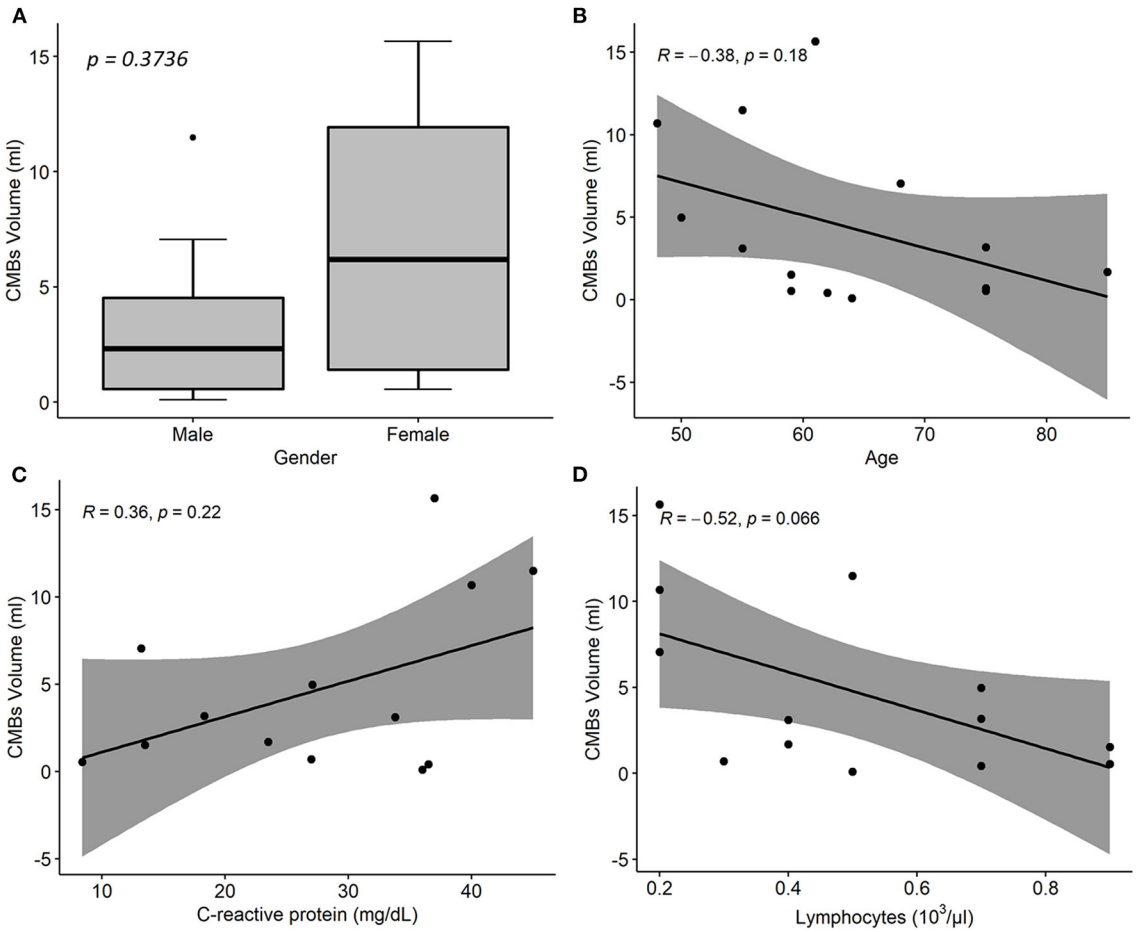

FIGURE 4 | Associations between cerebral microbleeds (CMBs) total volume and descriptive and laboratory parameters in 14 COVID-19 patients with neurological disorders and microhemorrhages detected on susceptibility-weighted images (SWI). **(A)** Distribution of CMBs total volume on SWI by patient sex. *p*-value was assessed by Wilcoxon test. **(B–D)** Linear regression of CMBs total volume on age **(B)**, CRP **(C)**, and lymphocytes concentration values **(C)**. *R* denotes the Spearman correlation coefficient with the pertinent *p*-value. CMBs, cerebral microbleeds; CRP, C-reactive protein.

In conclusion, patients with COVID-19 may develop a wide range of neurological symptoms, which can be associated with severe and fatal complications. Neuroimaging and MRI, in particular, can reveal brain changes in such patients. CMBs are a frequent imaging finding in critical patients with COVID and seem to be related to pro-inflammatory status. Future larger longitudinal studies are needed to confirm the current findings.

DATA AVAILABILITY STATEMENT

The raw data supporting the conclusions of this article will be made available by the authors, upon reasonable request.

ETHICS STATEMENT

The studies involving human participants were reviewed and approved by Local Ethics Committee as part of a Larger Observational Study (protocol reg 2020-144). The patients/participants provided their written informed consent to participate in this study.

AUTHOR CONTRIBUTIONS

AN and SG: study design. AN, AA, AC, and LL: analysis and interpretation of data. AN, AA, and AC: drafting of the manuscript. AN, AA, AC, LL, MC, AR, AB, RZ, FL, MS, and SG: critical revision of the manuscript. All authors contributed in the approval of the final version for submission.

FUNDING

The authors declare that this study received funding from Brembo S.p.a. (Curno, Bergamo, Italy), under the main funding project Progetto TrexUno. The funder was not involved in the study design, collection, analysis, interpretation of data, the writing of this article or the decision to submit it for publication.

REFERENCES

1. Livingston E, Bucher K. Coronavirus disease 2019 (COVID-19) in Italy. *J Am Med Assoc.* (2020) 323:1335. doi: 10.1001/jama.2020.4344
2. Mao L, Jin H, Wang M, Hu Y, Chen S, He Q, et al. Neurologic manifestations of hospitalized patients with coronavirus disease 2019 in Wuhan, China. *J Am Med Assoc Neurol.* (2020) 77:683–90. doi: 10.1001/jamaneurol.2020.1127
3. Román GC, Spencer PS, Reis J, Buguet A, Faris MEA, Katrak SM, et al. The neurology of COVID-19 revisited: a proposal from the Environmental Neurology Specialty Group of the World Federation of Neurology to implement international neurological registries. *J Neurol Sci.* (2020) 414:116884. doi: 10.1016/j.jns.2020.116884
4. Zubair AS, McAlpine LS, Gardin T, Farhadian S, Kuruvilla DE, Spudich S. Neuropathogenesis and neurologic manifestations of the coronaviruses in the age of coronavirus disease 2019: a review. *J Am Med Assoc Neurol.* (2020) 77:1018–27. doi: 10.1001/jamaneurol.2020.2065
5. Baig AM, Khaleeq A, Ali U, Syeda H. Evidence of the COVID-19 virus targeting the CNS: tissue distribution, host–virus interaction, and proposed neurotropic mechanisms. *ACS Chem Neurosci.* (2020) 11:995–8. doi: 10.1021/acschemneuro.0c00122
6. Varga Z, Flammer AJ, Steiger P, Haberecker M, Andermatt R, Zinkernagel AS, et al. Endothelial cell infection and endotheliitis in COVID-19. *Lancet.* (2020) 395:1417–8. doi: 10.1016/S0140-6736(20)30937-5
7. Go RS, Winters JL, Leung N, Murray DL, Willrich MA, Abraham RS, et al. Thrombotic microangiopathy care pathway: a consensus statement for the mayo clinic complement alternative pathway-thrombotic microangiopathy (CAP-TMA) disease-oriented group. *Mayo Clin Proc.* (2016) 91:1189–211. doi: 10.1016/j.mayocp.2016.05.015
8. Klironomos S, Tzortzakakis A, Kits A, Öhberg C, Kollia E, Ahoromazdae A, et al. Nervous system involvement in coronavirus disease 2019: results from a retrospective consecutive neuroimaging cohort. *Radiology.* (2020) 297:E324–34. doi: 10.1148/radiol.2020202791
9. Riech S, Kallenberg K, Moerer O, Hellen P, Bärtsch P, Quintel M, et al. The pattern of brain microhemorrhages after severe lung failure resembles the one seen in high-altitude cerebral edema. *Crit Care Med.* (2015) 43:1150. doi: 10.1097/CCM.0000000000001150
10. Neligan A, Rajakulendran S, Nortley R, Manji H. Extensive cerebral microhemorrhages caused by acute disseminated intravascular coagulation secondary to sepsis. *J Am Med Assoc Neurol.* (2014) 71:510–1. doi: 10.1001/jamaneurol.2013.223
11. Fitsiori A, Pugin D, Thieffry C, Lalive P, Vargas MI. COVID-19 is associated with an unusual pattern of brain microbleeds in critically ill patients. *J Neuroimag.* (2020) 30:593–7. doi: 10.1111/jon.12755
12. Thurnher MM, Boban J, Röggla M, Staudinger T. Distinct pattern of microsusceptibility changes on brain magnetic resonance imaging (MRI) in critically ill patients on mechanical ventilation/oxygenation. *Neuroradiology.* (2021) 63:1651–8. doi: 10.1007/s00234-021-02663-5
13. Toeback J, Depoortere SD, Vermassen J, Vereecke EL, Van Driessche V, Hemelsoet DM. Microbleed patterns in critical illness and COVID-19. *Clin Neurol Neurosurg.* (2021) 203:106594–106594. doi: 10.1016/j.clineuro.2021.106594
14. Bian W, Hess CP, Chang SM, Nelson SJ, Lupo JM. Computer-aided detection of radiation-induced cerebral microbleeds on susceptibility-weighted MR images. *NeuroImage: Clin.* (2013) 2:282–90. doi: 10.1016/j.nicl.2013.01.012
15. Loy G, Zelinsky A. Fast radial symmetry for detecting points of interest. *IEEE Trans Pattern Anal Machine Intellig.* (2003) 25:959–73. doi: 10.1109/TPAMI.2003.1217601
16. Horváth A, Spindler SJ, Szalay M, Rácz I. *Preprocessing Endoscopic Images of Colorectal Polyps*. (2016) 9:65–82. doi: 10.14513/actatechjaur.v9.n1.397
17. Tsivgoulis G, Palaiodimou L, Katsanos AH, Caso V, Köhrmann M, Molina C, et al. Neurological manifestations and implications of COVID-19 pandemic. *Ther Adv Neurol Disord.* (2020) 13:1756286420932036. doi: 10.1177/1756286420932036
18. Tsivgoulis G, Palaiodimou L, Zand R, Lioutas VA, Krogias C, Katsanos AH, et al. COVID-19 and cerebrovascular diseases: a comprehensive overview. *Ther Adv Neurol Disord.* (2020) 13:1756286420978004. doi: 10.1177/1756286420978004
19. Ladopoulos T, Zand R, Shahjouei S, Chang JJ, Motte J, Charles James J, et al. COVID-19: neuroimaging features of a pandemic. *J Neuroimaging.* (2021) 31:228–43. doi: 10.1111/jon.12819
20. Agarwal S, Jain R, Dogra S, Krieger P, Lewis A, Nguyen V, et al. Cerebral microbleeds and leukoencephalopathy in critically ill patients with COVID-19. *Stroke.* (2020) 51:2649–55. doi: 10.1161/STROKEAHA.120.030940
21. Fanou EM, Coutinho JM, Shannon P, Kiehl T-R, Levi MM, Wilcox ME, et al. Critical illness, associated cerebral microbleeds. *Stroke.* (2017) 48:1085–7. doi: 10.1161/STROKEAHA.116.016289
22. Liebeskind DS, Sanossian N, Sapo ML, Saver JL. Cerebral microbleeds after use of extracorporeal membrane oxygenation in children. *J Neuroimag.* (2013) 23:75–8. doi: 10.1111/j.1552-6569.2012.00723.x
23. Lersy F, Willaume T, Brisset J-C, Collange O, Helms J, Schneider F, et al. Critical illness-associated cerebral microbleeds for patients with severe COVID-19: etiologic hypotheses. *J Neurol.* (2021) 268:2676–84. doi: 10.1007/s00415-020-10313-8
24. Dixon L, Varley J, Gontsarova A, Mallon D, Tona F, Muir D, et al. COVID-19-related acute necrotizing encephalopathy with brain stem involvement in a patient with aplastic anemia. *Neurol Neuroimmunol Neuroinflamm.* (2020) 7:e789. doi: 10.1212/NXI.0000000000000789
25. Brisse E, Wouters CH, Andrei G, Matthys P. How viruses contribute to the pathogenesis of hemophagocytic lymphohistiocytosis. *Front Immunol.* (2017) 8:1102. doi: 10.3389/fimmu.2017.01102
26. Chow FC, Edlow BL, Frosch MP, Copen WA, Greer DM. Outcome in patients with H1N1 influenza and cerebrovascular injury treated with extracorporeal membrane oxygenation. *Neurocrit Care.* (2011) 15:156–60. doi: 10.1007/s12028-011-9534-7
27. Pellegrini D, Kawakami R, Guagliumi G, Sakamoto A, Kawai K, Gianatti A, et al. Microthrombi as a major cause of cardiac injury in COVID-19. *Circulation.* (2021) 143:1031–42. doi: 10.1161/CIRCULATIONAHA.120.051828
28. Halawa S, Pullamsetti SS, Bangham CRM, Stenmark KR, Dorfmüller P, Frid MG, et al. Potential long-term effects of SARS-CoV-2 infection on the pulmonary vasculature: a global perspective. *Nat Rev Cardiol.* (2021) 2:640. doi: 10.1038/s41569-021-00640-2
29. The RECOVERY Collaborative Group. Dexamethasone in hospitalized patients with covid-19 — preliminary report. *N Engl J Med.* (2020) 384:693–704. doi: 10.1056/NEJMoa2021436
30. Schurink B, Roos E, Radonic T, Barbe E, Bouman CSC, de Boer HH, et al. Viral presence and immunopathology in patients with lethal COVID-19: a prospective autopsy cohort study. *Lancet Microbe.* 1:290–9. doi: 10.1016/S2666-5247(20)30144-0
31. Zhou F, Yu T, Du R, Fan G, Liu Y, Liu Z, et al. Clinical course and risk factors for mortality of adult inpatients with COVID-19 in Wuhan, China: a retrospective cohort study. *Lancet.* (2020) 395:1054–62. doi: 10.1016/S0140-6736(20)30566-3
32. Fagiuoli S, Lorini FL, Remuzzi G. Covid-19 Bergamo hospital crisis unit. Adaptations and lessons in the province of Bergamo. *N Engl J Med.* (2020) 382:e71. doi: 10.1056/NEJMc2011599
33. Kuijf HJ, de Bresser J, Geerlings MI, Conijn MMA, Viergever MA, Biessels GJ, et al. Efficient detection of cerebral microbleeds on 70T MR images using the radial symmetry transform. *NeuroImage.* (2012) 59:2266–73. doi: 10.1016/j.neuroimage.2011.09.061
34. Morrison MA, Payabvash S, Chen Y, Avadiappan S, Shah M, Zou X, et al. A user-guided tool for semi-automated cerebral microbleed detection and volume segmentation: Evaluating vascular injury and data labelling for machine learning. *NeuroImag.* (2018) 20:498–505. doi: 10.1016/j.nicl.2018.08.002
35. Chen H, Yu L, Dou Q, Shi L, Mok VCT, Heng PA. Automatic detection of cerebral microbleeds *via* deep learning based 3D feature representation. In: *2015 IEEE 12th International Symposium on Biomedical Imaging (ISBI)*. Brooklyn, NY (2015). p. 764–7. doi: 10.1109/ISBI.2015.7163984
36. Dou Q, Chen H, Yu L, Zhao L, Qin J, Wang D, et al. Automatic detection of cerebral microbleeds from MR images *via* 3D convolutional neural networks. *IEEE Trans Medical Imag.* (2016) 35:1182–95. doi: 10.1109/TMI.2016.2528129
37. Al-masni MA, Kim WR, Kim EY, Noh Y, Kim DH. A two cascaded network integrating regional-based YOLO and 3D-CNN for cerebral microbleeds detection. In: *2020 42nd Annual International Conference of the IEEE*

Engineering in Medicine & Biology Society (EMBC), Montreal, QC. (2020). p. 1055–8. doi: 10.1109/EMBC44109.2020.9176073

38. Haller S, Vernooij MW, Kuijer JPA, Larsson E-M, Jäger HR, Barkhof F. Cerebral microbleeds: imaging and clinical significance. *Radiology.* (2018) 287:11–28. doi: 10.1148/radiol.2018170803

Conflict of Interest: The authors declare that the research was conducted in the absence of any commercial or financial relationships that could be construed as a potential conflict of interest.

Publisher's Note: All claims expressed in this article are solely those of the authors and do not necessarily represent those of their affiliated organizations, or those of the publisher, the editors and the reviewers. Any product that may be evaluated in this article, or claim that may be made by its manufacturer, is not guaranteed or endorsed by the publisher.

frontiers | Frontiers in Neurology

ORIGINAL RESEARCH
published: 02 June 2022
doi: 10.3389/fneur.2022.870909

Gradient Patterns of Age-Related Diffusivity Changes in Cerebral White Matter

Jasmina Boban[1,2], Majda M. Thurnher[3], Nikola Boban[4], Meng Law[5], Neda Jahanshad[6], Talia M. Nir[6], Dajana F. Lendak[7,8] and Dusko Kozic[1,2]*

[1] Faculty of Medicine Novi Sad, Department of Radiology, University of Novi Sad, Novi Sad, Serbia, [2] Vojvodina Institute of Oncology, Center for Diagnostic Imaging, Sremska Kamenica, Serbia, [3] Department for Biomedical Imaging and Image-guided Therapy, Medical University Vienna, Vienna, Austria, [4] Clinical Center of Vojvodina, Center for Radiology, Novi Sad, Serbia, [5] Department for Neuroscience, The Alfred Centre, Central Clinical School, Monash University, Melbourne, VIC, United States, [6] Imaging Genetics Center, Mark and Mary Stevens Neuroimaging and Informatics Institute, Keck School of Medicine, University of Southern California, Marina del Rey, CA, United States, [7] Faculty of Medicine Novi Sad, Department of Infectious Diseases, University of Novi Sad, Novi Sad, Serbia, [8] Clinical Center of Vojvodina, Clinic for Infectious Diseases, Novi Sad, Serbia

The current concept of brain aging proposes three gradient patterns of changes in white matter that occur during healthy brain aging: antero-posterior, supero-inferior, and the myelodegeneration-retrogenesis (or the "last-in-first-out") concept. The aim of this study was to correlate white matter diffusivity measures (fractional anisotropy-FA, mean diffusivity-MD, radial diffusivity-RD, and axial diffusivity-AD) in healthy volunteers with chronological age and education level, in order to potentially incorporate the findings with proposed patterns of physiological brain aging. The study was performed on 75 healthy participants of both sexes, with an average age of 37.32 ± 11.91 years underwent brain magnetic resonance imaging (MRI) with diffusion tensor imaging (DTI). DTI was performed using tract-based spatial statistics (TBSS), with the analysis of four parameters: FA, MD, RD, and AD. Skeletonized measures were averaged in 29 regions of interest in white matter. Correlations between age and DTI measures and between education-level and DTI measures were performed using Pearson's correlation test. To correct for multiple comparisons, we applied a Bonferroni correction to the *p*-values. Significance was set at $p \leq \mathbf{0.001}$. A significant negative correlation of FA with age was observed in posterior thalamic radiation (PTR) ($p < \mathbf{0.001}$). A significant positive correlation between age and MD was observed in sagittal stratum (SS) ($p < \mathbf{0.001}$), between age and RD in PTR, SS, and retrolenticular internal capsule ($p < \mathbf{0.001}$), and between age and AD in the body of the corpus callosum ($p < \mathbf{0.001}$). There were no significant correlations of DTI parameters with educational level. According to our study, RD showed the richest correlations with age, out of all DTI metrics. FA, MD, and RD showed significant changes in the diffusivity of projection fibers, while AD presented diffusivity changes in the commissural fibers. The observed heterogeneity in diffusivity changes across the brain cannot be explained by a single aging gradient pattern, since it seems that different patterns of degradation are true for different fiber tracts that no currently available theory can globally explain age-related changes in the brain. Additional factors, such as the effect of somatosensory decline, should be included as one of the important covariables to the existing patterns.

Keywords: diffusion-tensor imaging, brain aging, magnetic resonance imaging, physiological brain aging, pattern

OPEN ACCESS

Edited by:
Hans-Peter Müller,
University of Ulm, Germany

Reviewed by:
Jiajia Zhu,
First Affiliated Hospital of Anhui Medical University, China
Shun Takahashi,
Osaka University, Japan

****Correspondence:***
Jasmina Boban
jasmina.boban@mf.uns.ac.rs

Specialty section:
This article was submitted to Applied Neuroimaging, a section of the journal Frontiers in Neurology

Received: *07 February 2022*
Accepted: *25 April 2022*
Published: *02 June 2022*

Citation:
Boban J, Thurnher MM, Boban N, Law M, Jahanshad N, Nir TM, Lendak DF and Kozic D (2022) Gradient Patterns of Age-Related Diffusivity Changes in Cerebral White Matter. Front. Neurol. 13:870909. doi: 10.3389/fneur.2022.870909

INTRODUCTION

Healthy brain aging occurs as a result of numerous interconnected structural, chemical, and functional brain changes, and, in turn, can lead to a decline in cognitive function. Brain aging is associated with a decline in concentration, attention, and other executive functions, as well as global cognitive information processing (1). Optimal cognitive functioning, which is vital for independent living, productivity, and overall quality of life, relies on coordinated processes in different brain regions. Disturbances in communication (i.e., disconnections) between these regions during healthy aging may result in cognitive decline (2).

Over the years, many novel techniques of magnetic resonance imaging (MRI) were introduced in order to clarify the neuropathological process that lies behind neurological and psychiatric disorders. One of the most revolutionary techniques is diffusion-weighted imaging (DWI) which provides tissue contrast based on the magnitude of diffusion differences between water molecules (3). Diffusion of the water molecules represents the random motion of the molecules (Brownian motion), and it is restricted or facilitated depending on the ongoing pathological process (4). The more advanced technique, derived from DWI is called diffusion-tensor imaging (DTI) that analyzes the three-dimensional shape of diffusion, named diffusion tensor. The diffusion tensor is actually a 3D structure defined by three principal diffusivities (eigenvalues, λ1, λ2, and λ3) that are associated with three principal directions (eigenvectors) (5). This technique requires more robust post-processing but can provide valuable information about the microstructure of the brain tissue.

The concept of cortical disconnections has been confirmed in healthy brain aging (without the manifest neurological disorder), using this technique in previous studies (6–8). Given that DTI is a non-invasive imaging method, it represents a useful tool to probe brain network integrity and functionality (9). DTI fractional anisotropy (FA), mean diffusivity (MD), radial diffusivity (RD), and axial diffusivity (AD) measures can give insight into diffusivity changes in the brain which can be driven both by physiological brain aging and pathological processes (degeneration, inflammation, neoplastic and other diseases). Most published DTI studies on the aging brain have relied on the FA, which has been shown to decrease throughout the white matter of the brain during the aging process (10–12). Age-related increases in MD and RD have also been consistently observed (13). However, findings regarding AD have been inconsistent, with both increases and decreases observed in different settings (10, 13). The studies comprehensively exploring all four DTI metrics mainly explored pathological processes in the brain (neurodegenerative and genetic disorders) (14, 15). There are several methods for the evaluation of DTI data, with tract-based spatial statistics (TBSS) being one of the most popular and also used in this study. The main idea of the TBSS approach is to project volumetric data onto a white matter skeleton, in order to gain statistical power and skip some steps regarding data processing (16).

There are three proposed gradient patterns of white matter changes during healthy brain aging. The first is the antero-posterior pattern, with more extensive changes in the anterior/frontal parts of the brain preceding the posterior lobes (17). The second pattern is the supero-inferior, with extensive changes present in the cranial aspects of the brain parenchyma (18). The third pattern is myelodegeneration-retrogenesis or, the "last-in-first-out" hypothesis, which proposes that the degeneration of myelin observed during the aging process occurs in the opposite direction of myelin development and maturation (19, 20).

The aim of this study was to correlate white matter DTI anisotropy and diffusivity measures (FA, MD, RD, and AD) using TBSS in healthy volunteers, with chronological age and formal education level (expressed in years of education). The second aim was to determine whether the gradient pattern of white matter associations was consistent with any proposed patterns of physiological brain aging.

MATERIALS AND METHODS

Study Population

Of a total of 81 healthy volunteers who were enrolled in the study based on the initially performed power sample analysis ($\alpha = 0.05$ (p-value), $\beta = 0.2$ (correspondent to the ower of 80%), and $r > 0.30$, the required sample was 79), 75 participants, average age 37.32 ± 11.91 years (range: 22–62 years; 53 male and 22 female participants) were included into analyses after undergoing whole brain magnetic resonance imaging (MRI) from July 2011 to April 2017 at the University of Novi Sad. Six data sets were excluded from the initial sample of 81 subjects due to technically inadequate quality. All the patients were cognitively screened using Mini-Mental State Examination (MMSE) (21).

Inclusion criteria were over 18 years of age, MMSE score over 24 (thus excluding persons eligible for the evaluation of dementia), and right-handed. MMSE is a 30-point screening test for the global cognitive assessment, used for quick exclusion of subjects with signs of cognitive impairment. Right-handedness was based on the self-report of the preferred hand and on the results of the Waterloo Handedness Questionnaire (WHQ) (22). Criteria for the exclusion from the study were acute and chronic neurologic and psychiatric disorders, presence of diffuse or focal white matter lesions in the brain (tumors, infarctions, metastases, vascular malformations, white matter hyperintensities), post-operative state, head trauma history, patients with palsy or deep paresis of the dominant hand, visual and hearing disorders, MMSE score ≤24, history of drug and alcohol abuse according to Drug Abuse Screening Test and Michigan Alcohol Screening Test (MAST) (23), and contraindications for MRI scanning.

Neuroimaging

All participants underwent an MRI of the brain on a 3T clinical scanner (Siemens Trio Tim, Erlangen, Germany), using an 8-channel head array. Conventional MRI of the brain consisted of T1W sagittal spin echo [time of repetition (TR)/time of echo (TE) 440 ms/3.8 ms, slice thickness 5 mm, duration 2:00 min], T2W transversal turbo spin echo (TR/TE 5150 ms/105 ms, slice thickness 5 mm, duration 2:57 min), Fluid Attenuation Inversion Recovery (FLAIR) transversal (TR/TE

8,000 ms/101 ms, slice thickness 5 mm, duration 3:30 min), diffusion-weighted imaging (DWI) (TR/TE 4100 ms/91 ms, slice thickness 5 mm, duration 2:07 min), T2W coronal turbo spin echo (TR/TE 7150 ms/111 ms, slice thickness 5 mm, duration 2:17 min), and 3D T1W MPRAGE sagittal tomograms (TR/TE 1530 ms/2.97 ms, slice thickness 1 mm, duration 5:12 min).

Conventional MRI was necessary for obtaining anatomic information and detection of potential focal or diffuse brain lesions.

Diffusion tensor imaging was performed using MDDWI sequence (multidirectional diffusion weighted imaging) with two diffusion shells (b-values of 1,000 s/mm^2 and 1,500 s/mm^2) from 64 diffusion-weighted directions each and two non-diffusion weighted volumes (at b0). The data were acquired at 2 mm isotropic resolution; the fold over direction was A-P with a P shift. Field-of-view was 230. DWI images were denoised using the LPCA filter and corrected for motion by linearly aligning all DWI volumes to the b 0 image. T1-weighted images were denoised using the non-local means filter and underwent N3 intensity inhomogeneity normalization, and brain extraction. Data sets that did not fulfill the quality control criteria were excluded from the analyses (three due to extreme EPI distortion and three due to skeleton misregistration). T1 images were linearly aligned to diffusion images, and diffusion images were then non-linearly warped to their respective T1-weighted scans to correct for echo-planar imaging (EPI) induced susceptibility artifacts.

Diffusion gradient directions were rotated to accommodate linear registrations. DTI fractional anisotropy (FA), mean diffusivity (MD), radial diffusivity (RD), and axial diffusivity (AD) scalar maps were generated from corrected images (24).

Diffusion tensor imaging analysis was performed using the tract-based spatial statistics (TBSS) technique from the FSL software package (24) and publicly available ENIGMA-DTI protocols (http://enigma.usc.edu/protocols/dti-protocols/) (25). Each subject's FA map was warped to the ENIGMA-DTI FA template with ANTs (26) and the transformations were applied to all respective DTI maps. DTI measures were then projected onto the template skeleton. Skeletonized measures were averaged in a total of 29 regions of interest (ROIs) from the John Hopkins University White Matter Atlas (27) (**Table 1**).

TABLE 1 | List of analyzed locations (ROIs) according to the John Hopkins White Matter Atlas.

Location	Abbreviation
Anterior corona radiate	ACR
Anterior limb of internal capsule	AIC
Body of the corpus callosum	BCC
Corpus callosum	CC
Cingulate gyrus	CGC
Parahippocampal cingulate fibers	CGH
Corticospinal tract	CST
External capsule	EC
Fornix	FX
Fornix-stria terminalis	FXST
Genu of the corpus callosum	GCC
Inferior fronto-occipital fasciculus	IFO
Posterior corona radiata	PCR
Posterior thalamic radiation	PTR
Posterior limb of the internal capsule	PLIC
Retrolenticular limb of internal capsule	RLIC
Sagittal stratum	SS
Splenium of the corpus callosum	SCC
Superior fronto-occipital fasciculus	SFO
Superior longitudinal fasciculus	SLF
Uncinate fasciculus	UNC

Statistical Analysis

Statistical analysis was performed using the software package SPSS ver. 23.0 (IBM, Chicago, USA). Methods of descriptive and comparative statistics were used (mean, median, standard deviation, minimum, maximum, frequencies, and percentage, depending on the type of the variable). After confirmation of normal distribution, correlations between age and DTI measures and between education-level and DTI measures were performed using Pearson's correlation test. Additionally, a partial correlation was performed between age and diffusivity changes in observed DTI parameters, with education as a control variable. Permutation tests for Pearson's correlations were performed for age and localization, education and localization, and for partial correlation, using education as a control variable. Gender differences were also explored using the *t*-test.

To correct for multiple comparisons, we applied a Bonferroni correction to the *p*-values. Significance was set at $p \leq 0.001$ (21 ROIs $\times$ 2 tests $+ 4 = 46$, $0.05/42 = 0.00108$).

RESULTS

A total of 75 participants were included in the study, 53 men (70.7%) and 22 women (29.3%). No significant gender-related differences in white matter diffusivity metrics were observed. The average age of the participants was 37.32 ± 11.91 years (range 22–62). The average education level was 13.87 ± 2.38 years of formal education. MMSE scoring was 28.87 ± 1.14 points, no person scored lower than 26.

Table 2 summarizes the changes in FA on the observed localization in the brain, in correlation with the chronological age and educational level of the participants. A significant negative correlation was observed in PTR (on the left $p < \mathbf{0.001}$ and on the right $p = \mathbf{0.001}$) (**Figure 1**). All correlations were negative. No significant correlations of FA with the level of education or the MMSE score were detected. **Table 2A** shows the results of the partial correlation summarized.

Table 3 shows the correlations between MD and age and between MD and educational level of the participants are presented for the analyzed locations. A significant positive correlation was confirmed only in SS on the left side ($p = \mathbf{0.001}$) (**Figure 2**). There were no significant correlations of this parameter with the level of formal education or the MMSE score. In **Table 3A**, the results of the partial correlation are summarized.

TABLE 2 | Results of Pearson's correlation of FA with age and education level of the study participants in the observed locations (*r*-correlation coefficient).

Location	Age		Education level	
	r	*p*	*r*	*p*
ACR-L	−0.258	**0.026**	**0.024**	0.841
ACR-R	−0.244	**0.035**	0.050	0.669
ALIC-L	**0.023**	0.843	−0.157	0.179
ALIC-R	0.060	0.608	−0.129	0.269
BCC	0.116	0.324	−0.197	0.090
CC	**0.040**	0.736	−0.215	0.064
CGC-L	**−0.038**	0.749	**−0.046**	0.693
CGC-R	0.079	0.499	−0.054	0.644
CGH-L	−0.114	0.329	0.055	0.642
CGH-R	−0.128	0.272	0.160	0.171
CR-L	−0.294	**0.010**	**−0.001**	0.992
CR-R	−0.293	**0.011**	**−0.012**	0.922
CST-L	**−0.002**	0.986	**0.014**	0.908
CST-R	**−0.004**	0.971	0.091	0.437
EC-L	−0.102	0.382	**0.038**	0.747
EC-R	−0.102	0.386	0.074	0.530
FX	−0.235	**0.043**	0.185	0.112
FXST-L	**−0.049**	0.679	0.100	0.395
FXST-R	−0.111	0.345	0.153	0.190
GCC	−0.159	0.172	−0.119	0.311
IC-L	−0.197	0.091	−0.087	0.458
IC-R	−0.131	0.264	−0.080	0.496
IFO-L	**0.002**	0.989	−0.188	0.107
IFO-R	**0.002**	0.989	−0.057	0.624
PCR-L	−0.226	0.052	−0.144	0.217
PCR-R	−0.229	**0.048**	−0.233	**0.044**
PLIC-L	−0.113	0.335	−0.145	0.216
PLIC-R	−0.121	0.301	−0.162	0.165
PTR-L	**−0.457**	**<0.001**	−0.056	0.634
PTR-R	**−0.366**	**0.001**	**0.020**	0.864
RLIC-L	**−0.351**	**0.002**	0.082	0.482
RLIC-R	−0.247	**0.033**	0.100	0.394
SCC	0.108	0.358	−0.230	**0.047**
SCR-L	−0.244	**0.035**	**0.031**	0.792
SCR-R	−0.248	**0.032**	**0.018**	0.875
SFO-L	**0.001**	0.992	−0.085	0.466
SFO-R	−0.098	0.401	0.098	0.401
SLF-L	−0.189	0.105	**−0.022**	0.853
SLF-R	−0.155	0.183	**−0.034**	0.770
SS-L	**−0.341**	**0.003**	0.121	0.300
SS-R	**−0.340**	**0.003**	0.161	0.167
UNC-L	−0.297	**0.010**	−0.280	**0.015**
UNC-R	−0.100	0.392	−0.318	**0.005**

Significant results are presented in bold case.

TABLE 2A | The results of partial correlation of FA with age, using education level as a control variable.

Location	Age	
	R	*p*
ACR-L	−0.257	**0.027**
ACR-R	−0.240	**0.040**
ALIC-L	**0.001**	0.992
ALIC-R	**0.043**	0.717
BCC	0.091	0.443
CC	**0.010**	0.935
CGC-L	**−0.045**	0.706
CGC-R	0.072	0.539
CGH-L	−0.108	0.360
CGH-R	−0.109	0.357
CR-L	−0.297	**0.010**
CR-R	−0.298	**0.010**
CST-L	**<0.001**	0.999
CST-R	**0.009**	0.942
EC-L	−0.098	0.406
EC-R	−0.092	0.434
FX	−0.215	0.066
FXST-L	**−0.035**	0.766
FXST-R	−0.091	0.440
GCC	−0.179	0.127
IC-L	−0.212	0.070
IC-R	−0.144	0.222
IFO-L	**−0.025**	0.829
IFO-R	**−0.006**	0.957
PCR-L	−0.251	**0.031**
PCR-R	−0.272	**0.019**
PLIC-L	−0.136	0.249
PLIC-R	−0.147	0.211
PTR-L	**−0.470**	**<0.001**
PTR-R	**−0.366**	**0.001**
RLIC-L	−0.344	**0.003**
RLIC-R	−0.236	**0.043**
SCC	0.078	0.509
SCR-L	−0.242	**0.037**
SCR-R	−0.248	**0.033**
SFO-L	**−0.011**	0.926
SFO-R	−0.086	0.467
SLF-L	−0.194	0.098
SLF-R	−0.162	0.168
SS-L	−0.329	**0.004**
SS-R	−0.325	**0.005**
UNC-L	0.271	**0.020**
UNC-R	0.059	0.616

Significant results are presented in bold case.

Significant positive correlations were detected between RD and age in PTR (on the left $p < \mathbf{0.001}$ and on the right $p = \mathbf{0.001}$, **Figure 3A**), SS (on the left $p < \mathbf{0.001}$, and on the right $p < \mathbf{0.001}$, **Figure 3B**), and in RLIC (on the left $p = \mathbf{0.001}$). There were no significant correlations of this parameter with the level of formal education or the MMSE score (**Table 4**). In **Table 4A**, the results of the partial correlation are summarized.

TABLE 3 | Results of Pearson's correlation of MD with age and education level of the study participants in the observed locations (*r*-correlation coefficient).

Location	Age		Education level	
	r	*p*	*r*	*p*
ACR-L	0.214	0.066	−0.104	0.375
ACR-R	0.145	0.215	−0.109	0.353
ALIC-L	0.104	0.376	0.090	0.442
ALIC-R	**0.018**	0.881	**0.009**	0.941
BCC	0.232	**0.046**	**0.020**	0.862
CC	0.243	**0.036**	0.092	0.435
CGC-L	0.193	0.098	**0.030**	0.798
CGC-R	0.166	0.154	−0.111	0.343
CGH-L	0.229	**0.048**	−0.053	0.654
CGH-R	0.197	0.091	−0.092	0.430
CR-L	0.278	**0.016**	−0.086	0.462
CR-R	0.228	**0.049**	−0.058	0.619
CST-L	0.207	0.075	−0.067	0.570
CST-R	0.212	0.068	0.058	0.622
EC-L	0.304	**0.008**	**−0.008**	0.946
EC-R	0.304	**0.008**	**0.034**	0.775
FX	0.228	**0.049**	**−0.049**	0.677
FXST-L	**0.014**	0.904	0.119	0.310
FXST-R	0.119	0.308	0.061	0.605
GCC	0.247	**0.032**	−0.061	0.606
IC-L	0.171	0.141	0.184	0.113
IC-R	0.146	0.211	0.122	0.296
IFO-L	0.130	0.267	**0.004**	0.974
IFO-R	0.134	0.252	−0.116	0.321
PCR-L	0.320	**0.005**	0.055	0.640
PCR-R	0.238	**0.040**	0.113	0.335
PLIC-L	0.130	0.265	0.209	0.072
PLIC-R	0.095	0.420	0.215	0.064
PTR-L	0.309	**0.007**	0.152	0.193
PTR-R	0.266	**0.021**	0.176	0.132
RLIC-L	0.234	**0.044**	0.170	0.144
RLIC-R	0.248	**0.032**	0.067	0.567
SCC	0.156	0.180	0.313	**0.006**
SCR-L	0.279	**0.015**	−0.117	0.318
SCR-R	0.277	**0.016**	−0.085	0.468
SFO-L	0.296	**0.010**	−0.090	0.444
SFO-R	0.153	0.189	−0.141	0.229
SLF-L	0.256	**0.027**	**−0.042**	0.719
SLF-R	0.273	**0.018**	**0.010**	0.933
SS-L	**0.372**	**0.001**	**0.016**	0.893
SS-R	0.338	**0.003**	−0.056	0.633
UNC-L	0.068	0.562	0.078	0.507
UNC-R	0.214	0.065	0.239	**0.039**

Significant results are presented in bold case.

Significant positive correlations between AD and age were detected in BCC ($p = \mathbf{0.001}$, **Figure 4**). There were no significant correlations between AD and educational level (**Table 5**).

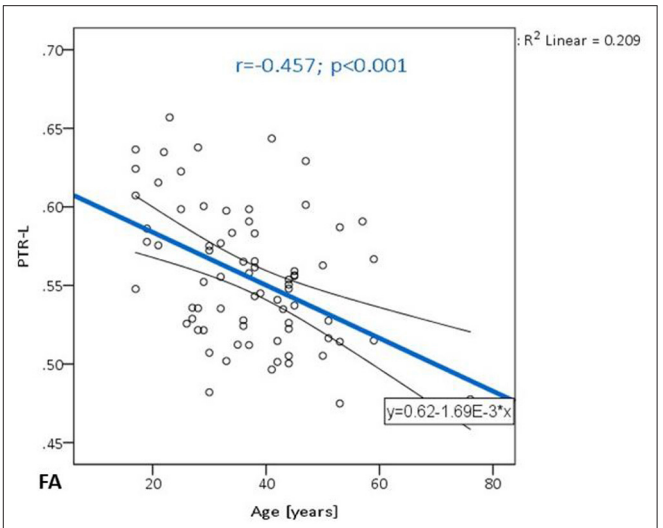

FIGURE 1 | The trend of FA decrease with advancing age in the posterior thalamic radiation on the left.

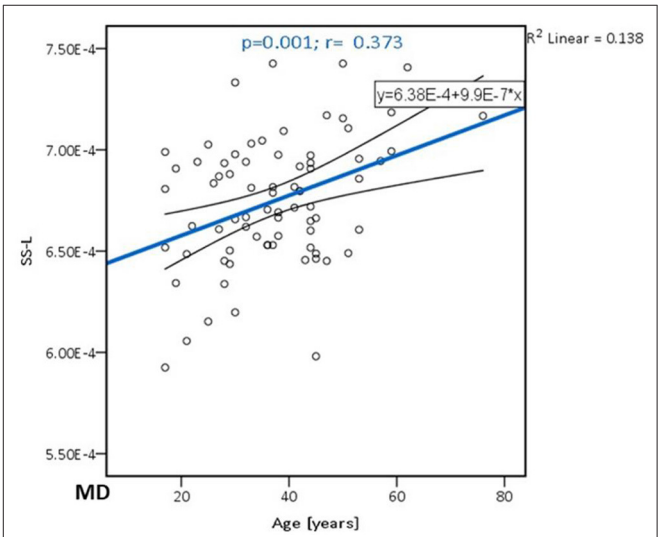

FIGURE 2 | The trend of MD increase with advancing age in the sagittal stratum on the left side.

However, with education level used as a control variable, the significance of the diffusivity decrease with age in the BCC was lost (**Table 5A**). There were no significant correlations with MMSE scores.

The results of permutation tests are provided in **Supplementary Material**.

DISCUSSION

The main goal of the study was to correlate white matter DTI anisotropy and diffusivity measures (FA, MD, RD, and AD) in healthy volunteers with chronological age and formal education level. Additionally, we aimed to determine whether the gradient

TABLE 3A | The results of partial correlation of MD with age, using education level as a control variable.

Location	Age	
	R	*p*
ACR-L	0.202	0.084
ACR-R	0.132	0.263
ALIC-L	0.118	0.316
ALIC-R	**0.019**	0.873
BCC	0.237	**0.042**
CC	0.259	**0.026**
CGC-L	0.199	0.089
CGC-R	0.153	0.193
CGH-L	0.224	0.055
CGH-R	0.186	0.112
CR-L	0.270	**0.020**
CR-R	0.223	0.056
CST-L	0.200	0.088
CST-R	0.223	0.057
EC-L	0.306	**0.008**
EC-R	0.312	**0.007**
FX	0.223	0.056
FXST-L	**0.031**	0.791
FXST-R	0.129	0.273
GCC	0.242	**0.038**
IC-L	0.203	0.083
IC-R	0.166	0.157
IFO-L	0.132	0.264
IFO-R	0.120	0.310
PCR-L	0.331	**0.004**
PCR-R	0.258	**0.027**
PLIC-L	0.165	0.160
PLIC-R	0.129	0.274
PTR-L	0.337	**0.003**
PTR-R	0.298	**0.010**
RLIC-L	0.264	**0.023**
RLIC-R	0.261	**0.025**
SCC	0.213	0.069
SCR-L	0.267	**0.021**
SCR-R	0.268	**0.021**
SFO-L	0.288	**0.013**
SFO-R	0.136	0.247
SLF-L	0.253	**0.030**
SLF-R	0.278	**0.017**
SS-L	**0.378**	**0.001**
SS-R	0.334	**0.004**
UNC-L	0.080	0.499
UNC-R	0.258	**0.026**

Significant results are presented in bold case.

pattern of these associations was consistent with any of the proposed physiological brain aging patterns.

In our study, FA values showed significant reduction with advancing age in the PTR, which is the dorsal part of thalamocortical radiations connecting the thalamus with cortical centers. It consists of fibers that start from the caudal thalamic nuclei (pulvinar and lateral geniculate) *via* the retrolenticular part of the IC toward the parietal and occipital cortices. The function of this tract is primarily somatosensory (comprises parts of visual, gustatory, and auditory tracts) (28, 29). The relationship between the decline in perceptive and cognitive abilities is well-established in the process of aging; however, growing evidence suggests that there is a direct association between sensory deprivation-decreased processing of sensory information- and cognitive decline (30). The decrease in FA was observed in women with anorexia nervosa (31), patients with a high risk of psychosis converting to manifest psychosis (32), methamphetamine addicts (33), and children with cerebral palsy (34). An interesting recent study showed the relationship between cigarette smoking and changes in FA and MD in the PTR (35), supporting the necessity to include the daily habits as a sine-qua-non in future DTI studies (eg., nicotine and alcohol consumption, substance abuse, and pharmaceuticals).

A significant increase in MD with advancing age was observed in the SS on the left side. This tract is positioned in the deep lateral aspect of the cerebral hemisphere and organized into three layers: superficial (consisting of inferior longitudinal fasciculus and inferior part of SLF), middle (fronto- occipital fasciculus), and deep (fibers of optic radiation) (36). It is included in the information transport from parietal, occipital, cingulate, and temporal gyri to the subcortical nuclei (thalamus and pontine nuclei). In the past studies, the increase in MD was detected in patients with essential tremors and has been suggested as one of the differentials from Parkinson's disease in these patients (37). It was also observed in the mild traumatic injury of the brain (38), children with ADHD (associated with aberrant myelination) (39) but was also observed in healthy cigarette smokers (40).

A significant increase in RD with advanced age was detected in the PTR, SS, and RLIC. RLIC is positioned dorsally to the corticospinal and corticopontineus tracts but represents a functionally separate entity because it carries parts of optic radiation, proximal part of PTR, and occipito-tectal and occipito-pontine fibers. Since the increase in this parameter was observed in the PTR and RLIC, it is clear that, along with the close anatomic relationship, there is also a functional connection between these two structures, mainly in the somatosensory information transmission. SS is also functionally associated with the latter two tracts. Disturbances in the diffusivity of RLIC have been priorly observed in depression (41), bipolar disorder (36), methadone addiction (42), and traumatic injury of the brain associated with sports (43).

A significant increase in AD with advancing age was detected in BCC. The corpus callosum is the biggest commissural tract that connects corresponding regions of cerebral hemispheres. Different parts of CC are included in the transmission of various information, with premotor and supplementary motor fibers of the cortex located in the body 409. Madden et al. did not show differences in AD with advanced age (44). However, Fan et al. presented differences in FA between young (20–28 years) and elderly adults (60–75 years) primarily in the anterior portion of CC (within interhemispheric fibers), that were positively

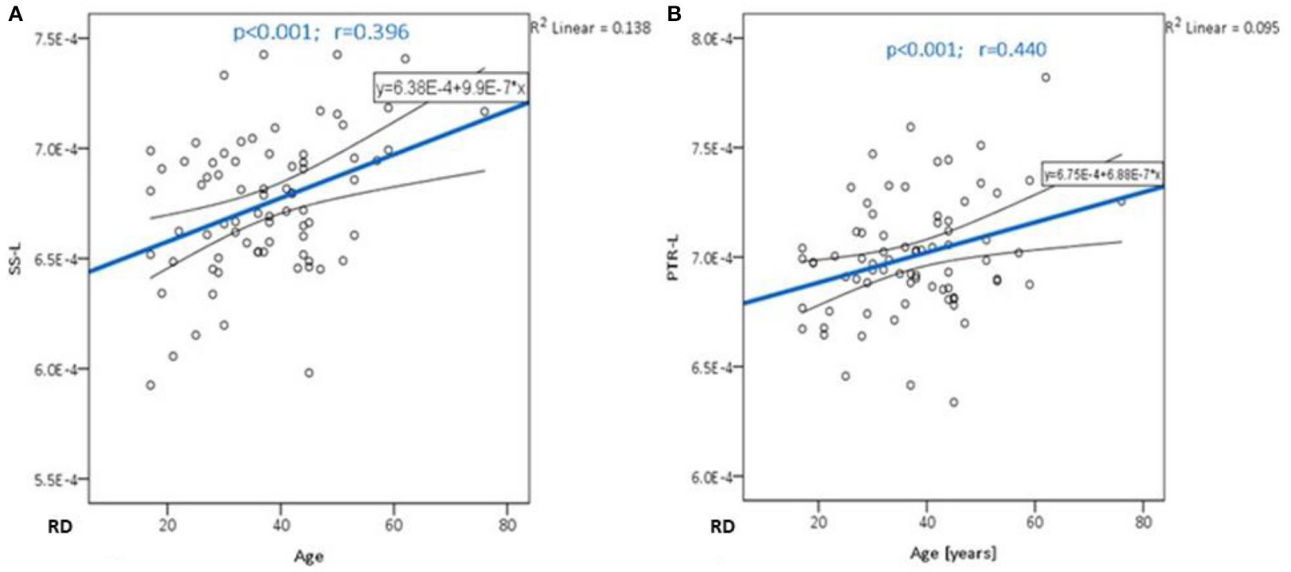

FIGURE 3 | The trend of RD increase with advancing age in the sagittal stratum **(A)** and posterior thalamic radiation **(B)**.

correlated with performance on the visuospatial tasks—AD was not explored in that particular study (45). Evidence supporting the "last-in-first-out" theory was also presented in the study of Davis et al. presenting greater age-related differences in RD than in AD in the CC and UNC, thus supporting the theory of myelodegeneration and retrogenesis (46). In our study, however, AD was more sensitive to the changes in these regions, thus indicating that these theoretical interpretations of the white matter diffusivity changes are in fact a simplification of the aging process. That is why we highlight the need for a deeper understanding of the age-related effect on the white matter integrity.

It is interesting to note that FA, MD, and RD were associated with the diffusivity changes in projection tracts (that connect cortical structures with the brainstem, cerebellum, and spinal medulla). On the contrary, the AD was associated with diffusivity changes in commissural tracts, connecting two hemispheres. In a recent longitudinal study, that followed healthy participants aged 50–84 years (at the moment of the first scan, the average age of women was 63.85 years and men was 67.31 years) during the follow-up period of 7 years, showed the most prominent changes in the FA and RD in commissural and projection tracts (47). It is possible that the changes in these two parameters are first observed in projection tracts, as shown in our study, and later during chronological aging, are followed by diffusivity changes in the commissural tracts as well.

Little is known about the oligodendrocyte dynamics and myelin sheath remodeling in the mature brain. However, recent studies confirmed that sensory enrichment could induce experience-dependent myelination and robustly increase the integration of oligodendrocytes (48). Reversely, the results of our study, with age-related changes detected mainly in the somatosensory tracts may imply that somatosensory deprivation during healthy aging negatively affects myelin sheaths (in the sense of myelin degradation and/ or disintegration) and results in DTI metrics changes. This effect of somatosensory deprivation on white matter integrity during the brain aging, should, in our opinion, be included in the current theories of the white matter degradation during aging process, along with the myelodegeneration-retrogenesis and gradients of degenerations (antero- posterior and supero-inferior).

It is interesting to see the overlap in the DTI metrics changes observed in specific tracts, which could potentially clear the etiology of age-related changes. We tried to group the differences in DTI metrics in the following patterns, as shown in **Table 6**. In our study, the observed patterns of age-related diffusivity changes were the FA-RD (detected in PTR) and the MD-RD pattern (detected in SS), speaking in favor of myleodegeneration over axonal damage in the named tracts (**Figure 5** showing brain maps). In RLIC, we found the diffusivity changes reflected as RD increased, also speaking in favor of myelodegeneration. Given the absence of manifest cognitive impairment and the strict exclusion criteria that we proposed for randomizing the subjects, in our opinion, patterns found in our study sample were expected. In the cohort of healthy, fully functional, and cognitively unchallenged subjects, age-related myelin degeneration and loss seem to be the leading mechanism of white matter diffusivity changes. One recent study also tried to group the findings in DTI metrics across the brain white matter tracts. The FA–RD pattern was observed only in the posterior thalamic radiation in our study sample, while in the study of Molloy et al., it was the most observed pattern, detected in more than 30% of the brain tracts (10). The FA–RD–AD pattern in this study was observed in almost 30% of the brain (10). Other patterns were more uncommon.

TABLE 4 | Results of Pearson's correlation of RD with age and education level of the study participants in the observed locations (*r*-correlation coefficient).

Location	Age		Education level	
	r	*p*	*r*	*p*
ACR-L	0.270	**0.019**	−0.067	0.568
ACR-R	0.242	**0.036**	−0.078	0.507
ALIC-L	0.079	0.498	0.148	0.206
ALIC-R	**0.000**	0.997	0.079	0.503
BCC	**0.037**	0.752	0.143	0.223
CC	0.090	0.443	0.186	0.109
CGC-L	0.116	0.320	**0.034**	0.772
CGC-R	0.116	0.320	−0.070	0.550
CGH-L	0.232	**0.045**	−0.080	0.497
CGH-R	0.228	**0.049**	−0.144	0.218
CR-L	0.347	**0.002**	**−0.044**	0.708
CR-R	0.331	**0.004**	**−0.017**	0.887
CST-L	0.138	0.236	−0.055	0.636
CST-R	0.167	0.153	**−0.038**	0.744
EC-L	0.287	**0.013**	**−0.026**	0.827
EC-R	0.257	**0.026**	**−0.007**	0.952
FX	0.234	**0.044**	−0.072	0.538
FXST-L	0.071	0.545	**0.010**	0.935
FXST-R	0.159	0.172	−0.060	0.612
GCC	0.214	0.065	0.063	0.592
IC-L	0.238	**0.040**	0.163	0.163
IC-R	0.179	0.125	0.115	0.327
IFO-L	**0.038**	0.744	0.070	0.553
IFO-R	0.071	0.546	**−0.031**	0.790
PCR-L	0.357	**0.002**	0.114	0.328
PCR-R	0.309	**0.007**	0.179	0.125
PLIC-L	0.140	0.232	0.206	0.076
PLIC-R	0.126	0.282	0.220	0.058
PTR-L	**0.440**	**<0.001**	0.108	0.357
PTR-R	**0.369**	**0.001**	0.075	0.521
RLIC-L	**0.377**	**0.001**	**0.043**	0.716
RLIC-R	0.303	**0.008**	**−0.019**	0.870
SCC	**0.017**	0.888	0.296	**0.010**
SCR-L	0.334	**0.003**	−0.075	0.521
SCR-R	0.334	**0.003**	**−0.043**	0.711
SFO-L	0.311	**0.007**	−0.102	0.383
SFO-R	0.184	0.114	−0.090	0.440
SLF-L	0.263	**0.023**	**−0.026**	0.825
SLF-R	0.246	**0.033**	**0.028**	0.812
SS-L	**0.396**	**<0.001**	−0.061	0.606
SS-R	**0.392**	**<0.001**	−0.121	0.299
UNC-L	−0.148	0.205	0.225	0.052
UNC-R	**0.043**	0.716	0.339	**0.003**

Significant results are presented in bold case.

TABLE 4A | The results of partial correlation of RD with age, using education level as a control variable.

Location	Age	
	R	*p*
ACR-L	0.254	**0.021**
ACR-R	0.241	**0.035**
ALIC-L	0.075	0.480
ALIC-R	**0.001**	0.956
BCC	**0.035**	0.777
CC	0.090	0.445
CGC-L	0.114	0.318
CGC-R	0.112	0.316
CGH-L	0.244	0.051
CGH-R	0.226	**0.048**
CR-L	0.345	0.054
CR-R	0.331	0.053
CST-L	0.141	0.235
CST-R	0.160	0.158
EC-L	0.257	**0.018**
EC-R	0.250	**0.020**
FX	0.234	**0.042**
FXST-L	0.068	0.532
FXST-R	0.159	0.172
GCC	0.202	0.075
IC-L	0.238	0.054
IC-R	0.179	0.125
IFO-L	**0.038**	0.744
IFO-R	0.071	0.546
PCR-L	0.357	0.201
PCR-R	0.309	0.207
PLIC-L	0.287	0.232
PLIC-R	0.185	0.282
PTR-L	0.323	**0.033**
PTR-R	0.356	**0.042**
RLIC-L	0.343	**0.028**
RLIC-R	0.373	0.064
SCC	**0.017**	0.880
SCR-L	0.289	0.052
SCR-R	0.300	0.060
SFO-L	0.222	0.075
SFO-R	0.184	0.114
SLF-L	0.263	**0.023**
SLF-R	0.246	**0.033**
SS-L	0.311	**0.020**
SS-R	0.325	**0.042**
UNC-L	0.140	0.211
UNC-R	**0.043**	0.716

Significant results are presented in bold case.

Burzynska et al. confirmed that FA was significantly correlated with age in more than half of the brain white matter (13). Molloy et al. showed that the highest percentage of voxels significantly correlated with age were found in the forceps minor (part of CC) (10). The FA–MD–RD pattern is related to chronic white matter degeneration, mainly dependent on the myelin loss during the aging process. The changes in AD, however, have

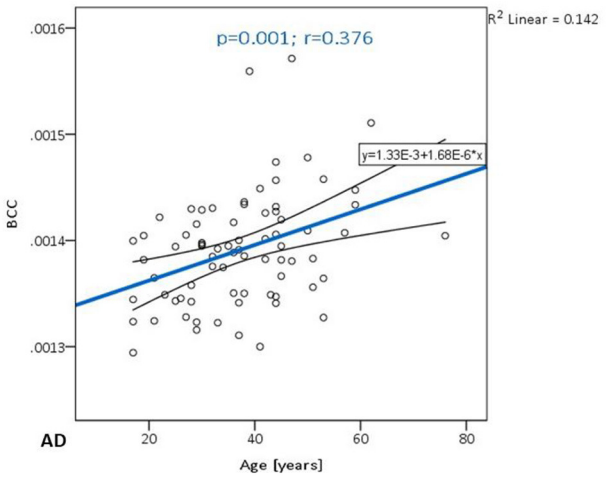

FIGURE 4 | The trend of AD increase in the body of the corpus callosum.

been linked to axonal damage (in combination with FA changes representing acute axonal swelling and fragmentation) (13). FA alone changes have been suggested to reflect mild microstructural changes with the loss of fiber structure without great tissue loss. Additional MD changes, following FA changes, reflect the presence of tissue loss and atrophy (46). The changes in RD (combined with FA and, sometimes AD) were related to gliosis and subsequent increase in extracellular tissue (48). Several studies confirmed that greater changes in RD (compared to AD) were found across the brain, similar to our results, suggesting that the leading mechanism of white matter degradation is to be associated with myelin degeneration (10, 13, 17, 46). The findings in AD were inconsistent in our study, similar to other studies from the available literature, showing both positive and negative correlations with age (10, 13, 46). The explanation for this finding in our study might be that our cohort had more prevalent chronic axonal damage (related to the increase in AD) or that these changes can be related to the incoherence in the regions of crossing fibers (which is, in our opinion, a more probable explanation).

Finally, no significant gender differences related to white matter diffusivity metrics were detected (**Figure 6**). However, this finding might be associated with the small sample with uneven distribution of men and women (males significantly outnumbering females).

Heterogeneity in findings in diffusivity changes across the brain, in our opinion, cannot be explained by one single gradient of physiological brain aging. It seems that different patterns of degradation are true for different fiber tracts in the brain and that no currently available theory can globally explain age-related changes in the brain. Furthermore, the effect of somatosensory decline should be included as one of the important covariables in the existing patterns.

In addition, a recent study by Behler et al. showed that diffusion properties of most white matter tracts in a healthy aging brain followed a triphasic pattern (in a simplified manner, FA showed a gradual increase during early adulthood followed by a stable state during middle age, and gradual decline in senium; RD, MD, and AD showed a decline during the early adulthood, followed by the stable state in middle age and increase

TABLE 5 | Results of Pearson's correlation of AD with age and education level of the study participants in the observed locations (*r*-correlation coefficient).

Location	Age		Education level	
	r	*p*	*r*	*p*
ACR-L	**−0.013**	0.911	−0.102	0.386
ACR-R	−0.097	0.407	−0.089	0.447
ALIC-L	0.084	0.475	**−0.009**	0.936
ALIC-R	**0.028**	0.814	−0.075	0.523
BCC	**0.376**	**0.001**	−0.162	0.166
CC	0.316	**0.006**	−0.088	0.451
CGC-L	0.152	0.192	**0.004**	0.974
CGC-R	0.104	0.374	−0.080	0.497
CGH-L	0.143	0.220	**0.000**	0.997
CGH-R	0.103	0.378	**−0.006**	0.957
CR-L	**0.034**	0.775	−0.108	0.356
CR-R	**−0.038**	0.747	−0.087	0.457
CST-L	0.177	0.130	**−0.046**	0.692
CST-R	0.176	0.132	0.130	0.265
EC-L	0.219	0.059	**0.024**	0.841
EC-R	0.253	**0.029**	0.096	0.410
FX	0.166	0.155	**0.036**	0.757
FXST-L	−0.053	0.652	0.184	0.114
FXST-R	**0.028**	0.813	0.155	0.186
GCC	0.144	0.216	−0.203	0.080
IC-L	**0.039**	0.743	0.144	0.217
IC-R	**0.039**	0.743	0.077	0.514
IFO-L	0.208	0.073	−0.092	0.434
IFO-R	0.142	0.225	−0.166	0.155
PCR-L	0.106	0.367	−0.052	0.657
PCR-R	**0.021**	0.859	**−0.037**	0.751
PLIC-L	0.082	0.484	0.152	0.193
PLIC-R	**0.008**	0.945	0.103	0.381
PTR-L	−0.203	0.081	0.088	0.451
PTR-R	−0.096	0.412	0.171	0.143
RLIC-L	−0.077	0.509	0.226	0.052
RLIC-R	0.061	0.601	0.143	0.222
SCC	0.238	**0.040**	0.155	0.184
SCR-L	**0.038**	0.748	−0.103	0.380
SCR-R	**0.015**	0.898	−0.078	0.507
SFO-L	0.133	0.254	**−0.030**	0.799
SFO-R	**0.020**	0.868	−0.123	0.293
SLF-L	0.075	0.524	**−0.042**	0.721
SLF-R	0.144	0.217	**−0.026**	0.825
SS-L	0.114	0.329	0.139	0.235
SS-R	0.074	0.528	0.071	0.544
UNC-L	0.340	**0.003**	−0.179	0.124
UNC-R	0.287	**0.013**	−0.052	0.659

Significant results are presented in bold case.

TABLE 5A | The results of partial correlation of AD with age, using education level as a control variable.

Location	Age	
	R	*p*
ACR-L	**−0.028**	0.814
ACR-R	−0.111	0.346
ALIC-L	0.083	0.480
ALIC-R	**0.017**	0.884
BCC	0.362	**0.002**
CC	0.308	**0.008**
CGC-L	0.154	0.189
CGC-R	0.094	0.424
CGH-L	0.145	0.219
CGH-R	0.103	0.381
CR-L	**0.019**	0.875
CR-R	−0.051	0.667
CST-L	0.172	0.143
CST-R	0.198	0.092
EC-L	0.225	0.054
EC-R	0.270	**0.020**
FX	0.173	0.141
FXST-L	**−0.028**	0.814
FXST-R	0.051	0.669
GCC	0.120	0.310
IC-L	0.060	0.610
IC-R	0.050	0.673
IFO-L	0.198	0.091
IFO-R	0.121	0.303
PCR-L	0.100	0.399
PCR-R	**0.016**	0.893
PLIC-L	0.106	0.370
PLIC-R	**0.023**	0.847
PTR-L	−0.193	0.099
PTR-R	−0.074	0.531
RLIC-L	**−0.047**	0.688
RLIC-R	0.083	0.482
SCC	0.265	**0.022**
SCR-L	**0.024**	0.841
SCR-R	**0.004**	0.972
SFO-L	0.131	0.268
SFO-R	**0.002**	0.984
SLF-L	0.070	0.556
SLF-R	0.142	0.227
SS-L	0.136	0.247
SS-R	0.085	0.471
UNC-L	0.323	**0.005**
UNC-R	0.283	**0.015**

Significant results are presented in bold case.

in senium), so that non-linear age correction should be applied to most of the tracts. Cerebellar tracts (superior and middle cerebellar pedunculi) showed basically no change over time (i.e., age correction is not applicable); optic radiation and anterior limb of the internal capsule showed linear regression with age, meaning that non-linear age correction is not necessary (49).

TABLE 6 | Patterns of significant findings in selected ROIs.

Location	FA	MD	RD	AD
Posterior thalamic radiation	↓↓↓		↑↑↑	
Sagittal stratum		↑↑↑	↑↑↑	
Retrolenticular internal capsule			↑↑↑	
Body of the corpus callosum				↑↑↑

The arrows represent significant decrease or increase, depending on the direction they are pointing to downward-decrease, upward-increase.

Study Limitations

There are some limitations to the study performed. Even though the number of participants was justified by the power analysis, it is possible that some correlations would have shown to be significant if the study sample were larger, and this might be resolved in a future study. However, it is important to highlight that the exclusion criterion for our study sample was the presence of white matter lesions including white matter hyperintensities (WMH) which represents a pertinent factor for the assessment of the changes in the white matter related to aging.

The second limitation of the study was the lack of a detailed neurocognitive assessment of our participants (only a screening cognitive test was performed as a part of the exclusion criteria). MMSE scoring test represents a screening test, of high clinical importance, but is not sensitive enough for the cases of early cognitive impairment, thus, in our opinion, suitable for the exclusion of cognitively challenged persons, but not suitable for detailed correlations. Some of the tracts we analyzed are known to be associated with affect and personality features, which means that additional assessment of depression and anxiety would be recommendable.

An additional limitation is a cross-sectional evaluation and the lack of longitudinal design, since the changes in diffusivity measurements may follow certain trajectories during chronological aging in an individual.

It is necessary to point out that the maturation of the fibers does not follow the identical dynamics in all observed tracts. Some of the tracts (IFO, AIC, PLIC, SCC, BCC, GCC, UNC, SFO, IFO, SLF) reach the full maturity (maximal FA and minimal MD values) between 20 and 40 years of age (50). In one part of our study sample, these tracts potentially did not develop their full maturity, given that the average age of the sample was around 37 years.

The final (small) limitation of the study is the lack of information on prematurity, which could also influence the changes in tract diffusivity (CC in the first place) (51).

Even though there were no significant comorbidities noted in the study sample, it will be reasonable to include additional information on metabolic function (blood glucose level, lipidemia, parameters of liver function, arterial tension, etc.) and lifestyle in the future studies (52, 53).

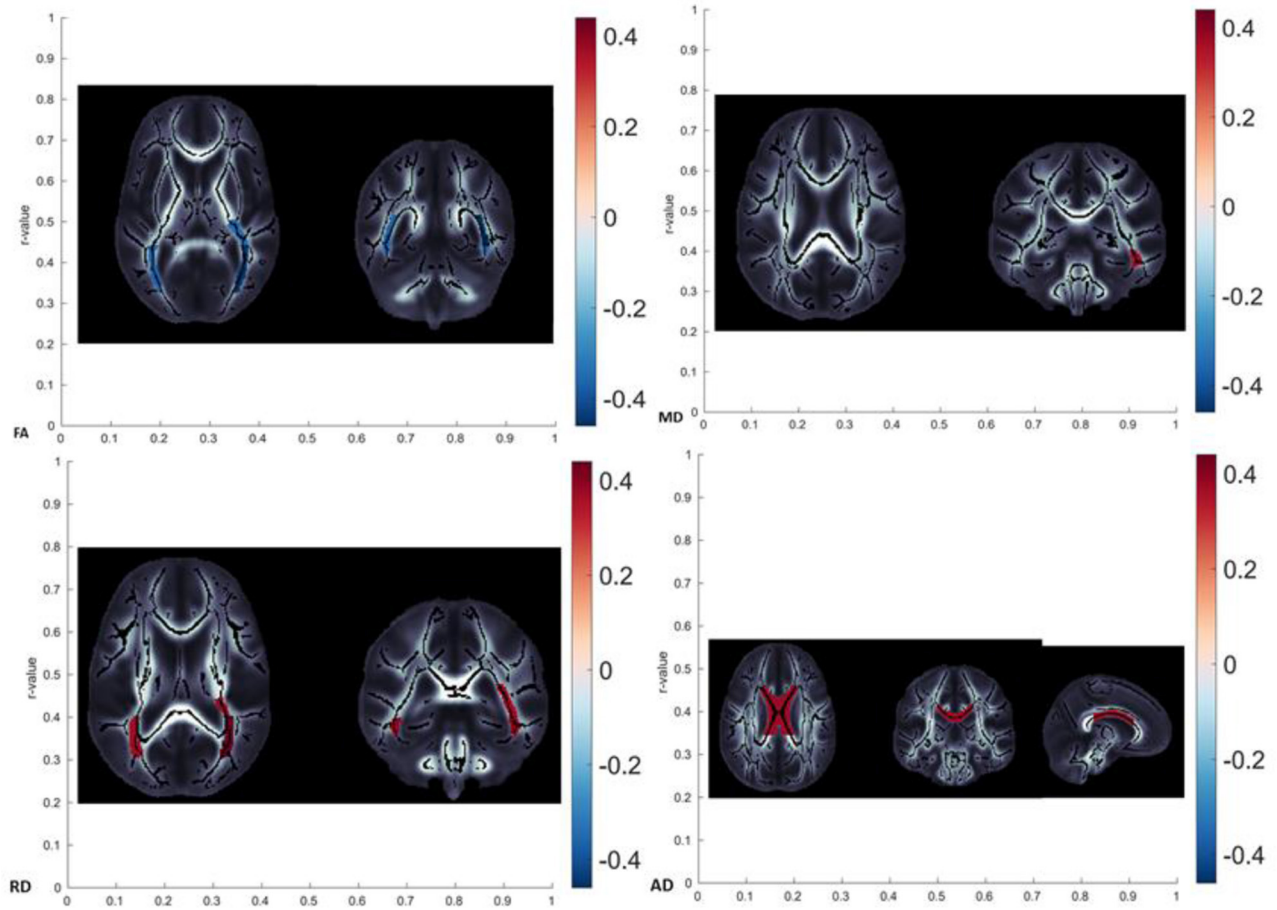

FIGURE 5 | Brain maps showing localization with significant age-related diffusivity changes (FA showed a significant decrease in posterior thalamic radiation, MD showed a significant increase in left sagittal stratum, RD showed a significant increase in posterior thalamic radiation, and AD showed significant changes in the body of corpus callosum).

It is also worth mentioning that advanced techniques for evaluation of DWI data could provide more detailed information than the DTI option (54) and added to the potential of longitudinal studies in revealing the gradients of changes in the DTI metrics are two main recommendations for the future studies.

CONCLUSION

All four DTI metrics showed significant correlations with the advancing age of healthy participants (FA in posterior thalamic radiation, MD in left sagittal stratum, RD in the posterior thalamic radiation, sagittal stratum, and retrolenticular limb of internal capsule, and AD in body of the corpus callosum). According to our study, RD showed the richest correlations with age, out of all DTI metrics. FA, MD, and RD showed significant changes in the diffusivity of projection fibers, while AD presented diffusivity changes in the commissural fibers.

It is important to realize that all four DTI metrics are necessary for the assessment of healthy brain aging effect on white matter integrity, given that routinely analyzed parameters (FA and MD) do not allow complete insight into diffusivity changes. Since the changes in the white matter integrity that we observed during healthy aging also overlap with changes observed in several pathological conditions—psychiatric disorders, traumatic lesions, and dementia/MCI—caution is necessary when interpreting these differences in a healthy individual. In such cases, a longitudinal follow-up is necessary to track the trajectories of degenerative changes associated with the aging brain.

Finally, the observed heterogeneity in diffusivity changes across the brain, in our opinion, cannot be explained by a single aging pattern (antero-posterior, supero-inferior, or myelodegeneration- retrogenesis). It seems that different patterns of degradation are true for different fiber tracts in the brain and that no currently available theory can globally explain age-related changes in the brain. Some additional factors, such as the effect of somatosensory decline, should be included as one of the important covariables in the existing patterns.

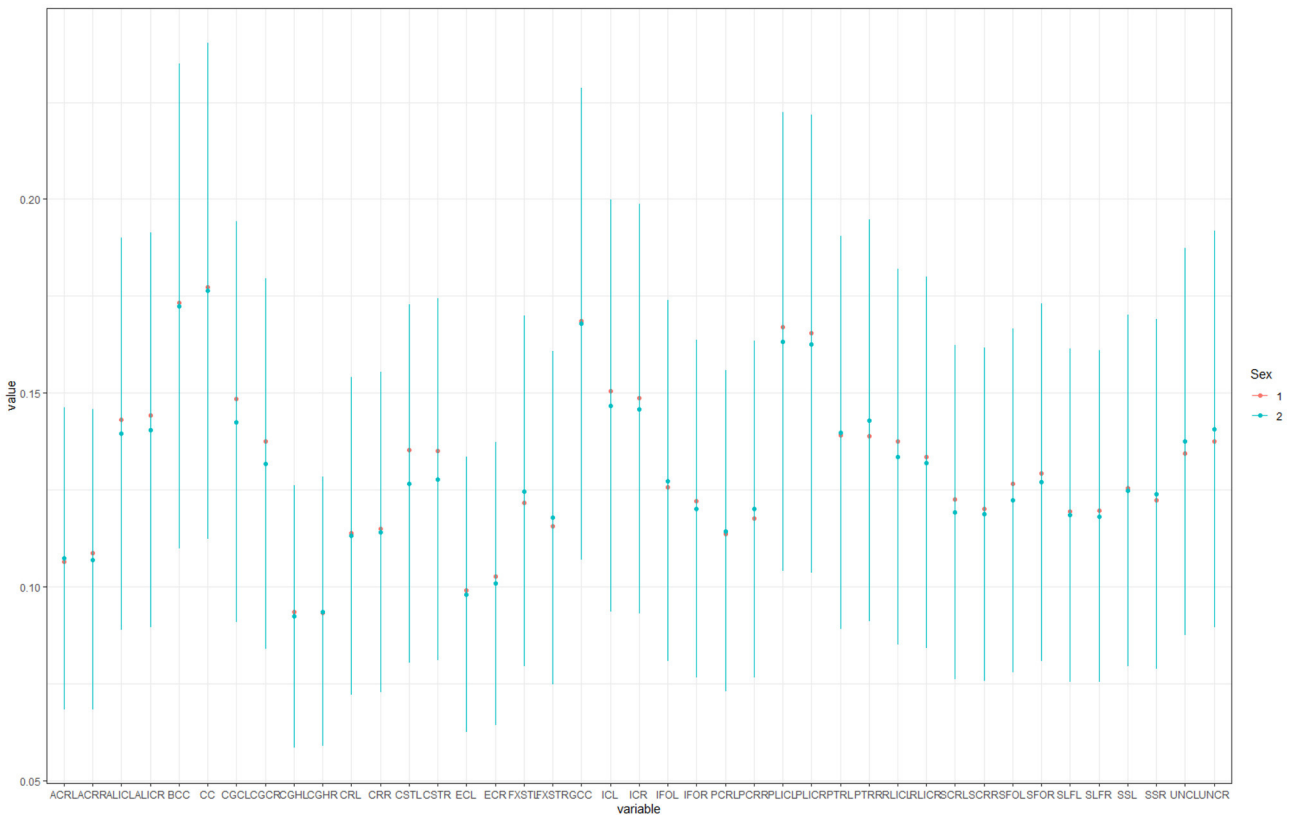

FIGURE 6 | Box plots showing gender differences in observed locations (1-male, 2- female).

DATA AVAILABILITY STATEMENT

The raw data supporting the conclusions of this article will be made available by the authors, without undue reservation.

ETHICS STATEMENT

The studies involving human participants were reviewed and approved by Ethical Committee of Faculty of Medicine University of Novi Sad. The patients/participants provided their written informed consent to participate in this study.

AUTHOR CONTRIBUTIONS

JB drafted the article. JB, MT, NB, DL, NJ, and TN were involved in acquisition, collection, and analysis of the data. DK, MT, and ML performed critical revision of intellectual content. All authors saw and approved the final version of drafted manuscript.

FUNDING

TN and NJ were funded, in part, by NIH grants: R01 AG059874, U54 EB020403, T32 AG058507, and U01 AG068057. The authors also received partial grant support from Biogen, Inc., for research unrelated to this work. JB, DK, and DL were funded by Provincial Secretariat for Higher Education and scientific Research, grant No. 142-451-2600/2021-01.

SUPPLEMENTARY MATERIAL

The Supplementary Material for this article can be found online at: https://www.frontiersin.org/articles/10.3389/fneur.2022.870909/full#supplementary-material

REFERENCES

1. Ishii R, Canuet L, Aoki Y, Hata M, Iwase M, Ikeda S, et al. Healthy and pathological brain aging: from the perspective of oscillations, functional connectivity and signal complexity. *Neuropsychology*. (2017) 75:151–61. doi: 10.1159/000486870
2. Desai AK, Grossberg GT, Chibnall JT. Healthy brain aging: a road map. *Clin Geriatr Med*. (2010) 26:1–16. doi: 10.1016/j.cger.2009.12.002
3. Huisman TAGM. Diffusion-weighted and diffusion tensor imaging of the brain made easy. *Cancerimaging*. (2010) 10: S163–71. doi: 10.1102/1470-7330.2010.9023

4. Drake-Perez M, Boto J, Fitsiori A, Lovblad K, Vargas MI. Clinial applications of diffusion weighted imaging in neuroradiology. *Insights Imaging*. (2018) 9:535–47. doi: 10.1007/s13244-018-0624-3
5. O'Donnell LJ, Westin CF. An introduction to diffusion tensor image analysis. *Neurosurg Clin N Am*. (2011) 22:185-VII. doi: 10.1016/j.nec.2010.12.004
6. O'Sullivan M, Jones DK, Summers PE, Morris RG, Williams SC, Markus HS. Evidence for cortical "disconnection" as a mechanism of age-related cognitive decline. *Neurology*. (2001) 57:632–8. doi: 10.1212/WNL.57.4.632
7. Andrews-Hanna JR, Snyder AZ, Vincent JL, Lustig C, Head D, Raichle ME, Buckner RL. Disruption of large-scale brain systems in advanced aging. *Neuron*. (2007) 56:924–35. doi: 10.1016/j.neuron.2007.10.038
8. Salat DH. The declining infrastructure of the aging brain. *Brain Connect*. (2011) 1:279–93. doi: 10.1089/brain.2011.0056
9. Vinke EJ, de Groot M, Venkatraghavan V, Klien S, Niessen WJ, Ikram MA, et al. Trajectories of imaging markers in brain aging: the Rotterdam study. *Neurobiol Aging*. (2018) 71:32–40. doi: 10.1016/j.neurobiolaging.2018.07.001
10. Molloy CJ, Nugent S, Bokde ALW. Alterations in diffusion measures of white matter integrity associated with healthy aging. *J Gerontol A Bio Sci Med Sci*. (2019) 22:945–54. doi: 10.1101/540443
11. Wasenaar TM, Yaffe C, van der Werf YD, Sexton C. Associations between modifiable risk factors and white matter of the aging brain: insights from diffusion tensor imaging studies. *Neurobiol Aging*. (2019) 80:56–70. doi: 10.1016/j.neurobiolaging.2019.04.006
12. Brickman AM, Meier IB, Korgaonkar MS, Provenzano FA, Grieve SM, Siedlecki KL, et al. Testing the white matter retrogenesis hypothesis of cognitive aging. *Neurobiol Aging*. (2012) 33:1699–715. doi: 10.1016/j.neurobiolaging.2011.06.001
13. Burzynska AZ, Preuschhof C, Backman L, Nyberg L, Li SC, Lindenberger U, et al. Age-related differences in white matter microstructure: region-sepcific patterns of diffusivity. *Neuroimage*. (2010) 49:2104–12. doi: 10.1016/j.neuroimage.2009.09.041
14. Mayo CD, Garcia-Barrera MA, Mazerolle EL, Ritchie LJ, Fisk JD, Gawryluk JR, et al. Relationship between DTI metrics and cognitive function in Alzheimer's disease. *Front Aging Neurosci*. (2019) 10:436. doi: 10.3389/fnagi.2018.00436
15. Ashrafi MR, Amanat M, Garshasbi M, Kameli R, Nilipour Y, Heidari M, et al. An update on clinical, pathological, diagnostic and therapeutic perspectives of childhood leukodystrophies. *Expert Rev Neurother*. (2020) 20:65–84. doi: 10.1080/14737175.2020.1699060
16. Bach M, Laun FB, Leemans A, Tax CMW, Biessels GJ, Stieltjes B, et al. Methodological considerations on tract-based spatial statistics (TBSS). *Neuroimage*. (2014) 100:358–69. doi: 10.1016/j.neuroimage.2014.06.021
17. Bennett IJ, Madden DJ, Vaidya CJ, Howard DV, Howard JH Jr. Age-related differencesin multiple measures of white matter integrity: a diffusion tensor imaging study of healthy aging. *Hum Brain Map*. (2010) 31:378–90. doi: 10.1002/hbm.20872
18. Zahr NM, Rohlfing T, Pfefferbaum A, Sullivan EV. Problem solving, working memory, and motor correltaes of association and commissural fiber bundles in normal aging: a quantitative fiber tracking study. *Neuroimage*. (2009) 44:1050–62. doi: 10.1016/j.neuroimage.2008.09.046
19. Tian L, Ma L. Microstructural changes of the human brain from early to mid-adulthood. *Front Hum Neurosci*. (2017) 11:393. doi: 10.3389/fnhum.2017.00393
20. Schmierer K, Scaravilli F, Altmann DR, Barker GJ, Miller DH. Magnetization transfer ratio and myelin in postmortem multiple sclerosis brain. *Ann Neurol*. (2004) 56:407–15. doi: 10.1002/ana.20202
21. Folstein MF, Folstein SE, McHugh PR. "Mini-mental state". A practical method for grading the cognitive state of patients for clinician. *J Psychiatr Res*. (1975) 12:189–98. doi: 10.1016/0022-3956(75)90026-6
22. Cavill S, Bryden P. Development of handedness: comparison of questionnaire and performance-based measures of preference. *Brain Cogn*. (2003) 53:149–51. doi: 10.1016/S0278-2626(03)00098-8
23. Lapham SC, Skipper BJ, Owen JP, Kleyboecker K, Teaf D, Thompson B, et al. Alcohol abuse screening instruments: normative test data collected from a first DWI offender screening programe. *J Stud Alcohol*. (1995) 56:51–9. doi: 10.15288/jsa.1995.56.51
24. Basser PJ Mattiello J, LeBihan D. MR diffusion tensor spectroscopy and imaging. *Biophys J*. (1994) 66:259–67. doi: 10.1016/S0006-3495(94)80775-1
25. Jahanshad N, Kochunov PV, Sprooten E, Mandl RC, Nichols TE, Almasy L, et al. Multi-site genetic analysis of diffusion images and voxelwise heritability analysis: a pilot project of the ENIGMA-DTI working group. *Neuroimage*. (2013) 81:455–69. doi: 10.1016/j.neuroimage.2013.04.061
26. Avants BB, Tustison NJ, Song G, Cook PA, Klein A, Gee JC. A reproducible evaluation of ANTs similarity metric performance in brain image registration. *Neuroimage*. (2011) 54:2033–44. doi: 10.1016/j.neuroimage.2010.09.025
27. Wakana S, Jiang H, Nagae-Poetscher LM, Van Zijl PCM, Mori S. Fiber tract-based atlas of human white matter anatomy. *Radiology*. (2004) 230:77–87. doi: 10.1148/radiol.2301021640
28. Hua K, Zhang J, Wakana S, Jiang H, Li X, Reich DS, et al. Tract probability maps in stereotaxic spaces: analyses of white matter anatomy and tract-specific quantification. *Neuroimage*. (2008) 39:336–47. doi: 10.1016/j.neuroimage.2007.07.053
29. Aralasmak A, Ulmer JL, Kocak M, Salvan CV, Hillis AE, Yousem DM. Association, commissural, and projection pathways and their functional deficit reported in literature. *J Comput Assist Tomogr*. (2006) 30:695–715. doi: 10.1097/01.rct.0000226397.43235.8b
30. Roberts KL, Allen HA. Perception and cognition in the ageing brain: a brief review of the short- and long-term links between perceptual and cognitive decline. *Front Aging Neurosci*. (2016) 8:39. doi: 10.3389/fnagi.2016.00039
31. Freiling H, Fischer J, Wilhelm J, Jiang H, Li X, Reich DS, et al. Microstructural abnormalities of the posterior thalamic radiation and the mediodorsal thalamic nuclei in females with anorexia nervosa- a voxel based diffusion tensor imaging (DTI) study. *J Psychiatr Res*. (2012) 46:1237–42. doi: 10.1016/j.jpsychires.2012.06.005
32. Leon-Ortiz P, Reyes-Madrigal F, Kochunov P, Gomez-Cruz G, Moncada-Habib T, Malacara M, et al. White matter alterations and the conversion to psychosis: a combined diffusion tensor imaging and glutamate 1H-MRS study. *Schizofrenia Res*. (2020) S0920-9964(20)30358-3. doi: 10.1016/j.schres.2020.06.006
33. Huang S, Yang W, Luo J, Yan C, Liu J. White matter abnormalities based on TBSS and its correlation with impulsivitiy behavior of methamphetamine addicts. *Front Psychiatry*. (2020) 11:452. doi: 10.3389/fpsyt.2020.00452
34. Hoon AH Jr, Stashinko EE, Nagae LM, Nagae LM, Lin DMD, Keller J, et al. Sensory and motor deficits in children with cerebral palsy born preterm correlate with diffusion tensor imaging abnormalities in thalamocortical pathways. *Dev Med Child Neurol*. (2009) 51:697–704. doi: 10.1111/j.1469-8749.2009.03306.x
35. Gray JC, Thompson M, Bachman C, Owens MM, Murphy M, Palmer R. Associations of cigarette smoking with gray and white matter in the UK Biobank. *Neuropsychopharmacology*. (2020) 45:1215–22. doi: 10.1038/s41386-020-0630-2
36. Di Carlo DT, Benedetto N, Duffau H, Cagnazzo F, Weiss A, Castagna M, et al. Microsurgical anatomy of the sagittal stratum. *Acta Neurochir*. (2019) 161:2319–27. doi: 10.1007/s00701-019-04019-8
37. Juttukonda MR, Franco G, Englot DJ, Lin YC, Petersen KJ, Trujillo P, et al. White matter differences between essential tremor and Parkinson disease. *Neurology*. (2019) 92:e30–9. doi: 10.1212/WNL.0000000000006694
38. Zhu J, Ling J, Ding N. Association between diffusion tensor imaging findings and cognitive outcomes following mild traumatic brain injury: a PRISMA-compliant meta-analysis. *ACS Chem Neurosci*. (2019) 10:4864–9. doi: 10.1021/acschemneuro.9b00584
39. Onnink AMH, Zwiers MP, Hoogman M, Mostert JC, Dammers J, Kan CC, et al. Deviant white matter structure in adults with attentiondeficit/hyperactivity disorder points to aberrant myelination and affects neuropsychological performance. *Prog Neuropsychopharmacol Biol Psychiatry*. (2015) 63:14–22. doi: 10.1016/j.pnpbp.2015.04.008
40. Liang H, Chang L, Chen R, Oishi K, Ernst T Independent and cobined effects of chronic HIV-infection and tobacco smoking on brain microstructure. *J Neuroimmune Pharmacol*. (2018) 13:509–22. doi: 10.1007/s11481-018-9810-9
41. Hyett MP, Perry A, Breakspear M, Wen W, Parker GB. White matter alterations in the internal capsule and psychomotor impairment in melancholic depression. *PLoS ONE*. (2018) 13:e0195672. doi: 10.1371/journal.pone.0195672
42. Bauer IE, Ouyang A, Mwangi B, Sanches M, Zunta-Soares GB, Keefe RS, et al. Reduced white matter integrity and verbal fluency impairment in young

adults with bipolar disorder: a diffusion tensor imaging study. *J Psychiatr Res*. (2015) 62:115–22. doi: 10.1016/j.jpsychires.2015.01.008
43. Li W, Zhu J, Li Q, Ye J, Chen J, Liu J, et al. Brain white matter integrity in heroin addicts during methadonema intenance treatment is related to relapse propensity. *Brain Behav*. (2016) 6:e00436. doi: 10.1002/brb3.436
44. Madden DJ, Spaniol J, Costello MC, Bucur B, White LE, Cabeza R, et al. Cerebral white matter integrity mediates adult age differencesin cognitive performance. *J Cogn Neurosci*. (2009) 21:289–302. doi: 10.1162/jocn.2009.21047
45. Fan YT, Fang YW, Chen YP, Leshikar ED, Lin CP, Tzeng OJL, et al. Aging, cognition, and the brain: effects of age-related variation in white matter integrity on neuropsychological function. *Aging Mental Health*. (2019) 23:831–9. doi: 10.1080/13607863.2018.1455804
46. Zhang Y, Du AT, Hayasaka S, Jahng GH, Hlavin J, Zhan W, et al. Patterns of age-related water diffusion changes in human brain by concordance and disconcordance analysis. *Neurobiol Aging*. (2010) 31:1991–2001. doi: 10.1016/j.neurobiolaging.2008.10.009
47. Bender AR, Völkle MC, Raz N. Differential aging of cerebral white matter in middle-aged and older adults: a seven-year follow-up. *Neuroimage*. (2016) 125:74–83. doi: 10.1016/j.neuroimage.2015.10.030
48. Hughes EG, Orthmann-Murohy JL, Langseth AJ, Bergles DE. Myelin remodeling through experiencedependent oligodendrogenesis in the adult somatosensory cortex. *Nat Neurosci*. (2018) 21:696–706. doi: 10.1038/s41593-018-0121-5
49. Behler A, Kassubek J, Muller HP. Age-related alterations in DTI metrics in the human brainconsequences for age correction. *Front Aging Neurosci*. (2021) 6:94. doi: 10.3389/fnagi.2021.682109
50. Olson IR, Von Der Heide RJ, Alm KH, Vyas G. Development of the uncinate fasciculus: implicationsfor theory and developmental disorders. *Dev Cogn Neurosci*. (2015) 14:50–61. doi: 10.1016/j.dcn.2015.06.003
51. Shim SY, Jeong HJ, Son DW, Jeong JS, Oh SH, Park SY, et al. Altered microstructure of white matter except the corpus callosum is independent of prematurity. *Neonatology*. (2012) 102:309–15. doi: 10.1159/000341867
52. Hofer S, Frahm J. Topography of the human corpus callosum revisited: comprehensive fiber tractography using diffusion tensor magnetic resonance imaging. *Neuroimage*. (2006) 32:989–94. doi: 10.1016/j.neuroimage.2006.05.044
53. Smith JC, Lancaster MA, Nielson KA, Woodard JL, Seidenberg M, Durgerian S, et al. Interactive effects of physical activity and APO-ξ4 on white matter tract diffusivity in healthy elders. *Neuroimage*. (2016) 131:102–12. doi: 10.1016/j.neuroimage.2015.08.007
54. Murugavel M, Cubon V, Putukian M, Echemendia R, Cabrera J, Osherson D, et al. A longitudinal diffusion tensor imaging study assessingwhite matter fiber tracts after sports-related concussion. *J Neurotrauma*. (2014) 31:1860–71. doi: 10.1089/neu.2014.3368

Conflict of Interest: The authors declare that the research was conducted in the absence of any commercial or financial relationships that could be construed as a potential conflict of interest.

Publisher's Note: All claims expressed in this article are solely those of the authors and do not necessarily represent those of their affiliated organizations, or those of the publisher, the editors and the reviewers. Any product that may be evaluated in this article, or claim that may be made by its manufacturer, is not guaranteed or endorsed by the publisher.

frontiers | Frontiers in Neurology

ORIGINAL RESEARCH
published: 27 July 2022
doi: 10.3389/fneur.2022.932219

Preoperative Brain Tumor Imaging: Models and Software for Segmentation and Standardized Reporting

David Bouget[1], André Pedersen[1,2,3], Asgeir S. Jakola[4,5], Vasileios Kavouridis[6], Kyrre E. Emblem[7], Roelant S. Eijgelaar[8,9], Ivar Kommers[8,9], Hilko Ardon[10], Frederik Barkhof[11,12], Lorenzo Bello[13], Mitchel S. Berger[14], Marco Conti Nibali[13], Julia Furtner[15], Shawn Hervey-Jumper[14], Albert J. S. Idema[16], Barbara Kiesel[17], Alfred Kloet[18], Emmanuel Mandonnet[19], Domenique M. J. Müller[8,9], Pierre A. Robe[20], Marco Rossi[13], Tommaso Sciortino[13], Wimar A. Van den Brink[21], Michiel Wagemakers[22], Georg Widhalm[17], Marnix G. Witte[23], Aeilko H. Zwinderman[24], Philip C. De Witt Hamer[8,9], Ole Solheim[6,25] and Ingerid Reinertsen[1,26]*

[1] Department of Health Research, SINTEF Digital, Trondheim, Norway, [2] Department of Clinical and Molecular Medicine, Norwegian University of Science and Technology, Trondheim, Norway, [3] Clinic of Surgery, St. Olavs Hospital, Trondheim University Hospital, Trondheim, Norway, [4] Department of Neurosurgery, Sahlgrenska University Hospital, Gothenburg, Sweden, [5] Department of Clinical Neuroscience, Institute of Neuroscience and Physiology, Sahlgrenska Academy, University of Gothenburg, Gothenburg, Sweden, [6] Department of Neurosurgery, St. Olavs Hospital, Trondheim University Hospital, Trondheim, Norway, [7] Division of Radiology and Nuclear Medicine, Department of Physics and Computational Radiology, Oslo University Hospital, Oslo, Norway, [8] Department of Neurosurgery, Amsterdam University Medical Centers, Vrije Universiteit, Amsterdam, Netherlands, [9] Cancer Center Amsterdam, Brain Tumor Center, Amsterdam University Medical Centers, Amsterdam, Netherlands, [10] Department of Neurosurgery, Twee Steden Hospital, Tilburg, Netherlands, [11] Department of Radiology and Nuclear Medicine, Amsterdam University Medical Centers, Vrije Universiteit, Amsterdam, Netherlands, [12] Institutes of Neurology and Healthcare Engineering, University College London, London, United Kingdom, [13] Neurosurgical Oncology Unit, Department of Oncology and Hemato-Oncology, Humanitas Research Hospital, Università degli Studi di Milano, Milan, Italy, [14] Department of Neurological Surgery, University of California, San Francisco, San Francisco, CA, United States, [15] Department of Biomedical Imaging and Image-Guided Therapy, Medical University Vienna, Wien, Austria, [16] Department of Neurosurgery, Northwest Clinics, Alkmaar, Netherlands, [17] Department of Neurosurgery, Medical University Vienna, Wien, Austria, [18] Department of Neurosurgery, Haaglanden Medical Center, The Hague, Netherlands, [19] Department of Neurological Surgery, Hôpital Lariboisière, Paris, France, [20] Department of Neurology and Neurosurgery, University Medical Center Utrecht, Utrecht, Netherlands, [21] Department of Neurosurgery, Isala, Zwolle, Netherlands, [22] Department of Neurosurgery, University Medical Center Groningen, University of Groningen, Groningen, Netherlands, [23] Department of Radiation Oncology, Netherlands Cancer Institute, Amsterdam, Netherlands, [24] Department of Clinical Epidemiology and Biostatistics, Amsterdam University Medical Centers, University of Amsterdam, Amsterdam, Netherlands, [25] Department of Neuromedicine and Movement Science, Norwegian University of Science and Technology, Trondheim, Norway, [26] Department of Circulation and Medical Imaging, Norwegian University of Science and Technology, Trondheim, Norway

OPEN ACCESS

Edited by:
Deqiang Qiu,
Emory University, United States

Reviewed by:
Jan Egger,
University Hospital Essen, Germany
Hamza Farooq,
University of Minnesota Twin Cities, United States

***Correspondence:**
David Bouget
david.bouget@sintef.no

Specialty section:
This article was submitted to Applied Neuroimaging, a section of the journal Frontiers in Neurology

Received: 29 April 2022
Accepted: 23 June 2022
Published: 27 July 2022

Citation:
Bouget D, Pedersen A, Jakola AS, Kavouridis V, Emblem KE, Eijgelaar RS, Kommers I, Ardon H, Barkhof F, Bello L, Berger MS, Conti Nibali M, Furtner J, Hervey-Jumper S, Idema AJS, Kiesel B, Kloet A, Mandonnet E, Müller DMJ, Robe PA, Rossi M, Sciortino T, Van den Brink WA, Wagemakers M, Widhalm G, Witte MG, Zwinderman AH, De Witt Hamer PC, Solheim O and Reinertsen I (2022) Preoperative Brain Tumor Imaging: Models and Software for Segmentation and Standardized Reporting. Front. Neurol. 13:932219. doi: 10.3389/fneur.2022.932219

For patients suffering from brain tumor, prognosis estimation and treatment decisions are made by a multidisciplinary team based on a set of preoperative MR scans. Currently, the lack of standardized and automatic methods for tumor detection and generation of clinical reports, incorporating a wide range of tumor characteristics, represents a major hurdle. In this study, we investigate the most occurring brain tumor types: glioblastomas, lower grade gliomas, meningiomas, and metastases, through four cohorts of up to 4,000 patients. Tumor segmentation models were trained using the AGU-Net architecture with different preprocessing steps and protocols. Segmentation performances were assessed in-depth using a wide-range of voxel and patient-wise metrics covering

volume, distance, and probabilistic aspects. Finally, two software solutions have been developed, enabling an easy use of the trained models and standardized generation of clinical reports: Raidionics and Raidionics-Slicer. Segmentation performances were quite homogeneous across the four different brain tumor types, with an average true positive Dice ranging between 80 and 90%, patient-wise recall between 88 and 98%, and patient-wise precision around 95%. In conjunction to Dice, the identified most relevant other metrics were the relative absolute volume difference, the variation of information, and the Hausdorff, Mahalanobis, and object average symmetric surface distances. With our Raidionics software, running on a desktop computer with CPU support, tumor segmentation can be performed in 16–54 s depending on the dimensions of the MRI volume. For the generation of a standardized clinical report, including the tumor segmentation and features computation, 5–15 min are necessary. All trained models have been made open-access together with the source code for both software solutions and validation metrics computation. In the future, a method to convert results from a set of metrics into a final single score would be highly desirable for easier ranking across trained models. In addition, an automatic classification of the brain tumor type would be necessary to replace manual user input. Finally, the inclusion of post-operative segmentation in both software solutions will be key for generating complete post-operative standardized clinical reports.

Keywords: metastasis, meningioma, glioma, RADS, MRI, deep learning, 3D segmentation, open-source software

1. INTRODUCTION

Prognosis in patients with brain tumors is heterogeneous with survival rates varying from weeks to several years depending on the tumor grade and type, and for which most patients will experience progressive neurological and cognitive deficit (1). Brain tumors can be classified as either primary or secondary. In the former, tumors originate from the brain itself or its supporting tissues whereas in the latter cancer cells have spread from tumors located elsewhere in the body to reach the brain (i.e., brain metastasis). According to the World Health Organization classification of tumors (2), primary brain tumors are graded by histopathological and genetic analyses and can be regrouped in 100 different subtypes with frequent to relatively rare occurrences. Among the most frequent subtypes, tumors arising from the brain's supportive cell population (i.e., glial tissue) are referred to as gliomas. The more aggressive entities are labeled as high-grade gliomas (HGGs) and are graded between 3 and 4, while the less aggressive entities are referred to as diffuse lower grade gliomas (LGGs) and are graded between 2 and 3. Tumors arising from the meninges, which form the external membranous covering the brain, are referred to as meningiomas. Aside from the aforementioned large categories, other and less frequent tumor types exist (e.g., in the pituitary, sellar, or pineal regions). Each tumor category has distinct biology, prognosis, and treatment (3, 4). The most common primary malignant brain tumor type in adults is high-grade glioma which remains among the most difficult cancers to treat with a limited 5-year overall survival (5).

For patients affected by brain tumors, prognosis estimation and treatment decisions are made by a multidisciplinary team (including neurosurgeons, oncologists, and radiologists), and based on a set of preoperative MR scans. High accuracy in the preoperative diagnostics phase is of utmost importance for patient outcomes. Judgments concerning the complexity or radicality of surgery, or the risks of postoperative complications hinge on data gleaned from MR scans. Additionally, tumor-specific characteristics such as volume and location, or cortical structures profile can to a large degree be collected (6). Retrospectively, such measurements can be gathered from the analysis of surgical cohorts, multicenter trials, or registries in order to devise patient outcome prediction models (7–9). Reliable measurements and reporting of tumor characteristics are, therefore, instrumental in patient care. Standard reporting and data systems (RADSs) have been established for several solid tumors such as prostate cancer (10) and lung cancer (11). Very few attempts have been made for brain cancer in general (12) or high-grade gliomas (13). The main goal of RADSs is to provide rules for imaging techniques, terminology of reports, definitions of tumor features, and treatment response to reduce practice variation and obtain reproducible tumor classification. A broad implementation can facilitate collaborations and stimulate evaluation for the development and improvement of RADSs.

Currently, the lack of standardized and automatic methods for tumor detection in brain MR scan represents a major hurdle toward the generation of clinical reports incorporating a wide range of tumor characteristics. Manual tumor delineation or assessment by radiologists is time-consuming and subject to intra and inter-rater variations that are difficult to characterize (14)

and, therefore, rarely done in clinical practice. As a result, informative tumor features (e.g., location or volume) are often estimated from the images solely based on crude measuring techniques (e.g., eyeballing) (15).

1.1. Related Study

From the fast-growing development in the field of deep learning, convolutional neural networks have demonstrated impressive performance in various segmentation tasks and benchmark challenges, with the added-value of being fully automatic and deterministic (16). Regarding brain tumor segmentation, performances have specifically been assessed on the Brain Tumor Segmentation Challenge (BraTS) dataset (17, 18). Occurring every year since 2012, the challenge focuses on gliomas (i.e., HGGs and LGGs) and has reached a notable cohort size with a total of 2,040 patients included in the 2021 edition, and multiple MR sequences included for each patient (i.e., T1c, T1w, T2, FLAIR). Segmentation performance has been assessed using the Dice similarity coefficient and the 95th percentile Hausdorff distance (HD95) as metrics (19). The current state-of-the-art is an extension of the nnU-Net architecture (20) with an asymmetrical number of filters between the encoding and decoding paths, the substitution of all batch normalization layers by group normalization, and the addition of axial attention (21). An average Dice score of 85% together with a 17.70 mm HD95 were obtained for the enhancing tumor segmentation task in high-grade gliomas. The segmentation of other brain tumor types has been sparsely investigated in the literature in comparison, possibly due to a lack of open-access annotated data, as illustrated by recent reviews or studies investigating brain tumor segmentation in general (22, 23). Grovik et al. used a multicentric and multi-sequence dataset of 165 metastatic patients to train a segmentation model with the DeepLabV3 architecture (24, 25). The best segmentation results were around 79% Dice score with 3.6 false positive detections per patient on average. Other prior studies have focused on using variations of the DeepMedic architecture (26), using contrast-enhanced T1-weighted MRI volumes as input, to train their segmentation models (27, 28). Datasets were of a similar magnitude with around 200 patients. However, in both cases the test sets were limited to up to 20 patients, making it difficult to assess the generalization ability of the trained models in the absence of cross-validation studies. Obtained average Dice scores over the contrast-enhancing tumor were approximating 75%, with almost 8 false positive detections per patient. From a recent review on the use of machine learning applied to different meningioma-related tasks using MRI scans (29), more than 30 previous studies have investigated automatic diagnosis or grading but only a handful focused on the segmentation task. In addition, the datasets' magnitude used for segmentation purposes has been consistently smaller than for the other tasks, with barely up to 126 patients in the reported studies. Laukamp et al. reported the best Dice scores using well-known 3D neural network architectures such as DeepMedic and BioMedIA, though at the expense of heavy preprocessing techniques the likes of atlas registration (30, 31). In a previous study, we achieved equally promising performance using an attention-based U-Net architecture, reaching an average Dice score of up to 88% on contrast-enhanced T1-weighted MRI volumes (32). In addition, the cross-validation studies performed over up to 600 patients with a wide range of tumor sizes, coming from the hospital and the outpatient clinic, exhibited a proper ability to generalize from the trained models.

To summarize, with the exception of the BraTS challenge, there is a dearth of high-quality MRI datasets for brain tumor segmentation. Furthermore, open-access pretrained models and inference codes are scarce and can be cumbersome to operate, hence hindering the generation of private datasets for brain tumor segmentation tasks. On the other hand, open-source tools are being developed to assist in image labeling and the generation of AI models for clinical evaluation, such as MONAI Label (33) or Biomedisa (34). Yet, they do not integrate nor provide access to the latest and highest performing brain tumor segmentation models from the literature, or provide only semi-automatic methods hence requiring manual inputs from the user. From a validation standpoint, the focus has been on reporting Dice scores and often Hausdorff distances, while many other meaningful and possibly more relevant metrics exist and could be investigated to better highlight the strengths and weaknesses of the different segmentation methods (35, 36).

The literature on RADSs for brain tumors is equally scarce with only few attempts for preoperative glioblastoma surgery (13) or post-treatment investigation (37). In the former, automatic segmentation and computation of relevant tumor features were provided, and an excellent agreement has been shown between characteristics computed over the manual and automatic segmentation. In the latter, the interpretation of the post-treatment MR scans was provided using a structured set of rules but deprived of any automatic tumor segmentation or image analysis support.

1.2. Contributions

While research is exceedingly ahead for glioma segmentation under the aegis of the BraTS challenge community, the segmentation of meningiomas and metastases is trailing behind. In addition, validation studies in the literature have too often been dominated by Dice score reporting and a broader inspection is essential to ensure clinical relevance. Finally, the outcome of this research is often not readily available, especially for the intended end-users who are clinicians without programming experience. As such, the contributions of our study are: (i) the training of robust segmentation models for glioblastomas, lower grade gliomas, meningiomas, and metastases assessed using a panel of more than 20 different metrics to better highlight performance, (ii) the development of two software solutions enabling easy and fully automatic use of the trained models and tumor features computation: Raidionics and Raidionics-Slicer, and (iii) open-access models and source code for the software and validation metrics computation.

2. DATA

For this study, four different datasets have been assembled, one for each main tumor type considered: glioblastoma, lower grade glioma, meningioma, and metastasis. The tumor type

TABLE 1 | Overview of the datasets gathered for the four brain tumor types considered.

Tumor type	Sequence type	# patients	# sources	Volume average (ml)	Volume range (ml)
Glioblastoma	T1c	2134	15	34.37 ± 28.83	[0.01, 243.39]
LGG	FLAIR	659	4	51.71 ± 78.60	[0.14, 478.83]
Meningioma	T1c	719	2	19.40 ± 28.62	[0.07, 209.38]
Metastasis	T1c	396	2	17.53 ± 17.97	[0.01, 114.77]

Only one MRI sequence is available for each patient, and T1c corresponds to Gd-enhanced T1-weighted MR scans.

was assessed at the time of surgery, when applicable, following the currently applicable guidelines (i.e., either (38) or (39)). Tumors were manually segmented in 3D by trained raters using as support either a region growing algorithm (40) or a grow cut algorithm (41, 42), and subsequent manual editing. Trained raters were supervised by neuroradiologists and neurosurgeons. On contrast-enhanced T1-weighted scans, the tumor was defined as gadolinium-enhancing tissue including non-enhancing enclosed necrosis or cysts. On FLAIR scans, the tumor was defined as the hyperintense region. The four datasets are introduced in-depth in the subsequent sections. An overall summary of the data available is reported in **Table 1**, and some visual examples are provided in **Figure 1**.

2.1. Glioblastomas

The glioblastoma dataset is made of a total of 2,134 Gd-enhanced T1-weighted MRI volumes originating from 14 different hospitals, and one public challenge.

The first 1,841 patients have been collected from 14 different hospitals worldwide: 38 patients from the Northwest Clinics, Alkmaar, Netherlands (ALK); 97 patients from the Amsterdam University Medical Centers, location VU medical center, Netherlands (AMS); 86 patients from the University Medical Center Groningen, Netherlands (GRO); 103 patients from the Medical Center Haaglanden, the Hague, Netherlands (HAG); 75 patients from the Humanitas Research Hospital, Milano, Italy (MIL); 74 patients from the Hôpital Lariboisière, Paris, France (PAR); 134 patients from the University of California San Francisco Medical Center, U.S. (SFR); 49 patients from the Medical Center Slotervaart, Amsterdam, Netherlands (SLO); 153 patients from the St Elisabeth Hospital, Tilburg, Netherlands (TIL); 171 patients from the University Medical Center Utrecht, Netherlands (UTR); 83 patients from the Medical University Vienna, Austria (VIE); 72 patients from the Isala hospital, Zwolle, Netherlands (ZWO); 456 patients from the St. Olavs Hospital, Trondheim University Hospital, Norway (STO); and 249 patients from the Sahlgrenska University Hospital, Gothenburg, Sweden. An in-depth description of most cohorts can be found in a recent study (13). The remaining 293 patients correspond to the training set of the BraTS challenge (edition 2020) but have already undergone preprocessing transformations such as skull-stripping.

Overall, MRI volume dimensions are covering $[159; 896] \times [86; 896] \times [17; 512]$ voxels, and the voxel size ranges $[0.26; 1.25] \times [0.26; 2.00] \times [0.47; 7.50]$ mm^3. An average MRI volume is $[303 \times 323 \times 193]$ pixels with a spacing of $[0.86 \times 0.84 \times 1.24]$ mm^3.

2.2. Lower Grade Gliomas

The lower grade glioma dataset is made of a total of 659 FLAIR MRI volumes, with mostly grade 2 diffuse gliomas, coming from four different hospitals: 330 patients from the Brigham and Women's Hospital, Boston, USA; 165 patients from the St. Olavs Hospital, Trondheim University Hospital, Norway; 154 patients from the Sahlgrenska University Hospital, Gothenburg, Sweden; and 10 from the University Hospital of North Norway, Norway.

Overall, MRI volume dimensions are covering $[192; 576] \times [240; 640] \times [16; 400]$ voxels, and the voxel size ranges $[0.34; 1.17] \times [0.34; 1.17] \times [0.50; 8.0]$ mm^3. An average MRI volume is $[349 \times 363 \times 85]$ pixels with a spacing of $[0.72 \times 0.72 \times 4.21]$ mm^3.

2.3. Meningiomas

The meningioma dataset is made of 719 Gd-enhanced T1-weighted MRI volumes, mostly built around a dataset previously introduced (43), showcasing patients either followed at the outpatient clinic or recommended for surgery at the St. Olavs Hospital, Trondheim University Hospital, Norway.

Overall, MRI volume dimensions are covering $[192; 512] \times [224; 512] \times [11; 290]$ voxels, and the voxel size ranges $[0.41; 1.05] \times [0.41; 1.05] \times [0.60; 7.00]$ mm^3. An average MRI volume is $[343 \times 350 \times 147]$ pixels with a spacing of $[0.78 \times 0.78 \times 1.67]$ mm^3.

2.4. Metastases

The metastasis dataset is made of a total of 396 Gd-enhanced T1-weighted MRI volumes, collected from two different hospitals: 329 patients from the St. Olavs Hospital, Trondheim University Hospital, Norway; and 67 patients from Oslo University Hospital, Oslo, Norway.

Overall, MRI volume dimensions are covering $[128; 560] \times [114; 560] \times [19; 561]$ voxels, and the voxel size ranges $[0.43; 1.33] \times [0.43; 1.80] \times [0.45; 7.0]$ mm^3. An average MRI volume is $[301 \times 370 \times 289]$ pixels with a spacing of $[0.85 \times 0.76 \times 1.08]$ mm^3.

3. METHODS

First, the process for automatic brain tumor segmentation including data preprocessing, neural network architecture, and training design is introduced in Section 3.1. Second, the tumor characteristics extraction process, using the generated tumor segmentation as input, is summarized in Section 3.2. Finally, a description of the two developed software solutions for performing segmentation and standardized reporting is given in Section 3.3.

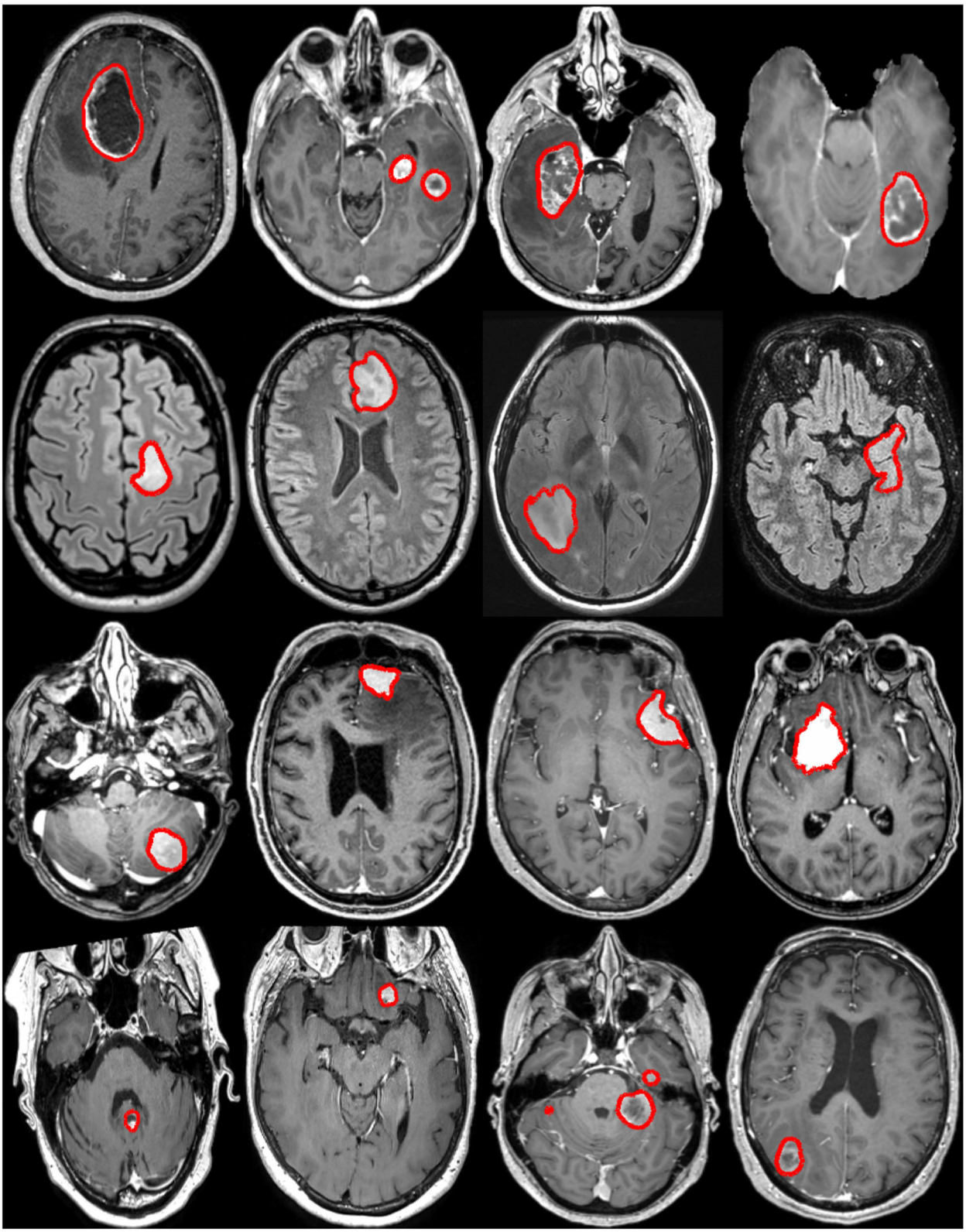

FIGURE 1 | Examples of brain tumors from the raw MRI volumes collected in this study. Each row illustrates a tumor type: glioblastoma, lower grade glioma, meningioma, and metastasis (from top to bottom). The manual annotation contours are overlaid in red.

TABLE 2 | Summary of the model training strategy followed for each tumor type.

Tumor type	Preprocessing	Strategy	Protocol
Glioblastoma	(ii) skull-stripping	(i) from-scratch	(i) leave-one-out
LGG	(i) tight clipping	(i) from-scratch	(ii) 5-fold
Meningioma	(i) tight clipping	(i) from-scratch	(ii) 5-fold
Metastasis	(ii) skull-stripping	(ii) transfer-learning	(ii) 5-fold

3.1. Tumor Segmentation

The architecture selected to train segmentation models for each brain tumor type is AGU-Net, which has shown to perform well on glioblastoma and meningioma segmentation (32, 44). In the following, the different training blocks are presented with some inner variations specified by roman numbers inside brackets. A global overview is provided in **Table 2** summarizing used variants.

Architecture: Single-stage approach leveraging multi-scale input and deep supervision to preserve details, coupled with a single attention module. The loss function used was the class-averaged Dice loss, excluding the background. The final architecture was as described in the original article with 5 levels and [16, 32, 128, 256, 256] as convolution blocks.

Preprocessing: The following preprocessing steps were used:

1. resampling to an isotropic spacing of $1\,\mathrm{mm}^3$ using spline interpolation of order 1 from NiBabel [1].
2. (i) tight clipping around the patient's head, excluding the void background, or (ii) skull-stripping using a custom brain segmentation model.
3. volume resizing to $128 \times 128 \times 144$ voxels using spline interpolation of order 1.
4. intensity normalization to the range $[0, 1]$.

Training strategy: Models were trained using the Adam optimizer over a batch size of 32 samples with accumulated gradients (actual batch size 2), stopped after 30 consecutive epochs without validation loss improvement, following either: (i) training from scratch with $1e^{-3}$ initial learning rate, or transfer learning with an initial learning rate of $1e^{-4}$ fine-tuning over the best glioblastoma model.

For the data augmentation strategy, the following transforms were applied to each input sample with a probability of 50%: horizontal and vertical flipping, random rotation in the range $[-20°, 20°]$, and translation up to 10% of the axis dimension.

Training protocol: Given the magnitude difference within our four datasets, two different protocols were considered: (i) a three-way split at the hospital level whereby MRI volumes from one hospital constituted the validation fold; MRI volumes from a second hospital constituted the test fold; and the remaining MRI volumes constituted the training fold. As such, each hospital was used in turn as the test set in order to properly assess the ability of the different models to generalize. Or (ii) a 5-fold cross-validation with a random two-way split over MRI volumes whereby four folds are used in turn as a training set and the remaining one as a validation set, without the existence of a proper separate test set.

[1]https://github.com/nipy/nibabel

3.2. Preoperative Clinical Reporting

For the generation of standardized preoperative clinical reports in a reproducible fashion, the computation of tumor characteristics was performed after alignment to a standard reference space. As described in-depth in our previous study (13), the reference space was constituted by the symmetric Montreal Neurological Institute ICBM2009a atlas (MNI) (45). The atlas space did not possess any brain average as FLAIR sequence, the T1 atlas file was used for all tumor types.

For each tumor type, the collection of features includes volume, laterality, multifocality, cortical structure location profile, and subcortical structure location profile. Specifically tailored for glioblastomas, resectability features are, therefore, not available for the other brain tumor types.

3.3. Proposed Software

In order to make our models and tumor features easily available to the community, we have developed two software solutions. The first one is a stand-alone software called Raidionics, and the second one is a plugin to 3D Slicer given its predominant and widespread use in the field (46). Both solutions provide access to a similar back-end including inference and processing code. However, the GUI and intended user interactions differ. The trained models are stored in a separate online location and are downloaded on the user's computer at runtime. Models can be improved over time and a change will be automatically detected, resulting in the replacement of outdated models to the user's machine. Raidionics can be seen as an improved solution to our initial GSI-RADS software, covering not only glioblastomas but all major brain tumor types, offering the option to compute a similar standardized report, and providing a refined graphical user interface enabling the user to visually assess the results.

3.3.1. Stand-Alone Solution: Raidionics

The software proposes two modes: (i) single-use where only one patient is to be processed and results can be visually assessed in the 2D viewer, and (ii) batch-mode whereby a collection of patients can be processed sequentially without any viewing possibility. In each mode, the option is left to the user to solely perform tumor segmentation or to compute the whole set of tumor characteristics and generate the standardized report. For each patient, the software expects an MRI scan as input (i.e., Gd-enhanced T1-weighted or FLAIR sequence) and the tumor type must be manually selected. Additionally, a pre-existing tumor segmentation mask can be provided to bypass the automatic segmentation, if collecting the tumor characteristics is the main interest and manual annotations have been performed beforehand. The total set of processed files saved on disk includes the standardized reports, brain and tumor segmentation masks in both patient and MNI space, cortical and subcortical structures masks in both patient and MNI space, and the registration files to navigate from patient to MNI space. To complement the reporting and give the possibility for follow-up statistical studies,

the complete set of computed features is also provided in comma separated value format (i.e., .csv).

The software has been developed in Python 3.6.9, using PySide2 v5.15.2 for the graphical user interface, and only uses the Central Processing Unit (CPU) for the various computations. The software has been tested and is compatible with Windows ($\geq$ 10), macOS ($\geq$ Catalina 10.15), and Ubuntu Linux ($\geq$ 18.04). An illustration of the software is provided in **Figure 2**. Cross-platform installers and source code are freely available at https://github.com/dbouget/Raidionics.

3.3.2. 3D Slicer Plugin: Raidionics-Slicer

The 3D Slicer plugin has been developed using the DeepInfer plugin as baseline (47) and is mostly intended for tumor segmentation purposes. Through a slider, the possibility is provided to manually alter the probability threshold cutoff in order to refine the proposed binary mask. Further manual editing can be performed thereafter using the existing 3D Slicer functionalities. The back-end processing code has been bundled into a Docker image for convenience, and therefore, administrator rights are required for the end-user to perform the installation locally. The same inputs, behavior, and outputs can be expected as for the stand-alone software.

The GitHub repository for the 3D Slicer plugin can be found at https://github.com/dbouget/Raidionics-Slicer, and an illustration is provided in **Figure 3**.

4. VALIDATION STUDIES

In the validation studies, only the automatic segmentation performances are assessed. The clinical validity and relevance of the extracted tumor features have been addressed thoroughly in a previous study (13). To better grasp the different aspects of the segmentation performance, a wider set of metrics is studied as described in Section 4.1. For the voxel-wise segmentation task, only two classes are considered as the whole tumor extent (including contrast-enhancing regions, cysts, and necrosis) is the target: non-tumor tissue or tumor tissue. In that sense, a positive voxel is a voxel exhibiting tumor tissue, whereas a negative voxel is a voxel exhibiting background or normal tissue.

4.1. Metrics

Following a review of metrics for evaluating 3D medical image segmentation (36), a broad spectrum of 25 metrics was selected, computed either voxel-wise or instance-wise,

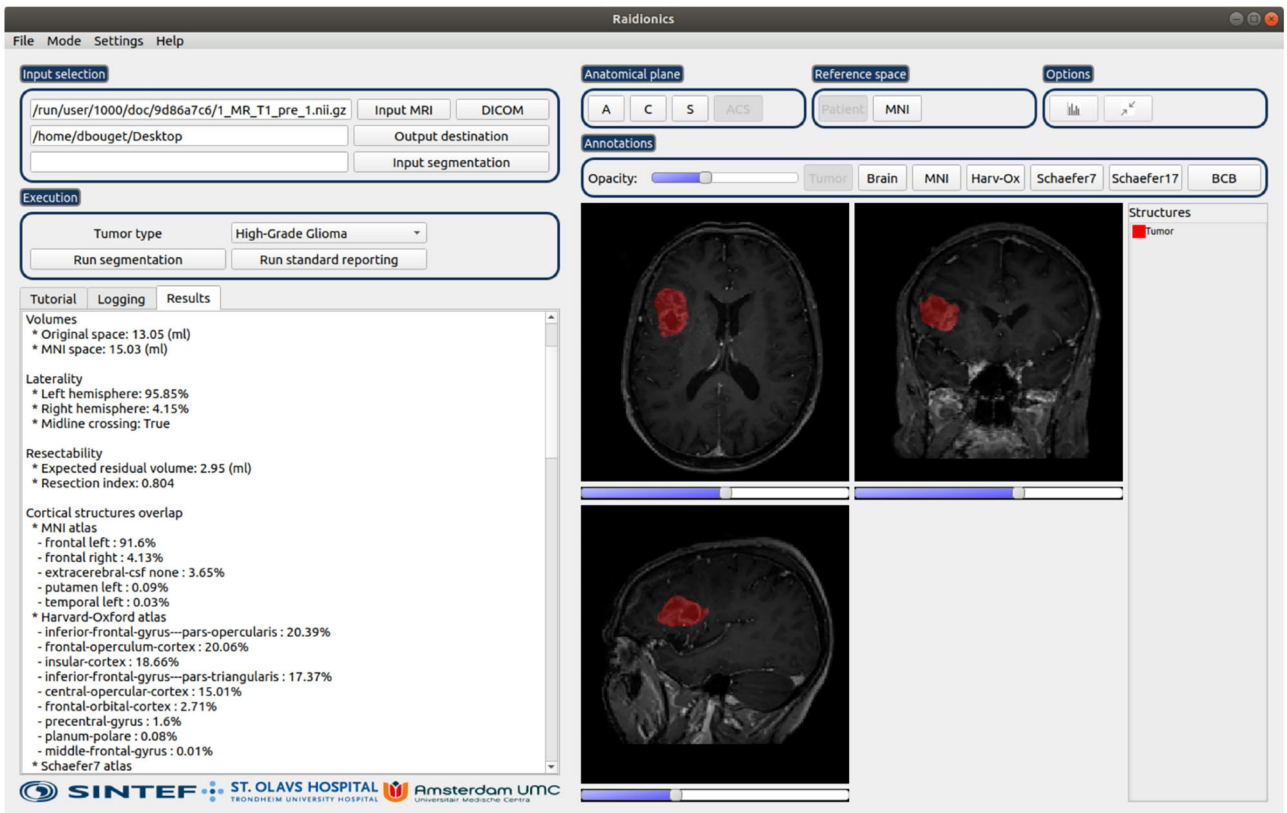

FIGURE 2 | Illustration of the Raidionics software after generating the standardized report for a patient suffering from glioblastoma. The left side presents the tumor characteristics belonging to the report, whereas the right side offers a simplistic view.

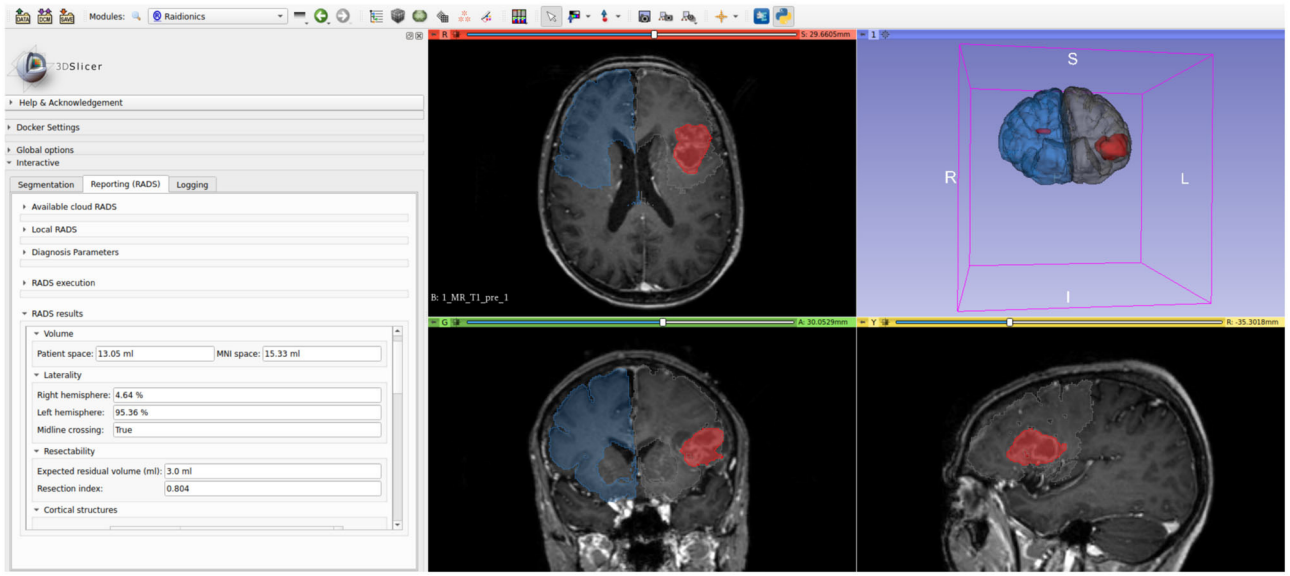

FIGURE 3 | Illustration of the Raidionics-Slicer plugin after generating the standardized report for a patient suffering from glioblastoma.

and grouped according to the following categories: overlap-based, volume-based, information theory-based, probabilistic, and spatial distance-based.

4.1.1. Voxel-Wise:

For quantifying semantic segmentation performance, we have selected the following metrics computed directly and indiscriminately over all voxels of a given patient MRI volume:

1. Overlap-based: (i) True Positive Rate (TPR), also called recall or sensitivity, is the probability that an actual positive voxel will test positive; (ii) True Negative Rate (TNR), also called specificity, is the probability that an actual negative voxel will test negative; (iii) False Positive Rate (FPR), is the probability that a false alarm will be raised (i.e., a negative voxel will test positive); (iv) False Negative Rate (FNR), also called missed rate, is the probability that a true positive voxel will test negative; (v) Positive Predictive Value (PPV), also referred to as precision, is the ratio of truly positive voxels over all voxels which tested positive; (vi) Dice score (Dice), also called the overlap index and gauging the similarity of two samples, is the most commonly used metric in validating medical volume segmentation (48); (vii) Dice True Positive score (Dice-TP) is similar to the Dice score but is only computed over the true positive predictions (i.e., when the model found the tumor); (viii) Intersection Over Union (IoU), also called the Jaccard index, measures the volume similarity as the size of the intersection divided by the size of the union of two samples (49); (ix) Global Consistency Error (GCE), defined as the error measure averaged over all voxels (50).
2. Volume-based: (i) Volumetric Similarity (VS), as the absolute volume difference divided by the sum of the compared volumes (51); (ii) Relative Absolute Volume Difference (RAVD), as the relative absolute volume difference between the joint binary objects in the two images. This is a percentage value in the range $[-1.0, \infty)$ for which a 0 denotes an ideal score.
3. Information theory-based: (i) Normalized Mutual Information (MI), normalization of the mutual information score to scale the results between 0 (no mutual information) and 1 (perfect correlation) (52); (ii) Variation Of Information (VOI), measuring the amount of information lost or gained when changing from one variable to the other, in this case, to compare clustering partitions (53).
4. Probabilistic: (i) Cohen's Kappa Score (CKS), measuring the agreement between two samples (54). The metric ranges between −1.0 and 1.0 whereby the maximum value means complete agreement, and zero or lower means chance agreement; (ii) Area Under the Curve (AUC), first presented as the measure of accuracy in the diagnostic radiology (55), further adjusted for the validation of machine learning algorithms; (iii) Volume Correlation (VC), as the linear correlation in binary object volume, measured through the Pearson product-moment correlation coefficient where the coefficient ranges $[-1., 1.]$; (iv) Matthews Correlation Coefficient (MCC), as a measure of the quality of binary and multiclass classifications, taking into account true and false positives and negatives and generally regarded as a balanced measure (56). The metric ranges between −1.0 and 1.0 whereby 1.0 represents a perfect prediction, 0.0 an average random prediction, and −1.0 an inverse prediction; (v) Probabilistic Distance (PBD), as a measure of the distance between fuzzy segmentation (57).
5. Spatial-distance-based: (i) 95th percentile Hausdorff distance (HD95), measuring the boundary delineation quality (i.e., contours). The 95% version is used to make measurements

more robust to small outliers (58); (ii) the Mahalanobis distance (MHD), measuring the correlation of all points and calculated according to the variant described for the validation of image segmentation (59); (iii) Average Symmetric Surface Distance (ASSD), as the average symmetric surface distance between the binary objects in two images.

4.1.2. Instance-Wise:

For quantifying instance detection performance, we chose the following metrics, reported in a patient-wise fashion (PW) or an object-wise fashion (OW). In the latter, and in case of multifocal tumors, each focus is considered as a separate tumor. The detection threshold has been set to 0.1% Dice to determine whether an automatic segmentation is eligible to be considered as a true detection or a false positive.

1. Overlap-based: (i) Recall, as the ratio in % of tumors properly identified; (ii) Precision, as the ratio in % of tumors incorrectly detected; (iii) F1-score (F1), measuring information retrieval as a trade-off between the recall and precision (60); (iv) False Positives Per Patient (FPPP), as the average number of incorrect detections per patient.
2. Probabilistic: (i) Adjusted Rand Index (ARI), as a similarity measure between two clusters by considering all pairs of samples and counting pairs that are assigned in the same or different clusters between the model prediction and the ground truth (61). The metric ranges from -1.0 to 1.0, whereby random segmentation has an ARI close to 0.0 and 1.0, stands for a perfect match.
3. Spatial-distance-based: (i) Object Average Symmetric Surface Distance (OASSD), as the average symmetric surface distance (ASSD) between the binary objects in two volumes.

4.2. Measurements

Pooled estimates, computed from each fold's results, are reported for each measurement (62). Overall, measurements are reported as mean and SD (indicated by $\pm$) in the tables.

Voxel-wise: For semantic segmentation performance, the Dice score is computed between the ground truth volume and a binary representation of the probability map generated by a trained model. The binary representation is computed for ten different equally-spaced probability thresholds (PT) in the range $[0, 1]$.

Instance-wise: For instance detection performance, a connected components approach coupled with a pairing strategy was employed to associate ground truth and detected tumor parts. A minimum size threshold of 50 voxels was set and objects below that limit were discarded. A detection was deemed true positive for any Dice score strictly higher than 0%.

4.3. Experiments

To validate the traied models, the following set of experiments was conducted:

1. **Overall performance study:** k-fold cross-validation studies for the different tumor types for assessing segmentation performance. For easy interpretation, only Dice scores together with patient-wise and object-wise recall, precision, and F1-score values are reported.
2. **Metrics analysis:** in-depth performance comparison using the additional metrics, and confusion matrix computation between the metrics to identify redundancy in their use.
3. **Representative models selection:** identification of one final segmentation model for each tumor type, which will be made available for use in our software solutions.
4. **Speed study:** computation of the pure inference speed and the total elapsed time required to generate predictions for a new patient, obtained with CPU support and reported in seconds. The operations required to prepare the data to be sent through the network, initialize the environment, load the trained model, and reconstruct the probability map in the referential space of the original volume are accounted for. The experiment was repeated ten consecutive times over the same MRI volume for each model, using a representative sample of each dataset in terms of dimension and spacing.

5. RESULTS

5.1. Implementation Details

Results were obtained using a computer with the following specifications: Intel Core Processor (Broadwell, no TSX, IBRS) CPU with 16 cores, 64GB of RAM, Tesla V100S (32GB) dedicated GPU and a regular hard-drive. Training and inference processes were implemented in Python 3.6 using TensorFlow v1.13.1, and the data augmentation was performed using the Imgaug Python library (63). The metrics were for the most part computed manually using the equations described in the **Supplementary Material**, or alternatively using the sklearn v0.24.2 (64) and medpy v0.4.0 (65) Python libraries. The source code used for computing the metrics and performing the validation studies is made publicly available at https://github.com/dbouget/validation_metrics_computation.

5.2. Overall Performance Study

An overall summary of brain tumor segmentation performance for all four tumor subtypes is presented in **Table 3**. Meningiomas and lower grade gliomas appear more difficult to segment given average Dice scores of 75%, compared to average Dice scores of 85% for glioblastomas and metastases. A similar trend, yet with a slightly smaller gap, can be noted for the Dice-TP scores ranging between 81 and 90% with a standard deviation of approximately 15%, indicating the quality and relative stability of the trained models. From a patient-wise perspective, those results demonstrate the difficulty of achieving good recall while keeping the precision steadily above 95%. Even though a direct comparison to the literature is impossible since different datasets have been used, obtained performance is on-par if not better than previously reported performances where Dice scores have been ranging from 75 to 85%.

Regarding the lower grade glioma tumor subtype, the diffuse nature of the tumors and less pronounced gradients over image intensities are possible explanations for the lower segmentation performance. For the meningioma category, the reason for the lower Dice-score and recall values can be attributed to the larger number of small tumors ($<$ 2 ml) compared to other subtypes. In addition, outliers have been identified in this dataset whereby a small extent of the tumors were either partly enhanced

TABLE 3 | Segmentation performance summary for each tumor type.

	Voxel-wise		Patient-wise			Object-wise		
Tumor type	**Dice**	**Dice-TP**	**F1-score**	**Recall**	**Precision**	**F1-score**	**Recall**	**Precision**
Glioblastoma	85.69 ± 16.97	87.36 ± 12.17	97.40 ± 01.01	98.08 ± 01.29	96.76 ± 01.43	89.61 ± 04.11	85.78 ± 07.95	94.19 ± 02.71
LGG	75.39 ± 25.95	81.24 ± 16.01	93.60 ± 01.74	92.86 ± 03.19	94.42 ± 01.07	81.58 ± 02.25	75.58 ± 02.41	88.70 ± 03.16
Meningioma	75.00 ± 30.52	84.81 ± 15.07	90.67 ± 01.42	88.46 ± 02.12	93.25 ± 04.76	83.85 ± 03.60	80.93 ± 04.34	87.77 ± 08.30
Metastasis	87.73 ± 18.94	90.02 ± 12.80	97.54 ± 00.76	97.46 ± 01.38	97.63 ± 00.77	88.71 ± 01.34	82.80 ± 02.38	95.60 ± 01.45

because of calcification, or non-enhancing due to intraosseous growth. For all tumor types, Dice-score distributions are reported against tumor volumes in **Figure 4** for 10 equally-sized bins. For meningiomas, four bins are necessary to group tumors with a volume of up to 4 ml while only one bin is necessary for the glioblastomas, indicating a volume distribution imbalance between the two types. The diamond-shaped points outside the boxes represent cases where the segmentation model did not perform well (cf. **Supplementary Figures S1–S4**).

While tumor volumes and outlier MR scans are reasons for the discrepancy in Dice and recall values across the board, precision is rather unaffected and more stable. The nature of the convolutional neural network architecture and training strategy used can explain those results. By leveraging volumes covering the full brain, global relationships can be learned by the trained model hence reducing the confusion between tumor regions and other contrast-enhancing structures such as blood vessels. Given GPU memory limitation, the preprocessed MR scans have undergone significant downsampling, and as such small tumors are reduced to very few voxels, impacting mainly recall performance.

Finally, an average decrease of $\sim$ 10% can be noticed between patient-wise and object-wise detection metrics, whereby satellite tumors are on average an order of magnitude smaller than the main tumor, and are hence more prone to be omitted or poorly segmented by our models. Segmentation performance is illustrated in **Figure 5**. Each row corresponds to one tumor type and each column depicts a different patient.

5.3. Metrics Analysis

Side-by-side voxel-wise performances regarding the overlap-based metrics are reported in **Tables 4**, **5**. Unsurprisingly, given the good precision performance and the absence of patients without a tumor, both TNR and its opposite FPR scores are almost perfect for all tumor types. Similarly, the TPR and its opposite FNR metrics are scoring similarly to Dice. Within each tumor category, the overlap-based metrics are following the same trend whereby a higher average Dice score would correlate with a higher score for any other metrics and vice versa (e.g., IoU). An exception can be made regarding the behavior of the GCE metric, scoring on average higher for glioblastomas than for meningiomas and as such not following the same pattern as Dice. Upon careful visual inspection, the GCE metric seems to be extremely sensitive to outliers, either coming from the image quality or manual ground truth correctness (cf. top row in **Supplementary Figures S1–S4**). Given the non-normalized state of the GCE metric, and its absence of any upper bound, an extremely poor agreement between manual ground truth and automatic segmentation will result in score orders of magnitude higher than its average expression over a given dataset. Regarding the two volume-based metrics, featured rightmost in the second table, an antagonistic pattern toward Dice can be observed. The VS metric has the same cross-type trend as Dice with similar yet slightly greater scores. On the other hand, while the RAVD metric scores best over the metastasis group similar to Dice, its worst average value is obtained for the glioblastoma group, hence potentially exhibiting the same frailty toward outliers as for the GCE metric.

Next off, voxel-wise performance for information theory-based and probabilistic metrics are regrouped in **Table 6**. The MI and VOI metrics, both based on information theory, are exhibiting an inverse behavior in line with observations about the relationship between Dice and GCE metrics. The normalized mutual information metric ranges from 0.668 to 0.829 for Dice scores between 75 and 87%, showcasing stability but also correlation. On the contrary, the VOI metric expresses a behavior concurrent to GCE whereby the worst performance is obtained for the lower grade gliomas and then glioblastomas categories, while it performs best over metastases where Dice also scores the highest. Alike the aforementioned metric groups exhibiting inner discrepancies, three of the five probabilistic metrics follow a similar trend scoring high alongside Dice, with an average gap of 0.1 corresponding to a $\sim$ 10% Dice score difference. Meanwhile, the PBD metric has a behavior of its own scoring order of magnitude worse for the meningioma category than for the three other subtypes. The metric is not normalized and an extremely poor agreement between the manual ground truth and automatic segmentation would result in an extremely large score, similar to the GCE metric, hence reporting the median score, in addition, might be of interest (cf. second row in **Supplementary Figures S1–S4**).

Finally, the voxel-wise distance-based metrics are reported in **Table 7**. Similar cross-type trends can also be noted whereby the best HD95 of 4.97 mm is obtained for the glioblastoma category and the worst HD95 of 10 mm for meningiomas, heavily correlated to Dice performance. Our average HD95 results appear lower than previously reported results in the literature, however, a strong statement can hardly be made as the tumors featured can vary highly in terms of volume and number of satellites which might reflect greatly on metrics' average scores.

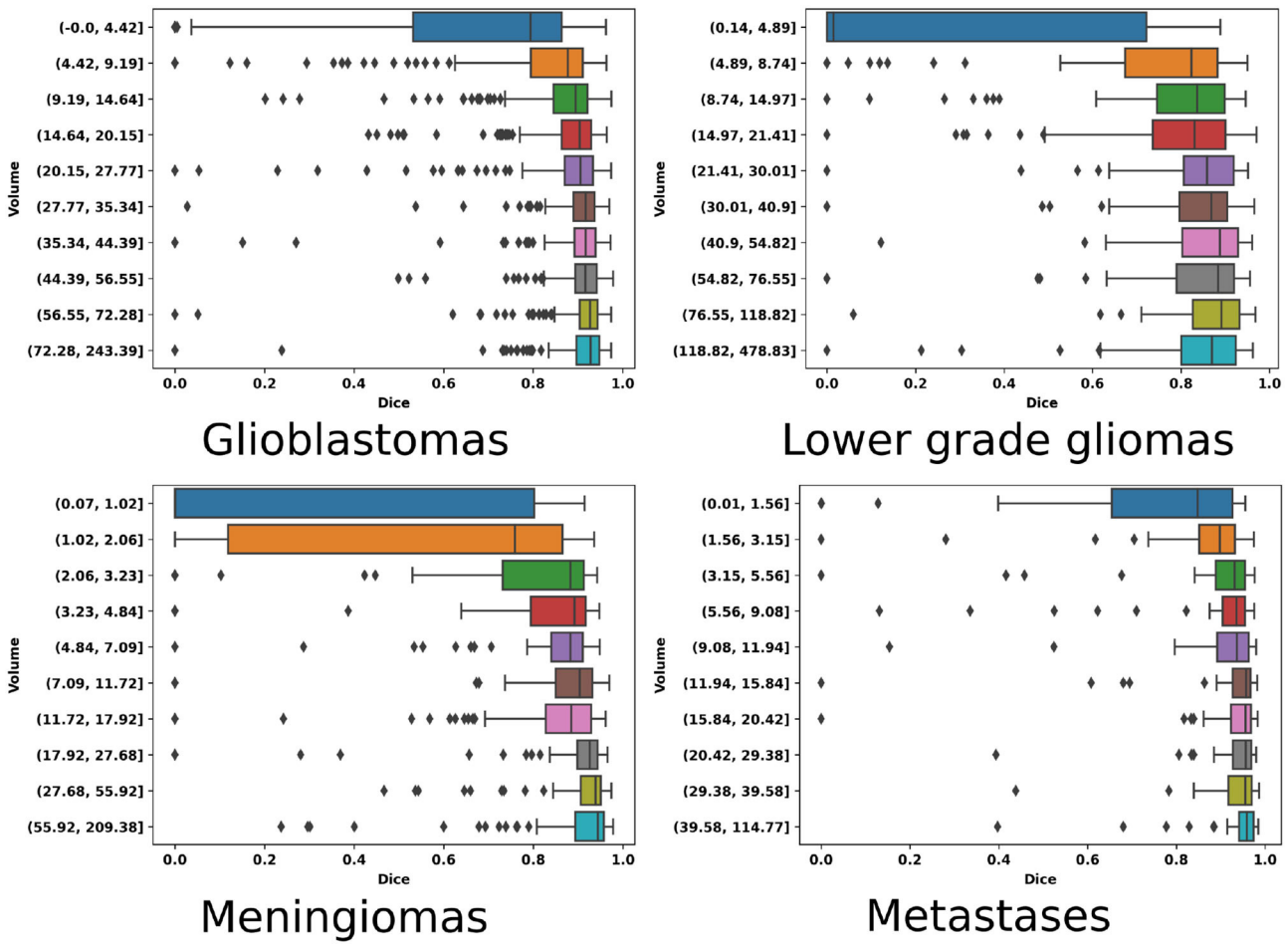

FIGURE 4 | Volume-wise (equally binned) Dice performance as boxplots for each of the four tumor types.

The other two spatial distance-based metrics display similar behavior to HD95, whereby tumor types can be ranked as follows based on best to worse performance: glioblastoma, metastasis, lower grade glioma, and meningioma.

Regarding instance-wise metrics, grouped in **Table 8**, the close OASSD average values between glioblastomas and meningiomas represent the most surprising outcome given the 5% difference in F1-score. Unsurprisingly, the lower grade glioma category achieves the highest average OASSD with 2.6 mm together with the lowest F1-score. As one might expect, the amount of FPPP correlates greatly with the average precision values obtained. Ultimately, the ARI metric generates scores extremely similar to voxel-wise Dice and correlates highly with the F1-score whereby the glioblastoma and metastasis categories obtain almost 0.1 more than for the meningioma and lower grade glioma subtypes.

For completeness, the correlation between the different metrics computed in this study has been assessed, and the results over the glioblastoma category are shown in **Table 9** (cf. other correlation matrices in **Supplementary Tables S2, S4, S6, S8**). Some metrics have been excluded given inherent correlation from their computation, such as FPR and FNR being the opposite of TNR and TPR. Similarly, metrics having computation in a voxel-wise, patient-wise, or instance-wise fashion were not considered in the matrix (i.e., recall, precision, and F1-score). Overall, the conclusions identified by analyzing the raw average results are further confirmed whereby a majority of voxel-wise metrics correlate with one another and thus do not bring any additional information to Dice. However, relevant insight can be obtained from the RAVD and GCE/VOI metrics given their low correlation to Dice and their higher sensitivity toward outliers, enabling to quantify the ability to generalize the model or potentially the quality of the data and manual ground truth (cf. third row in **Supplementary Figures S1–S4**). The correlation between HD95 and MHD appears also quite low for spatial distance-based metrics, indicating potential usefulness. Finally, in the instance-wise category, the OASSD is a stand-alone metric offering to properly assess model performance over the detection of satellite tumors. To conclude, a final pool of metrics to consider for benchmarking purposes and capturing all aspects of the segmentation performances are Dice, RAVD, VOI, HD95, MHD, and OASSD. Given the task, reporting patient-wise and

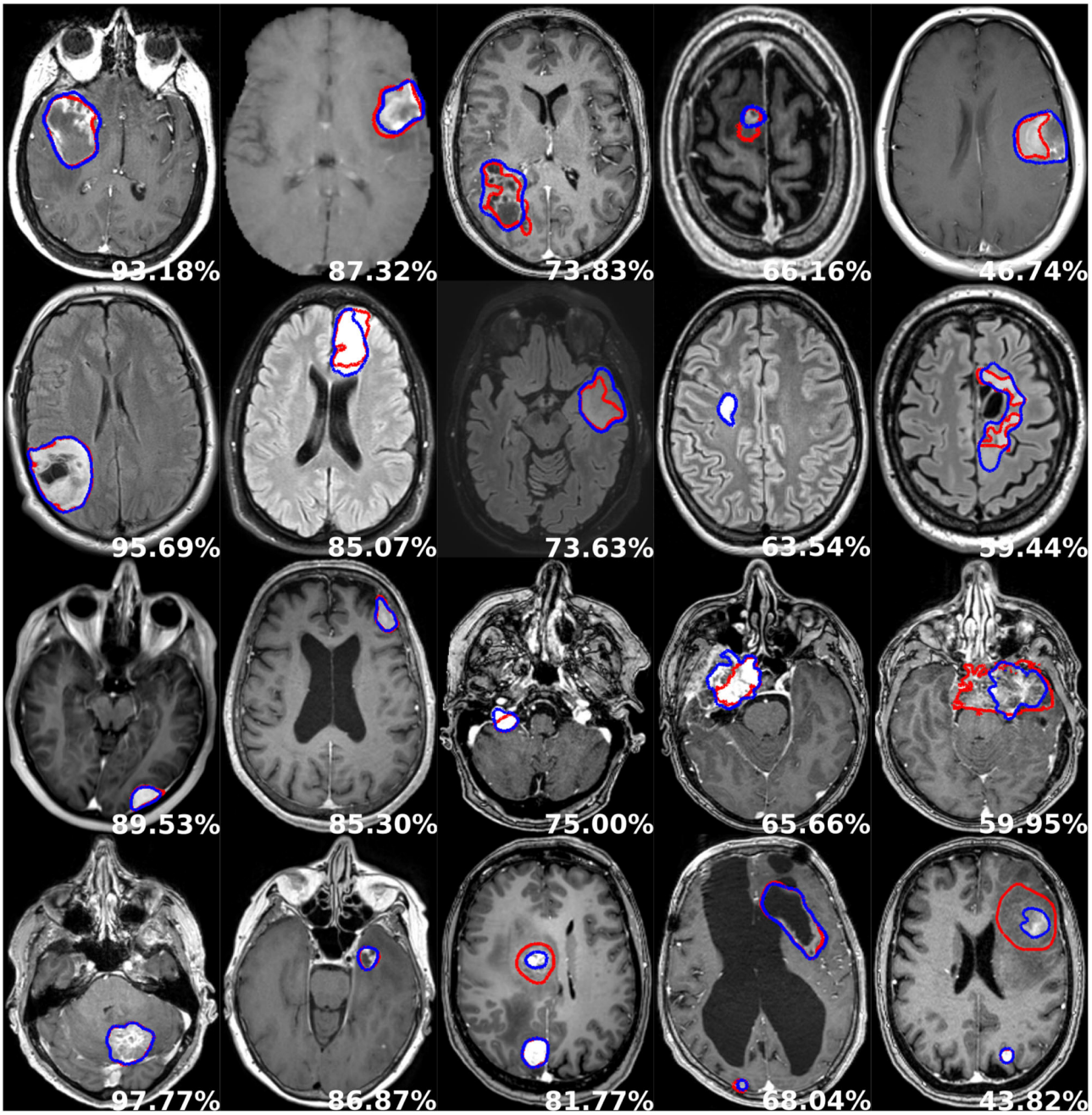

FIGURE 5 | Examples of segmentation performances. One row illustrates one tumor type: glioblastoma, lower grade glioma, meningioma, metastasis (from top to bottom), and each column depicts a different patient. The manual delineation is shown in red, the automatic segmentation in blue, and the patient-wise Dice score in white.

instance-wise recall, precision, and F1-score is always of interest because of an innate comprehension of their meaning, easy to interpret for clinicians or other end-users.

5.4. Representative Models Selection

Only one model can be provided in the software solutions for each tumor type, and the best model selection was done empirically according to the following criterion: the size of the validation or test set, average Dice score, and patient-wise F1-score performances. The exhaustive list of chosen models is the following: the model trained for fold 0 was selected for the glioblastomas, the model trained for fold 3 was selected for the lower grade gliomas, for the meningiomas the model trained for fold 2 was selected,

TABLE 4 | Voxel-wise overlap-based metrics performance summary for each tumor type.

Tumor type	TPR	TNR	FPR	FNR	PPV
Glioblastoma	87.88 ± 17.64	99.96 ± 00.06	00.04 ± 00.06	12.12 ± 17.64	87.35 ± 13.29
LGG	77.91 ± 27.89	99.90 ± 00.16	00.09 ± 00.16	22.08 ± 27.89	82.16 ± 17.01
Meningioma	77.44 ± 32.48	99.97 ± 00.04	00.02 ± 00.04	22.56 ± 32.48	84.77 ± 15.69
Metastasis	88.45 ± 20.82	99.98 ± 00.03	00.01 ± 00.03	11.54 ± 20.82	89.43 ± 16.78

TABLE 5 | Voxel-wise performance summary for each tumor type for overlap-based and volume-based metrics.

	Overlap-based				Volume-based	
Tumor type	Dice	Dice-TP	IoU	GCE (1e4)	VS	RAVD
Glioblastoma	85.69 ± 16.97	87.36 ± 12.17	77.59 ± 17.99	12.34 ± 12.57	90.43 ± 16.94	13.98 ± 171.2
LGG	75.39 ± 25.95	81.24 ± 16.01	65.72 ± 25.32	34.15 ± 46.34	82.20 ± 26.44	07.88 ± 60.14
Meningioma	75.00 ± 30.52	84.81 ± 15.07	67.13 ± 29.39	09.04 ± 17.53	80.21 ± 31.08	07.87 ± 61.31
Metastasis	87.73 ± 18.94	90.02 ± 12.80	81.56 ± 20.42	04.55 ± 07.62	91.37 ± 18.61	02.11 ± 55.35

TABLE 6 | Voxel-wise performance summary for each tumor type for information theory-based and probabilistic metrics.

	Information theory-based		Probabilistic				
Tumor type	MI	VOI	CKS	AUC	VC	MCC	PBD
Glioblastoma	0.787 ± 0.168	0.011 ± 0.009	0.856 ± 0.169	0.939 ± 0.088	0.978 ± 0.089	0.875 ± 0.122	0.840 ± 24.02
LGG	0.668 ± 0.246	0.026 ± 0.030	0.753 ± 0.259	0.889 ± 0.139	0.961 ± 0.119	0.812 ± 0.167	0.573 ± 04.82
Meningioma	0.691 ± 0.291	0.008 ± 0.013	0.749 ± 0.305	0.887 ± 0.162	0.954 ± 0.149	0.841 ± 0.171	5.358 ± 103.4
Metastasis	0.829 ± 0.191	0.004 ± 0.006	0.877 ± 0.189	0.942 ± 0.104	0.978 ± 0.100	0.901 ± 0.127	0.152 ± 0.623

TABLE 7 | Voxel-wise performance summary for each tumor type for spatial distance-based metrics.

Tumor type	HD95	MHD	ASSD
Glioblastoma	04.97 ± 09.06	00.41 ± 03.69	01.46 ± 03.22
LGG	08.37 ± 13.31	00.53 ± 03.27	02.19 ± 05.06
Meningioma	10.11 ± 21.82	00.72 ± 03.57	02.77 ± 07.91
Metastasis	07.54 ± 20.61	00.54 ± 04.56	01.73 ± 05.89

and finally for the metastases the model trained for fold 2 was selected.

5.5. Speed Study

A comparison in processing speed regarding pure tumor segmentation and complete generation of standardized reports is provided in **Table 10** when using the Raidionics software with CPU support. The high-end computer is the computer used for training the models, whereas the mid-end computer is a Windows laptop with an Intel Core Processor (*i7*@1.9GHz), and 16GB of RAM.

For the smallest MRI volumes on average, 17 s are needed to perform tumor segmentation whereas 4.5 min are required to generate the complete standardized report with the high-end computer. Unsurprisingly, the larger the MRI volume the more time required to perform the different processing operations (cf. **Supplementary Section S3**). For the largest MRI volumes overall, 54 s are needed to perform tumor segmentation whereas 15.1 min are required to generate the complete standardized report. When using the mid-end laptop, overall runtime is increased by 1.5 times for the different MRI volume sizes. On average, 9 min are necessary to generate the standardized report for MRI volumes of reasonable quality.

6. DISCUSSION

In this study, we have investigated the segmentation of a range of common main brain tumor types in 3D preoperative MR scans using a variant of the Attention U-Net architecture. We have conducted experiments to assess the performances of each trained model using close to 30 metrics and developed two software solutions for end-users to freely benefit from our segmentation models and standardized clinical reports. The main contributions are the high performances of the models, on-par with performances reported in the literature for the glioblastomas, with illustrated robustness and ability to generalize due to the multiple and widespread data sources. In addition, the two proposed open-access and open-source software solutions include our best models, together with a RADS for computing tumor characteristics. This is the first open RADS solution that supports all major brain tumor types. The software is user-friendly, requiring only a few clicks and no

TABLE 8 | Instance-wise performance for each tumor type.

Tumor type	F1-score	Recall	Precision	FPPP	ARI	OASSD
Glioblastoma	89.61 ± 04.11	85.78 ± 07.95	94.19 ± 02.71	0.078 ± 0.037	0.856 ± 0.169	01.45 ± 02.82
LGG	81.58 ± 02.25	75.57 ± 02.40	88.67 ± 03.16	0.129 ± 0.041	0.751 ± 0.259	02.60 ± 06.10
Meningioma	83.85 ± 03.60	80.93 ± 04.34	87.77 ± 08.30	0.151 ± 0.128	0.749 ± 0.305	01.62 ± 04.09
Metastasis	88.71 ± 01.34	82.79 ± 02.38	95.60 ± 01.45	0.061 ± 0.020	0.877 ± 0.189	0.672 ± 0.869

TABLE 9 | Metrics correlation matrix for glioblastoma segmentation.

	Overlap						Volume		Information theory		Probabilistic					Spatial distance			Instance-wise	
	Dice	TPR	TNR	PPV	IoU	GCE	VS	RAVD	MI	VOI	CKS	AUC	VC	MCC	PBD	HD95	MHD	ASSD	ARI	OASSD
Dice	1.0	0.7	0.29	0.62	0.98	-0.22	0.94	-0.35	0.99	-0.23	1.0	0.71	0.78	1.0	-0.34	-0.55	-0.43	-0.71	1.0	-0.3
TPR	0.7	1.0	-0.17	-0.07	0.71	-0.08	0.62	0.1	0.7	-0.08	0.7	1.0	0.51	0.71	-0.26	-0.38	-0.34	-0.47	0.7	-0.2
TNR	0.29	-0.17	1.0	0.58	0.28	-0.76	0.29	-0.36	0.33	-0.76	0.29	-0.17	0.23	0.29	-0.04	-0.16	-0.04	-0.27	0.29	-0.22
PPV	0.62	-0.07	0.58	1.0	0.64	-0.24	0.55	-0.49	0.64	-0.25	0.62	-0.07	0.47	0.63	-0.16	-0.38	-0.21	-0.47	0.62	-0.22
IoU	0.98	0.71	0.28	0.64	1.0	-0.24	0.9	-0.29	0.99	-0.24	0.98	0.71	0.71	0.99	-0.28	-0.55	-0.37	-0.7	0.98	-0.31
GCE	-0.22	-0.08	-0.76	-0.24	-0.24	1.0	-0.19	0.13	-0.3	1.0	-0.23	-0.09	-0.14	-0.23	0.02	0.18	0.03	0.29	-0.23	0.28
VS	0.94	0.62	0.29	0.55	0.9	-0.19	1.0	-0.37	0.9	-0.2	0.94	0.62	0.76	0.92	-0.36	-0.48	-0.43	-0.65	0.94	-0.26
RAVD	-0.35	0.1	-0.36	-0.49	-0.29	0.13	-0.37	1.0	-0.31	0.15	-0.35	0.1	-0.39	-0.34	0.18	0.19	0.14	0.28	-0.35	0.15
MI	0.99	0.7	0.33	0.64	0.99	-0.3	0.9	-0.31	1.0	-0.31	0.99	0.7	0.74	0.99	-0.31	-0.56	-0.4	-0.71	0.99	-0.32
VOI	-0.23	-0.08	-0.76	-0.25	-0.24	1.0	-0.2	0.15	-0.31	1.0	-0.23	-0.08	-0.15	-0.24	0.03	0.18	0.03	0.3	-0.24	0.28
CKS	1.0	0.7	0.29	0.62	0.98	-0.23	0.94	-0.35	0.99	-0.23	1.0	0.71	0.78	1.0	-0.34	-0.55	-0.43	-0.71	1.0	-0.3
AUC	0.71	1.0	-0.17	-0.07	0.71	-0.09	0.62	0.1	0.7	-0.08	0.71	1.0	0.51	0.71	-0.27	-0.38	-0.34	-0.47	0.71	-0.2
VC	0.78	0.51	0.23	0.47	0.71	-0.14	0.76	-0.39	0.74	-0.15	0.78	0.51	1.0	0.78	-0.49	-0.51	-0.58	-0.71	0.78	-0.22
MCC	1.0	0.71	0.29	0.63	0.99	-0.23	0.92	-0.34	0.99	-0.24	1.0	0.71	0.78	1.0	-0.36	-0.55	-0.44	-0.71	1.0	-0.31
PBD	-0.34	-0.26	-0.04	-0.16	-0.28	0.02	-0.36	0.18	-0.31	0.03	-0.34	-0.27	-0.49	-0.36	1.0	0.16	0.97	0.29	-0.34	0.05
HD95	-0.55	-0.38	-0.16	-0.38	-0.55	0.18	-0.48	0.19	-0.56	0.18	-0.55	-0.38	-0.51	-0.55	0.16	1.0	0.25	0.89	-0.55	0.14
MHD	-0.43	-0.34	-0.04	-0.21	-0.37	0.03	-0.43	0.14	-0.4	0.03	-0.43	-0.34	-0.58	-0.44	0.97	0.25	1.0	0.4	-0.43	0.06
ASSD	-0.71	-0.47	-0.27	-0.47	-0.7	0.29	-0.65	0.28	-0.71	0.3	-0.71	-0.47	-0.71	-0.71	0.29	0.89	0.4	1.0	-0.71	0.2
ARI	1.0	0.7	0.29	0.62	0.98	-0.23	0.94	-0.35	0.99	-0.24	1.0	0.71	0.78	1.0	-0.34	-0.55	-0.43	-0.71	1.0	-0.3
OASSD	-0.3	-0.2	-0.22	-0.22	-0.31	0.28	-0.26	0.15	-0.32	0.28	-0.3	-0.2	-0.22	-0.31	0.05	0.14	0.06	0.2	-0.3	1.0

The color intensity of each cell represents the strength of the correlation, where blue denotes direct correlation and red denotes inverse correlation.

TABLE 10 | Segmentation (Segm.) and standardized reporting (SR) execution speeds for each tumor subtype, using our Raidionics software.

		High-end computer (Desktop)		Mid-end computer (Laptop)	
	Dimensions (voxels)	Segm. (s)	SR (m)	Segm. (s)	SR (m)
LGG	394 × 394 × 80	16.69 ± 0.426	04.50 ± 0.09	28.69 ± 0.577	07.32 ± 0.07
Meningioma	256 × 256 × 170	17.21 ± 0.425	05.48 ± 0.12	31.41 ± 0.862	09.09 ± 0.32
Glioblastoma	320 × 320 × 220	21.99 ± 0.177	05.89 ± 0.03	33.65 ± 1.429	09.06 ± 0.24
Metastasis	560 × 560 × 561	59.06 ± 1.454	15.35 ± 0.41	98.54 ± 2.171	24.06 ± 0.93

programming to use, making it easily accessible for clinicians. The overall limitations are those already known for deep learning approaches whereby a higher amount of patients or data sources would improve the ability to generalize, boost segmentation performances, and increase the immunity toward rare tumor expressions. The employed architecture also struggles with smaller tumors given the large downsampling to feed the entire 3D MR scan in the network, hence the need for a better design combining local and global features either through multiple steps or ensembling.

The architecture and training strategy used in this study were identical to our previously published work considering that the intent was not to directly make advances on the segmentation task. Nevertheless, the stability and robustness

to train efficient models had been documented, alongside performance comparison to another well-known architecture [e.g., nnU-Net (20)], thus not precluding its use to train models for other brain tumor types. Aside from evident outliers in the datasets, where either tumors with partial or missing contrast uptake or suboptimal manual annotations were identified, the major pitfall of using the AGU-Net architecture lies in its struggle to segment equally satisfactorily small tumor pieces with a volume below 2 ml. Overall, the glioblastoma model is expected to be the most robust and able to generalize since patient data from 15 different sources were used. For other models trained on data from much fewer hospitals, with an expected limited variability in MR scan quality, their robustness is likely to be inferior. While larger datasets are often correlated with improved segmentation performance, the metastasis model is the best performing with the lowest amount of patients included. The relative easiness of the task from a clear demarcation of the tumor from surrounding normal tissue in contrast-enhanced T1-weighted volumes, and the potentially low variance in tumor characteristics with patient data coming from two hospitals only, can explain the results. Additionally, the metastasis model has been trained by transfer-learning using as input the second best performing glioblastoma model where the most data was used, which may have been the compelling factor. Lower-grade gliomas represent the most difficult type to manually segment since tumors are diffuse and infiltrating with an average volume in FLAIR sequences a lot higher than in T1 sequences for the other tumor types, and as such overall worse performances were expected.

The in-depth assessment of a larger pool of metrics allowed us to identify redundancy and uniqueness and proved that the Dice score is overall quite robust and indicative of expected performance. However, the sole use of the Dice score cannot cover all aspects of model performance, and spatial distance-based metrics (e.g., HD95 and MHD) are suggested to be used in conjunction as providing values uncorrelated to Dice. In addition, some metrics were identified to be more sensitive to outliers and are as such powerful to either assess the ability to generalize a model across data acquired on different scanners from multiple sources or quickly identify potential issues in a large body of data. Finally, and depending on the nature of the patients included in one's study and the number of satellite tumors, specific object-wise metrics are imperative to use (e.g., OASSD). Only a combination of various metrics computed either voxel-wise, patient-wise, or instance-wise can give the full picture of a model's performance. Unfortunately, interpreting and comparing sets of metrics can prove challenging, and as such further investigations regarding their merging into a unique informative and coherent score are fundamental [e.g., Roza (66)]. Furthermore, an inadequacy lies in the nature of the different metrics whereby some can be computed across all segmentations generated by a trained model, whereas others are exclusively eligible on true positive cases, i.e., when the model has correctly segmented to some extent of the tumor. For models generating perfect patient-wise recall, all metrics will be eligible for every segmentation. However, in this field of research and as of today, no trained model can fulfill this requirement due to the substantially large inter-patient variability. Ideally, the identification of relevant metrics, bringing unique information for interpreting the results, should not be confined to the validation studies. More metrics should be considered to be a part of the loss function computation during the training of neural network architectures. Attempts have been made toward using the Hausdorff distance as a loss function, but a direct minimization is challenging from an optimization viewpoint. For example, approximation of Hausdorff distance based on distance transforms, on morphological operations, or with circular and spherical kernels showed potential for medical image segmentation (67). In general, a careful mix between losses (e.g., Dice, cross-entropy, and HD95) is challenging to achieve and adaptive strategies might be required to avoid reaching a local minimum where overall segmentation performance may suffer (68).

As a current trend in the community, inference code and trained segmentation models are often at best available on GitHub repositories. As a consequence, only engineers, or people with some extent of knowledge in machine learning and programming, can benefit from such research advances. Besides, the research focus is heavily angled toward gliomas, due to the BraTS challenge influence, whereby segmentation models are expected to yield superior performance than for meningiomas and metastases. By developing and giving free and unrestricted access to our two proposed software solutions, we hope to facilitate more research on all brain tumor types. Willing research institutes have the opportunity to generate private annotated datasets at a faster pace than through fully manual labor by exploiting our trained models. Having made all source code available on GitHub, as customarily done, we made the effort to further make stand-alone solutions with easy-to-use GUIs. Hopefully, clinicians and other non-programming end-users should feel more comfortable manipulating such tools, available across the three major operating systems and necessitating only a computer with average hardware specifications. For the generation of standardized clinical reports, the computation of tumor characteristics relies heavily on the quality of the automatic segmentation, occasional mishaps are expected as models are not perfect and can omit the tumor. Therefore, manual inputs will be required sporadically to correct the tumor segmentation. Over time, new and better models will be generated and made available seamlessly into the two software through regular updates. For the time being, support for AGU-Net models only is provided due to its lighter codebase compared to nnU-Net, for similar overall performances. From a software bundling and deployment perspective, integrating a heavier inference framework and mixing backend engines (i.e., TensorFlow and Torch) will make it more challenging to create stable executables for Raidionics on Mac, Windows, and Ubuntu. Support for other architectures will be considered if new models clearly outperform the current models.

In the future, an approach incorporating a set of metrics and converting them into one final score would be highly

desirable (e.g., Roza). Not only would it help to automatically select the best model from a k-fold validation study from one unique score, but a proper assessment and ranking across multiple methods would be enabled. With all preoperative brain tumor types available for segmentation and reporting in our software, a key missing component is the automatic tumor type classification to supplement manual user input. Concurrently, the variety and amount of tumor characteristics to compute should be extended, considering more type-specific features similar to the resection index for glioblastomas. Alternatively, bringing a similar focus on post-operative segmentation of residual tumors is of great interest to both assess the quality of the surgery and refine the estimated patient outcome. The generation of a complete post-operative standardized clinical report would also be permitted with new features such as the extent of resection. Otherwise, intensifying the gathering of patient data from more widespread hospital centers and a larger array of MRI scanners is always of importance. The inclusion of more than one MR sequence per patient as segmentation input has the potential to boost overall performance, but at the same time might reduce models' potency as not always routinely available across all centers worldwide.

7. CONCLUSION

Efficient and robust segmentation models have been trained on pre-operative MR scans for the four main brain tumor types: glioblastoma, lower grade glioma, meningioma, and metastasis. In-depth performance assessment allowed to identify the most relevant metrics from a large panel, computed either voxel-wise, patient-wise, or instance-wise. Trained models and standardized reporting have been made publicly available and packaged into a stand-alone software and a 3D Slicer plugin to enable effortless widespread use.

DATA AVAILABILITY STATEMENT

The datasets presented in this article are not readily available because access to them is restricted under strict General Data Protection Regulation (GDPR) regulations. Requests to access the datasets should be directed to DB, david.bouget@sintef.no.

ETHICS STATEMENT

Ethical review and approval was not required for the study on human participants in accordance with the local legislation and institutional requirements. The patients/participants provided their written informed consent to participate in this study.

AUTHOR CONTRIBUTIONS

IR, OS, PD, KE, and AJ: funding acquisition. AJ, KE, VK, IK, DB, HA, FB, LB, MB, MC, JF, SH-J, AI, BK, AK, EM, DM, PR, MR, TS, WV, MWa, GW, OS, and PD: data curation. DB, AP, IR, OS, and PD: conceptualization. DB: methodology and visualization. DB and AP: software and validation. IR, OS, and PD: supervision and project administration. DB, AP, IR, OS, AJ, KE, and PD: writing—original draft. HA, FB, LB, MB, MC, JF, SH-J, AI, BK, AK, EM, DM, PR, MR, TS, WV, MWa, GW, MWi, and AZ: writing—review and editing. All authors have read and agreed to the published version of the manuscript.

FUNDING

This study was funded by the Norwegian National Advisory Unit for Ultrasound and Image-Guided Therapy (usigt.org); South-Eastern Norway Regional Health Authority; Contract Grant Nos. 2016102 and 2013069; Contract grant sponsor: Research Council of Norway; Contract Grant No. 261984; Contract grant sponsor: Norwegian Cancer Society; Contract Grant Nos. 6817564 and 3434180; Contract grant sponsor: European Research Council under the European Union's Horizon 2020 Program; Contract Grant No. 758657-ImPRESS; an unrestricted grant of Stichting Hanarth fonds, Machine learning for better neurosurgical decisions in patients with glioblastoma; a grant for public-private partnerships (Amsterdam UMC PPP-grant) sponsored by the Dutch government (Ministry of Economic Affairs) through the Rijksdienst voor Ondernemend Nederland (RVO) and Topsector Life Sciences and Health (LSH), Picturing predictions for patients with brain tumors; a grant from the Innovative Medical Devices Initiative program, project number 10-10400-96-14003; The Netherlands Organisation for Scientific Research (NWO), 2020.027; a grant from the Dutch Cancer Society, VU2014-7113; the Anita Veldman foundation, CCA2018-2-17. The funders were not involved in the study design, collection, analysis, interpretation of data, the writing of this article or the decision to submit it for publication.

ACKNOWLEDGMENTS

Data were processed in digital labs at HUNT Cloud, Norwegian University of Science and Technology, Trondheim, Norway.

SUPPLEMENTARY MATERIAL

The Supplementary Material for this article can be found online at: https://www.frontiersin.org/articles/10.3389/fneur.2022.932219/full#supplementary-material

REFERENCES

1. Day J, Gillespie DC, Rooney AG, Bulbeck HJ, Zienius K, Boele F, et al. Neurocognitive deficits and neurocognitive rehabilitation in adult brain tumors. *Curr Treat Options Neurol.* (2016) 18:1–16. doi: 10.1007/s11940-016-0406-5
2. Louis DN, Perry A, Wesseling P, Brat DJ, Cree IA, Figarella-Branger D, et al. The 2021. WHO classification of tumors of the central nervous system: a summary. *Neuro Oncol.* (2021) 23:1231–51. doi: 10.1093/neuonc/noab106
3. DeAngelis LM. Brain tumors. *N Engl J Med.* (2001) 344:114–23. doi: 10.1056/NEJM200101113440207

4. Fisher JL, Schwartzbaum JA, Wrensch M, Wiemels JL. Epidemiology of brain tumors. *Neurol Clin*. (2007) 25:867–90. doi: 10.1016/j.ncl.2007.07.002
5. Lapointe S, Perry A, Butowski NA. Primary brain tumours in adults. *Lancet*. (2018) 392:432–46. doi: 10.1016/S0140-6736(18)30990-5
6. Kickingereder P, Burth S, Wick A, Götz M, Eidel O, Schlemmer HP, et al. Radiomic profiling of glioblastoma: identifying an imaging predictor of patient survival with improved performance over established clinical and radiologic risk models. *Radiology*. (2016) 280:880–9. doi: 10.1148/radiol.2016160845
7. Sawaya R, Hammoud M, Schoppa D, Hess KR, Wu SZ, Shi WM, et al. Neurosurgical outcomes in a modern series of 400 craniotomies for treatment of parenchymal tumors. *Neurosurgery*. (1998) 42:1044–55. doi: 10.1097/00006123-199805000-00054
8. Mathiesen T, Peredo I, Lönn S. Two-year survival of low-grade and high-grade glioma patients using data from the Swedish Cancer Registry. *Acta Neurochir*. (2011) 153:467–71. doi: 10.1007/s00701-010-0894-0
9. Zinn PO, Colen RR, Kasper EM, Burkhardt JK. Extent of resection and radiotherapy in GBM: A 1973 to 2007 surveillance, epidemiology and end results analysis of 21,783 patients. *Int J Oncol*. (2013) 42:929–34. doi: 10.3892/ijo.2013.1770
10. Weinreb JC, Barentsz JO, Choyke PL, Cornud F, Haider MA, Macura KJ, et al. PI-RADS prostate imaging-reporting and data system: 2015 version 2. *Eur Urol*. (2016) 69:16–40. doi: 10.1016/j.eururo.2015.08.052
11. Dyer SC, Bartholmai BJ, Koo CW. Implications of the updated Lung CT Screening Reporting and Data System (Lung-RADS version 1.1) for lung cancer screening. *J Thorac Dis*. (2020) 12:6966. doi: 10.21037/jtd-2019-cptn-02
12. Ellingson BM, Bendszus M, Boxerman J, Barboriak D, Erickson BJ, Smits M, et al. Consensus recommendations for a standardized brain tumor imaging protocol in clinical trials. *Neuro Oncol*. (2015) 17:1188–98. doi: 10.1093/neuonc/nov095
13. Kommers I, Bouget D, Pedersen A, Eijgelaar RS, Ardon H, Barkhof F, et al. Glioblastoma surgery imaging–reporting and data system: standardized reporting of tumor volume, location, and resectability based on automated segmentations. *Cancers*. (2021) 13:2854. doi: 10.3390/cancers13122854
14. Binaghi E, Pedoia V, Balbi S. Collection and fuzzy estimation of truth labels in glial tumour segmentation studies. *Comput Methods Biomech Biomed Eng*. (2016) 4:214–28. doi: 10.1080/21681163.2014.947006
15. Berntsen EM, Stensjøen AL, Langlo MS, Simonsen SQ, Christensen P, Moholdt VA, et al. Volumetric segmentation of glioblastoma progression compared to bidimensional products and clinical radiological reports. *Acta Neurochir*. (2020) 162:379–87. doi: 10.1007/s00701-019-04110-0
16. Minaee S, Boykov YY, Porikli F, Plaza AJ, Kehtarnavaz N, Terzopoulos D. Image segmentation using deep learning: a survey. *IEEE Trans Pattern Anal Mach Intell*. (2021) 44:3523–42. doi: 10.1109/TPAMI.2021.3059968
17. Menze BH, Jakab A, Bauer S, Kalpathy-Cramer J, Farahani K, Kirby J, et al. The multimodal brain tumor image segmentation benchmark (BRATS). *IEEE Trans Med Imaging*. (2014) 34:1993–2024. doi: 10.1109/TMI.2014.2377694
18. Bakas S, Akbari H, Sotiras A, Bilello M, Rozycki M, Kirby JS, et al. Advancing the cancer genome atlas glioma MRI collections with expert segmentation labels and radiomic features. *Scientific Data*. (2017) 4:1–13. doi: 10.1038/sdata.2017.117
19. Baid U, Ghodasara S, Mohan S, Bilello M, Calabrese E, Colak E, et al. The rsna-asnr-miccai brats 2021 benchmark on brain tumor segmentation and radiogenomic classification. *arXiv[Preprint].arXiv:210702314*. (2021). doi: 10.48550/arXiv.2107.02314
20. Isensee F, Petersen J, Klein A, Zimmerer D, Jaeger PF, Kohl S, et al. nnu-net: self-adapting framework for u-net-based medical image segmentation. *arXiv[Preprint].arXiv:180910486*. (2018) doi: 10.1007/978-3-658-25326-4_7
21. Luu HM, Park SH. Extending nn-UNet for brain tumor segmentation. *arXiv[Preprint].arXiv:211204653*. (2021). doi: 10.48550/arXiv.2112.04653
22. Tiwari A, Srivastava S, Pant M. Brain tumor segmentation and classification from magnetic resonance images: review of selected methods from 2014 to 2019. *Pattern Recognit Lett*. (2020) 131:244–60. doi: 10.1016/j.patrec.2019.11.020
23. Pereira S, Pinto A, Alves V, Silva CA. Brain tumor segmentation using convolutional neural networks in MRI images. *IEEE Trans Med Imaging*. (2016) 35:1240–51. doi: 10.1109/TMI.2016.2538465
24. Grøvik E, Yi D, Iv M, Tong E, Rubin D, Zaharchuk G. Deep learning enables automatic detection and segmentation of brain metastases on multisequence MRI. *J Mag Reson Imaging*. (2020) 51:175–82. doi: 10.1002/jmri.26766
25. Grøvik E, Yi D, Iv M, Tong E, Nilsen LB, Latysheva A, et al. Handling missing MRI sequences in deep learning segmentation of brain metastases: a multicenter study. *NPJ Digit Med*. (2021) 4:1–7. doi: 10.1038/s41746-021-00398-4
26. Kamnitsas K, Ferrante E, Parisot S, Ledig C, Nori AV, Criminisi A, et al. DeepMedic for brain tumor segmentation. In: *International Workshop on Brainlesion: Glioma, Multiple Sclerosis, Stroke and Traumatic Brain Injuries*. Athens: Springer (2016). p. 138–49.
27. Liu Y, Stojadinovic S, Hrycushko B, Wardak Z, Lau S, Lu W, et al. A deep convolutional neural network-based automatic delineation strategy for multiple brain metastases stereotactic radiosurgery. *PLoS One*. (2017) 12:e0185844. doi: 10.1371/journal.pone.0185844
28. Charron O, Lallement A, Jarnet D, Noblet V, Clavier JB, Meyer P. Automatic detection and segmentation of brain metastases on multimodal MR images with a deep convolutional neural network. *Comput Biol Med*. (2018) 95:43–54. doi: 10.1016/j.compbiomed.2018.02.004
29. Neromyliotis E, Kalamatianos T, Paschalis A, Komaitis S, Fountas KN, Kapsalaki EZ, et al. Machine learning in meningioma MRI: past to present. A narrative review. *J Mag Reson Imaging*. (2022) 55:48–60. doi: 10.1002/jmri.27378
30. Laukamp KR, Thiele F, Shakirin G, Zopfs D, Faymonville A, Timmer M, et al. Fully automated detection and segmentation of meningiomas using deep learning on routine multiparametric MRI. *Eur Radiol*. (2019) 29:124–32. doi: 10.1007/s00330-018-5595-8
31. Laukamp KR, Pennig L, Thiele F, Reimer R, Görtz L, Shakirin G, et al. Automated meningioma segmentation in multiparametric MRI. *Clin Neuroradiol*. (2020) 31:357–66. doi: 10.1007/s00062-020-00884-4
32. Bouget D, Pedersen A, Hosainey SAM, Solheim O, Reinertsen I. Meningioma segmentation in t1-weighted mri leveraging global context and attention mechanisms. *arXiv[Preprint].arXiv:210107715*. (2021). doi: 10.3389/fradi.2021.711514
33. Consortium TM. *Project MONAI*. Zenodo (2020).
34. Lösel PD, van de Kamp T, Jayme A, Ershov A, Faragó T, Pichler O, et al. Introducing Biomedisa as an open-source online platform for biomedical image segmentation. *Nat Commun*. (2020) 11:1–14. doi: 10.1038/s41467-020-19303-w
35. Reinke A, Eisenmann M, Tizabi MD, Sudre CH, Rädsch T, Antonelli M, et al. Common limitations of image processing metrics: a picture story. *arXiv preprint arXiv:210405642*. (2021). doi: 10.48550/arXiv.2104.05642
36. Taha AA, Hanbury A. Metrics for evaluating 3D medical image segmentation: analysis, selection, and tool. *BMC Med Imaging*. (2015) 15:29. doi: 10.1186/s12880-015-0068-x
37. Weinberg BD, Gore A, Shu HKG, Olson JJ, Duszak R, Voloschin AD, et al. Management-based structured reporting of posttreatment glioma response with the brain tumor reporting and data system. *J Am Coll Radiol*. (2018) 15:767–71. doi: 10.1016/j.jacr.2018.01.022
38. Fuller GN, Scheithauer BW. The 2007 Revised World Health Organization (WHO) classification of tumours of the central nervous system: newly codified entities. *Brain Pathology* (2007) 17:304–7. doi: 10.1111/j.1750-3639.2007.00084.x
39. Louis DN, Perry A, Reifenberger G, von Deimling A, Figarella-Branger D, Cavenee WK, et al. The 2016 World Health Organization classification of tumors of the central nervous system: a summary. *Acta Neuropathol*. (2016) 131:803–20. doi: 10.1007/s00401-016-1545-1
40. Huber T, Alber G, Bette S, Boeckh-Behrens T, Gempt J, Ringel F, et al. Reliability of semi-automated segmentations in glioblastoma. *Clin Neuroradiol*. (2017) 27:153–61. doi: 10.1007/s00062-015-0471-2
41. Vezhnevets V, Konouchine V. GrowCut: interactive multi-label ND image segmentation by cellular automata. In: *Proceedings of Graphicon, Vol. 1*. Novosibirsk: Citeseer (2005). p. 150–6.
42. Egger J, Kapur T, Fedorov A, Pieper S, Miller JV, Veeraraghavan H, et al. GBM volumetry using the 3D Slicer medical image computing platform. *Sci Rep*. (2013) 3:1–7. doi: 10.1038/srep01364
43. Bouget D, Pedersen A, Hosainey SAM, Vanel J, Solheim O, Reinertsen I. Fast meningioma segmentation in T1-weighted magnetic resonance imaging

volumes using a lightweight 3D deep learning architecture. *J Med Imaging*. (2021) 8:024002. doi: 10.1117/1.JMI.8.2.024002
44. Bouget D, Eijgelaar RS, Pedersen A, Kommers I, Ardon H, Barkhof F, et al. Glioblastoma Surgery Imaging-Reporting and Data System: Validation and Performance of the Automated Segmentation Task. *Cancers*. (2021) 13:4674. doi: 10.3390/cancers13184674
45. Fonov VS, Evans AC, McKinstry RC, Almli CR, Collins D. Unbiased nonlinear average age-appropriate brain templates from birth to adulthood. *Neuroimage*. (2009) 47:S102. doi: 10.1016/S1053-8119(09)70884-5
46. Fedorov A, Beichel R, Kalpathy-Cramer J, Finet J, Fillion-Robin JC, Pujol S, et al. 3D Slicer as an image computing platform for the quantitative imaging network. *Mag Reson Imaging*. (2012) 30:1323–41. doi: 10.1016/j.mri.2012.05.001
47. Mehrtash A, Pesteie M, Hetherington J, Behringer PA, Kapur T, Wells III WM, et al. DeepInfer: open-source deep learning deployment toolkit for image-guided therapy. In: *Medical Imaging 2017: Image-Guided Procedures, Robotic Interventions, and Modeling. vol. 10135*. SPIE(2017). p. 410–6.
48. Dice LR. Measures of the amount of ecologic association between species. *Ecology*. (1945) 26:297–302. doi: 10.2307/1932409
49. Jaccard P. The distribution of the flora in the alpine zone[1]. *New Phytol*. (1912) 11:37–50. doi: 10.1111/j.1469-8137.1912.tb05611.x
50. Martin D, Fowlkes C, Tal D, Malik J. A database of human segmented natural images and its application to evaluating segmentation algorithms and measuring ecological statistics. In: *Proceedings Eighth IEEE International Conference on Computer Vision. ICCV, Vol. 2*. Vancouver, BC: IEEE (2001). p. 416–23.
51. Cárdenes R, de Luis-Garcia R, Bach-Cuadra M. A multidimensional segmentation evaluation for medical image data. *Comput Methods Programs Biomed*. (2009) 96:108–24. doi: 10.1016/j.cmpb.2009.04.009
52. Russakoff DB, Tomasi C, Rohlfing T, Maurer CR. Image similarity using mutual information of regions. In: *European Conference on Computer Vision*. Prague: Springer (2004). p. 596–607.
53. Meilă M. Comparing clusterings by the variation of information. In: *Learning Theory and Kernel Machines*. Washington: Springer (2003). p. 173–87.
54. Cohen J. A coefficient of agreement for nominal scales. *Educ Psychol Meas*. (1960) 20:37–46. doi: 10.1177/001316446002000104
55. Bradley AP. The use of the area under the ROC curve in the evaluation of machine learning algorithms. *Pattern Recognit*. (1997) 30:1145–59. doi: 10.1016/S0031-3203(96)00142-2
56. Baldi P, Brunak S, Chauvin Y, Andersen CA, Nielsen H. Assessing the accuracy of prediction algorithms for classification: an overview. *Bioinformatics*. (2000) 16:412–24. doi: 10.1093/bioinformatics/16.5.412
57. Gerig G, Jomier M, Chakos M. Valmet: a new validation tool for assessing and improving 3D object segmentation. In: *International Conference on Medical Image Computing and Computer-Assisted Intervention*. Utrecht: Springer (2001). p. 516–23. doi: 10.1007/3-540-45468-3_62
58. Huttenlocher DP, Klanderman GA, Rucklidge WJ. Comparing images using the hausdorff distance. *IEEE Trans Pattern Anal Mach Intell*. (1993) 15:850–63. doi: 10.1109/34.232073
59. McLachlan GJ. Mahalanobis distance. *Resonance*. (1999) 4:20–6. doi: 10.1007/BF02834632
60. Chinchor N, Sundheim BM. MUC-5 evaluation metrics. In: *Fifth Message Understanding Conference (MUC-5)*: *Proceedings of a Conference Held in Baltimore, Maryland, August 25–27, 1993*. Baltimore, MD (1993).
61. Hubert L, Arabie P. Comparing partitions. *J Classificat*. (1985) 2:193–218. doi: 10.1007/BF01908075
62. Killeen PR. An alternative to null-hypothesis significance tests. *Psychol Sci*. (2005) 16:345–53. doi: 10.1111/j.0956-7976.2005.01538.x
63. Jung AB, Wada K, Crall J, Tanaka S, Graving J, Reinders C, et al. *Imgaug*. (2020). Available online at: https://github.com/aleju/imgaug (accessed on February 01, 2020).
64. Pedregosa F, Varoquaux G, Gramfort A, Michel V, Thirion B, Grisel O, et al. Scikit-learn: machine learning in python. *J Mach Learn Res*. (2011) 12:2825–30. doi: 10.48550/arXiv.1201.0490
65. Maier O, Rothberg A, Raamana PR, Bèges R, Isensee F, Ahern M, et al. *loli/medpy: MedPy 0.4.0*. Zenodo (2019).
66. Melek M, Melek N. Roza: a new and comprehensive metric for evaluating classification systems. *Comput Methods Biomech Biomed Engin*. (2021) 25:1–13. doi: 10.1080/10255842.2021.1995721
67. Karimi D, Salcudean SE. Reducing the hausdorff distance in medical image segmentation with convolutional neural networks. *IEEE Trans Med Imaging*. (2019) 39:499–513. doi: 10.1109/TMI.2019.2930068
68. Heydari AA, Thompson CA, Mehmood A. Softadapt: techniques for adaptive loss weighting of neural networks with multi-part loss functions. *arXiv[Preprint].arXiv:191212355*. (2019). doi: 10.48550/arXiv.1912.12355

Conflict of Interest: The authors declare that the research was conducted in the absence of any commercial or financial relationships that could be construed as a potential conflict of interest.

frontiers | Frontiers in Neurology

TYPE Review
PUBLISHED 17 August 2022
DOI 10.3389/fneur.2022.890425

OPEN ACCESS

EDITED BY
Peter Sörös,
University of Oldenburg, Germany

REVIEWED BY
Philippe Corcia,
Université de Tours, France
Dongsheng Fan,
Peking University Third Hospital, China

*CORRESPONDENCE
Freimut D. Juengling
fjuengli@ualberta.ca

SPECIALTY SECTION
This article was submitted to Applied Neuroimaging, a section of the journal Frontiers in Neurology

RECEIVED 05 March 2022
ACCEPTED 20 July 2022
PUBLISHED 17 August 2022

CITATION
Juengling FD, Wuest F, Kalra S, Agosta F, Schirrmacher R, Thiel A, Thaiss W, Müller H-P and Kassubek J (2022) Simultaneous PET/MRI: The future gold standard for characterizing motor neuron disease—A clinico-radiological and neuroscientific perspective. *Front. Neurol.* 13:890425. doi: 10.3389/fneur.2022.890425

Simultaneous PET/MRI: The future gold standard for characterizing motor neuron disease—A clinico-radiological and neuroscientific perspective

Freimut D. Juengling[1,2,3]*, Frank Wuest[1], Sanjay Kalra[2,4], Federica Agosta[5], Ralf Schirrmacher[1,6], Alexander Thiel[7], Wolfgang Thaiss[8,9], Hans-Peter Müller[10] and Jan Kassubek[10]

[1]Division of Oncologic Imaging, University of Alberta, Edmonton, AB, Canada, [2]Neuroscience and Mental Health Institute, University of Alberta, Edmonton, AB, Canada, [3]Faculty of Medicine, University Bern, Bern, Switzerland, [4]Department of Neurology, University of Alberta, Edmonton, AB, Canada, [5]Division of Neuroscience, San Raffaele Scientific Institute, University Vita Salute San Raffaele, Milan, Italy, [6]Medical Isotope and Cyclotron Facility, University of Alberta, Edmonton, AB, Canada, [7]Lady Davis Institute for Medical Research, Department of Neurology and Neurosurgery, McGill University, Montreal, QC, Canada, [8]Department of Nuclear Medicine, University of Ulm Medical Center, Ulm, Germany, [9]Department of Diagnostic and Interventional Radiology, University of Ulm Medical Center, Ulm, Germany, [10]Department of Neurology, Ulm University Medical Center, Ulm, Germany

Neuroimaging assessment of motor neuron disease has turned into a cornerstone of its clinical workup. Amyotrophic lateral sclerosis (ALS), as a paradigmatic motor neuron disease, has been extensively studied by advanced neuroimaging methods, including molecular imaging by MRI and PET, furthering finer and more specific details of the cascade of ALS neurodegeneration and symptoms, facilitated by multicentric studies implementing novel methodologies. With an increase in multimodal neuroimaging data on ALS and an exponential improvement in neuroimaging technology, the need for harmonization of protocols and integration of their respective findings into a consistent model becomes mandatory. Integration of multimodal data into a model of a continuing cascade of functional loss also calls for the best attempt to correlate the different molecular imaging measurements as performed at the shortest inter-modality time intervals possible. As outlined in this perspective article, simultaneous PET/MRI, nowadays available at many neuroimaging research sites, offers the perspective of a one-stop shop for reproducible imaging biomarkers on neuronal damage and has the potential to become the new gold standard for characterizing motor neuron disease from the clinico-radiological and neuroscientific perspectives.

KEYWORDS

ALS, motor neuron disease, PET/MRI, DTI, fMRI, SV2A, TrkB/BDNF

Introduction

Based on current guidelines, clinical workup of amyotrophic lateral sclerosis (ALS) will include neuroimaging to rule out structural lesions and neurologic conditions that sometimes account for early clinical features seen in patients suspected of having primary motor neuron disease (1). The clinical management of this highly invalidating condition, however, clearly necessitates, as early as possible, accurate diagnostic and prognostic information on the associated motor neuron degeneration to direct appropriate clinical handling of the individual patient. Neuroimaging has proven to provide reliable *in vivo* biomarkers to better define the various clinical entities within ALS and to provide additional complementary information to the standard clinical workup (2).

Current situation of neuroimaging for motor neuron disease

Instrumentation and image processing—MRI

Recent MRI applications for motor neuron disease including ALS have focused both on quantitative and qualitative analysis of structural changes in T1-weighted images as assessed by automatic analysis approaches and, in a body of more recent studies, on the analysis of microstructural alterations within the brain and spinal cord by the application of varieties of diffusion-weighted MRI sequences.

Additionally, substantial efforts have been made utilizing PET to generate newer and more biologically based classifications of ALS and its subtypes (3–5). PET, as a non-invasive *in vivo* imaging technique, provides quantitative data at the molecular level, with novel radiotracers targeting neurons, microglia and astrocytes metabolism, receptor and protein density, as well as oxidative stress.

Advances in computational analyses of multimodal imaging datasets, including deep learning-based applications of artificial intelligence (AI), are just opening the door for a more comprehensive understanding of the pathophysiological cascade of neurodegeneration in motor neuron disease. Here, hypothesis-guided approaches including neuropathological concepts and network-based analyses will be center stage and will eventually find their way into clinical practice.

Crucial information will also be derived from neuroimaging fingerprinting of genetically defined ALS phenotypes like the association with *C9orf72* hexanucleotide repeat expansions, especially in longitudinal investigations of presymptomatic mutation carriers. Neuroimaging offers the possibility to stratify ALS patients according to their intrinsic progression rate, based on cross-sectional and longitudinal studies, thus helping to optimize disease management, enhancing the design of drug trials, and guiding the use of novel individualized treatments when these become available (6, 7).

Further advances in the clinical application of neuroimaging in motor neuron disease will have to rely extensively on a new stage of neuroscientific cooperation, building on existing collaborations between researchers and infrastructures specialized in ALS and facilitating multicenter joint projects that enable grand-scale projects, such as those, for example, led by the Neuroimaging Society in Amyotrophic Lateral Sclerosis (8) or the Canadian ALS Neuroimaging Consortium (CALSNIC) (9). While multicentric studies are most welcome to increase the number of observations in subgroups and different disease stages, the accordingly increasing amount of data collected is paralleled by the need for harmonization of protocols, being the foundation for deducting evidence out of data, and integration of their respective findings into a consistent model of a possible continuing cascade of functional loss.

Integration of multimodal data into a consistent model aiming to correlate the different anatomical, functional, and molecular imaging measurements also calls for the best attempt to perform all measurements to correlate at the shortest intermodality time intervals possible, which is most important in a rapidly progressing disease. But even in the case of a primarily slowly progressing disease, pathological processes can be expected to be accentuated at times, as typically is the case for inflammatory cascades. Any attempt to draw conclusions from observations even a few days apart may thus be jeopardized by the underlying pathological process itself.

The advent of simultaneous PET/MRI, which industries had quickly turned from prototype research instruments into reliable, integrated commercial scanners, has proven to provide a stable, reproducible, and calibrated hybrid modality that not only by design acquires data simultaneously, but also adds value by its potential of dynamically mutually informing their reconstruction algorithms with either modality data. With PET/MRI available at many neuroimaging research sites, the perspective of a one-stop shop for reproducible imaging biomarkers on neuronal damage gains importance, and the call for harmonization of protocols becomes feasible, as the stringent design of hybrid PET/MRI eases the implementation of research protocols and research MR sequences at the existent sites.

The two available PET/MRI scanner models built by the industry providers GE Medical and Siemens Healthineers make use of their respective provider's 3T MRI platform and state-of-the-art PET technology, enabling rapid adaption of advances in image acquisition and reconstruction to their clinical platforms. Improved MR sequences, e.g., providing diffusion imaging at a resolution of $1 \times 1 \times 1$ mm^3, necessary to characterize microstructural abnormalities (10), can thus be easily adopted and distributed throughout the neuroimaging research sites. Harmonization of MR protocols across different vendors also has proven feasible for the specific needs to characterize microstructural changes in corticospinal,

corticorubral, corticostriatal, and hippocampal tracts at different stages of disease progression in ALS (8). The same holds true for protocols for resting state fMRI (11) and MR spectroscopy (MRS) (12).

While PET measurements, in principle, allow for absolute quantitation measures, such as regional cerebral blood volume, regional cerebral glucose metabolism, or regional receptor occupancy, the evaluation of multicentric data makes procedures for harmonization of data acquisition and processing mandatory (13–16), which is simplified for PET/MRI, where, by design, variability of the underlying technology is limited. Given that technical prerequisites have been met, quantitative measures of different systems relevant to motor neuron disease can be non-invasively acquired and PET/MRI proves useful for individual assessment of the stage of disease (Figure 1).

Molecular imaging of disease-inherent pathological alterations—PET

Glucose metabolism and regional inflammatory changes

While many of the more recent radiotracers are still experimental, measures of regional glucose metabolism using ^{18}F-FDG-PET have reached clinical utility in ALS, as evaluated by a panel of experts in the field of nuclear medicine and neurology. By an analysis of the most relevant ^{18}F-FDG-PET investigations by the Population, Intervention, Comparison, Outcome (PICO) model, the provided incremental value as compared with the information resulting from the clinical tests routinely performed had been assessed, concluding that ^{18}F-FDG-PET offers good evidence to support ALS diagnosis (17). This analysis, however, was based on stand-alone ^{18}F-FDG-PET investigations, which did not take into account same-time structural or functional MRI measures. The metabolic patterns identified in ALS consisted of significant hypometabolism in prefrontal, frontal, precentral, and postcentral regions, bilaterally, associated with significant hypermetabolism in posterior occipital and middle temporal cortices, cerebellum, midbrain, and corticospinal tracts, findings which are atypical in functional studies investigating neurodegenerative diseases. Clinically relevant is that the extent of metabolic brain changes in frontal lobes is correlated with cognitive dysfunction (18), thus distinguishing patients with cognitive impairment and possible overlap with frontotemporal dementia from those with pure motor disease (19). The pattern of glucose metabolism also was found to discriminate ALS patients from patients with Parkinson's plus syndromes (20), and, if using machine learning-based techniques, such as support-vector machine discriminant analysis, FDG PET also has proven to be useful for automatically classifying patients with amyotrophic lateral sclerosis vs. controls (21).

More recent studies have found an inverse correlation between precentral and postcentral metabolic activity and clinical stages (22), as well as an inverse correlation between prefrontal and limbic metabolism and apathy (23). When coregistered MRI for partial volume correction was used, FDG PET was able to identify metabolic changes in presymptomatic carriers of the *C9orf72* repeat expansion (24). Also, precentral metabolism distinguished patients with the *SOD1* mutations (SOD-1 ALS) from sporadic ALS (sALS). Specifically, right precentral and paracentral metabolism was relatively increased in patients with SOD-1 ALS as compared to sALS (25). It was hypothesized that a relative increase of ^{18}F-FDG-related signal in ALS patients in pyramidal cells in the motor cortex and in their projections to the spinal cord is secondary to a widespread microglial activation and astrocytosis reactive to the reduced neuronal density, with the proliferation of astrocytes being the main determinant of glucose uptake from the intraparenchymal capillaries (26). To better delineate the spatial pattern of metabolic changes in the brain stem and cervical spinal cord, an innovative study capitalized on the potential of integrated PET/MRI to improve result accuracy in small anatomic structures by separately analyzing glucose metabolic patterns in the midbrain/pons, medulla oblongata and cervical spinal cord of ALS and frontotemporal dementia (FTD) patients as compared to normal controls (27). They found a significant and intercorrelating increment in glucose metabolism in the midbrain/pons and medulla oblongata in ALS/FTD patients (spinal-ALS and FTD-motor neuron disease subgroups), interpreted to relate to neuroinflammation, namely activated microglia. While they did not report relevant associations between clinical and metabolic features, medulla oblongata hypermetabolism was associated with shortened survival of ALS patients. In the context of their study, the simultaneously available MRI was instrumental for the identification of corticospinal tract hyperintensities to differentiate ALS from clinically overlapping FTD patients of the motor neuron subgroup, and for the detection of the brain stem and cervical spinal cord hypermetabolism in favor of regional neuro-inflammation linked to activated microglia. Confirmatory studies, directly measuring microglial activation using radioligands targeting TSPO (18 kDa translocator protein), have been performed either using the first-generation TSPO ligand ^{11}C-PK-11195 (28, 29) or one of the second-generation ligands ^{18}F-FEPPA (30), ^{18}F-DPA714 (31), or ^{11}C-PBR28, the latter of which has proven to allow for microglia imaging of fiber tracts (32). Technical issues that have not been addressed by a "PET-only" approach for those investigations include the need for partial volume correction, as the measured signal would depend on the regional volume of the anatomical structure of interest. Partial volume correction, however, is extensively dependent on coincident, morphological imaging,

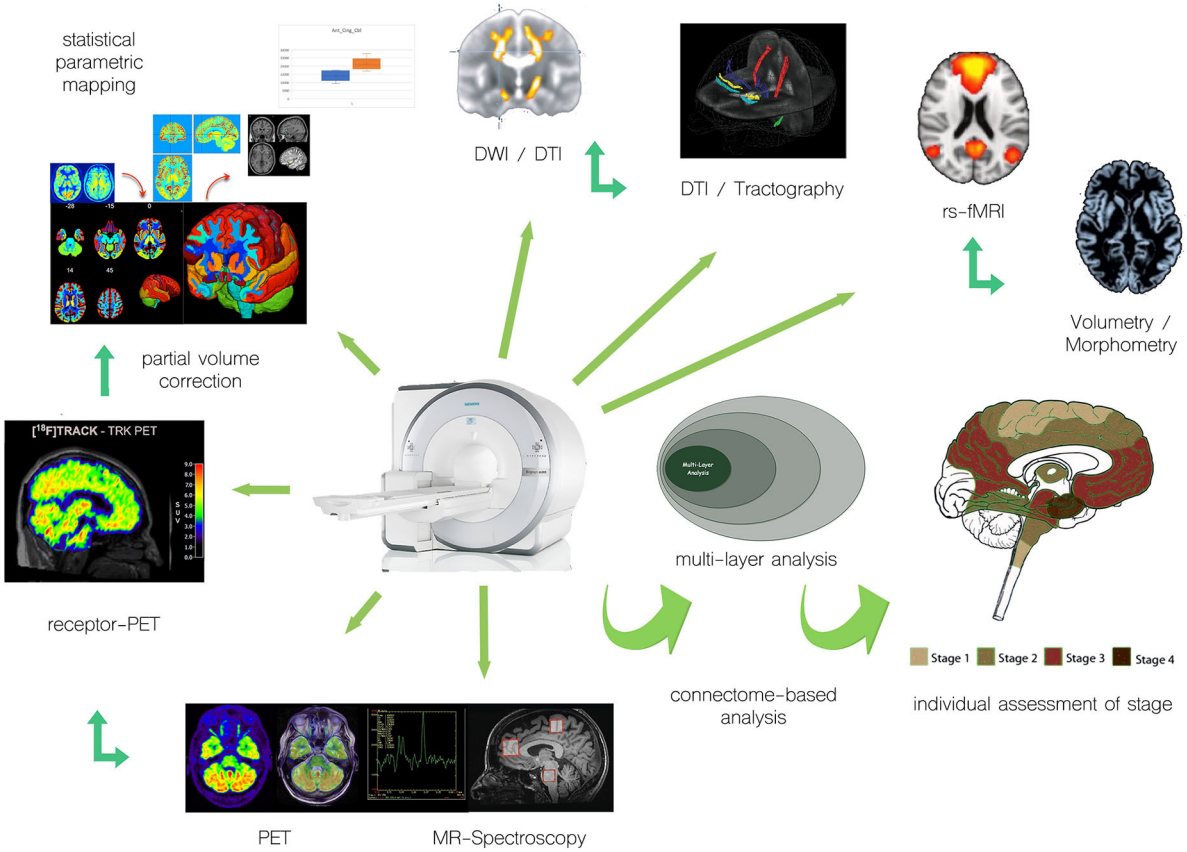

FIGURE 1
Examples of integration of multimodal PET and MR approaches for individual assessment of motor neuron disease/ALS.

where the quality of coregistration of sequentially acquired datasets is a major determinant of bias. It can therefore be expected that using combined information out of a single coordinate system of acquisition, TSPO-PET/MRI will represent an even more useful biomarker in cross-sectionally and longitudinally evaluating the spread of inflammatory lesions.

Novel markers for neuroinflammation

Purinergic P2X7 ionotropic receptor

More recently, novel markers for neuroinflammation targeting the purinergic P2X7 ionotropic receptor (P2X7R) have been successfully introduced into human PET-imaging [(33) brain kinetic modeling and quantification of brain P2X7 receptors in patients with Parkinson's disease and healthy volunteers] (34). As P2X7R is expressed in astrocytes, microglia, and oligodendrocytes, where they mediate inflammasome signaling (35). A couple of preclinical and clinical studies suggest the implication of P2X7Rs in ALS pathogenesis (36–38). As a whole group of P2X7-Receptor antagonists is currently under development, posing a possible new therapeutic approach for ALS (39). A quantitative assessment of P2X7R as an initial and longitudinal biomarker, along with morphological and functional MR measures will be a basic necessity in according clinical studies, naturally favoring PET/MRI as an imaging modality of choice.

C-X-C motif chemokine receptor antagonists

Another promising candidate target suitable as a biomarker for neuroinflammation is the cyclooxygenase-enzyme-2 (COX-2), the possible involvement of which in ALS is indicated by preclinical data (36) and clearly needs systematic *in vivo* studies that will be enabled by the very recent development of appropriate radiopharmaceutical targets (40–42). If a significant involvement of COX-2 could be documented at any stage of disease, this could open the rationale for stage-dependent antioxidative treatment (43, 44), and would again need to be reflected in MRI-based functional measures.

More experimental measures for neuroinflammation are based on findings indicating the implication of C-X-C motif chemokine receptor (CXCR)-4 and CXCR-3, which critically

contribute to the disease process in systemic inflammation (45–47), opening another door to possible future therapeutic principles targeting the respective C-X-C motif chemokine receptor (48, 49). As a couple of specific radiopharmaceutical targets have been developed for preclinical and clinical use (40–42, 50), the selection of an appropriate tracer as a biomarker in motor neuron disease would depend on binding characteristics, kinetic analysis, and correlation with functional measures derived from MRI. Again, interpretation of novel preclinical and clinical neuropharmacological imaging data will crucially depend on its supportive correlation with coincident imaging findings using a different modality.

Neurotrophins

Tyrosine kinase receptor antagonists

There is growing evidence for neurotrophins being involved in neurodegenerative diseases including ALS (40–42, 50, 51). While neurotrophins have not yet proven a significant therapeutic potential in clinical trials, partly because of the difficulties of protein delivery and pharmacokinetics in the nervous system, the binding target of neurotrophins includes a family of tyrosine kinase (TrK) receptors. Within this class of receptors, synthetic antibodies have recently been linked to PET-radioligands targeting the TrK-B receptor, which have passed the preclinical and clinical assessments (52–54). Quantitative characterization of TrK-B alterations in ALS is currently underway by the same research group, accounting for the volumetric changes inherent in the disease by applying PET/MRI in the first place, complemented by magnetic resonance spectroscopy data. The recent development of TrkB agonistic antibodies and BDNF-targeted gene therapies (55, 56) could prove useful, and changes in TrK-B alterations as measured by PET/MRI during targeted therapy could potentially qualify as an imaging endpoint in clinical trials in motor neuron disease (52–54, 57).

Markers of neuronal integrity

GABA-A—Benzodiazepine receptor complex

The selective PET ligands ^{11}C-Flumazenil and 2′-^{18}F-Fluoroflumazenil, binding to the GABA-A—receptor, widely expressed on pyramidal neurons, have been suggested to be used as a surrogate *in vivo* marker of neuronal density (58–62). First, applications in neurodegenerative disease have shown a regional neuronal loss in the motor and premotor cortex as well as in extramotor areas in ALS (63, 64), which were also associated with specific cognitive deficits (65, 66). The specificity of GABA-A receptor antagonists to characterize neuronal loss without a possible confound by GABAergic dysfunction has however been questioned, and quantitation methods applied have been scrutinized (67). It has been demonstrated that PET imaging and quantitation using Flumazenil-based radioligands highly depend on the availability of concurrent high-resolution MRI (68), which would ideally be conceptualized by PET/MRI.

Antagonists to synaptic vesicle protein 2A

The synaptic vesicle protein 2A (SV2A), a 12-transmembrane domain glycoprotein, is ubiquitously expressed in normal synaptic vesicles throughout the brain, with a particularly high regional expression in the thalamus and basal ganglia (69), only sparing the trigeminal and facial nerve nuclei (70, 71). SV2A has thus been claimed as a potential biomarker for synaptic vesicle density. While it is critical to Ca^{2+}-dependent exocytosis (72), its exact physiological role still is subject to further research, and deficiencies in the expression of SV2A have been described in a growing number of neurodegenerative disorders, including frontotemporal dementia (FTD), Parkinson's Disease (PD), Alzheimer's disease (AD), corticobasal degeneration (73–77), as well as further neurological conditions, such as epilepsy (78–80), where it has been identified as the binding site for the antiepileptic drug levetiracetam (81).

In analyses of rat brain homogenates, the number of expressed SV2a proteins per vesicle was found to be highly reproducible at 2–5 copies per vesicle (82, 83). It has been suggested that SV2A plays a central role in exocytosis mediated by Ca^{2+} (71). The deficiency of SV2A in SV2A knockout mice resulted in presynaptic Ca^{2+} accumulation, destabilizing synaptic circuits, and inducing seizures (84). It has also been suggested that SV2A is modulating endocytosis to the SV of the SV protein synaptotagmin-1 (SYT1), and by this mechanism is involved in the homeostasis of the readily releasable pool of SVs (85).

SV2A has thus attracted attention as a target binding site for PET-tracers, and subsequently, with the SV2A antagonist levetiracetam serving as a blueprint, a number of suitable ligands have been developed and translated into human studies (86, 87). The binding of the PET ligand ^{11}C-UCB-J to SV2A has been demonstrated to quantitatively correlate and co-localize with synaptophysin (SYN), a key protein located in the pre- or postsynaptic neurons, using a combined *in vivo–in vitro* validation, furthering evidence for SV2A targeting PET tracers to serve as synaptic density marker, which allows for the quantification of synaptic density *in vivo* (88).

Recently, a second-generation SV2A antagonist ^{18}F-SynVesT-1 (SDM-8) (89) has been introduced with superior SV2A binding affinity, improved imaging properties, enhanced metabolic stability, and an easier path for radiochemical synthesis (90, 91). For SV2A-markers to prove useful for longitudinal studies of neuronal density in progressive neurodegenerative diseases, such as ALS, confounding effects due to atrophy have to be accounted for, and simultaneous PET/MRI delivers the most accurate, concurrent quantitative anatomic information to perform partial volume correction

reflecting the state of morphologic changes at the exact same time point of PET data acquisition.

Further understanding of ALS pathophysiology will be achieved by the study of multimodal MRI and PET data through network-based analyses with hypothesis-guided approaches, including neuropathological concepts, although advanced neuroimaging still awaits translation into clinical settings.

Proteinopathy—PET surrogate markers

ALS and the ALS-FTLD spectrum disease are characterized as TDP-43 proteinopathy, where TAR DNA-Binding Protein 43 kDa (TDP-43) links both familial and sporadic forms of ALS. Cytoplasmatic aggregates of TDP-43 are a hallmark of the disease on a cellular level, and protein mislocalization is often regarded as a key mechanism underlying ALS. Up to now, there is no direct PET imaging ligand successfully targeting TDP-43, and out of the notion that multiple pathological proteins may be present in neurodegenerative disease, several groups have investigated the utility of established tau-directed PET tracers to characterize ALS (76, 77, 92–94). As diffusion tensor MR imaging (DTI) has been previously established to identify TDP-43 associated alterations (95), combined PET/MRI will be the modality of choice to further elucidate the role of tau PET imaging in ALS.

Imaging of disease-inherent pathological alterations—MRI

Neuroimaging with MRI has an essential role in the clinical diagnostic processes for ALS in the exclusion of other etiologies of the clinical presentation (96). In addition, MRI approaches with advanced postprocessing have been established as biological markers of the disease with reliable measures for monitoring disease progression and have greatly improved our understanding of its *in vivo* pathoanatomy (6). Here, diffusion-weighted imaging techniques including diffusion tensor imaging (DTI) had been a focus of research in many studies to investigate microstructural white matter tract alterations in MND (97, 98).

Diffusion tensor imaging

By using the DTI, diffusivity in human brain white matter can be non-invasively mapped to first quantify its regional directional dependence, and second, to obtain a reconstruction of fiber tracts by fiber tracking techniques (99). DTI has been established as a robust non-invasive technical tool to investigate the WM neuronal tracts *in vivo* to define anatomical signatures of the different phenotypes of MND and to track *in vivo* the progressive spread of pathological protein aggregates (100). As the neuropathological basis of the ALS-associated propagation patterns in the brain, four neuropathological stages have been defined for ALS, based upon the distribution patterns of phosphorylated 43 kDa TAR DNA-binding protein (101, 102): the sequential protein pathology is spreading initially from the motor neocortex toward the spinal cord and brainstem, followed by spreading to frontal, parietal, and, ultimately, anteromedial temporal lobes. This corticoefferent spreading model has been transferred to DTI-based concepts by a tract of interest (TOI)-based mapping, and DTI seems to be a valid surrogate marker to assess the spreading of TDP-43 pathology *in vivo* within the corresponding neuronal WM tracts (103–105). TOI-based mapping as a hypothesis-driven approach images the neuropathologically proposed sequential progression of ALS in the respective cerebral tract systems, i.e., the CST (as a correlate of ALS-stage 1), the corticorubral and corticopontine tracts (corresponding to ALS stage 2), the corticostriatal pathway (as a correlate of ALS stage 3), and the proximal portion of the perforant path (corresponding to ALS stage 4) (106). This tract-based *in vivo*-staging concept was applied to further ALS variants like primary lateral sclerosis (PLS) (104), lower motor neuron disease/progressive muscular atrophy (107), progressive bulbar palsy (108), and flail limb syndrome (109). In all of these restricted phenotypical ALS variants, an ALS-like *in vivo* alteration pattern of corticoefferent fibers according to the ALS disease propagation model could be shown. DTI-based methods, thus, seem to be a valuable tool for guiding the pathoanatomy definition of MND subtypes, in accordance with current proposals for clinical diagnosis, i.e., the Gold Coast Criteria (110). These results encourage future neuroimaging studies across the phenotypical ALS spectrum to contribute to our understanding of potential modifiers of the clinical presentations in ALS (109).

To this end, it is important to acquire longitudinal imaging data given that longitudinal MRI studies have the potential to provide crucial insights into the natural trajectory of ALS-associated neurodegenerative processes, although it has to be considered that standardized design is required to enable meaningful data interpretation (111). Longitudinal MRI studies in ALS have already been applied to subject groups of heterogeneous sample size (112–116), and reported fractional anisotropy (FA) reduction in the CST as the common core finding. Other DTI measures beyond FA add information on the ALS-associated pathoanatomy, such as a segmental radial diffusivity profile developed by Schuster and colleagues (111). Neurite orientation dispersion and density imaging (NODDI), a multicompartment model of diffusion MRI, demonstrated axonal loss within the CST together with dendritic alterations within the precentral gyrus, suggesting microstructural cortical dendritic changes occur together with CST axonal damage (117).

Protocol standardization and multisite MRI data

Advanced imaging protocols with more sophisticated techniques to analyze ever-increasing datasets to guide in the understanding of the anatomical and temporal factors of

the biological processes of ALS benefit from collaborations across the entire ALS research community (118). Multicenter approaches like the Neuroimaging Society in Amyotrophic Lateral Sclerosis (NiSALS) with up-to-date, ultimately harmonized neuroimaging protocols aim to obtain high subject numbers and therefore to increase the reliability of results (8, 119, 120). Given that multicenter imaging studies have the limitation of scanner and protocol variability, there were successful approaches to merge data recorded at different sites and/or with different DTI protocols (8, 121, 122).

The Canadian ALS Neuroimaging Consortium (CALSNIC) was established in part to address the challenges associated with protocol variability when pooling multisite data. CALSNIC is a multicenter imaging biomarker validation platform that established from its inception harmonized clinical and imaging protocols across multiple MR platforms. Operating at research sites in Canada and the USA, the platform has conducted two prospective longitudinal studies (CALSNIC1 and CALSNIC2), each including multimodal MRI, neurocognitive assessments, and speech recordings (9). To date, there have been 250 patients with ALS/MND and 200 healthy controls enrolled, with CALSNIC2 ongoing. A recent study of longitudinal DTI-based microstructural alterations in ALS from CALSNIC determined a time interval of about 110 days is the minimum follow-up time to detect longitudinal microstructural alterations (123). Other longitudinal observations within this time frame reported by this consortium include gray and white matter atrophy with deformation-based morphometry (124), altered motor and prefrontal cortex neurochemistry using magnetic resonance spectroscopy (125), and regional texture changes in T1-weighted images (126). Collaborative and multicenter projects like this will be useful in ascertaining the reliability of imaging biomarkers under development (127).

MR findings with respect to genetic phenotype

The field of genetic ALS continues to develop rapidly with multiple disease gene discoveries per year (128), with the autosomal dominant inheritance of a hexanucleotide expansion in the first intron of the *C9orf72* gene being the most common cause of familial ALS in people of Northern European ancestry, also as a major contributor to frontotemporal pathology in ALS. DTI studies in patients with *C9orf72* expansion in cross-sectional and longitudinal design demonstrated alterations in motor tracts (129–131); in addition, further white matter areas were found to be affected, e.g., in the frontal white matter (132) and segmentally in the corpus callosum (133). In addition, the *in vivo* histopathological staging approach was also applied to *C9orf72*-associated ALS and demonstrated a corticoefferent involvement pattern according to the staging scheme—a pattern that was not observed in *Super Oxide Dismutase 1*-associated ALS (134). In the last decade, the pre-symptomatic phase of the disease has gained increasing interest, addressing people with family history and genetic risk for ALS without manifestations of the disease (135). Neuroimaging studies in presymptomatic ALS offer opportunities to characterize early genotype-associated signatures and propagation patterns and factors (7). Current initiatives have, thus, integrated natural history and biomarker data on presymptomatic ALS for the design and implementation of pre-symptomatic ALS trials (136). Specifically, in *C9orf72* mutation carriers, DTI studies reported regional reductions of white matter integrity (131, 137), as an indicator of general developmental tardiness. At the spinal level, *C9orf72*-positive subjects older than 40 years were shown to exhibit considerable WM atrophy at C2–C7 vertebral levels in conjunction with progressive pyramidal tract FA reductions (138).

Resting-state functional MRI

Brain regions that are co-activated under resting conditions delineate the so-called "resting-state" (RS) functional networks. The assessment of connectivity alterations between RS networks has provided important insights into brain functional reorganization in several neurodegenerative diseases, including ALS, in which motor and—when present—cognitive impairment may undermine the use of task-based fMRI (139–141).

Several studies showed decreased functional connectivity of the sensorimotor network in ALS patients (142), whereas others found increased connectivity (143), or complex regional patterns of decreased and increased functional connectivity (144, 145). Altered functional connectivity has also been shown in brain networks related to cognition and behavior (especially the default mode and frontoparietal networks) (146, 147), consistent with the multisystem involvement of ALS pathology. It has been suggested that an increase in brain functional connectivity might prevail in earlier stages of the disease as a compensatory mechanism, with a subsequent decrease as pathological burden accumulates. Consistent with this hypothesis, increased functional connectivity was found to be higher in patients with less severe microstructural damage to the CST (148), and associated with a lower rate of disease progression, shorter disease duration (145), and preserved motor function (148). Decreased RS functional connectivity in the sensorimotor and thalamic networks, paralleling progression of structural alterations and clinical decline, was observed over a 2-year period in ALS patients (149). The co-occurrent progressive increase of functional connectivity in extra-motor networks, such as the left fronto-parietal and the temporal RS networks (147, 149), is also consistent with a "disconnection" hypothesis due to the loss of compensation. However, some studies also showed increased functional connectivity within the regions of structural disruption in ALS correlating with faster disease progression (142), and

greater clinical and executive cognitive impairment (143, 146). Therefore, a more direct pathogenic involvement of increased functional connectivity related to the loss of local inhibitory circuitry within the primary motor and frontal cortex is also possible.

Graph analysis and connectomics

The human brain is a highly integrated neural network consisting of several cortical and subcortical regions that are structurally and functionally interconnected, forming co-operating sub-networks. Graph theoretical models have conceptualized such complex organization as the brain "connectome", consisting of anatomic regions defined as "nodes", which are linked by "edges" (i.e., structural or functional connections). In ALS, graph analysis and connectomics might represent a powerful approach to detect upper motor neuron degeneration, extramotor brain changes, and network reorganization associated with the disease.

Two independent studies applied network-based statistics to DT MRI of patients with ALS, both demonstrating the presence of an impaired sub-network including bilateral primary motor regions, supplementary motor areas, basal ganglia, and associative parietal areas (150, 151). Patients with a *C9orf72* mutation showed a more widespread white matter involvement (152). In a longitudinal study, the sub-network of impaired connectivity expanded over time, involving frontal, temporal, and parietal regions (150), consistent with the proposed model of TDP-43 pathological spreading. In line with such hypothesis, a study evaluated brain structural connectivity in a consistent set of healthy controls, showing that regions involved in subsequent stages of ALS pathology are highly interconnected by WM tracts, which may serve as anatomical "infrastructures" facilitating TDP-43 spread (153). More recently, a computational model was applied to the MRI scan of ALS patients to simulate this progressive network degeneration (154). Computer-simulated aggregation levels mimic true disease patterns in ALS patients. Simulated patterns of involvement across cortical areas show significant overlap with the patterns of empirically impaired brain regions on later scans, in accordance with established pathological staging systems (152).

Few studies applied network-based analyses to the assessment of functional alterations in ALS patients using resting-state functional MRI (rs-fMRI), demonstrating complex connectivity alterations encompassing frontal, temporal, and occipital regions (155, 156). A recent study assessed the functional and structural connectivity patterns across the ALS-FTD spectrum, investigating whether and where MRI connectivity alterations of ALS patients with any degree of cognitive impairment (i.e., ALS-ci/bi and ALS-FTD) resembled more the pattern of connectome damage of ALS or bvFTD (157). As compared with controls, ALS-ci/bi patients demonstrated an "ALS-like" pattern of structural damage, diverging from ALS without cognitive impairment with similar motor impairment for the presence of enhanced functional connectivity within sensorimotor areas and decreased functional connectivity within the "bvFTD-like" pattern. On the other hand, ALS-FTD patients resembled both structurally and functionally the bvFTD-like pattern of connectome damage with, in addition, the structural ALS-like damage in the motor areas. A maladaptive role of functional rearrangements in ALS-ci/bi concomitantly with similar structural alterations compared to ALS without cognitive impairment supports the hypothesis that ALS-ci/bi might be considered as a phenotypic variant of ALS, rather than a consequence of disease worsening.

In a multicenter study (158), compared with healthy controls, patients with ALS and patients with PLS showed altered structural global network properties, as well as local topologic alterations and decreased structural connectivity in sensorimotor, basal ganglia, frontal, and parietal areas. Patients with PMA showed, instead, preserved global structure. Increased local functional connectivity was observed in patients with ALS in the precentral, middle, and superior frontal areas, and in patients with PLS in the sensorimotor, basal ganglia, and temporal networks. In patients with ALS and patients with PLS, structural connectivity alterations correlated with motor impairment, whereas functional connectivity disruption was closely related to executive dysfunction and behavioral disturbances (158).

Magnetic resonance spectroscopy

In addition to evaluating structural, microstructural, and functional changes, magnetic resonance spectroscopy (MRS) permits the probing of neurochemical correlates of neurodegeneration in ALS (12). Numerous studies using varying techniques (single voxel or multivoxel) have consistently revealed reduced N-acetylaspartate (NAA, a chemical marker of neuronal integrity) in motor and extra-motor regions in ALS. Other metabolites of interest include myo-inositol (mIns, a glial marker), and the excitatory and inhibitory neurotransmitter system involving glutamate, glutamine, and GABA (159). Technological advances in MR hardware and spectral acquisition and editing methods have increased the ability to more readily resolve such metabolites. For example, this includes ultra-high field studies at 7 tesla for glutamate, glutamine, and GABA (160, 161) and MEGA-PRESS for GABA (162, 163) detection. Combined PET-MR imaging with MRS provides the opportunity to explore complementary pathological or pathophysiological mechanisms simultaneously from the molecular and neurochemical perspectives. In a PET-MR study in ALS that included MRS motor cortex inflammation, measured using the TSPO tracer [^{11}C]-PBR28, and gliosis, measured using the myo-inositol signal, were found to be directly correlated in the motor cortex (164).

Machine learning classifiers

One of the overarching aims in advanced neuroimaging biomarker development in neurodegenerative disorders like ALS is the observer-independent classification of imaging data for individual patient's stratification for later use in multicenter therapeutic trials; to this end, there is a rapidly growing interest in Machine Learning (ML) models, classifiers, and predictive modeling in ALS (165). The choice of the ML model in ALS neuroimaging needs to be carefully tailored to a proposed application based on the characteristics of the available data and the profile of the candidate model, as proposed by Grollemund et al. (166). A recent systematic review on MRI feature selection for ML-based neuroimaging classifiers in ALS suggested the integration of DTI, volumetric, and texture data (167), but potential future applications might include a multiparametric MRI combination of more approaches such as intrinsic functional connectivity MRI. Connectome-based analyses of multiparametric MRI have already demonstrated their potential as a tool for patient stratification and as a prognostic biomarker in ALS to predict disease progression (154). PET/MRI is able to provide a multiparametric protocol, where a multimodal composite score may combine the aforementioned PET and MR techniques to address specific questions [e.g., (168)]—for a review see (169).

Summary

Neuroimaging fingerprinting of genetically defined ALS phenotypes will be important, especially longitudinal investigations of presymptomatic mutation carriers. Neuroimaging offers the possibility to undertake cross-sectional and longitudinal studies to stratify ALS patients according to their intrinsic progression rate, thus helping to optimize disease management, enhancing the design of drug trials, and guiding the use of individualized treatments when these become available. Recent research has contributed to the change in perception of neuroimaging in motor neuron disease, which traditionally had been primarily an academic tool with limited direct relevance to individualized patient care, but, with the advances in computational imaging, has emerged as a viable clinical tool with true biomarker potential (170).

MRI and PET provide methodologically different and partially complementary information on disease pathology. There are multiple aspects where applied neuroimaging and biomarker imaging strategies in neurodegenerative disease are influenced by and directly benefit from simultaneous PET/MRI:

- Concurrent acquisition and analysis augment the precision of partial volume correction for PET data by minimizing the main confounds introduced by small misregistration and data resampling inaccuracies of *post-hoc* coregistration of PET and segmented MRI acquired at different time points and in different scanner coordinate systems (171, 172).
- Novel regularized PET image reconstruction techniques based on anatomical priors derived from concurrent MRI significantly improve PET image quality (173–175).
- Novel readout and quantitation techniques including radiomics and machine learning/artificial intelligence informed algorithms benefit directly from inherently coregistered data and the high degree of standardization possible in PET/MRI, likely to result in improved performance of AI applications (176–180).
- Data consistency of simultaneous PET/MRI improves data pooling of different varieties of radioligands of the same functional target, assisting in moving toward multicenter therapeutic trials.
- Simultaneous PET/MRI and the inherent temporal synchronicity of findings will be instrumental in the development of tailored imaging probes or assessing the effects of drug challenges in treatments (181–184).
- PET/MRI enables to the design of more complex prospective trials using multiple tracers to characterize a disease, capitalizing on an intelligent spread of complex MR protocols over consecutive PET/MRI sessions using different tracers to max out the gain of information by each session and still ensure patient compliance (185).

Future developments may include a possible combination of rapid multi-tracer PET in a single PET/MRI session, making use of the high spatial information provided by MRI to improve signal separation in multi-tracer and multi-isotope studies, where typically staggered injection of ultra-short lived radionuclides combined with longer half-lived ones is practiced, and where spatial registration between different stages is crucial (186). Other future applications might include the combination of simultaneous PET/MRI with hyperpolarized MR imaging (187), to add even more layers of complementary metabolic information.

To summarize, the roles of MRI and PET as straight-forward diagnostic tools in ALS and further neurodegenerative disorders are emerging; the concepts to use them as a biological marker or as a read-out in clinical trials are existing and have to be probed for their clinical relevance. Combined PET/MRI has the potential as a future gold standard for characterizing motor-neuron disease and offers an important contribution to the standardization of imaging across multiple centers.

Author contributions

FJ, JK, and H-PM contributed to conception and design. FJ wrote the first draft of the manuscript and designed the figure and done the final revision of the manuscript. JK, H-PM, SK, and FA contributed complete sections. FW, AT,

WT, and RS performed a review for intellectual and scientific content. All authors contributed to the article and approved the submitted version.

Conflict of interest

FJ serves as Associate Editor for Frontiers in Neurology, Section Applied Neuroimaging and as Associate Editor for Frontiers in Oncology, Section Cancer Imaging and Image-directed Interventions. He has received the ALS Canada-Brain Canada Discovery Grant 2021 and receives or has received research operating funds from Biogen and the University of Alberta. SK has received research operating funds from Biogen. FA serves as Section Editor of NeuroImage: Clinical. She has received speaker honoraria from Roche and Biogen Idec; and receives or has received research supports from the Italian Ministry of Health, AriSLA (Fondazione Italiana di Ricerca per la SLA), the European Research Council and Foundation Research on Alzheimer Disease. H-PM serves as Associate Editor for Frontiers in Neurology, Section Applied Neuroimaging. JK serves as Specialty Chief Editor for Frontiers in Neurology, Section Applied Neuroimaging and as Associate Editor Neurology for Therapeutic Advances in Chronic Disease. He has received consulting fees as an advisory board member or honoraria as a speaker from AbbVie, BIAL, Biogen, Boehringer Ingelheim, Desitin, Esteve, Licher MT, Medtronic, Novartis, STADA, UCB Pharma, Zambon.

The remaining authors declare that the research was conducted in the absence of any commercial or financial relationships that could be construed as a potential conflict of interest.

Publisher's note

All claims expressed in this article are solely those of the authors and do not necessarily represent those of their affiliated organizations, or those of the publisher, the editors and the reviewers. Any product that may be evaluated in this article, or claim that may be made by its manufacturer, is not guaranteed or endorsed by the publisher.

References

1. Brooks BR. El escorial world federation of neurology criteria for the diagnosis of amyotrophic lateral sclerosis. *J Neurol Sci.* (1994) 124:96–107. doi: 10.1016/0022-510X(94)90191-0

2. Kassubek J, Pagani M. Imaging in amyotrophic lateral sclerosis: MRI and pet. *Curr Opin Neurol.* (2019) 32:740–6. doi: 10.1097/WCO.0000000000000728

3. Marini C, Cistaro A, Campi C, Calvo A, Caponnetto C. Flavio, et al. A Pet/Ct approach to spinal cord metabolism in amyotrophic lateral sclerosis. *Eur J Nucl Med Mol Imaging.* (2016) 43:2061–71. doi: 10.1007/s00259-016-3440-3

4. Massone AM, Campi C, Beltrametti MC, Marini C (editors). FDG-PET and the assessment of spinal cord metabolism in amyotrophic lateral sclerosis (ALS). In: *2016 IEEE Nuclear Science Symposium, Medical Imaging Conference and Room-Temperature Semiconductor Detector Workshop (NSS/MIC/RTSD)*, (2016).

5. Sala A, Iaccarino L, Fania P, Vanoli EG, Fallanca F, Pagnini C, et al. Testing the diagnostic accuracy of [18f]Fdg-pet in discriminating spinal- and bulbar-onset amyotrophic lateral sclerosis. *Eur J Nucl Med Mol Imaging.* (2019) 46:1117–31. doi: 10.1007/s00259-018-4246-2

6. Chiò A, Pagani M, Agosta F, Calvo A, Cistaro A, Filippi M. Neuroimaging in amyotrophic lateral sclerosis: Insights into structural and functional changes. *The Lancet Neurol.* (2014) 13:1228–40. doi: 10.1016/S1474-4422(14)70167-X

7. Chipika RH, Siah WF, McKenna MC, Li Hi Shing S, Hardiman O, Bede P. The presymptomatic phase of amyotrophic lateral sclerosis: are we merely scratching the surface? *J Neurol.* (2021) 268:4607–29. doi: 10.1007/s00415-020-10289-5

8. Müller H-P, Turner MR, Grosskreutz J, Abrahams S, Bede P, Govind V, et al. A large-scale multicentre cerebral diffusion tensor imaging study in amyotrophic lateral sclerosis. *J Neurol Neurosurg Psychiatry.* (2016) 87:570–9. doi: 10.1136/jnnp-2015-311952

9. Kalra S, Khan M, Barlow L, Beaulieu C, Benatar M, Briemberg H, et al. *The Canadian Als Neuroimaging Consortium (Calsnic) - a Multicentre Platform for Standardized Imaging and Clinical Studies in Als* (2020). Available online at: https://www.medrxiv.org/content/10.1101/2020.07.10.20142679v2 (accessed July 15, 2020).

10. Treit S, Steve T, Gross DW, Beaulieu C. High resolution *in-vivo* diffusion imaging of the human hippocampus. *Neuroimage.* (2018) 182:479–87. doi: 10.1016/j.neuroimage.2018.01.034

11. Agosta F, Spinelli EG, Filippi M. Neuroimaging in amyotrophic lateral sclerosis: current and emerging uses. *Expert Rev Neurother.* (2018) 18:395–406. doi: 10.1080/14737175.2018.1463160

12. Kalra S. Magnetic resonance spectroscopy in als. *Front Neurol.* (2019) 10:482. doi: 10.3389/fneur.2019.00482

13. Armstrong IS, Thomson KE, Rowley LM, McGowan DR. Harmonizing standardized uptake value recovery between two Pet/Ct systems from different manufacturers when using resolution modelling and time-of-flight. *Nucl Med Commun.* (2017) 38:650–5. doi: 10.1097/MNM.0000000000000682

14. de Jong EEC, van Elmpt W, Hoekstra OS, Groen HJM, Smit EF, Boellaard R, et al. Quality assessment of positron emission tomography scans: recommendations for future multicentre trials. *Acta Oncol.* (2017) 56:1459–64. doi: 10.1080/0284186X.2017.1346824

15. Namías M, Bradshaw T, Menezes VO, Machado MAD, Jeraj R. A novel approach for quantitative harmonization in pet. *Phys Med Biol.* (2018) 63:095019. doi: 10.1088/1361-6560/aabb5f

16. Ferretti A, Chondrogiannis S, Rampin L, Bellan E, Marzola MC, Grassetto G, et al. How to harmonize suvs obtained by hybrid Pet/Ct scanners with and without point spread function correction. *Phys Med Biol.* (2018) 63:235010. doi: 10.1088/1361-6560/aaee27

17. Agosta F, Altomare D, Festari C, Orini S, Gandolfo F, Boccardi M, et al. Clinical utility of Fdg-pet in amyotrophic lateral sclerosis and huntington's disease. *Eur J Nucl Med Mol Imaging.* (2018) 45:1546–56. doi: 10.1007/s00259-018-4033-0

18. Canosa A, Pagani M, Cistaro A, Montuschi A, Iazzolino B, Fania P, et al. 18f-Fdg-pet correlates of cognitive impairment in Als. *Neurology.* (2016) 86:44–9. doi: 10.1212/WNL.0000000000002242

19. Canosa A, Moglia C, Manera U, Vasta R, Torrieri MC, Arena V, et al. Metabolic brain changes across different levels of cognitive impairment in als: a (18)F-Fdg-pet study. *J Neurol Neurosurg Psychiatry.* (2020). doi: 10.1136/jnnp-2020-323876

20. Devrome M, Van Weehaeghe D, De Vocht J, Van Damme P, Van Laere K, Koole M. Glucose metabolic brain patterns to discriminate amyotrophic lateral sclerosis from parkinson plus syndromes. *Eur J Necl Med Mol Imaging Res.* (2018) 8:110. doi: 10.1186/s13550-018-0458-5

21. D'Hulst L, Van Weehaeghe D, Chiò AA-O, Calvo A, Moglia C, Canosa A, et al. Multicenter validation of [(18)F]-FDG PET and support-vector machine discriminant analysis in automatically classifying patients with amyotrophic lateral sclerosis versus controls. *Amyotroph Lateral Scler Frontotemporal Degener.* (2018) 19:570–7. doi: 10.1080/21678421.2018.1476548

22. Canosa A, Calvo A, Moglia C, Manera U, Vasta R, Di Pede F, et al. Brain metabolic changes across king's stages in amyotrophic lateral sclerosis: a (18)F-2-Fluoro-2-Deoxy-D-glucose-positron emission tomography study. *Eur J Nucl Med Mol Imaging.* (2021) 48:1124–33. doi: 10.1007/s00259-020-05053-w

23. Canosa A, Vacchiano V, D'Ovidio F, Calvo A, Moglia C, Manera U, et al. Brain metabolic correlates of apathy in amyotrophic lateral sclerosis: an 18f-Fdg-positron emission tomography study. *Eur J Neurol.* (2021) 28:745–53. doi: 10.1111/ene.14637

24. De Vocht J, Blommaert J, Devrome M, Radwan A, Van Weehaeghe D, De Schaepdryver M, et al. Use of multimodal imaging and clinical biomarkers in presymptomatic carriers of C9orf72 repeat expansion. *JAMA Neurol.* (2020) 77:1008–17. doi: 10.1001/jamaneurol.2020.1087

25. Canosa A, Calvo A, Moglia C, Vasta R, Palumbo F, Solero L, et al. Amyotrophic lateral sclerosis with sod1 mutations shows distinct brain metabolic changes. *Eur J Nucl Med Mol Imaging.* (2022) 49:2242–50. doi: 10.1007/s00259-021-05668-7

26. Pagani M, Chiò A, Valentini MC, Öberg J, Nobili F, Calvo A, et al. Functional pattern of brain Fdg-pet in amyotrophic lateral sclerosis. *Neurology.* (2014) 83:1067–74. doi: 10.1212/WNL.0000000000000792

27. Zanovello M, Soraru G, Campi C, Anglani M, Spimpolo A, Berti S, et al. Brain stem glucose hypermetabolism in amyotrophic lateral sclerosis/frontotemporal dementia and shortened survival: an (18)F-Fdg Pet/MRI Study. *J Nucl Med.* (2022) 63:777–84. doi: 10.2967/jnumed.121.262232

28. Sitte HH, Wanschitz J, Budka H, Berger ML. Autoradiography with [3h]Pk11195 of spinal tract degeneration in amyotrophic lateral sclerosis. *Acta Neuropathol.* (2001) 101:75–8. doi: 10.1007/s004010000312

29. Turner MR, Cagnin A, Turkheimer FE, Miller CCJ, Shaw CE, Brooks DJ, et al. Evidence of widespread cerebral microglial activation in amyotrophic lateral sclerosis: an [11c](R)-Pk11195 positron emission tomography study. *Neurobiol Dis.* (2004) 15:601–9. doi: 10.1016/j.nbd.2003.12.012

30. Suridjan I, Rusjan PM, Kenk M, Verhoeff NP, Voineskos AN, Rotenberg D, et al. Quantitative imaging of neuroinflammation in human white matter: a positron emission tomography study with translocator protein 18 Kda Radioligand, [18f]-Feppa. *Synapse.* (2014) 68:536–47. doi: 10.1002/syn.21765

31. Le Pogam A, Vercouilly J, Corcia P, Praline J, Guilloteau D, Baulieu JL, et al. Preliminary results of pet with 18f-Dpa 714 in humans for detection of microglial activation in amyotrophic lateral sclerosis (Als). *J Nucl Med.* (2008) 49(supplement 1):231P.

32. Radlinska BA, Ghinani SA, Lyon P, Jolly D, Soucy J-P, Minuk J, et al. Multimodal microglia imaging of fiber tracts in acute subcortical stroke. *Ann Neurol.* (2009) 66:825–32. doi: 10.1002/ana.21796

33. Koole M, Schmidt ME, Hijzen A, Ravenstijn P, Vandermeulen C, Van Weehaeghe D, et al. (18)F-Jnj-64413739, a novel pet ligand for the P2x7 ion channel: radiation dosimetry, kinetic modeling, test-retest variability, and occupancy of the P2x7 antagonist Jnj-54175446. *J Nucl Med.* (2019) 60:683–90. doi: 10.2967/jnumed.118.216747

34. Hagens MHJ, Golla SSV, Janssen B, Vugts DJ, Beaino W, Windhorst AD, et al. The P2x7 Receptor Tracer [11c]Smw139 as an *in vivo* marker of neuroinflammation in multiple sclerosis: a first-in man study. *Eur J Nucl Med Mol Imaging.* (2020) 47:379–89. doi: 10.1007/s00259-019-04550-x

35. Franceschini A, Capece M, Chiozzi P, Falzoni S, Sanz JM, Sarti AC, et al. The P2x7 receptor directly interacts with the Nlrp3 inflammasome scaffold protein. *FASEB J.* (2015) 29:2450–61. doi: 10.1096/fj.14-268714

36. Yiangou Y, Facer P, Durrenberger P, Chessell IP, Naylor A, Bountra C, et al. Cox-2, Cb2 and P2x7-immunoreactivities are increased in activated microglial cells/macrophages of multiple sclerosis and amyotrophic lateral sclerosis spinal cord. *BMC Neurol.* (2006) 6:12. doi: 10.1186/1471-2377-6-12

37. Gandelman M, Peluffo H, Beckman JS, Cassina P, Barbeito L. Extracellular Atp and the P2x7 receptor in astrocyte-mediated motor neuron death: implications for amyotrophic lateral sclerosis. *J Neuroinflamm.* (2010) 7:33. doi: 10.1186/1742-2094-7-33

38. Liu J, Prell T, Stubendorff B, Keiner S, Ringer T, Gunkel A, et al. Down-regulation of purinergic P2x7 receptor expression and intracellular calcium dysregulation in peripheral blood mononuclear cells of patients with amyotrophic lateral sclerosis. *Neurosci Lett.* (2016) 630:77–83. doi: 10.1016/j.neulet.2016.07.039

39. Ruiz-Ruiz C, Calzaferri F, García AG. P2x7 receptor antagonism as a potential therapy in amyotrophic lateral sclerosis. *Front Mol Neurosci.* (2020) 13:93. doi: 10.3389/fnmol.2020.00093

40. Bhardwaj A, Kaur J, Wuest M, Wuest F. *In situ* click chemistry generation of cyclooxygenase-2 inhibitors. *Natu Commun.* (2017) 8:1. doi: 10.1038/s41467-016-0009-6

41. Tietz O, Marshall A, Bergman C, Wuest M, Wuest F. Impact of structural alterations on the radiopharmacological profile of 18f-Labeled pyrimidines as cyclooxygenase-2 (Cox-2) imaging agents. *Nucl Med Biol.* (2018) 62–3:9–17. doi: 10.1016/j.nucmedbio.2018.05.001

42. Litchfield M, Wuest M, Glubrecht D, Wuest F. Radiosynthesis and biological evaluation of [18 F]triacoxib: a new radiotracer for pet imaging of Cox-2. *Mol Pharm.* (2020) 17:251–61. doi: 10.1021/acs.molpharmaceut.9b00986

43. Carrera-Juliá S, Moreno ML, Barrios C, de la Rubia Ortí JE, Drehmer E. Antioxidant alternatives in the treatment of amyotrophic lateral sclerosis: a comprehensive review. *Front Physiol.* (2020) 11:63. doi: 10.3389/fphys.2020.00063

44. McCombe PA, Lee JD, Woodruff TM, Henderson RD. The peripheral immune system and amyotrophic lateral sclerosis. *Front Neurol.* (2020) 11:279. doi: 10.3389/fneur.2020.00279

45. Luo Y, Xue H, Pardo AC, Mattson MP, Rao MS, Maragakis NJ. Impaired Sdf1/Cxcr4 signaling in glial progenitors derived from Sod1(G93a) mice. *J Neurosci Res.* (2007) 85:2422–32. doi: 10.1002/jnr.21398

46. Perner C, Perner F, Stubendorff B, Förster M, Witte OW, Heidel FH, et al. Dysregulation of chemokine receptor expression and function in leukocytes from als patients. *J Neuroinflamm.* (2018) 15:99. doi: 10.1186/s12974-018-1135-3

47. Calvo A, Moglia C, Canosa A, Cammarosano S, Ilardi A, Bertuzzo D, et al. Common polymorphisms of chemokine (C-X3-C Motif) receptor 1 gene modify amyotrophic lateral sclerosis outcome: a population-based study. *Muscle Nerve.* (2018) 57:212–6. doi: 10.1002/mus.25653

48. Lapa C, Kircher S, Schirbel A, Rosenwald A, Kropf S, Pelzer T, et al. Targeting Cxcr4 with [68ga]pentixafor: a suitable theranostic approach in pleural mesothelioma? *Oncotarget.* (2017) 8:96732–7. doi: 10.18632/oncotarget.18235

49. Kircher M, Herhaus P, Schottelius M, Buck AK, Werner RA, Wester H-J, et al. Cxcr4-directed theranostics in oncology and inflammation. *Ann Nucl Med.* (2018) 32:503–11. doi: 10.1007/s12149-018-1290-8

50. Burke BP, Miranda CS, Lee RE, Renard I, Nigam S, Clemente GS, et al. Copper-64 pet imaging of the cxcr4 chemokine receptor using a cross-bridged cyclam bis-tetraazamacrocyclic antagonist. *J Nucl Med.* (2020) 61:123–8. doi: 10.2967/jnumed.118.218008

51. Dawbarn D, Allen SJ. Neurotrophins and neurodegeneration. *Neuropathol Appl Neurobiol.* (2003) 29:211–30. doi: 10.1046/j.1365-2990.2003.00487.x

52. Bailey JJ, Kaiser L, Lindner S, Wust M, Thiel A, Soucy JP, et al. First-in-human brain imaging of [(18)F]Track, a pet tracer for tropomyosin receptor kinases. *ACS Chem Neurosci.* (2019) 10:2697–702. doi: 10.1021/acschemneuro.9b00144

53. Schirrmacher R, Bailey JJ, Mossine AV, Scott PJH, Kaiser L, Bartenstein P, et al. Radioligands for tropomyosin receptor kinase (Trk) positron emission tomography imaging. *Pharmaceuticals.* (2019) 12:7. doi: 10.3390/ph12010007

54. Singleton TA, Bdair H, Bailey JJ, Choi S, Aliaga A, Rosa-Neto P, et al. Efficient radiosynthesis and preclinical evaluation of [18 F]fompyd as a positron emission tomography tracer candidate for Trkb/C receptor imaging. *J Labell Comp Radiopharm.* (2020) 63:144–50. doi: 10.1002/jlcr.3827

55. Tuszynski MH, Yang JH, Barba D. U HS, Bakay RA, Pay MM, et al. Nerve growth factor gene therapy: activation of neuronal responses in Alzheimer disease. *JAMA Neurol.* (2015) 72:1139–47. doi: 10.1001/jamaneurol.2015.1807

56. Osborne A, Wang AXZ, Tassoni A, Widdowson PS, Martin KR. Design of a novel gene therapy construct to achieve sustained brain-derived neurotrophic factor signaling in neurons. *Hum Gene Ther.* (2018) 29:828–41. doi: 10.1089/hum.2017.069

57. Guo W, Pang K, Chen Y, Wang S, Li H, Xu Y, et al. Trkb agonistic antibodies superior to bdnf: utility in treating motoneuron degeneration. *Neurobiol Dis.* (2019) 132:104590. doi: 10.1016/j.nbd.2019.104590

58. Hammers A, Koepp MJ, Richardson MP, Hurlemann R, Brooks DJ, Duncan JS. Grey and white matter flumazenil binding in neocortical epilepsy with normal MRI. A pet study of 44 patients. *Brain.* (2003) 126:1300–18. doi: 10.1093/brain/awg138

59. Andersson JD, Matuskey D, Finnema SJ. Positron emission tomography imaging of the gamma-aminobutyric acid system. *Neurosci Lett.* (2019) 691:35–43. doi: 10.1016/j.neulet.2018.08.010

60. Yamauchi H, Kudoh T, Kishibe Y, Iwasaki J, Kagawa S. Selective neuronal damage and borderzone infarction in carotid artery occlusive disease: a 11c-flumazenil pet study. *J Nucl Med.* (2005) 46:1973–9.

61. Ihara M, Tomimoto H, Ishizu K, Yoshida H, Sawamoto N, Hashikawa K, et al. Association of vascular parkinsonism with impaired neuronal integrity in the striatum. *J Neural Transm.* (2007) 114:577–84. doi: 10.1007/s00702-006-0610-7

62. Mitterhauser M, Wadsak W, Wabnegger L, Mien LK, Tögel S, Langer O, et al. Biological evaluation of 2′-[18f]fluoroflumazenil ([18f]Ffmz), a potential gaba receptor ligand for pet. *Nucl Med Biol.* (2004) 31:291–5. doi: 10.1016/j.nucmedbio.2003.09.003

63. Lloyd CM, Richardson MP, Brooks DJ, Al-Chalabi A, Leigh PN. Extramotor involvement in Als: pet studies with the Gaba(a) Ligand [11c]Flumazenil. *Brain.* (2000) 123:2289–96. doi: 10.1093/brain/123.11.2289

64. Turner MR, Hammers A, Al-Chalabi A, Shaw CE, Andersen PM, Brooks DJ, et al. Cortical involvement in four cases of primary lateral sclerosis using [(11)C]-flumazenil pet. *J Neurol.* (2007) 254:1033–6. doi: 10.1007/s00415-006-0482-7

65. Wicks P, Turner MR, Abrahams S, Hammers A, Brooks DJ, Leigh PN, et al. Neuronal loss associated with cognitive performance in amyotrophic lateral sclerosis: an (11c)-flumazenil pet study. *Amyotr Lateral Scler.* (2008). doi: 10.1080/17482960701737716

66. Yabe I, Tsuji-Akimoto S, Shiga T, Hamada S, Hirata K, Otsuki M, et al. Writing errors in als related to loss of neuronal integrity in the anterior cingulate gyrus. *J Neurol Sci.* (2012) 315:55–9. doi: 10.1016/j.jns.2011.11.039

67. Millet P, Graf C, Buck A, Walder B, Ibáñez V. Evaluation of the reference tissue models for pet and spect benzodiazepine binding parameters. *Neuroimage.* (2002) 17:928–42. doi: 10.1006/nimg.2002.1233

68. Richardson MP, Fristen KJ, Sisodiya SM, Koepp MJ, Ashburner J, Free SL, et al. Cortical grey matter and benzodiazepine receptors in malformations of cortical development. A voxel-based comparison of structural and functional imaging data. *Brain.* (1997) 120:1961–73.

69. Bajjalieh SM, Frantz GD, Weimann JM, McConnell SK, Scheller RH. Differential expression of synaptic vesicle protein 2 (Sv2) isoforms. *J Neurosci.* (1994) 14:5223. doi: 10.1523/JNEUROSCI.14-09-05223.1994

70. Bartholome O, Van den Ackerveken P, Sanchez Gil J, de la Brassinne Bonardeaux O, Leprince P, Franzen R, et al. Puzzling out synaptic vesicle 2 family members functions. *Front Mol Neurosci.* (2017) 10:148. doi: 10.3389/fnmol.2017.00148

71. Mendoza-Torreblanca JG, Vanoye-Carlo A, Phillips-Farfan BV, Carmona-Aparicio L, Gomez-Lira G. Synaptic vesicle protein 2a: basic facts and role in synaptic function. *Eur J Neurosci.* (2013) 38:3529–39. doi: 10.1111/ejn.12360

72. Vogl C, Tanifuji S, Danis B, Daniels V, Foerch P, Wolff C, et al. Synaptic vesicle glycoprotein 2a modulates vesicular release and calcium channel function at peripheral sympathetic synapses. *Eur J Neurosci.* (2015) 41:398–409. doi: 10.1111/ejn.12799

73. Chen MK, Mecca AP, Naganawa M, Finnema SJ, Toyonaga T, Lin SF, et al. Assessing synaptic density in alzheimer disease with synaptic vesicle glycoprotein 2a positron emission tomographic imaging. *JAMA Neurol.* (2018) 75:1215–24. doi: 10.1001/jamaneurol.2018.1836

74. Malpetti M, Holland N, Jones PS, Ye R, Cope TE, Fryer TD, et al. Synaptic density in carriers of C9orf72 mutations: a [(11) C]Ucb-J Pet Study. *Ann Clin Transl Neurol.* (2021) 8:1515–23. doi: 10.1002/acn3.51407

75. Delva A, Van Weehaeghe D, Koole M, Van Laere K, Vandenberghe W. Loss of presynaptic terminal integrity in the substantia nigra in early Parkinson's disease. *Mov Disord.* (2020) 35:1977–86. doi: 10.1002/mds.28216

76. Holland N, Jones PS, Savulich G, Wiggins JK, Hong YT, Fryer TD, et al. Synaptic loss in primary tauopathies revealed by [(11) C]Ucb-J positron emission tomography. *Mov Disord.* (2020) 35:1834–42. doi: 10.1002/mds.28188

77. Holland N, Malpetti M, Rittman T, Mak EE, Passamonti L, Kaalund SS, et al. Molecular pathology and synaptic loss in primary tauopathies: an 18f-Av-1451 and 11c-Ucb-J Pet Study. *Brain.* (2022) 145:340–8. doi: 10.1093/brain/awab282

78. Finnema SJ, Toyonaga T, Detyniecki K, Chen MK, Dias M, Wang Q, et al. Reduced synaptic vesicle protein 2a binding in temporal lobe epilepsy: a [(11) C]Ucb-J positron emission tomography study. *Epilepsia.* (2020) 61:2183–93. doi: 10.1111/epi.16653

79. Crowder KM, Gunther JM, Jones TA, Hale BD, Zhang HZ, Peterson MR, et al. Abnormal neurotransmission in mice lacking synaptic vesicle protein 2a (Sv2a). *Proc Natl Acad Sci U A.* (1999) 96:15268–73. doi: 10.1073/pnas.96.26.15268

80. Crevecoeur J, Kaminski RM, Rogister B, Foerch P, Vandenplas C, Neveux M, et al. Expression pattern of synaptic vesicle protein 2 (Sv2) Isoforms in patients with temporal lobe epilepsy and hippocampal sclerosis. *Neuropathol Appl Neurobiol.* (2014) 40:191–204. doi: 10.1111/nan.12054

81. Lynch BA, Lambeng N, Nocka K, Kensel-Hammes P, Bajjalieh SM, Matagne A, et al. The synaptic vesicle protein Sv2a is the binding site for the antiepileptic drug levetiracetam. *Proc Natl Acad Sci USA.* (2004) 101:9861–6. doi: 10.1073/pnas.0308208101

82. Mutch SA, Kensel-Hammes P, Gadd JC, Fujimoto BS, Allen RW, Schiro PG, et al. Protein quantification at the single vesicle level reveals that a subset of synaptic vesicle proteins are trafficked with high precision. *J Neurosci.* (2011) 31:1461–70. doi: 10.1523/JNEUROSCI.3805-10.2011

83. Takamori S, Holt M, Stenius K, Lemke EA, Gronborg M, Riedel D, et al. Molecular anatomy of a trafficking organelle. *Cell.* (2006) 127:831–46. doi: 10.1016/j.cell.2006.10.030

84. Janz R, Goda Y, Geppert M, Missler M, Sudhof TC. Sv2a and Sv2b function as redundant Ca2+ regulators in neurotransmitter release. *Neuron.* (1999) 24:1003–16. doi: 10.1016/S0896-6273(00)81046-6

85. Yao J, Nowack A, Kensel-Hammes P, Gardner RG, Bajjalieh SM. Cotrafficking of Sv2 and synaptotagmin at the synapse. *J Neurosci.* (2010) 30:5569–78. doi: 10.1523/JNEUROSCI.4781-09.2010

86. Bretin F, Bahri MA, Bernard C, Warnock G, Aerts J, Mestdagh N, et al. Biodistribution and radiation dosimetry for the novel Sv2a Radiotracer [(18)F]Ucb-H: first-in-human study. *Mol Imaging Biol.* (2015) 17:557–64. doi: 10.1007/s11307-014-0820-6

87. Nabulsi NB, Mercier J, Holden D, Carr S, Najafzadeh S, Vandergeten MC, et al. Synthesis and preclinical evaluation of 11c-Ucb-J as a pet tracer for imaging the synaptic vesicle glycoprotein 2a in the brain. *J Nucl Med.* (2016) 57:777–84. doi: 10.2967/jnumed.115.168179

88. Finnema SJ, Nabulsi NB, Eid T, Detyniecki K, Lin S-F, Chen M-K, et al. Imaging synaptic density in the living human brain. *Sci Transl Med.* (2016) 8:348ra96. doi: 10.1126/scitranslmed.aaf6667

89. Naganawa M, Li S, Nabulsi N, Henry S, Zheng MQ, Pracitto R, et al. First-in-human evaluation of (18)F-Synvest-1, a radioligand for pet imaging of synaptic vesicle glycoprotein 2a. *J Nucl Med.* (2021) 62:561–7. doi: 10.2967/jnumed.120.249144

90. Cai Z, Li S, Zhang W, Pracitto R, Wu X, Baum E, et al. Synthesis and preclinical evaluation of an (18)F-labeled synaptic vesicle glycoprotein 2a pet imaging probe: [(18)F]Synvest-2. *ACS Chem Neurosci.* (2020) 11:592–603. doi: 10.1021/acschemneuro.9b00618

91. Sadasivam P, Fang XT, Toyonaga T, Lee S, Xu Y, Zheng MQ, et al. Quantification of Sv2a binding in rodent brain using [(18)F]synvest-1 and pet imaging. *Mol Imaging Biol.* (2021) 23:372–81. doi: 10.1007/s11307-020-01567-9

92. Kokubo Y. The current state of amyotrophic lateral sclerosis/parkinsonism-dementia complex in the Kii Peninsula, Japan, 2019. *Brain Nerve.* (2019) 71:1236–44. doi: 10.11477/mf.1416201433

93. Shinotoh H, Shimada H, Kokubo Y, Tagai K, Niwa F, Kitamura S, et al. Tau imaging detects distinctive distribution of tau pathology in Als/Pdc on the Kii Peninsula. *Neurology.* (2019) 92:e136–e47. doi: 10.1212/WNL.0000000000006736

94. Fujishiro H, Hasegawa M, Arai T. The molecular pathology of frontotemporal lobar degeneration. *Seishin Shinkeigaku Zasshi.* (2010) 112:313–24.

95. Muller HP, Brenner D, Roselli F, Wiesner D, Abaei A, Gorges M, et al. Longitudinal diffusion tensor magnetic resonance imaging analysis at the cohort level reveals disturbed cortical and callosal microstructure with spared corticospinal tract in the Tdp-43 (G298s) Als Mouse Model. *Transl Neurodegener.* (2019) 8:27. doi: 10.1186/s40035-019-0163-y

96. Kassubek J, Muller HP. Advanced neuroimaging approaches in amyotrophic lateral sclerosis: refining the clinical diagnosis. *Expert Rev Neurother.* (2020) 20:237–49. doi: 10.1080/14737175.2020.1715798

97. Ciccarelli O, Behrens TE, Johansen-Berg H, Talbot K, Orrell RW, Howard RS, et al. Investigation of white matter pathology in Als and Pls using tract-based spatial statistics. *Hum Brain Mapp.* (2009) 30:615–24. doi: 10.1002/hbm.20527

98. Filippini N, Douaud G, Mackay CE, Knight S, Talbot K, Turner MR. Corpus callosum involvement is a consistent feature of amyotrophic lateral sclerosis. *Neurology.* (2010) 75:1645–52. doi: 10.1212/WNL.0b013e3181fb84d1

99. Mori S, van Zijl PC. Fiber tracking: principles and strategies - a technical review. *NMR Biomed.* (2002) 15:468–80. doi: 10.1002/nbm.781

100. Basaia S, Filippi M, Spinelli EG, Agosta F. White matter microstructure breakdown in the motor neuron disease spectrum: recent advances using diffusion magnetic resonance imaging. *Front Neurol.* (2019) 10:193. doi: 10.3389/fneur.2019.00193

101. Braak H, Brettschneider J, Ludolph AC, Lee VM, Trojanowski JQ, Del Tredici K. Amyotrophic lateral sclerosis–a model of corticofugal axonal spread. *Nat Rev Neurol.* (2013) 9:708–14. doi: 10.1038/nrneurol.2013.221

102. Jucker M, Walker LC. Self-propagation of pathogenic protein aggregates in neurodegenerative diseases. *Nature.* (2013) 501:45–51. doi: 10.1038/nature12481

103. Kassubek J, Muller HP, Del Tredici K, Lulé D, Gorges M, Braak H, et al. Imaging the pathoanatomy of amyotrophic lateral sclerosis *in vivo*: targeting a propagation-based biological marker. *J Neurol Neurosurg Psychiatry.* (2018) 89:374–81. doi: 10.1136/jnnp-2017-316365

104. Muller HP, Agosta F, Gorges M, Kassubek R, Spinelli EG, Riva N, et al. Cortico-efferent tract involvement in primary lateral sclerosis and amyotrophic lateral sclerosis: a two-centre tract of interest-based DTI analysis. *Neuroimage Clin.* (2018) 20:1062–9. doi: 10.1016/j.nicl.2018.10.005

105. Gorges M, Del Tredici K, Dreyhaupt J, Braak H, Ludolph AC, Muller HP, et al. Corticoefferent pathology distribution in amyotrophic lateral sclerosis: *in vivo* evidence from a meta-analysis of diffusion tensor imaging data. *Sci Rep.* (2018) 8:15389. doi: 10.1038/s41598-018-33830-z

106. Kassubek J, Muller HP, Del Tredici K, Brettschneider J, Pinkhardt EH, Lulé D, et al. Diffusion tensor imaging analysis of sequential spreading of disease in amyotrophic lateral sclerosis confirms patterns of Tdp-43 pathology. *Brain.* (2014) 137(Pt 6):1733–40. doi: 10.1093/brain/awu090

107. Rosenbohm A, Muller HP, Hubers A, Ludolph AC, Kassubek J. Corticoefferent pathways in pure lower motor neuron disease: a diffusion tensor imaging study. *J Neurol.* (2016) 263:2430–7. doi: 10.1007/s00415-016-8281-2

108. Muller HP, Gorges M, Del Tredici K, Ludolph AC, Kassubek J. The same cortico-efferent tract involvement in progressive bulbar palsy and in 'classical' als: a tract of interest-based MRI study. *Neuroimage Clin.* (2019) 24:101979. doi: 10.1016/j.nicl.2019.101979

109. Rosenbohm A, Del Tredici K, Braak H, Huppertz HJ, Ludolph AC, Muller HP, et al. Involvement of cortico-efferent tracts in flail arm syndrome: a tract-of-interest-based DTI study. *J Neurol.* (2022) 269:2619–26. doi: 10.1007/s00415-021-10854-6

110. Hannaford A, Pavey N, van den Bos M, Geevasinga N, Menon P, Shefner JM, et al. Diagnostic utility of gold coast criteria in amyotrophic lateral sclerosis. *Ann Neurol.* (2021) 89:979–86. doi: 10.1002/ana.26045

111. Schuster C, Elamin M, Hardiman O, Bede P. Presymptomatic and longitudinal neuroimaging in neurodegeneration–from snapshots to motion picture: a systematic review. *J Neurol Neurosurg Psychiatry.* (2015) 86:1089–96. doi: 10.1136/jnnp-2014-309888

112. Agosta F, Pagani E, Petrolini M, Caputo D, Perini M, Prelle A, et al. Assessment of white matter tract damage in patients with amyotrophic lateral sclerosis: a diffusion tensor MR imaging tractography study. *Am J Neuroradiol.* (2010) 31:1457–61. doi: 10.3174/ajnr.A2105

113. Zhang Y, Schuff N, Woolley SC, Chiang GC, Boreta L, Laxamana J, et al. Progression of white matter degeneration in amyotrophic lateral sclerosis: a diffusion tensor imaging study. *Amyotroph Lateral Scler.* (2011) 12:421–9. doi: 10.3109/17482968.2011.593036

114. Kwan JY, Meoded A, Danielian LE, Wu T, Floeter MK. Structural imaging differences and longitudinal changes in primary lateral sclerosis and amyotrophic lateral sclerosis. *Neuroimage Clin.* (2012) 2:151–60. doi: 10.1016/j.nicl.2012.12.003

115. Abhinav K, Yeh FC, El-Dokla A, Ferrando LM, Chang YF, Lacomis D, et al. Use of diffusion spectrum imaging in preliminary longitudinal evaluation of amyotrophic lateral sclerosis: development of an imaging biomarker. *Front Hum Neurosci.* (2014) 8:270. doi: 10.3389/fnhum.2014.00270

116. Cardenas-Blanco A, Machts J, Acosta-Cabronero J, Kaufmann J, Abdulla S, Kollewe K, et al. Structural and diffusion imaging versus clinical assessment to monitor amyotrophic lateral sclerosis. *Neuroimage Clin.* (2016) 11:408–14. doi: 10.1016/j.nicl.2016.03.011

117. Broad RJ, Gabel MC, Dowell NG, Schwartzman DJ, Seth AK, Zhang H, et al. Neurite orientation and dispersion density imaging (noddi) detects cortical and corticospinal tract degeneration in Als. *J Neurol Neurosurg Psychiatry.* (2019) 90:404–11. doi: 10.1136/jnnp-2018-318830

118. Barritt AW, Gabel MC, Cercignani M, Leigh PN. Emerging magnetic resonance imaging techniques and analysis methods in amyotrophic lateral sclerosis. *Front Neurol.* (2018) 9:1065. doi: 10.3389/fneur.2018.01065

119. Turner MR, Grosskreutz J, Kassubek J, Abrahams S, Agosta F, Benatar M, et al. Towards a neuroimaging biomarker for amyotrophic lateral sclerosis. *Lancet Neurol.* (2011) 10:400–3. doi: 10.1016/S1474-4422(11)70049-7

120. Filippi M, Agosta F, Grosskreutz J, Benatar M, Kassubek J, Verstraete E, et al. Progress towards a neuroimaging biomarker for amyotrophic lateral sclerosis. *Lancet Neurol.* (2015) 14:786–8. doi: 10.1016/S1474-4422(15)00134-9

121. Pagani E, Hirsch JG, Pouwels PJ, Horsfield MA, Perego E, Gass A, et al. Intercenter differences in diffusion tensor MRI acquisition. *J Magn Reson Imaging.* (2010) 31:1458–68. doi: 10.1002/jmri.22186

122. Rosskopf J, Muller HP, Dreyhaupt J, Gorges M, Ludolph AC, Kassubek J. Ex post facto assessment of diffusion tensor imaging metrics from different MRI protocols: preparing for multicentre studies in Als. *Amyotroph Lateral Scler Frontotemporal Degener.* (2015) 16:92–101. doi: 10.3109/21678421.2014.977297

123. Kalra S, Muller HP, Ishaque A, Zinman L, Korngut L, Genge A, et al. A Prospective harmonized multicenter DTI study of cerebral white matter degeneration in Als. *Neurology.* (2020) 95:e943–52. doi: 10.1212/WNL.0000000000010235

124. Dadar M, Manera AL, Zinman L, Korngut L, Genge A, Graham SJ, et al. Cerebral atrophy in amyotrophic lateral sclerosis parallels the pathological distribution of Tdp43. *Brain Commun.* (2020) 2:fcaa061. doi: 10.1093/braincomms/fcaa061

125. Ta D, Ishaque A, Srivastava O, Hanstock C, Seres P, Eurich DT, et al. Progressive neurochemical abnormalities in cognitive and motor subgroups of amyotrophic lateral sclerosis: a prospective multicenter study. *Neurology.* (2021) 97:e803–13. doi: 10.1212/WNL.0000000000012367

126. Ishaque A, Ta D, Khan M, Zinman L, Korngut L, Genge A, et al. Distinct patterns of progressive gray and white matter degeneration in amyotrophic lateral sclerosis. *Hum Brain Mapp.* (2022) 43:1519–34. doi: 10.1002/hbm.25738

127. Ta D, Khan M, Ishaque A, Seres P, Eurich D, Yang YH, et al. Reliability of 3d texture analysis: a multicenter MRI study of the brain. *J Magn Reson Imaging.* (2020) 51:1200–9. doi: 10.1002/jmri.26904

128. Brenner D, Weishaupt JH. Update on amyotrophic lateral sclerosis genetics. *Curr Opin Neurol.* (2019) 32:735–9. doi: 10.1097/WCO.0000000000000737

129. Agosta F, Ferraro PM, Riva N, Spinelli EG, Domi T, Carrera P, et al. Structural and functional brain signatures of C9orf72 in motor neuron disease. *Neurobiol Aging.* (2017) 57:206–19. doi: 10.1016/j.neurobiolaging.2017.05.024

130. Floeter MK, Danielian LE, Braun LE, Wu T. Longitudinal diffusion imaging across the C9orf72 clinical spectrum. *J Neurol Neurosurg Psychiatry.* (2018) 89:53–60. doi: 10.1136/jnnp-2017-316799

131. Floeter MK, Gendron TF. Biomarkers for amyotrophic lateral sclerosis and frontotemporal dementia associated with hexanucleotide expansion mutations in C9orf72. *Front Neurol.* (2018) 9:1063. doi: 10.3389/fneur.2018.01063

132. Westeneng HJ, Walhout R, Straathof M, Schmidt R, Hendrikse J, Veldink JH, et al. Widespread structural brain involvement in als is not limited to the C9orf72 repeat expansion. *J Neurol Neurosurg Psychiatry.* (2016) 87:1354–60. doi: 10.1136/jnnp-2016-313959

133. Müller HP, Lule D, Roselli F, Behler A, Ludolph AC, Kassubek J. Segmental involvement of the corpus callosum in C9orf72-associated als: a tract of interest-based DTI study. *Ther Adv Chronic Dis.* (2021) 12:20406223211002969. doi: 10.1177/20406223211002969

134. Müller H-P, Del Tredici K, Lulé D, Müller K, Weishaupt JH, Ludolph AC, et al. *In vivo* histopathological staging in C9orf72-associated als: a tract of interest DTI study. *NeuroImage Clin.* (2020) 27:102298. doi: 10.1016/j.nicl.2020.102298

135. Benatar M, Turner MR, Wuu J. Defining pre-symptomatic amyotrophic lateral sclerosis. *Amyotroph Lateral Scler Frontotemporal Degener.* (2019) 20:303–9. doi: 10.1080/21678421.2019.1587634

136. Benatar M, Wuu J, McHutchison C, Postuma RB, Boeve BF, Petersen R, et al. Preventing amyotrophic lateral sclerosis: insights from pre-symptomatic neurodegenerative diseases. *Brain.* (2021) 145:27–44. doi: 10.1093/brain/awab404

137. Lulé DE, Muller HP, Finsel J, Weydt P, Knehr A, Winroth I, et al. Deficits in verbal fluency in presymptomatic C9orf72 mutation gene carriers-a developmental disorder. *J Neurol Neurosurg Psychiatry.* (2020) 91:1195–200. doi: 10.1136/jnnp-2020-323671

138. Querin G, Bede P, El Mendili MM Li M, Pelegrini-Issac M, Rinaldi D, et al. Presymptomatic spinal cord pathology in C9orf72 mutation carriers: a longitudinal neuroimaging study. *Ann Neurol.* (2019) 86:158–67. doi: 10.1002/ana.25520

139. Mohammadi B, Kollewe K, Samii A, Krampfl K, Dengler R, Münte TF. Changes of resting state brain networks in amyotrophic lateral sclerosis. *Exp Neurol.* (2009) 217:147–53. doi: 10.1016/j.expneurol.2009.01.025

140. Fekete T, Zach N, Mujica-Parodi LR, Turner MR. Multiple kernel learning captures a systems-level functional connectivity biomarker signature in amyotrophic lateral sclerosis. *PLoS ONE.* (2014) 8:e85190. doi: 10.1371/journal.pone.0085190

141. Trojsi F, Esposito F, de Stefano M, Buonanno D, Conforti FL, Corbo D, et al. Functional overlap and divergence between Als and Bvftd. *Neurobiol Aging.* (2015) 36:413–23. doi: 10.1016/j.neurobiolaging.2014.06.025

142. Douaud G, Filippini N, Knight S, Talbot K, Turner MR. Integration of structural and functional magnetic resonance imaging in amyotrophic lateral sclerosis. *Brain.* (2011) 134(Pt 12):3470–9. doi: 10.1093/brain/awr279

143. Agosta F, Canu E, Inuggi A, Chiò A, Riva N, Silani V, et al. Resting state functional connectivity alterations in primary lateral sclerosis. *Neurobiol Aging.* (2014) 35:916–25. doi: 10.1016/j.neurobiolaging.2013.09.041

144. Agosta F, Canu E, Valsasina P, Riva N, Prelle A, Comi G, et al. Divergent brain network connectivity in amyotrophic lateral sclerosis. *Neurobiol Aging.* (2013) 34:419–27. doi: 10.1016/j.neurobiolaging.2012.04.015

145. Luo C, Chen Q, Huang R, Chen X, Chen K, Huang X, et al. Patterns of spontaneous brain activity in amyotrophic lateral sclerosis: a resting-state Fmri Study. *PLoS ONE.* (2012) 7:e45470-e. doi: 10.1371/journal.pone.0045470

146. Schulthess I, Gorges M, Müller HP, Lulé D, Del Tredici K, Ludolph AC, et al. Functional connectivity changes resemble patterns of Ptdp-43 pathology in amyotrophic lateral sclerosis. *Sci Rep.* (2016) 6:38391. doi: 10.1038/srep38391

147. Castelnovo V, Canu E, Calderaro D, Riva N, Poletti B, Basaia S, et al. Progression of brain functional connectivity and frontal cognitive dysfunction in Als. *Neuroimage Clin.* (2020) 28:102509. doi: 10.1016/j.nicl.2020.102509

148. Agosta F, Valsasina P, Absinta M, Riva N, Sala S, Prelle A, et al. Sensorimotor functional connectivity changes in amyotrophic lateral sclerosis. *Cereb Cortex.* (2011) 21:2291–8. doi: 10.1093/cercor/bhr002

149. Menke RAL, Proudfoot M, Talbot K, Turner MR. The two-year progression of structural and functional cerebral MRI in amyotrophic lateral sclerosis. *Neuroimage Clin.* (2018) 17:953–61. doi: 10.1016/j.nicl.2017.12.025

150. Verstraete E, Veldink JH, van den Berg LH, van den Heuvel MP. Structural brain network imaging shows expanding disconnection of the motor system in amyotrophic lateral sclerosis. *Hum Brain Mapp.* (2014) 35:1351–61. doi: 10.1002/hbm.22258

151. Buchanan CR, Pettit LD, Storkey AJ, Abrahams S, Bastin ME. Reduced structural connectivity within a prefrontal-motor-subcortical network in amyotrophic lateral sclerosis. *J Magn Reson Imaging.* (2015) 41:1342–52. doi: 10.1002/jmri.24695

152. van der Burgh HK, Westeneng HJ, Walhout R, van Veenhuijzen K, Tan HHG, Meier JM, et al. Multimodal longitudinal study of structural brain involvement in amyotrophic lateral sclerosis. *Neurology.* (2020) 94:e2592–604. doi: 10.1212/WNL.0000000000009498

153. Schmidt R, de Reus MA, Scholtens LH, van den Berg LH, van den Heuvel MP. Simulating disease propagation across white matter connectome reveals anatomical substrate for neuropathology staging in amyotrophic lateral sclerosis. *Neuroimage.* (2016) 124(Pt A):762–9. doi: 10.1016/j.neuroimage.2015.04.005

154. Meier JM, van der Burgh HK, Nitert AD, Bede P, de Lange SC, Hardiman O, et al. Connectome-based propagation model in amyotrophic lateral sclerosis. *Ann Neurol.* (2020) 87:725–38. doi: 10.1002/ana.25706

155. Zhou C, Hu X, Hu J, Liang M, Yin X, Chen L, et al. Altered brain network in amyotrophic lateral sclerosis: a resting graph theory-based network study at voxel-wise level. *Front Neurosci.* (2016) 10:204. doi: 10.3389/fnins.2016.00204

156. Geevasinga N, Korgaonkar MS, Menon P, Van den Bos M, Gomes L, Foster S, et al. Brain functional connectome abnormalities in amyotrophic lateral sclerosis are associated with disability and cortical hyperexcitability. *Eur J Neurol.* (2017) 24:1507–17. doi: 10.1111/ene.13461

157. Cividini C, Basaia S, Spinelli EG, Canu E, Castelnovo V, Riva N, et al. Amyotrophic lateral sclerosis-frontotemporal dementia: shared and divergent neural correlates across the clinical spectrum. *Neurology.* (2021) 98:e402–15. doi: 10.1212/wnl.0000000000013123

158. Basaia S, Agosta F, Cividini C, Trojsi F, Riva N, Spinelli EG, et al. Structural and functional brain connectome in motor neuron diseases: a multicenter MRI study. *Neurology.* (2020) 95:e2552–64. doi: 10.1212/WNL.0000000000010731

159. Caldwell S, Rothman DL. (1)H Magnetic resonance spectroscopy to understand the biological basis of als, diagnose patients earlier, and monitor disease progression. *Front Neurol.* (2021) 12:701170. doi: 10.3389/fneur.2021.701170

160. Cheong I, Marjanska M, Deelchand DK, Eberly LE, Walk D, Oz G. Ultra-high field proton MR spectroscopy in early-stage amyotrophic lateral sclerosis. *Neurochem Res.* (2017) 42:1833–44. doi: 10.1007/s11064-017-2248-2

161. Atassi N, Xu M, Triantafyllou C, Keil B, Lawson R, Cernasov P, et al. Ultra high-field (7tesla) magnetic resonance spectroscopy in amyotrophic lateral sclerosis. *PLoS ONE.* (2017) 12:e0177680. doi: 10.1371/journal.pone.0177680

162. Foerster BR, Pomper MG, Callaghan BC, Petrou M, Edden RA, Mohamed MA, et al. An imbalance between excitatory and inhibitory neurotransmitters in amyotrophic lateral sclerosis revealed by use of 3-T proton magnetic resonance spectroscopy. *JAMA Neurol.* (2013) 70:1009–16. doi: 10.1001/jamaneurol.2013.234

163. Weerasekera A, Peeters R, Sima D, Dresselaers T, Sunaert S, De Vocht J, et al. Motor cortex metabolite alterations in amyotrophic lateral sclerosis assessed *in vivo* using edited and non-edited magnetic resonance spectroscopy. *Brain Res.* (2019) 1718:22–31. doi: 10.1016/j.brainres.2019.04.018

164. Ratai EM, Alshikho MJ, Zurcher NR, Loggia ML, Cebulla CL, Cernasov P, et al. Integrated imaging of [(11)C]-Pbr28 pet, MR diffusion and magnetic resonance spectroscopy (1)H-Mrs in amyotrophic lateral sclerosis. *Neuroimage Clin.* (2018) 20:357–64. doi: 10.1016/j.nicl.2018.08.007

165. Bede P. From qualitative radiological cues to machine learning: MRI-based diagnosis in neurodegeneration. *Futur Neurol.* (2017) 12:5–8. doi: 10.2217/fnl-2016-0029

166. Grollemund V, Pradat PF, Querin G, Delbot F, Le Chat G, Pradat-Peyre JF, et al. Machine learning in amyotrophic lateral sclerosis: achievements, pitfalls, and future directions. *Front Neurosci.* (2019) 13:135. doi: 10.3389/fnins.2019.00135

167. Kocar TD, Muller HP, Ludolph AC, Kassubek J. Feature selection from magnetic resonance imaging data in als: a systematic review. *Ther Adv Chronic Dis.* (2021) 12:20406223211051002. doi: 10.1177/20406223211051002

168. Lulé D, Michels S, Finsel J, Braak H, Del Tredici K, Strobel J, et al. Clinicoanatomical substrates of selfish behaviour in amyotrophic lateral sclerosis - an observational cohort study. *Cortex.* (2022) 146:261–70. doi: 10.1016/j.cortex.2021.11.009

169. Bede P, Hardiman O. Lessons of als imaging: pitfalls and future directions - a critical review. *Neuroimage Clin.* (2014) 4:436–43. doi: 10.1016/j.nicl.2014.02.011

170. Bede P, Querin G, Pradat PF. The changing landscape of motor neuron disease imaging: the transition from descriptive studies to precision clinical tools. *Curr Opin Neurol.* (2018) 31:431–8. doi: 10.1097/WCO.0000000000000569

171. Greve DN, Salat DH, Bowen SL, Izquierdo-Garcia D, Schultz AP, Catana C, et al. Different partial volume correction methods lead to different conclusions: an (18)F-Fdg-pet study of aging. *Neuroimage.* (2016) 132:334–43. doi: 10.1016/j.neuroimage.2016.02.042

172. Hellem MNN, Vinther-Jensen T, Anderberg L, Budtz-Jorgensen E, Hjermind LE, Larsen VA, et al. Hybrid 2-[18f] Fdg Pet/MRI in premanifest huntington's disease gene-expansion carriers: the significance of partial volume correction. *PLoS ONE.* (2021) 16:e0252683. doi: 10.1371/journal.pone.0252683

173. Kang SK, Lee JS. Anatomy-guided pet reconstruction usingl1bowsher prior. *Phys Med Biol.* (2021) 66. doi: 10.1088/1361-6560/abf2f7

174. Xie N, Gong K, Guo N, Qin Z, Wu Z, Liu H, et al. Penalized-likelihood pet image reconstruction using 3d structural convolutional sparse coding. *IEEE Trans Biomed Eng.* (2022) 69:4–14. doi: 10.1109/TBME.2020.3042907

175. Xie Z, Li T, Zhang X, Qi W, Asma E, Qi J. Anatomically aided pet image reconstruction using deep neural networks. *Med Phys.* (2021) 48:5244–58. doi: 10.1002/mp.15051

176. Wang J, Guo K, Cui B, Hou Y, Zhao G, Lu J. Individual [(18)F]Fdg Pet and functional MRI based on simultaneous Pet/MRI may predict seizure recurrence after temporal lobe epilepsy surgery. *Eur Radiol.* (2022) 32:3880–8. doi: 10.1007/s00330-021-08490-9

177. Gong K, Catana C, Qi J, Li Q. Direct reconstruction of linear parametric images from dynamic pet using nonlocal deep image prior. *IEEE Trans Med Imaging.* (2022) 41:680–9. doi: 10.1109/TMI.2021.3120913

178. Poirier SE, Kwan BYM, Jurkiewicz MT, Samargandy L, Steven DA, Suller-Marti A, et al. (18)F-Fdg pet-guided diffusion tractography reveals white matter abnormalities around the epileptic focus in medically refractory epilepsy: implications for epilepsy surgical evaluation. *Eur J Hybrid Imaging.* (2020) 4:10. doi: 10.1186/s41824-020-00079-7

179. Ladefoged CN, Hansen AE, Henriksen OM, Bruun FJ, Eikenes L, Oen SK, et al. Ai-driven attenuation correction for brain pet/MRI: clinical evaluation of a dementia cohort and importance of the training group size. *Neuroimage.* (2020) 222:117221. doi: 10.1016/j.neuroimage.2020.117221

180. Tondo G, Esposito M, Dervenoulas G, Wilson H, Politis M, Pagano G. Hybrid Pet- MRI applications in movement disorders. *Int Rev Neurobiol.* (2019) 144:211–57. doi: 10.1016/bs.irn.2018.10.003

181. Schoenberger M, Schroeder FA, Placzek MS, Carter RL, Rosen BR, Hooker JM, et al. *In vivo* [(18)F]Ge-179 brain signal does not show nmda-specific modulation with drug challenges in rodents and nonhuman primates. *ACS Chem Neurosci.* (2018) 9:298–305. doi: 10.1021/acschemneuro.7b00327

182. Wimalarathne DDN, Ruan W, Sun X, Liu F, Gai Y, Liu Q, et al. Impact of tof on brain pet with short-lived (11)C-labeled tracers among suspected patients with Ad/Pd: using hybrid Pet/MRI. *Front Med.* (2022) 9:823292. doi: 10.3389/fmed.2022.823292

183. Delva A, Van Weehaeghe D, van Aalst J, Ceccarini J, Koole M, Baete K, et al. Quantification and discriminative power of (18)F-Fe-Pe2i pet in patients with parkinson's disease. *Eur J Nucl Med Mol Imaging.* (2020) 47:1913–26. doi: 10.1007/s00259-019-04587-y

184. Van Weehaeghe D, Koole M, Schmidt ME, Deman S, Jacobs AH, Souche E, et al. [(11)C]Jnj54173717, a Novel P2x7 receptor radioligand as marker for neuroinflammation: human biodistribution, dosimetry, brain kinetic modelling and quantification of brain P2x7 receptors in patients with Parkinson's disease and healthy volunteers. *Eur J Nucl Med Mol Imaging.* (2019) 46:2051–64. doi: 10.1007/s00259-019-04369-6

185. Emsell L, Laroy M, Van Cauwenberge M, Vande Casteele T, Vansteelandt K, Van Laere K, et al. The leuven late life depression (L3d) study: pet-MRI biomarkers of pathological brain ageing in late-life depression: study protocol. *BMC Psychiatry.* (2021) 21:64. doi: 10.1186/s12888-021-03063-y

186. Kadrmas DJ, Hoffman JM. Methodology for quantitative rapid multi-tracer pet tumor characterizations. *Theranostics.* (2013) 3:757–73. doi: 10.7150/thno.5201

187. Li Y, Vigneron DB, Xu D. Current human brain applications and challenges of dynamic hyperpolarized carbon-13 labeled pyruvate MR metabolic imaging. *Eur J Nucl Med Mol Imaging.* (2021) 48:4225–35. doi: 10.1007/s00259-021-05508-8

frontiers | Frontiers in Neurology

TYPE Systematic Review
PUBLISHED 18 August 2022
DOI 10.3389/fneur.2022.972336

OPEN ACCESS

EDITED BY
Jan Kassubek,
University of Ulm, Germany

REVIEWED BY
Elanagan Nagarajan,
University of Tennessee at Chattanooga, United States
Antonio Giorgio,
University of Siena, Italy

*CORRESPONDENCE
Ching-Hui Sia
ching_hui_sia@nuhs.edu.sg

†These authors share first authorship

SPECIALTY SECTION
This article was submitted to Applied Neuroimaging, a section of the journal Frontiers in Neurology

RECEIVED 18 June 2022
ACCEPTED 25 July 2022
PUBLISHED 18 August 2022

CITATION
Yeo JYP, Goh CXY, Tan YK, Sim BTS, Chan BLX, Syn NL, Lim Y, Chan ACY, Sharma VK, Ong JJY, Yeo LLL, Sia C-H and Tan BYQ (2022) Evaluating the relationship between right-to-left shunt and white matter hyperintensities in migraine patients: A systematic review and meta-analysis. *Front. Neurol.* 13:972336. doi: 10.3389/fneur.2022.972336

Evaluating the relationship between right-to-left shunt and white matter hyperintensities in migraine patients: A systematic review and meta-analysis

Joshua Y. P. Yeo[1†], Claire X. Y. Goh[2†], Ying Kiat Tan[2], Bryan T. S. Sim[2], Beverly L. X. Chan[2], Nicholas L. Syn[2], Yinghao Lim[3], Amanda C. Y. Chan[4], Vijay K. Sharma[2], Jonathan J. Y. Ong[4], Leonard L. L. Yeo[2], Ching-Hui Sia[2]* and Benjamin Y. Q. Tan[2]

[1]Department of Medicine, National University Health System, Singapore, Singapore, [2]Yong Loo Lin School of Medicine, National University of Singapore, Singapore, Singapore, [3]Department of Cardiology, National University Heart Centre, Singapore, Singapore, [4]Division of Neurology, Department of Medicine, National University Health System, Singapore, Singapore

Introduction: White matter hyperintensities (WMHs) have been observed with greater frequency in patients with migraine and are thought to be associated with impaired cognition and function. The relationship between WMHs and right-to-left shunt (RLS) in migraine patients is unknown. We performed a systematic review to determine if there is an association between RLS and WMHs in patients with migraine.

Methods: A systematic search of the literature was performed in PubMed and Embase using a suitable keyword search strategy from inception up to 16th June 2021. All studies that included patients with migraine and studied RLS and WMHs were included.

Results: A total of 8 non-randomized observational studies comprising 1125 patients with migraine were included; 576 had an RLS, compared to 549 patients with no RLS. The mean age of the study populations ranged from 28.4 to 43 years, while the average duration from migraine diagnosis ranged from 5.1 to 19 years. The proportion of female to male patients was consistently higher in all studies (60.0–94.4%). Amongst migraine patients with RLS, 338 patients (58.7%) had WMHs. In contrast, 256 (46.6%) of migraine patients without RLS had WMHs. RLS was significantly associated with the presence of WMHs in migraine patients (OR: 1.56, 95% CI: 1.05–2.34, $p = 0.03$).

Conclusion: In migraine patients, RLS was significantly associated with the presence of WMHs. Longitudinal studies are warranted to establish RLS as a risk factor for WMHs in patients with migraine, and to establish the significance of these changes.

KEYWORDS

migraine, migraine with aura, white matter, patent foramen ovale, ultrasonography, doppler, transcranial, arteriovenous malformations

Introduction

White matter hyperintensities (WMHs) have been observed with greater frequency in patients with migraine. A recent review showed that in a patient population of <50 years old without risk factors, WMH prevalence of up to 70% was noted in patients with migraine with a 3.9-fold increase in the odds of WMH being present compared with controls. This effect was less obvious in population-based studies that included patients up to 74 years old or only included patients older than 55 years old, leading the reviewers to conclude that the effect of migraine on developing WMH may be overwhelmed by other risk factors in middle age (1). An earlier study that used a 1.5T magnetic resonance (MR) scanner reported a 39% prevalence (2); later studies with higher resolution MR imaging with 3T showed a prevalence closer to 70% in patients with migraine without traditional cardiovascular risk factors (3, 4). Two longitudinal studies also showed more rapid progression of deep WMHs in female patients with migraine compared to controls (5, 6). WMHs are inversely associated with mobility, cognition and function (7). In a recent study, baseline WMHs were found to be associated with poorer functional status and cognition as measured by mini-mental state examination (MMSE), while progression of WMHs was associated with a decrease in executive function score (8). Other types of migraines have also been evaluated for relationships with WMH; of interest, 1 population study was found which sporadic hemiplegic migraines (SMH) to patients with migraine and found no significant difference in the overall rate of WMH (9). This study did not review any association with vascular risk factors or RLS.

There is recent interest in the relationship between migraine, aura status and RLS (1, 10, 11). One hypothesis is that vasoactive substances bypass the pulmonary circulation to directly enter the systemic circulation in patients with RLS, inducing migraine attacks and the aura symptoms (12). While some studies reported an association of RLS with migraine with aura (2), other studies showed no difference in the prevalence of RLS between migraine subtypes (10, 11). Of the types of RLS, a patent foramen ovale (PFO) is the most common and is present in >25% of the healthy population (13), while other subtypes such as pulmonary arteriovenous malformations are rarer and associated with specific hereditary conditions (14). Accordingly, various clinical trials have sought to demonstrate a reduction in migraine frequency post-RLS closure. The MIST trial showed no significant difference between patients who had PFO closure vs. patients who had a sham procedure done (15). It is worth noting that the primary outcome studied was complete cessation of migraines and might not have been able to detect subtle improvements. Subsequent trials performed include the PRIMA and PREMIUM trials (16, 17); PRIMA failed to show a reduction in its primary endpoint (reduction in days with migraine) while PREMIUM showed a statistically significant reduction in headache days (secondary endpoint) but again failed to show a reduction in its primary outcome (responder rate with 50% reduction in migraine attacks).

Given the uncertain relationship between RLS and WMHs in patients with migraine, we performed a systematic review and meta-analysis of the literature to describe the prevalence of WMHs in migraine patients with or without RLS.

Abbreviations: WMH, white matter hyperintensities; RLS, right-to-left shunt; MR, magnetic resonance; PFO, patent foramen ovale; PRISMA, Preferred Reporting Items of Systematic Reviews and Meta-Analysis; TEE, transesophageal echocardiography.

Methods

Search strategy

We conducted the systematic review in accordance with the Preferred Reporting Items of Systematic Reviews and Meta-Analysis (PRISMA) guidelines. A literature search was performed on PubMed and Embase for articles published from inception up to 16th June 2021. The search strategy consisted of combinations of the following search terms relating to migraines, (e.g. "migraine," "migraine with aura," "MWOA," "migraine without aura") white matter lesions (e.g. "white matter lesions," "WML," "WMH," "white matter hyperintensit*," "leukoenceplaopa*," "leukoaraiosis," "silent brain infarct*," "SBI," "ischemic brain lesions") and RLS (e.g "patent foramen ovale," "PFO," "pulmonary arteriovenous malformations," "RLS," "RILES" and "right to left shunt"). The references from included studies were searched to detect studies missed by the electronic search. The search was performed by two independent reviewers (JY and CG), with any disagreements regarding study relevance resolved by a senior author (BT).

Eligibility criteria

The study population included patients diagnosed with migraine. We included all studies that reported the prevalence of WMHs and evaluated the presence of RLS in patients with migraine. Identification and confirmation of WMHs using MR imaging was required. The presence of RLS was defined as any abnormal communication between right and left cardiac chambers including patent foramen ovale, atrial septal defects and pulmonary arteriovenous malformation. Seven of the studies employed contrast-enhanced transcranial Doppler (TCD) at rest and with Valsalva, while one study used echocardiographic data (precise modality not stated). All the studies except for one (not reported) employed a 1.5T MRI scanner for diagnosis of WMHs. Only studies

published in the English language and included the full text (not conference proceedings) were included. All the studies that were included relied on the International Headache Society criteria for classification of migraines (18). We excluded studies that were reviews, case reports, case series, studies that studied pediatric populations, studies that did not diagnose WMHs on MRI, and studies that did not report RLS. The specific inclusion and exclusion criteria are detailed in Table 1.

Data extraction

Quantitative data collected was extracted from the included studies by two authors (JY and BS). Absolute numbers were included along with the percentages as appropriate. Where available, the data included study design, study population, duration of disease, type of migraine/WMHs and patient demographics (age and gender). We also included descriptions of how RLS or WMHs were diagnosed. Where data were reported in an incomplete fashion, we contacted the authors to obtain the relevant data.

Risk of bias assessment

The quality and risk of bias of included studies were assessed using the GRADE Assessment Tool and the Newcastle Ottawa Scale respectively. The GRADE Assessment tool assesses quality of evidence in terms of study limitations, inconsistency, indirectness, imprecision and publication bias. The Newcastle Ottawa scale evaluates quality of evidence based on selection of study groups (4/5 points), comparability of groups (2 points), and ascertainment of exposure and outcomes (3 points). These were graded with the consensus of 3 researchers (YKT, CG & BT).

Statistical analysis

We performed a random-effects meta-analysis on the odds ratio of outcome identified (prevalence of WMHs), comparing patients with migraine with and without RLS. Further analysis with pooled effect size estimates was performed on two studies which reported adjusted odds ratios. Numerical data points were presented with the absolute number or means as appropriate. Categorical variables were stated as percentages. Heterogeneity was assessed with the I^2 statistic. All data analysis was conducted using the Cochrane Collaboration's Review Manager (RevMan 5.4) Software Package. A $p < 0.05$ was taken as the criterion for statistical significance.

Results

Study assessment and grading

A total of 4,926 studies were identified on initial search, of which 8 were finally selected (19–26) for analysis. The study selection process is illustrated in the PRISMA flowchart (Figure 1).

Study characteristics

Among the 8 studies included for analysis, there were 5 cross-sectional studies, 2 case-control studies and 1 prospective cohort study. All studies included patients with migraine, but with different migraine subtypes. Three studies included only migraine with aura (22, 23, 25), one study included only migraine without aura (26), three studies included both migraine with and without aura (19, 20, 24), and one study did not specify the subtype of migraine (21).

A total of 1125 patients with migraine were included across all studies, with the number of patients in each study varying from 40 to 334. The mean age of the study populations ranged from 28.4 to 43 years, while the average duration from migraine onset ranged from 5.1 to 19 years. The proportion of female to male patients was consistently higher in all studies (60.0% to 94.4%). All studies diagnosed WMHs on MR imaging with at least 2 independent neurologists or neuroradiologists, except one study which did not specify. Characteristics of all the included studies are reported in Table 2. Of the 1125 patients, 576 (58.7%) of patients had a RLS. Three of the studies reported the specific type of RLS (Table 3) while the others left the type unspecified.

Prevalence of white matter hyperintensities

With regards to prevalence of WMHs, a total of 1,125 patients across all 8 studies were assessed. Amongst migraine patients with RLS, 338 patients (58.7%) had WMHs. In comparison, 256 (46.6%) of migraine patients without RLS had WMHs. RLS was associated with a higher prevalence of WMHs in patients with migraine (OR: 1.56, 95% CI: 1.05–2.34), with low-moderate heterogeneity ($I^2 = 48\%$) as shown in Figure 2. To mitigate the effect of known confounders such as age, hypertension, smoking and sex, studies which reported adjusted odds ratios were analyzed for a pooled effect size estimate. As illustrated in Figure 3, the pooled effect size estimate for RLS showed that there was a significantly larger number of patients with WMHs in migraine patients with RLS, compared to those without RLS (OR: 3.84, 95% CI: 2.05–7.19).

TABLE 1 PECOS (Population Exposure Comparison Outcomes Study Design) table.

PECOS	Inclusion criteria	Exclusion criteria
Population	Patients with migraine	Stroke/pediatric population
		WMH not diagnosed on MRI
		No mention of RLS
Exposure	Presence of RLS (patent foramen ovale, pulmonary arteriovenous malformation, atrial septal defect)	
Comparison	Patients with migraine without any RLS	
Outcome	Prevalence of WMH	
Study design	Articles in English	Articles not available in English
	Published up to 16th June 2021	Conference abstracts or poster presentations for which full text unavailable
	Database: PubMed and Embase	Studies that were not observational cohort studies

WMH, white matter hyperintensities; MRI, magnetic resonance imaging; RLS, right-to-left shunt.

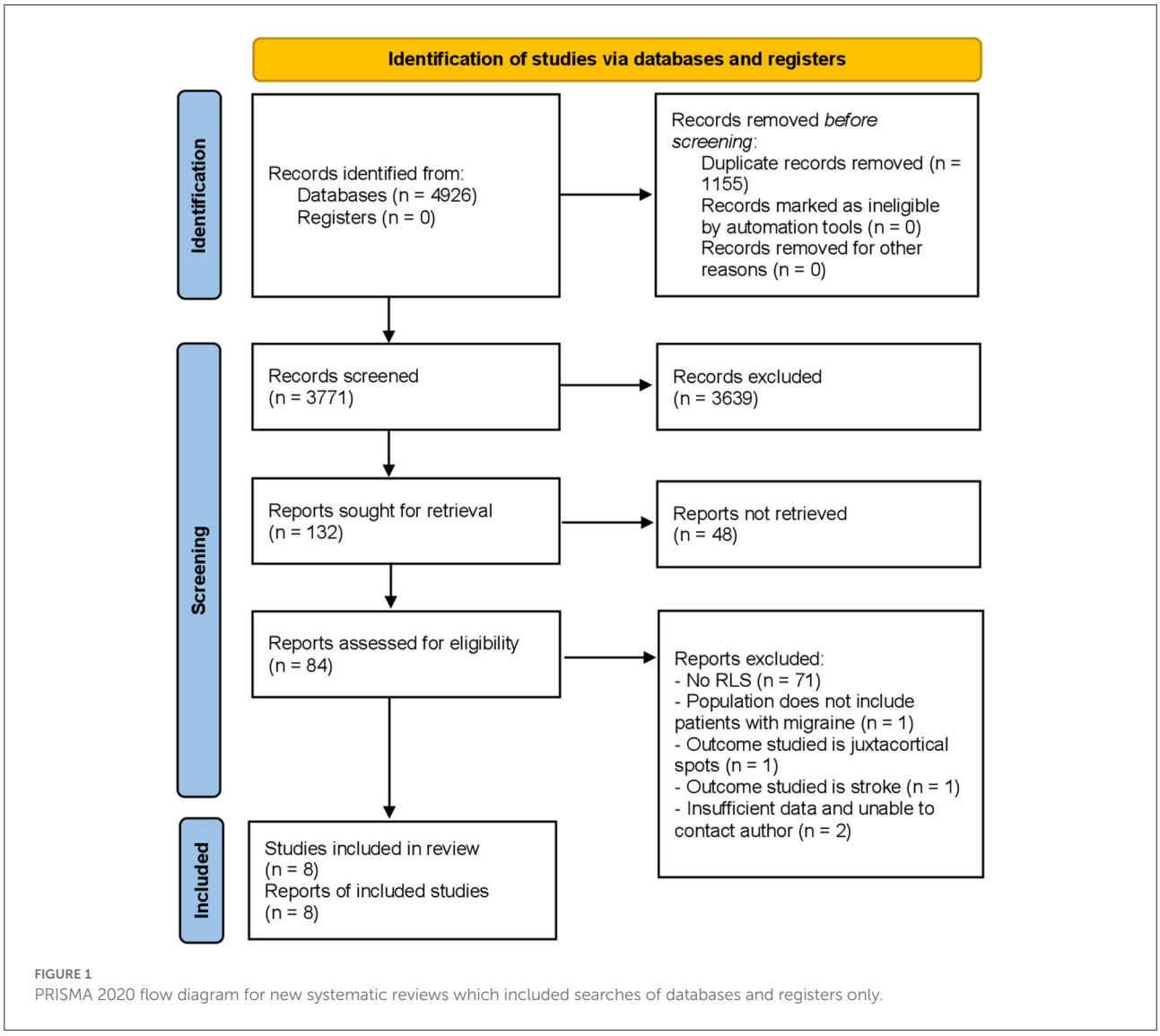

FIGURE 1
PRISMA 2020 flow diagram for new systematic reviews which included searches of databases and registers only.

TABLE 2 Characteristics of included studies.

References	Study design	Patients	Age (mean otherwise stated)	Females (%)	Duration of disease	Migraine type	WML diagnosed by	MRI magnet strength	Type of WMH reported	Analysis
Del Sette et al. (23)	Cross-sectional study	80	37.2	Not reported	16.14	Migraine with aura	2 neuroradiologists	1.5T	Not specified	Mann–Whitney *U*-test Kruskal–Wallis ANOVA test Spearman rank order test
Rao et al. (24)	Case-control study	100	40	60 (60.0)	19	Both with and without aura	2 neuroradiologist	Not specified	Not specified	Pearson χ^2 tests
Adami et al. (22)	Cross-sectional study	185	36	143 (77.3)	Not reported	Migraine with aura	1 neuroradiologist and 2 neurologists	1-1.5T	PV-WML, D-WML	Pearson χ^2 Fisher exact, unpaired t, and Mann–Whitney *U*-tests Spearman rank correlation tests Logistic regression analysis
Park et al. (19)	Cross-sectional	242	28.4	183 (71.5)	5.1	Both with and without aura	2 neurologists	1.5T	D-WML	Pearson χ^2 tests Unpaired Student's *T*-tests Bootstrapping methods Multiple binary regression tests
Dinia et al. (25)	Prospective study	41	41.8	33 (80.5)	16.9	Migraine with aura	2 neuroradiologists	1.5T	Not specified	Mann-Whitney *U*-test Fisher's exact test Pearson's correlation test
Uçar et al. (26)	Case-control study	40	36.2	37 (90.0)	WMH group: 8 Control group: 4	Migraine without aura	Not reported	1.5T	Not specified	Pearson χ^2 test Fisher's exact tests Student t-test Mann–Whitney U-test Spearman correlation analysis
Iwasaki et al. (20)	Cross-sectional study	107	39.0 (median)	101 (94.4)	18.0 (median)	Both with and without aura	2 neurologists	1.5T	Not specified	Pearson χ^2 tests Mann–Whitney U test Logistic regression
Jiang et al. (21)	Cross-sectional study	334	43.0	241 (72.2)	11.69	Not specified	2 neurologists	1.5T	D-WML and PV-WML	Pearson's χ^2 test Unpaired *t*-tests Binary logistic regression models (odds ratio [OR], 95% confidence interval [CI]) for MRI outcomes

WMH, white matter hyperintensities; PV-WML, periventricular white matter lesions; D-WML, deep white matter lesions.

10.3389/fneur.2022.972336

TABLE 3 RLS reported in included studies.

References	Total patients	Presence of RLS	Number of RLS (percentage)	Method of diagnosis	Type of RLS reported
Del Sette et al. (23)	80	36	45%	Contrast-enhanced transcranial Doppler at rest and with Valsalva, counting micro-bubbles in MCA	Not specified
Rao et al. (24)	100	41	41.0%	Transcranial doppler	Patent foramen ovale
Adami et al. (22)	185	114	61.6%	Contrast-enhanced transcranial Doppler at rest and with Valsalva, counting micro-bubbles in MCA	Not specified
Park et al. (19)	242	89	36.8%	Contrast-enhanced multifrequency -transcranial Doppler at rest and with Valsalva, counting micro-embolic signals (MES) with RLS defined as ≥ 11 MESs.	Not specified
Dinia et al. (25)	41	13	31.7%	Contrasted transcranial doppler	Not specified
Uçar et al. (26)	40	2	5%	Echocardiographic data	Atrial septal defect, inter-atrial septum
Iwasaki et al. (20)	107	57	53.2%	Contrast-enhanced transcranial Doppler at rest and with Valsalva, counting high-intensity transient signals	Patent foramen ovale, pulmonary arteriovenous malformations
Jiang et al. (21)	334	224	67%	Contrast-enhanced transcranial Doppler at rest and with Valsalva, counting micro-bubbles in MCA	Not specified

RLS, right-to-left shunts; MCA, middle cerebral artery.

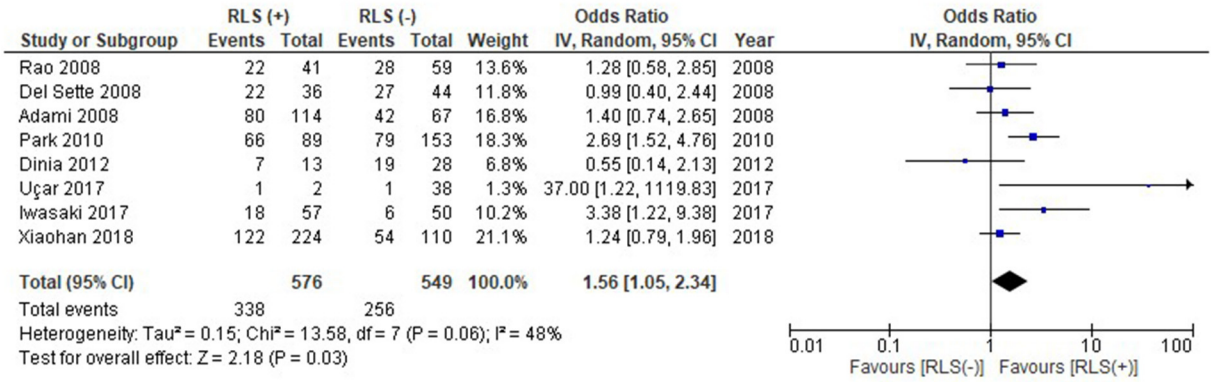

FIGURE 2
Forest plot of the association of RLS with prevalence of WMH (odds ratio).

Quality assessment

Using the GRADE tool, the quality of evidence was assessed to be high for prevalence of WMHs (Supplementary Table 1). Following assessment with the Newcastle-Ottawa scale, the cross-sectional studies achieved 9–10 out of a maximum 10 points on the Newcastle-Ottawa scale, while the lone cohort study achieved 9 out of a maximum of 9 points on the Newcastle-Ottawa Scale. This signifies the high quality and low risk of bias for selection for these studies. However, the case control studies achieved 7–8 points out of a maximum 9 points on the Newcastle-Ottawa scale, suggesting a moderate risk of bias for selection (Supplementary Tables 2–4).

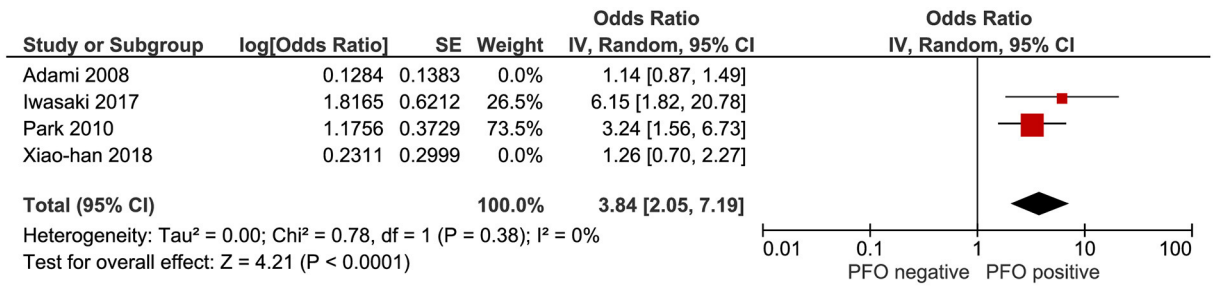

FIGURE 3
Forest plot of the association of RLS with prevalence of WMH (adjusted odds ratio).

Discussion

This study aimed to provide a comprehensive systematic review and meta-analysis of the available literature regarding prevalence of WMHs, and the mediating effect of RLS in patients with migraine. It demonstrates that there is a significant difference in the prevalence of WMHs in migraine patients with and without RLS.

RLS had previously been postulated as a possible mechanism of WMHs in patients with migraine (1). However, conflicting results have been reported. Five of the included studies suggested that RLS had no effect on the load or presence of WMHs in patients with migraine, while 3 studies did in fact show a statistically significant effect on the presence of WMHs (19–26). Our meta-analysis demonstrated a statistically significant difference with an odds ratio of 1.56 [95% CI, 1.05–2.34, $p = 0.03$], bolstering the case for RLS as a possible mechanism of WMHs in migraine patients. This effect was demonstrated as well with a pooled effect size estimate for the studies which reported an odds ratio adjusting for known confounders such as age, sex, smoking or hypertension.

Previous studies have noted an increase of up to 3.9 times in the odds of WMHs in patients with migraine compared to controls with a particularly strong effect in younger populations aged <50 with no vascular risk factors, possibly because vascular risk factors tend to overwhelm the relative contribution of migraine for the development of WMHs in older patients (10). Owing to the manner in which data was reported, we were unable to adjust for the effect of age in our study beyond the studies which reported an adjusted odds ratio.

Of interest, other studies have sought to show headache improvement in patients with migraine who undergo PFO closure (27, 28). It is postulated that incomplete transit of venous blood through the lung filter allows vasoactive substances to circumvent the filter and thus precipitate migraine attacks (29). Typically, headache improvement is assessed by clinical scoring systems such as the MIDAS questionnaire. Considering our study's findings, it may be worthwhile including outcomes related to WMH prevalence in PFO closure trials. A meta-analysis showed that there were significant associations between WMHs and incident stroke, incident dementia, global cognitive decline as well as mortality (30). WMHs may well be considered a suitable surrogate measure for these other clinical outcomes of stroke and cognitive decline. It may be appropriate to assess the effectiveness of PFO closure as a treatment in reducing incident stroke or cognitive impairment.

Strengths and limitations

This study reveals a potentially interesting relationship between WMHs and RLS in the context of patients with migraine. WMHs have been associated with stroke, dementia and mortality (30). Our findings support an association with RLS and to our knowledge is the first systematic review to aggregate existing studies regarding RLS in patients with migraine and WMH burden. This effect held with a pooled effect size estimate. While we found a significant association between RLS and WMH in migraine patients, the effect size was moderate and causality cannot be interpreted due to the retrospective nature of the studies that were included in this systematic review. Further longitudinal studies are necessary to establish causality between RLS and WMH in this patient cohort.

One important limitation was that the type of RLS was not always reported in the included studies. Only 3 studies (20, 24, 26) specified the type of RLS. Another limitation was that not all studies reported if the WMHs were in the periventricular or deep regions, nor were they classified in a standardized manner. Only 2 studies presented the data for both deep and periventricular regions, whilst 1 study reported on deep WMHs, with the remaining studies leaving the type of WMHs unspecified. Previous studies have suggested that periventricular WMHs were associated with impaired cognitive function, but less so if they were in the deep locations (31). Future studies that differentiate between the location of WMHs found in association with presence of RLS may prove to be more illuminating with regards to the clinical implications of our findings.

A further limitation worth considering is that the quantitative data reported was not granular enough to be stratified according to variables such as age or gender. This was partially mitigated by applying an analysis of the pooled effect size estimate where published in the studies reviewed. It should also be noted that not all studies consistently reported on the number, volume, confluence, accrual over time and gadolinium enhancement of the white matter hyperintensity lesions. As such, differential diagnoses like demyelinating disorders including multiple sclerosis may have been neglected in this meta-analysis.

Finally, an important limitation lies in the way that RLS was diagnosed. All the studies detected RLS *via* TCD, except for Uçar 2017 as opposed to the gold standard of diagnosis which remains transesophageal echocardiography (TEE). Studies comparing TCD vs. TEE found a higher sensitivity for TEE (31–33); it is notable that most of the advantage for TEE came from minimal shunts which may not be clinically relevant. More recent studies have suggested that TCD may have comparable sensitivity of 94–100% (34, 35) and remains valuable as a complementary, non-invasive option for screening, while TEE remains the best modality for delineating anatomy and detection of other cardiac abnormalities such as atrial septal defects (36).

Conclusion

In migraine patients, RLS was significantly associated with the presence of WMHs. Longitudinal studies are warranted to establish RLS as a risk factor for WMHs in patients with migraine, and to establish the significance of these changes.

Data availability statement

The original contributions presented in the study are included in the article/Supplementary material, further inquiries can be directed to the corresponding author.

Author contributions

JY: writing–original draft (lead), reviewing and editing (equal), investigation (equal), and formal analysis (equal). CG and YT: writing–original draft (supporting), reviewing and editing (equal), investigation (equal), and formal analysis (equal). BS: reviewing and editing (equal) and investigation (equal). BC, YL, AC, VS, and JO: reviewing and editing (equal). NS: reviewing and editing (equal) and methodology (equal). LY and C-HS: reviewing and editing (equal) and conceptualization (equal). BT: reviewing and editing (equal), methodology (equal), and conceptualization (equal). All authors contributed to the article and approved the submitted version.

Funding

LY was supported by the National Medical Research Council (NMRC), Singapore (NMRC/MOH-TA19Nov-003). C-HS was supported by the National University of Singapore Yong Loo Lin School of Medicine's Junior Academic Fellowship Scheme.

Conflict of interest

The authors declare that the research was conducted in the absence of any commercial or financial relationships that could be construed as a potential conflict of interest.

Publisher's note

All claims expressed in this article are solely those of the authors and do not necessarily represent those of their affiliated organizations, or those of the publisher, the editors and the reviewers. Any product that may be evaluated in this article, or claim that may be made by its manufacturer, is not guaranteed or endorsed by the publisher.

Supplementary material

The Supplementary Material for this article can be found online at: https://www.frontiersin.org/articles/10.3389/fneur.2022.972336/full#supplementary-material

References

1. Lee M, Moon S, Chung C. White matter hyperintensities in migraine: a review. *Precis Futur Med.* (2019) 3:146–57. doi: 10.23838/pfm.2019.00128

2. Fazekas F, Koch M, Schmidt R. 0ffenbacher H, Payer F, Freidl W et al. The prevalence of cerebral damage varies with migraine type: a MRI study headache. *J Head Face Pain.* (1992) 32:287–91. doi: 10.1111/j.1526-4610.1992.hed3206287.x

3. Cheng C, Cheng H, Chen S, Chung C, Lin Y, Hu H et al. White matter hyperintensities in migraine: Clinical significance and central pulsatile hemodynamic correlates. *Cephalalgia.* (2017) 38:1225–36. doi: 10.1177/0333102417728751

4. Lee M, Park B, Cho S, Park H, Chung C. Cerebrovascular reactivity as a determinant of deep white matter hyperintensities in migraine. *Neurology.* (2019) 92:e342–50. doi: 10.1212/WNL.0000000000006822

5. Palm-Meinders I, Koppen H, Terwindt G, Launer L, Konishi J, Moonen J et al. Structural brain changes in migraine. *JAMA.* (2012) 308:1889. doi: 10.1001/jama.2012.14276

6. Hamedani A, Rose K, Peterlin B, Mosley T, Coker L, Jack C et al. Migraine and white matter hyperintensities: the ARIC MRI study. *Neurology*. (2013) 81:1308–13. doi: 10.1212/WNL.0b013e3182a8235b

7. Wardlaw J, Valdés Hernández M, Muñoz-Maniega S. What are white matter hyperintensities made of? Relevance to vascular cognitive impairment. *J Am Heart Assoc*. (2015) 4:001140. doi: 10.1161/JAHA.114.001140

8. Pantoni L. 2001–2011: A Decade of the LADIS (Leukoaraiosis And DISability) study: what have we learned about white matter changes and small-vessel disease? *Cerebrovasc Dis*. (2011) 32:577–88. doi: 10.1159/000334498

9. Nagarajan E. "Author Index." *Cephalalgia*. (2004) 24:1104–11. doi: 10.1111/j.1468-2982.2004.00921.x

10. Swartz R, Kern R. Migraine is associated with magnetic resonance imaging white matter abnormalities. *Arch Neurol*. (2004) 61:1366. doi: 10.1001/archneur.61.9.1366

11. Dobrynina L, Suslina A, Gubanova M, Belopasova A, Sergeeva A, Evers S et al. White matter hyperintensity in different migraine subtypes. *Sci Rep*. (2021) 11:10881. doi: 10.1038/s41598-021-90341-0

12. Liu K, Wang B, Hao Y, Song S, Pan M. The correlation between migraine and patent foramen ovale. *Front Neurol*. (2020) 11:543485. doi: 10.3389/fneur.2020.543485

13. Homma S, Sacco R. Patent foramen ovale and stroke. *Circulation*. (2005) 112:1063–72. doi: 10.1161/CIRCULATIONAHA.104.524371

14. Swanson K, Prakash U, Stanson A. Pulmonary arteriovenous fistulas: mayo clinic experience, 1982-1997. *Mayo Clin Proc*. (1999) 74:671–80. doi: 10.4065/74.7.671

15. Dowson A, Mullen M, Peatfield R, Muir K, Khan A, Wells C et al. Migraine Intervention With STARFlex Technology (MIST) trial. *Circulation*. (2008) 117:1397–404. doi: 10.1161/CIRCULATIONAHA.107.727271

16. Mattle H, Evers S, Hildick-Smith D, Becker W, Baumgartner H, Chataway J et al. Percutaneous closure of patent foramen ovale in migraine with aura, a randomized controlled trial. *Eur Heart J*. (2016) 37:2029–36. doi: 10.1093/eurheartj/ehw027

17. Tobis J, Charles A, Silberstein S, Sorensen S, Maini B, Horwitz P et al. Percutaneous closure of patent foramen ovale in patients with migraine. *J Am Coll Cardiol*. (2017) 70:2766–74. doi: 10.1016/j.jacc.2017.09.1105

18. Headache Classification Subcommittee of the International Headache Society. The international classification of headache disorders, 2nd edn. *Cephalalgia*. (2004) 24 (Suppl 1):9–160. doi: 10.1111/j.1468-2982.2003.00824.x

19. Park H, Lee S, Kim S, Yun C, Kim S. Small deep white matter lesions are associated with right-to-left shunts in migraineurs. *J Neurol*. (2010) 258:427–33. doi: 10.1007/s00415-010-5771-5

20. Iwasaki A, Suzuki K, Takekawa H, Takashima R, Suzuki A, Suzuki S et al. The relationship between right-to-left shunt and brain white matter lesions in Japanese patients with migraine: a single center study. *J Headache Pain*. (2017) 18:3. doi: 10.1186/s10194-016-0714-x

21. Jiang X, Wang S, Tian Q, Zhong C, Zhang G, Li Y, et al. Right-to-left shunt and subclinical ischemic brain lesions in Chinese migraineurs: a multicentre MRI study. *BMC Neurol*. (2018) 18:18. doi: 10.1186/s12883-018-1022-7

22. Adami A, Rossato G, Cerini R, Thijs V, Pozzi-Mucelli R, Anzola G et al. Right-to-left shunt does not increase white matter lesion load in migraine with aura patients. *Neurology*. (2008) 71:101–7. doi: 10.1212/01.wnl.0000316798.25510.f2

23. Del Sette M, Dinia L, Bonzano L, Roccatagliata L, Finocchi C, Parodi R et al. White Matter lesions in migraine and right-to-left shunt: a conventional and diffusion MRI study. *Cephalalgia*. (2008) 28:376–82. doi: 10.1111/j.1468-2982.2008.01544.x

24. Rao R, Rosati A, Liberini P, Gipponi S, Venturelli E, Sapia E et al. Cerebrovascular risk factors and MRI abnormalities in migraine. *Neurol Sci*. (2008) 29:144–5. doi: 10.1007/s10072-008-0907-4

25. Dinia L, Bonzano L, Albano B, Finocchi C, Del Sette M, Saitta L et al. White matter lesions progression in migraine with aura: a clinical and MRI longitudinal study. *J Neuroimag*. (2012) 23:47–52. doi: 10.1111/j.1552-6569.2011.00643.x

26. Ataç Uçar C. Cardiovascular risk factors and white matter hyperintensities in migraine without aura patients. *Agri*. (2017) 29:157–161. doi: 10.5505/agri.2017.43765

27. Shi Y, Lv J, Han X, Luo G. Migraine and percutaneous patent foramen ovale closure: a systematic review and meta-analysis. *BMC Cardiovasc Disord*. (2017) 17:203. doi: 10.1186/s12872-017-0644-9

28. Mojadidi M, Kumar P, Mahmoud A, Elgendy I, Shapiro H, West B, et al. Pooled analysis of PFO occluder device trials in patients with PFO and migraine. *J Am Coll Cardiol*. (2021) 77:667–76. doi: 10.1016/j.jacc.2020.11.068

29. Wilmshurst P, Nightingale S. The role of cardiac and pulmonary pathology in migraine: a hypothesis. *Headache*. (2006) 46:429–34. doi: 10.1111/j.1526-4610.2006.00374.x

30. Debette S, Markus H. The clinical importance of white matter hyperintensities on brain magnetic resonance imaging: systematic review and meta-analysis. *BMJ*. (2010) 341:c3666. doi: 10.1136/bmj.c3666

31. Tubi M, Feingold F, Kothapalli D, Hare E, King K, Thompson P et al. White matter hyperintensities and their relationship to cognition: effects of segmentation algorithm. *Neuroimage*. (2020) 206:116327. doi: 10.1016/j.neuroimage.2019.116327

32. Di Tullio M, Sacco R, Venketasubramanian N, Sherman D, Mohr J, Homma S. Comparison of diagnostic techniques for the detection of a patent foramen ovale in stroke patients. *Stroke*. (1993) 24:1020–4. doi: 10.1161/01.STR.24.7.1020

33. Job F, Ringelstein E, Grafen Y, Flachskampf F, Doherty C, Stockmanns A et al. Comparison of transcranial contrast Doppler sonography and transesophageal contrast echocardiography for the detection of patent foramen ovale in young stroke patients. *Am J Cardiol*. (1994) 74:381–4. doi: 10.1016/0002-9149(94)90407-3

34. Droste D, Schmidt-Rimpler C, Wichter T, Dittrich R, Ritter M, Stypmann J, et al. Right-to-left-shunts detected by transesophageal echocardiography and transcranial doppler sonography. *Cerebrovasc Dis*. (2003) 17:191–6. doi: 10.1159/000075790

35. Droste D, Lakemeier S, Wichter T, Stypmann J, Dittrich R, Ritter M et al. Optimizing the technique of contrast transcranial doppler ultrasound in the detection of right-to-left shunts. *Stroke*. (2002) 33:2211–6. doi: 10.1161/01.STR.0000027884.03365.AC

36. Blersch W, Draganski B, Holmer S, Koch H, Schlachetzki F, Bogdahn U, et al. Transcranial duplex sonography in the detection of patent foramen ovale. *Radiology*. (2002) 225:693–9. doi: 10.1148/radiol.2253011572

frontiers | Frontiers in Neurology

TYPE Original Research
PUBLISHED 12 September 2022
DOI 10.3389/fneur.2022.921984

OPEN ACCESS

EDITED BY
Hans-Peter Müller,
University of Ulm, Germany

REVIEWED BY
Christina Tsien,
Johns Hopkins Medicine, United States
Marita Partanen,
Princess Maxima Center for Pediatric Oncology, Netherlands

*CORRESPONDENCE
Melanie A. Morrison
melanie.morrison@ucsf.edu

†PRESENT ADDRESS
Erin Felton,
Sutter Santa Rosa Family Medicine Residency, Santa Rosa, CA, United States

SPECIALTY SECTION
This article was submitted to Applied Neuroimaging, a section of the journal Frontiers in Neurology

RECEIVED 17 April 2022
ACCEPTED 22 August 2022
PUBLISHED 12 September 2022

CITATION
Morrison MA, Walter S, Mueller S, Felton E, Jakary A, Stoller S, Molinaro AM, Braunstein SE, Hess CP and Lupo JM (2022) Functional network alterations in young brain tumor patients with radiotherapy-induced memory impairments and vascular injury. *Front. Neurol.* 13:921984. doi: 10.3389/fneur.2022.921984

Functional network alterations in young brain tumor patients with radiotherapy-induced memory impairments and vascular injury

Melanie A. Morrison[1]*, Sadie Walter[1,2], Sabine Mueller[3,4], Erin Felton[3†], Angela Jakary[1], Schuyler Stoller[3], Annette M. Molinaro[4,5], Steve E. Braunstein[6], Christopher P. Hess[1,3] and Janine M. Lupo[1]

[1]Department of Radiology and Biomedical Imaging, University of California, San Francisco, San Francisco, CA, United States, [2]College of Osteopathic Medicine, Pacific Northwest University of Health Sciences, Washington, DC, United States, [3]Department of Neurology, University of California, San Francisco, San Francisco, CA, United States, [4]Department of Neurological Surgery, University of California, San Francisco, San Francisco, CA, United States, [5]Department of Epidemiology & Biostatistics, University of California, San Francisco, San Francisco, CA, United States, [6]Department of Radiation Oncology, University of California, San Francisco, San Francisco, CA, United States

Background: Cognitive impairment and cerebral microbleeds (CMBs) are long-term side-effects of cranial radiation therapy (RT). Previously we showed that memory function is disrupted in young patients and that the rate of cognitive decline correlates with CMB development. However, vascular injury alone cannot explain RT-induced cognitive decline. Here we use resting-state functional MRI (rsfMRI) to further investigate the complex mechanisms underlying memory impairment after RT.

Methods: Nineteen young patients previously treated with or without focal or whole-brain RT for a brain tumor underwent cognitive testing followed by 7T rsfMRI and susceptibility-weighted imaging for CMB detection. Global brain modularity and efficiency, and rsfMRI signal variability within the dorsal attention, salience, and frontoparietal networks were computed. We evaluated whether MR metrics could distinguish age- and sex-matched controls ($N = 19$) from patients and differentiate patients based on RT exposure and aggressiveness. We also related MR metrics with memory performance, CMB burden, and risk factors for cognitive decline after RT.

Results: Compared to controls, patients exhibited widespread hyperconnectivity, similar modularity, and significantly increased efficiency ($p < 0.001$) and network variability ($p < 0.001$). The most abnormal values were detected in patients treated with high dose whole-brain RT, having supratentorial tumors, and who did not undergo RT but had hydrocephalus. MR metrics and memory performance were correlated ($R = 0.34–0.53$), though MR metrics were more strongly related to risk factors for cognitive worsening and CMB burden with evidence of functional recovery.

Conclusions: MR metrics describing brain connectivity and variability represent promising candidate imaging biomarkers for monitoring of long-term cognitive side-effects after RT.

KEYWORDS

fMRI, brain connectivity, 7T MRI, radiation therapy, brain tumors, memory, vascular injury

Introduction

The long-term effects of brain tumor therapies on neurocognitive function and the development of young patients are well known. In the years following radiation therapy (RT), a key contributor to these side-effects, gradual declines in intelligence quotient have been observed (1–3) with notable impairments in memory and executive function (4–6). Several groups have reported more severe impairments in patients treated with RT at younger ages, higher doses, larger irradiated volumes, and for specific tumor subtypes, based on whether they received proton vs. photon RT (1, 2, 4, 5, 7). The mechanisms underlying neurocognitive decline after RT are not fully understood but are thought to be related to RT-induced white matter necrosis, functional changes in neural networks (8), as well as vascular brain injuries that can be observed on magnetic resonance imaging (MRI) as early as 1-year following RT (4, 6, 9).

Previously we leveraged the enhanced spatial resolution and susceptibility contrast benefits of 7 Tesla (7T) susceptibility-weighted imaging (SWI) to investigate the relationship between RT-induced vascular injury and cognitive performance. Vascular injury, in the form of arterial thinning and tiny hemosiderin brain deposits called cerebral microbleeds (CMBs), worsened over time at the same rate with which verbal memory performance was declining (4, 10). Cross-sectional studies at lower field strengths have also linked RT-induced CMBs to cognition (6), which is not surprising as similar pathology has been shown to be related to the cognitive impairments experienced by dementia patients and even healthy aging adults (11, 12). The finding that irradiated patients without detectable white matter necrosis experience long-term cognitive deficits further emphasizes this link between vascular injury and cognition (8), however, vascular injury alone cannot explain other examples of neurocognitive decline such as in non-irradiated patients, suggesting a functional abnormality. While increased alterations in functional connectivity derived from functional MRI (fMRI) have indeed been associated with poorer neurocognitive performance before and after brain tumor therapy (13), there remains little functional data to explain long-term cognitive outcomes, especially after RT.

Resting-state functional MRI (rsfMRI) is a powerful research tool in clinical neuroscience that can detect network alterations by way of indirectly measuring spontaneous fluctuations in brain activity during rest (14). Within millimeter partitions of the brain, the time-varying amplitude of blood-oxygen metabolism in response to neural activity is recorded, and the spatiotemporal synchronicity of the rsfMRI "blood-oxygenation level dependent" (BOLD) signal between brain areas is typically evaluated to measure connection strength and define brain networks. Prior studies have used rsfMRI to demonstrate, for example, that adult survivors of childhood posterior fossa tumors have hyperconnected frontal brain areas relative to controls (15–17). Similarly, task-based fMRI studies involving neurocognitive testing during image acquisition, have revealed long-term functional differences in brain tumor patients as a result of treatment (17) and exposure to cognitive rehabilitative interventions (16, 18). The ability of fMRI to probe cognition (19–21) and predict neurocognitive outcomes in diverse patient groups (22–25) *via* the detection of network alterations, makes it especially useful for investigating the complex mechanisms underlying RT-induced neurocognitive decline. In this study, we acquired rsfMRI and SWI at 7T in a cohort of 19 patients previously treated for a brain tumor in order to relate measures of functional brain network organization and activity to memory performance and vascular injury alongside known clinical risk factors for cognitive decline after RT. Here 7T MRI was used strategically to achieve increased image spatial resolution, enhanced tissue susceptibility and BOLD signal contrast, and ultimately gains in statistical power (26, 27). We also performed a small reproducibility study to investigate the stability of our functional imaging metrics with different preprocessing and analysis parameters, given their known influence on fMRI reliability.

Methods

Participants

With institutional review board approval and parental or patient written informed consent, 19 patients (mean age 18 years, range 12–25 years; 47% female) previously treated for a brain tumor underwent 7T rsfMRI, SWI and T1-weighted

TABLE 1 Patient demographics.

Patient	Sex	Race	Cancer Type	Tumorlocation	RT	Age (years)		RT dose, max (Gy)	Surgery	Chemo	Other Dx
						RT	1st MRI				
1	M	Hispanic	Medu	p. fossa	wb	3	22	37, 53.5	gtr × 4	Vincristine	–
2	F	White	Medu	p. fossa	wb	18	22	36, 55.8	biopsy	Cisplatin, cyclophosphamide, vincristine	–
3	M	White	Medu	p. fossa	wb	14	22	23.5, 54	gtr	Carboplatin, CCNU, cytoxan, VP-16, vincristine	–
4	M	White	Medu	p. fossa	wb	6	25	36, 55	gtr	Carboplatin, CCNU, vincristine	Hypertension
5	M	White	Medu	p. fossa	wb	7	22	23.4, 55.8	gtr	CCNU, cisplatin, vincristine	–
6	M	White	Medu	p. fossa	wb	12	14	36, 54	str	Carboplatin, vincristine	–
7	F	White	Medu	p. fossa	wb	9	14	23.4, 54	gtr	Carboplatin, CCNU, cisplatin, cyclophosphamide, cytoxan, vincristine	–
8	M	Asian	Germ	Ventricle	wv	9	19	24, 45	ETV, biopsy	Carboplatin, VP-16	Diabetes, hydro cephalus
9	M	White	Germ	Ventricle	wv	22	22	18, 30	str	Carboplatin, etopside, ifosfamide	Diabetes
10	F	White	Germ	Ventricle	wv	9	22	24, 40.5	biopsy	Carboplatin, VP-16	Diabetes
11	F	Other	Germ	Ventricle	wv	12	14	18, 30	biopsy	Carboplatin, VP-16	Diabetes
12	F	Asian	Germ	Ventricle	wv	24	25	18, 33	biopsy	Carboplatin, VP-16	–
13*	M	White	PPT	p. fossa	wb	9	12	23.4, 54.9	gtr, ETV	Cisplatin, cyclophosphamide	Hydro cephalus, stroke
14	M	White	gAnglio	Occipital	focal	15	17	59.4, 59.4	gtr	Vemurafenib	–
15	M	Black	Astro	Parietal	focal	22	22	59.4, 59.4	gtr	–	–
16	F	White	OLIGO	Temporal	–	–	15	–	gtr	Everolimus	–
17	F	White	JPA	p. fossa	–	–	18	–	gtr	–	–
18	F	White	JPA	p. fossa	–	–	13	–	gtr	–	Hydro cephalus
19	F	Hispanic	JPA	p. fossa	–	–	14	–	ETV, biopsy	–	Hydro cephalus

medu, medulloblastoma; germ, germinoma; PPT, pineal parenchymal; ganglio, anaplastic ganglioglioma; astro, pleomorphic xanthoastrocytoma; oligo, oligodendroglioma; JPA, juvenile pilocytic astrocytoma; p.fossa, posterior fossa; wb, whole brain; wv, whole ventricular; n/a, data affected by motion; gtr, gross total resection; str, sub-total resection; ETV, endoscopic third ventriculostomy.

10.3389/fneur.2022.921984

imaging [see Table 1 for demographics and our prior work (4) for further details on the cohort and recruitment criteria]. Compared to 1.5 or 3T MRI, 7T imaging is associated with heightened risk of claustrophobia and more pronounced patient bioeffects such as dizziness due to the increased field strength, nonetheless the technique remains safe and was well-tolerated by the present cohort. Recruited patients were either non-irradiated or received RT at least 1 month prior to the MRI. Of the 19 patients, eight were treated with whole-brain RT (WBRT) for a medulloblastoma in the posterior fossa, except for one patient who had a pineal parenchymal tumor in the same location. Five patients were treated with whole-ventricular focal RT (WVRT) for a ventricular germinoma; two others were treated with supratentorial focal RT for gliomas located in the occipital and parietal lobe. The remaining four control patients were treated with surgery but not RT for lower-grade gliomas primarily in the posterior fossa. On average, the WBRT group (mean age 19.1 years, range 14–25) was treated 9.8 years prior (range 3.1–19.9); the focal group (including WVRT; mean age 20.1 years, range 14–25) 4.3 years prior (0.1–13); and non-irradiated controls (mean age 15 years, range 13–18) 3.7 years prior (range 0.8–8 years). While several patients had a history of hydrocephalus, a common side-effect of brain tumors linked to cognitive dysfunction (28), only two patients (#13 and #19 in Table 1) showed evidence of ventricle enlargement on MRI. A random selection of 19 age- and sex-matched healthy control data (approx. mean age 19 years, range 11–25; 47% female) from two publicly available 3T rsfMRI datasets (29, 30) were also evaluated in this study for comparison with the patient data (full datasets can be accessed *via* openneuro.org using data accession numbers ds000221 and ds000256).

Neurocognitive testing

Prior to the MRI exam, a battery of seven computerized cognitive tests (Cogstate, Inc.; Newhaven, CT) were administered (4). In a previous analysis of this cohort we found the verbal memory test involving recall of items on a shopping list (International Shopping List; ISL) to be most useful for distinguishing patients who were treated with vs. without RT (4). We therefore focused the present work on the ISL test and corresponding brain networks involved in episodic memory (31, 32). The total number of correct items recalled was converted into an age normalized z-score based on mean test scores of healthy controls from Cogstate's database.

Imaging protocols

Imaging was performed on a 7T General Electric (GE) Healthcare scanner equipped with a 2-channel transmit and 32-channel receive head coil. Resting-state fMRI scans were acquired using an interleaved, gradient-echo sequence with 125 time points [repetition time (TR) = 4 s, minimum echo time (TE), flip angle = 90, 1.8 mm isotropic resolution, 23 cm field-of-view (FOV)]. TRs for the public fMRI acquired at clinical field-strengths were 1.4 s (29) and 2.5 s (30). SWI and T1-weighted images were also acquired; key MR parameters for these sequences are included in Morrison et al. (4), with a more in-depth description of the simultaneous MRA-SWI sequence and reconstruction methods provided in Bian et al. (33).

Data analysis

We investigated aspects of brain network organization and activity from the rsfMRI data by computing: (1) theoretical graph metrics representing brain network modularity and efficiency and (2) measures of BOLD variability thought to represent the brain's cognitive flexibility, namely its ability to efficiently process and respond to unexpected external stimuli (34). These metrics were chosen as modularity has previously been shown to predict the efficacy of cognitive rehabilitative interventions in young adults (35), while efficiency appears to mediate risk for vascular injury and the development of cognitive impairments (36) and is linked to cognitive flexibility in pediatric brain tumor survivors (37).

fMRI preprocessing

Preprocessing was performed using the default pipeline in CONN (38). Steps included motion estimation and realignment correction, slice-timing correction, outlier detection, segmentation of the brain tissue, registration of the data to an atlas space (Montreal Neurological Institute (MNI) brain atlas), and spatial smoothing with an 8mm Gaussian kernel (Figures 1A,B). Bandpass filtering (0.01–0.25 Hz) and linear regression thereafter removed the effects of confounding covariates including outliers based on >2 mm translation (N_{max} = 30), motion parameters (N = 12), and noise components in regions dominated by the white matter (N = 15) and cerebrospinal fluid (N = 5). The same denoising parameters were used for all subjects but adjusted such that each subject's whole brain connectivity values were normally distributed after denoising while maintaining minimum 30 degrees of freedom.

Network modularity and efficiency

Graph metric analysis was performed using CONN (38) and the Brain Connectivity Toolbox (BTC) (39). For each subject, an adjacency matrix representing nondirected, whole brain functional connectivity was generated by correlating the mean BOLD signal across pairs of brain regions derived from 132 atlas parcellations (Figure 1C). In this way, the nodes of the graph represent the brain parcels, while the edges correspond

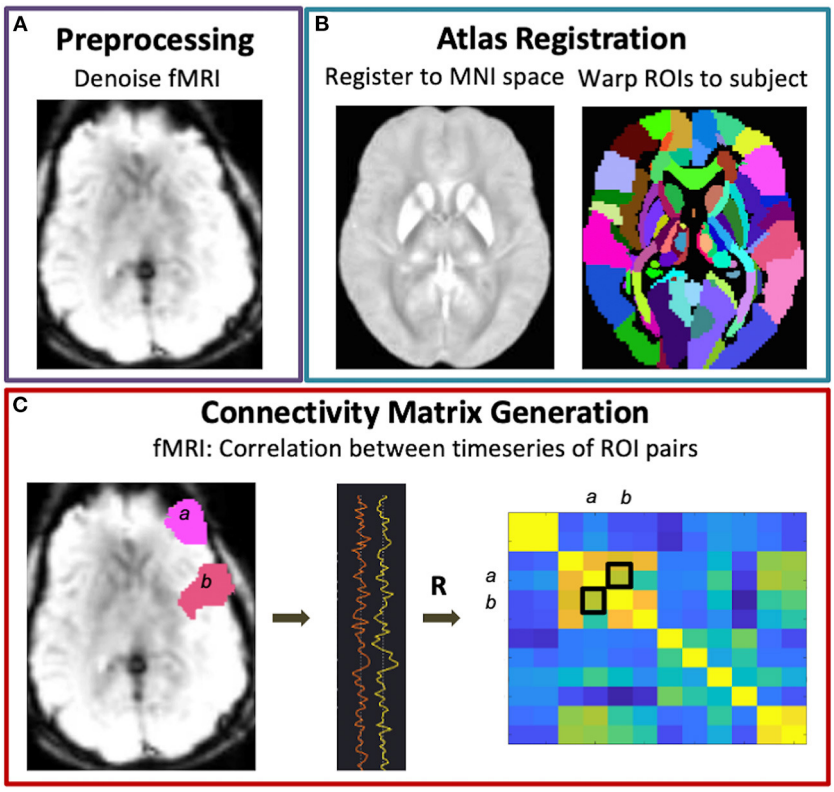

FIGURE 1
Functional connectivity matrix generation. Following fMRI data preprocessing **(A)** and warping of the brain atlas regions-of-interest (ROIs) to subject space **(B)**, connectivity matrices were generated *via* Pearson correlations between all pairs of brain ROIs **(C)**.

to connections. A threshold of $r > 0.5$ was applied to the subject-level matrices such that only positive, moderate-to-strong connections were used to compute global modularity and efficiency. Modularity is a measure of the degree to which the network is divided into smaller, nonoverlapping subgroups such that within-group edges are maximized while between-group edges are minimized, and was computed as

$$\sum_{i=1}^{N} \left(e_{ii} - a_i^2 \right) \quad (1)$$

where N is total number of subgroups, e_i is the proportion of edges connecting any two nodes within subgroup i, and $a_i$is the proportion of edges connecting an individual node in subgroup i to any other nodes including nodes in other subgroups (40). Global efficiency is an inverse measure of the average shortest path length (or smallest number of edges) between all pairs of nodes, and was computed as

$$\frac{\Sigma \left(di\,(:) \right)}{\left(n^2 - n \right)} \quad (2)$$

where di is the inverse shortest distance between nodes, and n is the total number of nodes (41).

Network variability

BOLD variability was computed as the standard deviation of time series data corresponding to three networks of interest, isolated *via* independent component analysis (ICA) decomposition in CONN (40 components with 64 component subject-level dimensionality reduction). These networks included the salience, frontoparietal, and dorsal attention networks that are commonly engaged during working memory processes based on a meta-analysis search in neurosynth.org of 1,091 imaging studies. The networks were identified using a spatial matching template and if left and right network activity appeared as two separate components, both components were used in the analysis. To verify that our cohort of patients had altered functional connectivity involving nodes of these networks, we performed an atlas- and voxel- based t-test comparing connectivity maps for patient vs. control using seed-based correlations to generate the maps for each network. Here the mask of the entire atlas-defined network was used

as the seed. Since ICA decomposition can return different solutions based on the choice of preprocessing and analysis parameters, we also performed a small reproducibility study using data from the present cohort and a separate cohort of adult patients with Parkinson's disease imaged at 3T to evaluate the effects of bandpass filtering (0.008–0.09 Hz vs. 0.008–0.06 Hz vs. 0.016–0.09Hz), spatial smoothing (none vs. 4 vs. 8 mm) and number of ICA components (20 vs. 40, where 20 is the minimum to extract a complete set of resting-state networks) on the variability of the dorsal attention network (DAN).

Statistical analysis

We used Wilcoxon rank sum tests to determine whether MR metrics could distinguish healthy controls from patients and amongst patient subgroups: no RT, focal RT (including supratentorial focal and whole ventricular focal RT), and WBRT (including low and high dose whole brain RT). Pearson correlation coefficients were estimated for relationships between age-normalized MR metrics and ISL performance scores, as well as total CMB burden. We used linear regression to test whether known risk factors for RT-induced neurocognitive impairment, such as age during RT and time since RT, were related to ISL performance scores and MR metrics to further evaluate the potential of modularity, efficiency, and BOLD variability as markers of cognition.

Results

Reliability of network variability metric

The results of our reproducibility study are shown in Figure 2. Upon increasing the number of ICA components from 20 to 40, the DAN was reduced into left and right hemisphere subnetworks (Figure 2A). Network variability computed from the DAN time courses corresponding to 20- vs. 40-component ICA were significantly correlated (Figure 2B). The left hemisphere subnetwork was more strongly correlated with the overall DAN variability than the right subnetwork (L-DAN$_{40}$ vs. DAN$_{20}$: $R = 0.79$, $p < 0.0001$; R-DAN$_{40}$ vs. DAN$_{20}$: $R = 0.56$, $p < 0.0001$), while healthy control data appeared to be more tightly correlated than patient data. Though not significant, the use of a narrower and lower frequency bandwidth i.e., 0.008–0.06 Hz yielded lower variability than the use of a wider bandwidth, i.e., 0.008–0.09 Hz (Figure 2C). Unsmoothed data also produced lower variability values on average, a finding that was significant when compared to standard 4mm and 8mm kernel smoothing (Figure 2C). Nonetheless, the overall effect size was small relative to the range of values typically measured across healthy controls and patients (see Figure 2B). Taken together, these results reiterate that the BOLD variability metric derived from ICA-based network time series data is reproducible and stable across different preprocessing and ICA parameters.

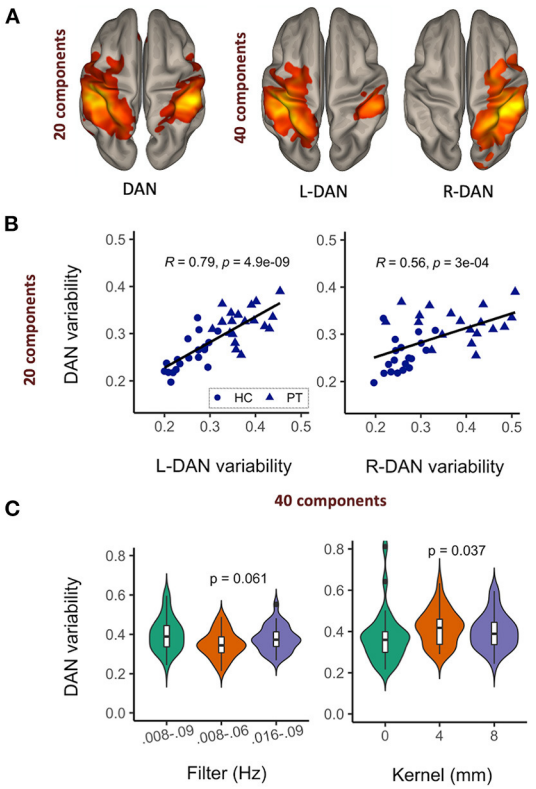

FIGURE 2
Network variability is a reproducible and stable MR metric. Upon increasing the number of ICA components, the dorsal attention network (DAN) was reduced to left and right hemisphere sub-networks **(A)**, with corresponding variability metrics remaining significantly correlated **(B)** and relatively stable across different data filtering bandwidths and spatial smoothing kernels **(C)**.

Distinguishing types of RT exposure and aggressiveness with rsfMRI metrics

Figure 3A shows brain networks of interest averaged across patients and controls, from which network variability was computed. Based on a 40-component ICA, a total of four networks were identified including the left and right hemisphere DAN, salience network (SN), and frontoparietal network (FPN). Individual subject networks constructed *via* backprojection spatially reflected the total group average; tumor sites did not overlap with the networks. Comparison of network connectivity for patients vs. controls using seed-based correlations confirmed altered patient connectivity, including hyperconnectivity in medial frontal nodes of the

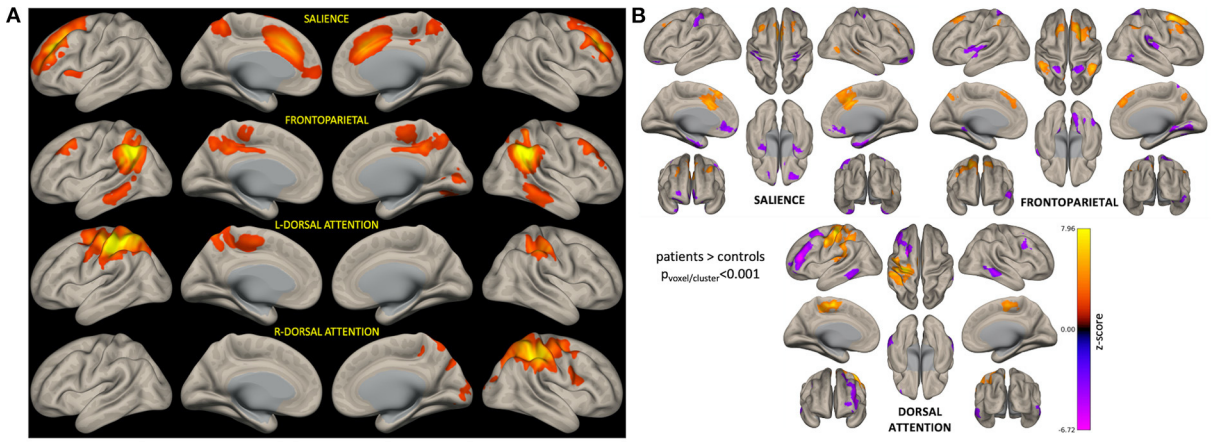

FIGURE 3
ICA-derived brain networks for all subjects and seed-based analysis confirming altered networks connectivity in patients. For each patient, BOLD variability was computed as the standard deviation of network-specific timeseries data **(A)**. Seed-based analysis confirmed that patients had significantly altered connectivity (relative to controls) involving nodes of the networks of interest **(B)**. In **(B)**, orange corresponds to brain areas that are hyperconnected to respective network nodes in patients (relative to controls), while purple represents hypoconnected areas.

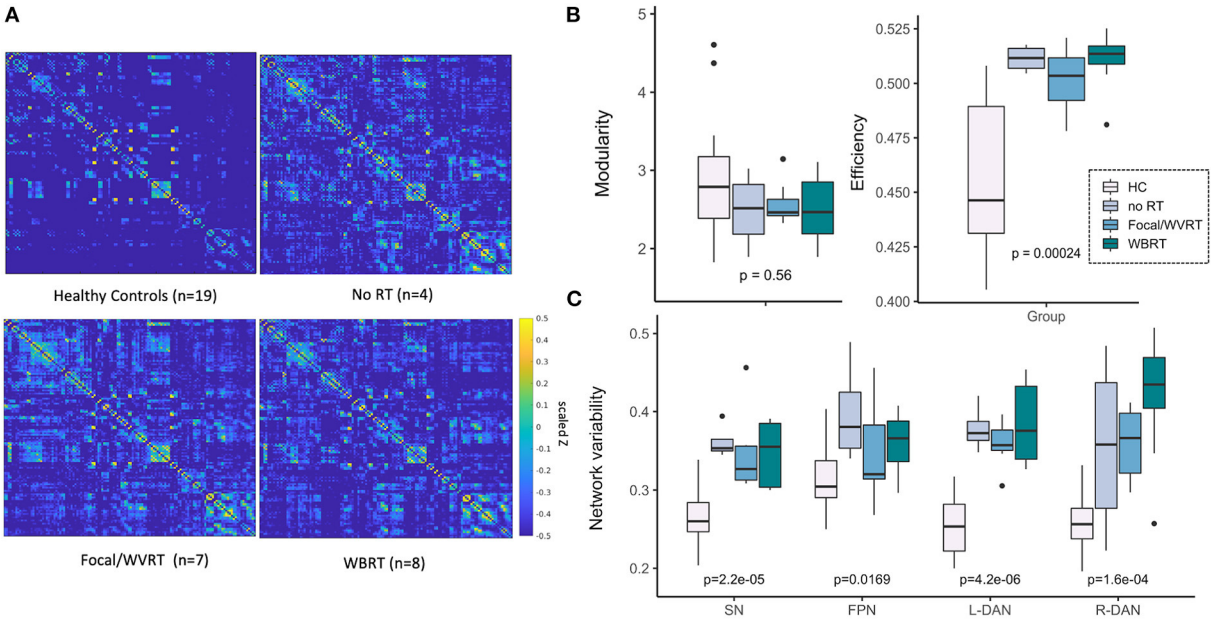

FIGURE 4
MR metrics can distinguish healthy controls and patient subgroups. Scaled and Fisher transformed functional connectivity (FC) matrices reveal notable group differences in global connectivity **(A)**. MR metrics derived from FC matrices and ICA brain networks show significant group trends related to group exposure to radiation therapy (RT) and/or the degree of RT treatment aggressiveness **(B, C)**. HC, healthy controls; no RT, non-irradiated patients; WVRT, whole-ventricular focal RT; Focal, focal RT to the supratentorial brain; WBRT, whole-brain RT.

SN and FPN, and parietal nodes of the FPN and DAN (Figure 3B). Reduced connectivity was also observed between lateral frontal areas involved in memory and language, and the DAN and FPN. Qualitative evaluation of group-averaged functional connectivity matrices, from which global efficiency and modularity were computed, revealed noticeable global connectivity differences (Figure 4A). Compared to the healthy controls (n = 19), all patients had more widespread hyperconnectivity. Upon separating patients into finer group (Supplementary Figure 1), those treated with focal RT to the supratentorial brain (n = 2) exhibited extensive hyperconnectivity, followed by those treated with high-dose

WBRT ($n = 4$), no RT ($n = 4$), low-dose WBRT ($n = 4$), and WVRT ($n = 5$).

All imaging metrics except network modularity showed significant group differences (Figures 4B,C). We expected to observe trends in imaging metrics across the groups according to whether RT was received, followed by treatment aggressiveness based on the approximate volume, location, and dose of RT. In this way and to maintain sufficiently sized groups, we first ranked the groups as follows: healthy controls < no RT < focal/WVRT RT < WBRT. In a supplementary analysis we investigated finer groupings: healthy controls < no RT < WVRT < supratentorial focal < low-dose WBRT < high-dose WBRT. As seen in Figures 4B,C, global efficiency and local SN and DAN variability best reflected this expected trend where group-level RT exposure and increasing treatment aggressiveness appeared to be associated with higher global efficiency ($p < 0.001$) and SN and DAN variability (all $p < 0.001$). While healthy controls nearly consistently yielded significantly lower values than patients, high values were unexpectedly recorded for non-irradiated patients, often exceeding that of the focal RT patients. Similar plots in Supplementary Figure 1 with patients separated into finer groups, showed the same trends plus a consistent effect of dose whereby high-dose WBRT was associated with higher MR metrics.

rsMRI metrics and memory performance

Correlation tests between patients' age-normalized MR metrics and the ISL test scores, representative of memory performance, revealed a significant positive correlative relationship between global modularity and efficiency and ISL scores (modularity: $R = 0.53$, $p < 0.02$; efficiency: $R = 0.49$, $p < 0.05$; Figure 5B). Network variability metrics similarly showed near significant, positive correlative trends with ISL scores except for R-DAN variability (Figure 5A). Division of the MR metrics by age at the time of imaging to produce age-normalized values, limits direct interpretation of trend lines in Figure 5 where performance decline appears to be associated with lower MR values. Nonetheless, age-normalization here was necessary as ISL test scores are normalized to age-appropriate healthy control data, and furthermore functional connectivity and network variability metrics have shown age-related changes across the lifespan (20).

Relationship between CMB burden and rsfMRI metrics and memory performance

In our prior work (4), CMB burden defined as the total number of CMBs detected on a patient's SWI images (Figure 6A), showed only longitudinal correlations with neurocognitive performance and here our results reiterate that cross-sectional ISL test scores do not show any clear trend with CMB burden (Figure 6B, *yellow bars*). Our approach of regrouping patients by their CMB burden based on the distribution of the data allowed for the inclusion of patients with no CMBs and revealed an interesting trend for L-DAN variability and modularity. Notably, L-DAN variability appeared to follow a parabolic trend where patients with low (0–2 CMBs) and very high CMB burden (>91 CMBs) averaged low variability, while patients with moderate CMB counts (4–47) averaged high variability (Figure 6C, top row). The opposite was observed for modularity where high modularity was detected in patients with very low and very high CMB counts, while low modularity was found in patients with moderate CMB counts (Figure 6D, top row). Plotting of the individual patient data points for those who had at least 1 CMB (Figures 6C,D, bottom rows) showed that the results are largely dependent on imaging values from the few subjects with >100 CMBs. These parabolic-like trends for L-DAN variability and modularity can also be mildly appreciated in Figures 4B,C, despite grouping patients based on RT exposure and aggressiveness as opposed to CMB burden.

Association of risk factors for cognitive decline after RT with rsfMRI metrics and memory performance

Younger age during RT and increased time elapsed since RT are known risk factors for neurocognitive decline and CMB development after radiation exposure (1, 3, 4, 9). Multiple regression analysis revealed significant associations between age-normalized imaging metrics and risk factors for neurocognitive decline, with global efficiency yielding the strongest association followed by SN variability; ISL test scores were not significantly associated with the risk factors (Table 2). Although these results are illustrated in Figure 7 as three-dimensional scatter plots, normalization of the MR metrics by age at the time of imaging again limits the direct interpretation of these trends.

Discussion

This cross-sectional imaging study investigated how rsfMRI measures of brain connectivity and network variability differ among patients with varying exposure to RT and degree of treatment aggressiveness compared to age- and sex-matched healthy controls. The strength of functional brain connections as well as variability within certain networks was related to: (1) neurocognitive measures of memory performance, (2) vascular injury in the form of CMBs, and (3) known risk factors for neurocognitive decline after RT, demonstrating that functional

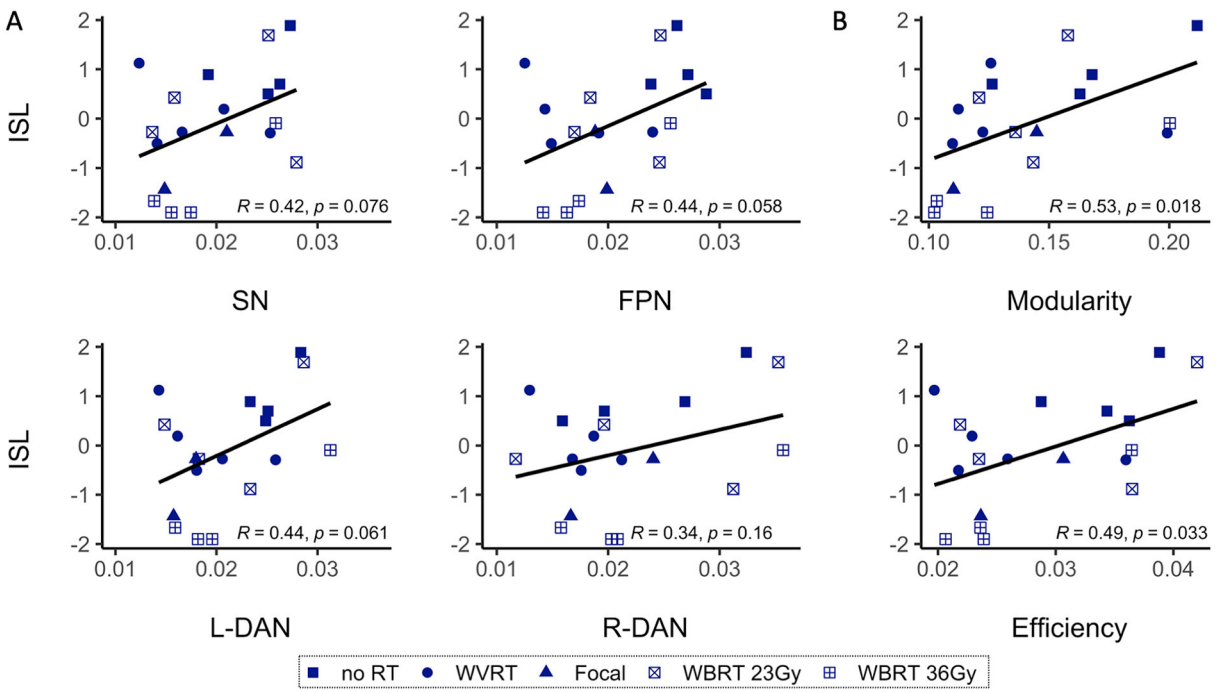

FIGURE 5
Age-normalized MR metrics and ISL test scores are correlated. Age-normalized network variability **(A)** and functional connectivity **(B)** metrics show a positive correlative trend with the age-normalized International Shopping List (ISL) test scores, representative of neurocognitive memory performance. As shown in B, only modularity and efficiency are significantly correlated with ISL. SN, salience network; FPN, frontoparietal network; L-DAN, left hemisphere dorsal attention network; R-DAN, right hemisphere DAN.

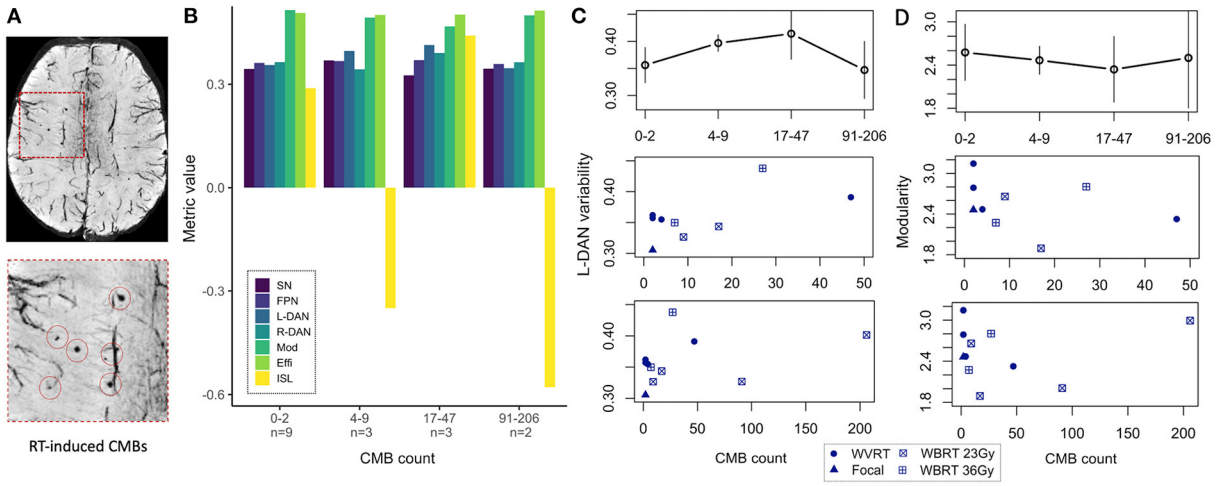

FIGURE 6
MR metrics change parabolically with increasing CMB burden. Degree of cerebral microbleed (CMB) burden detected on SWI **(A)** reveals parabolic-like changes in left hemisphere dorsal attention network (L-DAN) variability and modularity **(B)** with increasing CMB burden (based on within-group averages). Isolated plots for L-DAN variability and modularity are shown respectively in the top row of **(C, D)**; the bottom rows show the individual patient data points for CMB counts ranging 1–50 (magnified) and 1–205 (full range). In **(B)**, modularity values have been reduced by a factor of 5 for visualization purposes. Two of the 19 patients had poor SWI data quality and therefore CMB burden could not be evaluated. SN, salience network; FPN, frontoparietal network; L-DAN, left hemisphere dorsal attention network; R-DAN, right hemisphere DAN; Mod, modularity; Effi, efficiency; ISL, International Shopping List test score.

TABLE 2 Multivariate analysis of risks factors for neurocognitive decline after RT.

Neurocognitive outcome metric[a]	Age during RT		Time since RT	
	Incidence rate ratio [95% confidence interval]	*p*-Value	Incidence rate ratio [95% confidence interval]	*p*-Value
Neurocognitive performance:				
International shopping list	−0.06 [−0.20, 0.08]	NS	−0.11 [−0.23, 0.02]	NS
Network variability:				
Salience	−0.001 [−0.0015, −0.0009]	<0.0001	−0.001 [−0.0014, −0.0008]	<0.0001
Frontoparietal	−0.0008	<0.002	−0.0008	<0.002
L-dorsal attention	−0.001 [−0.0015, −0.0007]	<0.0001	−0.001 [−0.0014, −0.0006]	<0.002
R-dorsal attention	−0.0015 [−0.0022, −0.0008]	<0.002	−0.0013 [−0.0020, −0.0007]	<0.002
Functional connectivity:				
Modularity	−0.0055 [−0.0087, −0.0023]	<0.005	−0.0057 [−0.0087, −0.0023]	<0.002
Efficiency	−0.0017 [−0.0019, −0.0014]	<0.0001	−0.0016 [−0.0018, −0.0014]	<0.0001

[a]Imaging metrics represent surrogate measures of neurocognitive status and are normalized by age at the time of imaging.

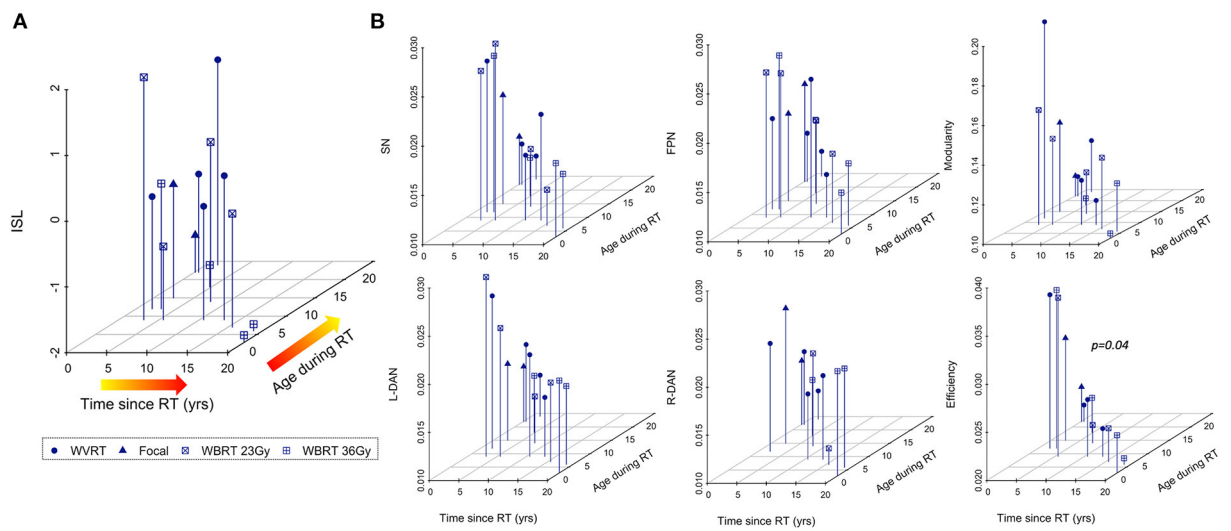

FIGURE 7
Age-normalized MR metrics are strongly associated with risk factors for cognitive decline after RT. Neurocognitive memory performance measured *via* the international shopping list (ISL) task is less associated with known risk factors for neurocognitive decline after RT **(A)** than MR metrics **(B)** representing surrogate markers of neurocognitive status.

MR metrics could be useful surrogate markers of cognition in brain tumor patients for reliable evaluation of the long-term treatment side-effects.

Reliability of the BOLD signal in patients with brain tumors has previously been shown to vary with disease aggressiveness (42). Since BOLD variability has not yet to our knowledge been investigated as a potential biomarker of brain tumor features or treatment side-effects, the first aim of this study was to demonstrate its reproducibility. Overall, we found that BOLD variability metrics were relatively stable across fMRI preprocessing and ICA postprocessing parameters, though unsmoothed data yielded several outliers. Spatial smoothing is generally considered an essential preprocessing step to improve data signal-to-noise ratio, with previous studies having shown stable functional connectivity as a function of resolution after smoothing (43). However, other studies have argued that spatial smoothing should be avoided in network analyses (44). While the results cannot inform the optimal approach, they do show that BOLD variability is more reproducible among different smoothing kernels, and that unsmoothed data significantly reduces the relative group average.

By nature of the ICA decomposition method, fMRI data-driven outputs (spatial brain maps and associated time courses) vary with each iteration (45). The desired number of components typically chosen in line with the experimental hypothesis can also significantly alter the solution, yielding brain maps of (sub)-networks of different granularity [as shown in Figure 2A and thoroughly explored by Wang and Li (46)]. Our finding that 20 and 40 component ICA produces BOLD variability metrics that are considerably correlated in patients, provides impetus for proceeding to use these metrics for biomarker discovery, and demonstrates that while ICA solutions can appear spatially distinct with increased number of components, the time courses can look relatively similar. Compared to the patient data, the control subject data were even more tightly correlated despite being derived from two different public datasets, providing further evidence that the BOLD variability metric is also robust against scanner and acquisition parameters.

Independent component analysis with 40 components (twice the minimum to extract a complete set of resting-state networks) was used to resolve more fine-grained representations of the network that may better characterize the underlying neurophysiological complexity of working memory processes. Seed-based analysis detected significant differences in SN, FPN, and DAN connectivity between patients and controls, providing further rationale for their inclusion as networks of interest to compute BOLD variability. Specifically, the finding of frontal lobe hyperconnectivity in patients agrees with previous reports of survivors of childhood tumors exhibiting frontal hyperconnectivity in the FPN and SN relative to controls, (15) as well as increased frontal engagement during working memory tasks (47). In young patients this is not surprising as frontal regions have been shown to develop post-adolescence and thus remain highly susceptible to plasticity (48).

On average, with the exception of global brain modularity, patients exhibited higher functional connectivity metrics than age- and sex-matched controls, providing further evidence of functional alterations in patients associated with treatment related side-effects despite the likely influence of previous structural changes due to lesion growth. Increased BOLD variability has previously been detected linearly across the lifespan and associated with age-related reductions in cognitive performance (49–51). In adults with Alzheimer's disease, Scarapicchia and colleagues also found that during rest whole-brain BOLD variability was increased in patients relative to controls and furthermore related to lower memory scores (52). Functional imaging studies of network efficiency have similarly shown enhanced efficiency in patients relative to controls (53). Given that both these metrics capture information about cognitive flexibility, their elevation in patients with increasing RT exposure and aggressiveness in this study could reflect underlying compensatory neural mechanisms directly related to the severity of their experienced brain injury. It is also important to note that while structural network efficiency reflecting impaired white matter architecture is often *decreased* in patients (36, 37), fMRI metrics are uniquely advantageous in that they can capture polysynaptic activity and early neuroplastic changes that might not be reflected structurally. Although brain modularity was not as sensitive to patient vs. control differences, controls on average exhibited slightly higher modularity which aligns with prior evidence of young individuals with higher baseline modularity performing better over iterative cognitive training sessions (35).

Qualitative evaluation of the group averaged functional connectivity matrices and the inclusion of age- and sex-matched controls in addition to non-irradiated controls was especially critical to realizing group trends in the data involving RT exposure and aggressiveness. Interestingly, no RT visually exhibited more hyperconnectivity than patients treated with more aggressive high and low dose WBRT regimens for a posterior fossa tumor, respectively. This highlights concerns that non-irradiated patients may not always be suitable controls for evaluating the impact of RT on brain connectivity, and that structural changes due to supratentorial lesion growth or hydrocephalus (detected in 50% of nonirradiated patients) (54) may have a greater impact on functional connectivity than RT effects. Patients treated with focal WVRT had the most normal appearing connectivity profiles, which could be explained by the location and relatively small size of their pre-treatment lesions, as well as the fact that some of the patients were treated as young adults which has previously been associated with a better prognosis (4). Quantitatively, some of the rsfMRI metrics mimicked these visual trends, but we also observed instances in which patients treated with focal RT had more favorable functional connectivity metrics than the WBRT group. While individual patient variations likely influenced differences in the group trends observed across connectivity metrics, the effect of dose within the WBRT group was one trend that remained consistent, providing strong evidence that higher whole-brain doses lead to more functional brain alterations.

Positive correlations observed between the ISL test scores and rsfMRI metrics reaffirm that functional imaging can indeed probe cognition in pediatric brain tumor patients. From the results in Figure 6 relating ISL scores and functional connectivity metrics with CMB burden, we can appreciate the added value of rsfMRI metrics which allowed for meaningful trends in the data to be extracted that otherwise could not be explained by memory task performance alone. Parabolic trends in modularity and DAN variability suggest that there may be a process of functional neural recovery unfolding over the course of years, simultaneous to the development of CMBs over time (4, 6, 9). In this way, one might reconsider the relative influence that vascular injury vs. microstructural and network-level functional changes have on the cognitive abilities of these patients. While severe vascular brain injury can independently lead to functional reorganization, there is evidence for example of re-emergence

of modular brain networks in stroke patients that are driven by changes in brain connectivity (55). Given this knowledge, it is not surprising that patients in this study with upward of 100 CMBs (who are also at high risk for stroke), approached normal modularity values. Biologically, modular networks have been proven more functionally efficient than non-modular networks (56), therefore, it also makes sense that we see a re-emergence of cognitive flexibility in the DAN as it relates to the brain's ability to efficiently process and respond to unexpected external stimuli (34).

Further emphasizing the utility of rsfMRI for the evaluation of cognitive side-effects after RT was the finding that risk factors (i.e., time since RT, age during RT) were more strongly associated with rsfMRI metrics than ISL test scores. Although cognitive testing batteries represent the gold standard for detecting cognitive impairments, their cross-sectional reproducibility in young patients is limited (57). Individual performance on a given task can fluctuate with testing fatigue during the exam and even the time of day (58). While rsfMRI metrics have their own limitations with respect to reproducibility (59), our results demonstrate that despite sources of variation influencing reliability, consistent and clinically meaningful trends in the data can still be elucidated using standard preprocessing methods.

There are several limitations to this study, with the most notable ones being the limited cohort size and patient heterogeneity with respect to age, tumor location and pathology, the presence of hydrocephalus, treatment strategy, and time since treatment. We used 7T MRI to enhance statistical power, and to minimize within-group variations and allow for meaningful results to be derived from the limited cohort, we grouped patients based on the similarity of their treatment strategy and naturally the alikeness of their tumor type and location. Nonetheless, factors such as hydrocephalus, although only mildly present in few patients across the groups, may have confounded the results given known independent effects of hydrocephalus on white matter structure and cognition (54). Especially in the non-irradiated control groups where two out of four patients presented with hydrocephalus, we expect that this side-effect significantly influenced the observed connectivity patterns.

Much of these limitations are largely due to unforeseen challenges with recruiting patients for a 7T research scan in addition to their clinical scan, as well as a delay in acquiring rsfMRI data as part of the study protocol. Specifically, challenges in recruiting patients who received WBRT for a posterior fossa tumor >1 year prior resulted in a widening of our inclusion criteria leading to the recruitment of two patients treated <1 year before 7T imaging. Consequently, some of the observed memory impairment and functional alterations in these patients may be caused by acute as opposed to late RT effects, which differ in pathophysiology. Otherwise, a delay in acquiring functional data for this study led to our inability to collect sufficient longitudinal rsfMRI data which, based on our prior work (4), may provide better insight into the relationship between risk factors, cognitive decline, and vascular injury. One final limitation worth noting was our inability to access age-appropriate control data acquired at 7T, thus requiring utilization of public 3T data. Variations in image signal-to-noise ratio (SNR) caused by the differing field strengths may have contributed to the distinction of patient and control metrics; nonetheless, given extensive prior evidence of abnormal brain activity in patients with neurological conditions, the underlying biological effects are still thought to be largely influencing the results. Our control dataset arising from two different studies, scanners, and sequence parameters further demonstrate that the imaging metrics are robust against differences in scanning methods that may affect SNR.

Overall, despite these limitations, the results of this work demonstrate that cross-sectional measures of functional brain connectivity and variability derived from rsfMRI may provide surrogate markers of cognition for monitoring the long-term effects of RT, including the complex relationship between vascular injury, network connectivity, and cognition. While we did not investigate the impact of underlying structural connectivity changes and presence of white matter pathologies on patient outcomes in this study, it is the subject of our ongoing work.

Conclusion

Collectively, the results demonstrate that rsfMRI metrics describing global brain modularity, efficiency, and local network variability hold promise for monitoring the long-term cognitive side-effects of RT in young patients being treated for a brain tumor. These neuroimaging metrics correlated with memory performance and were also able to effectively differentiate patients based on exposure to and aggressiveness of RT. Compared to memory performance, these functional connectivity metrics were more strongly associated with risk factors for cognitive decline and severity of RT-induced vascular injury.

Data availability statement

The raw data supporting the conclusions of this article will be made available by the authors, without undue reservation.

Ethics statement

The studies involving human participants were reviewed and approved by University of California San Francisco Institutional Review Board. Written informed consent to participate in this study was provided by the participant or their legal guardian/next of kin.

Author contributions

JL and SM designed and directed the overarching study. EF and SS performed recruitment and scheduling and cognitive testing. SM and SB supported patient recruitment. AJ performed MRI data collection and transfer. MM conceptualized the methods and approach and conducted the analyses alongside SW who performed the metric reproducibility analysis. AM provided statistics support for the analyses. CH provided neuroradiology support for the analysis of vascular injury. MM prepared the manuscript and figures. All authors discussed the results and provided written feedback on the manuscript.

Funding

This work was funded by R01HD079568 NIH NICHD grant.

Acknowledgments

The authors would like to thank the patients and their families for participating in this study and acknowledge the support of the MRI technicians and nurses in the Surbeck Laboratory for Advanced Imaging.

Conflict of interest

The authors declare that the research was conducted in the absence of any commercial or financial relationships that could be construed as a potential conflict of interest.

Publisher's note

Supplementary material

The Supplementary Material for this article can be found online at: https://www.frontiersin.org/articles/10.3389/fneur.2022.921984/full#supplementary-material

SUPPLEMENTARY FIGURE 1 |
MR metrics can distinguish healthy controls and patient subgroups. Scaled and Fisher transformed functional connectivity (FC) matrices reveal notable group differences in global connectivity **(A)**. MR metrics derived from FC matrices and ICA brain networks show significant group trends related to group exposure to radiation therapy (RT) and/or the degree of RT treatment aggressiveness **(B, C)**. HC, healthy controls; no RT, non-irradiated patients; WVRT, whole-ventricular focal RT; Focal, focal RT to the supratentorial brain; WBRT, whole-brain RT.

References

1. Kahalley LS, Ris MD, Grosshans DR, Okcu MF, Paulino AC, Chintagumpala M, et al. Comparing intelligence quotient change after treatment with proton versus photon radiation therapy for pediatric brain tumors. *J Clin Oncol.* (2016) 34:1043–9. doi: 10.1200/JCO.2015.62.1383

2. Kahalley LS, Peterson R, Ris MD, Janzen L, Okcu MF, Grosshans DR, et al. Superior intellectual outcomes after proton radiotherapy compared with photon radiotherapy for pediatric medulloblastoma. *J Clin Oncol.* (2020) 38:454–61. doi: 10.1200/JCO.19.01706

3. Palmer SL, Goloubeva O, Reddick WE, Glass JO, Gajjar A, Kun L, et al. Patterns of intellectual development among survivors of pediatric medulloblastoma: a longitudinal analysis. *J Clin Oncol.* (2001) 19:2302–8. doi: 10.1200/JCO.2001.19.8.2302

4. Morrison MA, Mueller S, Felton E, Jakary A, Stoller S, Avadiappan S, et al. Rate of radiation-induced microbleed formation on 7T MRI relates to cognitive impairment in young patients treated with radiation therapy for a brain tumor. *Radiother Oncol.* 154:145–53. (2020) doi: 10.1016/j.radonc.2020.09.028

5. Acharya S, Wu S, Ashford JM, Tinkle CL, Lucas JT, Qaddoumi I, et al. Association between hippocampal dose and memory in survivors of childhood or adolescent low-grade glioma: a 10-year neurocognitive longitudinal study. *Neuro Oncol.* (2019) 21:1175–83. doi: 10.1093/neuonc/noz068

6. Roddy E, Sear K, Felton E, Tamrazi B, Gauvain K, Torkildson J, et al. Presence of cerebral microbleeds is associated with worse executive function in pediatric brain tumor survivors. *Neuro Oncol.* (2016) 18:1548–58. doi: 10.1093/neuonc/now163

7. Goda JS, Dutta D, Krishna U, Goswami S, Kothavade V, Kannan S, et al. Hippocampal radiotherapy dose constraints for predicting long-term neurocognitive outcomes: mature data from a prospective trial in young patients with brain tumors. *Neuro Oncol.* (2020) 22:1677–85. doi: 10.1093/neuonc/noaa076

8. Sundgren PC, Cao Y. Brain irradiation: effects on normal brain parenchyma and radiation injury. *Neuroimaging Clin N Am.* (2009) 19:657–68. doi: 10.1016/j.nic.2009.08.014

9. Morrison MA, Hess CP, Clarke JL, Butowski N, Chang SM, Molinaro AM, et al. Risk factors of radiotherapy-induced cerebral microbleeds and serial analysis of their size compared with white matter changes: a 7T MRI study in 113 adult patients with brain tumors. *J Magn Reson Imaging.* (2019) 50:868–77. doi: 10.1002/jmri.26651

10. Avadiappan S, Morrison MA, Jakary A, Felton E, Stoller S, Hess CP, et al. Relationship between 7T MR-angiography features of vascular injury and cognitive decline in young brain tumor patients treated with radiation therapy. *J Neurooncol.* (2021) 153:143–52. doi: 10.1007/s11060-021-03753-3

11. Poels MMF, Ikram MA, Van Der Lugt A, Hofman A, Niessen WJ, Krestin GP, et al. Cerebral microbleeds are associated with worse cognitive function: the Rotterdam Scan Study. *Neurology.* (2012) 78:326–33. doi: 10.1212/WNL.0b013e318245 2928

12. Martinez-Ramirez S, Greenberg SM, Viswanathan A. Cerebral microbleeds: overview and implications in cognitive impairment. *Alzheimers Res Ther.* (2014) 6:33. doi: 10.1186/alzrt263

13. Manan HA, Franz EA, Yahya N. Functional connectivity changes in patients with brain tumours—a systematic review on resting state-fMRI. *Neurol Psychiatry Brain Res.* (2020) 36:73–82. doi: 10.1016/j.npbr.2020.03.003

14. Fox MD, Raichle ME. Spontaneous fluctuations in brain activity observed with functional magnetic resonance imaging. *Nat Rev Neurosci.* (2007) 8:700–11. doi: 10.1038/nrn2201

15. Chen H, Wang L, King TZ, Mao H. Increased frontal functional networks in adult survivors of childhood brain tumors. *NeuroImage Clin.* (2016) 11:339–46. doi: 10.1016/j.nicl.2016.02.010

16. Zou P, Conklin HM, Scoggins MA Li Y, Li X, Jones MM, Palmer SL, et al. Functional MRI in medulloblastoma survivors supports prophylactic reading intervention during tumor treatment. *Brain Imaging Behav.* (2016) 10:258–71. doi: 10.1007/s11682-015-9390-8

17. King TZ, Na S, Mao H. Neural underpinnings of working memory in adult survivors of childhood brain tumors. *J Int Neuropsychol Soc.* (2015) 21:494–505. doi: 10.1017/S135561771500051X

18. Zou P, Li Y, Conklin HM, Mulhern RK, Butler RW, Ogg RJ. Evidence of change in brain activity among childhood cancer survivors participating in a cognitive remediation program. *Arch Clin Neuropsychol.* (2012) 27:915–29. doi: 10.1093/arclin/acs095

19. Shen X, Cox SR, Adams MJ, Howard DM, Lawrie SM, Ritchie SJ, et al. Resting-state connectivity and its association with cognitive performance, educational attainment, and household income in the UK biobank. *Biol Psychiatry Cogn Neurosci Neuroimaging.* (2018) 3:878–86. doi: 10.1016/j.bpsc.2018.06.007

20. Bagarinao E, Watanabe H, Maesawa S, Mori D, Hara K, Kawabata K, et al. Reorganization of brain networks and its association with general cognitive performance over the adult lifespan. *Sci Rep.* (2019) 9:11352. doi: 10.1038/s41598-019-47922-x

21. Liu Y, Yang K, Hu X, Xiao C, Rao J, Li Z, et al. Altered rich-club organization and regional topology are associated with cognitive decline in patients with frontal and temporal gliomas. *Front Hum Neurosci.* (2020) 14:23. doi: 10.3389/fnhum.2020.00023

22. Kesler SR, Rao A, Blayney DW, Oakley-Girvan IA, Karuturi M, Palesh O. Predicting long-term cognitive outcome following breast cancer with pre-treatment resting state fMRI and random forest machine learning. *Front Hum Neurosci.* (2017) 11:555. doi: 10.3389/fnhum.2017.00555

23. Collin G, Nieto-Castanon A, Shenton ME, Pasternak O, Kelly S, Keshavan MS, et al. Brain functional connectivity data enhance prediction of clinical outcome in youth at risk for psychosis. *NeuroImage Clin.* (2020) 26:102108. doi: 10.1016/j.nicl.2019.102108

24. Wagner F, Hänggi M, Weck A, Pastore-Wapp M, Wiest R, Kiefer C. Outcome prediction with resting-state functional connectivity after cardiac arrest. *Sci Rep.* (2020) 10:11695. doi: 10.1038/s41598-020-68683-y

25. Reggente N, Moody TD, Morfini F, Sheen C, Rissman J, O'Neill J, et al. Multivariate resting-state functional connectivity predicts response to cognitive behavioral therapy in obsessive–compulsive disorder. *Proc Natl Acad Sci.* (2018) 115:2222–7. doi: 10.1073/pnas.1716686115

26. Torrisi S, Chen G, Glen D, Bandettini PA, Baker CI, Reynolds R, et al. Statistical power comparisons at 3T and 7T with a GO / NOGO task. *Neuroimage.* (2018) 175:100–10. doi: 10.1016/j.neuroimage.2018.03.071

27. Bian W, Hess CP, Chang SM, Nelson SJ, Lupo JM. Susceptibility-weighted MR imaging of radiation therapy- induced cerebral microbleeds in patients with glioma: a comparison between 3T and 7T. *Neuroradiology.* (2014) 56:91–6. doi: 10.1007/s00234-013-1297-8

28. Margelisch K, Studer M, Ritter BC, Steinlin M, Leibundgut K, Heinks T. Cognitive dysfunction in children with brain tumors at diagnosis. *Pediatr Blood Cancer.* (2015) 62:1805–12. doi: 10.1002/pbc.25596

29. Babayan A, Erbey M, Kumral D, Reinelt JD, Reiter AMF, Röbbig J, et al. A mind-brain-body dataset of MRI, EEG, cognition, emotion, and peripheral physiology in young and old adults. *Sci Data.* (2019) 6:180308. doi: 10.1038/sdata.2018.308

30. Greene DJ, Koller JM, Hampton JM, Wesevich V, Van AN, Nguyen AL, et al. Behavioral interventions for reducing head motion during MRI scans in children. *Neuroimage.* (2018) 171:234–45. doi: 10.1016/j.neuroimage.2018.01.023

31. Gavett BE, Horwitz JE. Immediate list recall as a measure of short-term episodic memory: insights from the serial position effect and item response theory. *Arch Clin Neuropsychol.* (2012) 27:125–35. doi: 10.1093/arclin/acr104

32. Simon-Vermot L, Taylor ANW, Araque Caballero MÀ, Franzmeier N, Buerger K, Catak C, et al. Correspondence between resting-state and episodic memory-task related networks in elderly subjects. *Front Aging Neurosci.* (2018) 10:362. doi: 10.3389/fnagi.2018.00362

33. Bian W, Banerjee S, Kelly DAC, Hess CP, Larson PEZ, Chang SM, et al. Simultaneous imaging of radiation-induced cerebral microbleeds, arteries and veins, using a multiple gradient echo sequence at 7 Tesla. *J Magn Reson Imaging.* (2015) 42:269–79. doi: 10.1002/jmri.24802

34. Grady CL, Garrett DD. Understanding variability in the BOLD signal and why it matters for aging. *Brain Imaging Behav.* (2014) 8:274–83. doi: 10.1007/s11682-013-9253-0

35. Baniqued PL, Gallen CL, Kranz MB, Kramer AF, D'Esposito M. Brain network modularity predicts cognitive training-related gains in young adults. *Neuropsychologia.* (2019) 131:205–15. doi: 10.1016/j.neuropsychologia.2019.05.021

36. Shen J, Tozer DJ, Markus HS, Tay J. Network efficiency mediates the relationship between vascular burden and cognitive impairment. *Stroke.* (2020) 51:1682–9. doi: 10.1161/STROKEAHA.119.028587

37. Na S, Li L, Crosson B, Dotson V, MacDonald TJ, Mao H, et al. White matter network topology relates to cognitive flexibility and cumulative neurological risk in adult survivors of pediatric brain tumors. *NeuroImage Clin.* (2018) 20:485–97. doi: 10.1016/j.nicl.2018.08.015

38. Whitfield-Gabrieli S, Nieto-Castanon A. Conn: a functional connectivity toolbox for correlated and anticorrelated brain networks. *Brain Connect.* (2012) 2:125–41. doi: 10.1089/brain.2012.0073

39. Rubinov M, Sporns O. Complex network measures of brain connectivity: uses and interpretations. *Neuroimage.* (2010) 52:1059–69. doi: 10.1016/j.neuroimage.2009.10.003

40. Newman MEJ. Finding community structure in networks using the eigenvectors of matrices. *Phys Rev E.* (2006) 74:036104. doi: 10.1103/PhysRevE.74.036104

41. Latora V, Marchiori M. Efficient behavior of small-world networks. *Phys Rev Lett.* (2001) 87:198701. doi: 10.1103/PhysRevLett.87.198701

42. Morrison MA, Churchill NW, Cusimano MD. Reliability of task-based fmri for preoperative planning : a test-retest study in brain tumor patients and healthy controls. *PLoS ONE.* (2016) 11:e0149547. doi: 10.1371/journal.pone.0149547

43. Molloy EK, Meyerand ME, Birn RM. The influence of spatial resolution and smoothing on the detectability of resting-state and task fMRI. *Neuroimage.* (2014) 86:221–30. doi: 10.1016/j.neuroimage.2013.09.001

44. Alakörkkö T, Saarimäki H, Glerean E, Saramäki J, Korhonen O. Effects of spatial smoothing on functional brain networks. *Eur J Neurosci.* (2017) 46:2471–80. doi: 10.1111/ejn.13717

45. Himberg J, Hyvärinen A, Esposito F. Validating the independent components of neuroimaging time series *via* clustering and visualization. *Neuroimage.* (2004) 22:1214–22. doi: 10.1016/j.neuroimage.2004.03.027

46. Wang Y, Li T-Q. Dimensionality of ICA in resting-state fMRI investigated by feature optimized classification of independent components with SVM. *Front Hum Neurosci.* (2015) 9:259. doi: 10.3389/fnhum.2015.00259

47. Fox ME, Turner JA, Crosson B, Morris RD, King TZ. Functional connectivity networks and their recruitment during working memory tasks in adult survivors of childhood Brain Tumors. *Brain Connect.* (2021) 11:822–37. doi: 10.1089/brain.2020.0800

48. Sowell ER, Thompson PM, Holmes CJ, Jernigan TL, Toga AW. *In vivo* evidence for post-adolescent brain maturation in frontal and striatal regions. *Nat Neurosci.* (1999) 2:859–61. doi: 10.1038/13154

49. Boylan MA, Foster CM, Pongpipat EE, Webb CE, Rodrigue KM, Kennedy KM. Greater BOLD variability is associated with poorer cognitive function in an adult lifespan sample. *Cereb Cortex.* (2021) 31:562–74. doi: 10.1093/cercor/bhaa243

50. Nomi JS, Bolt TS, Ezie CEC, Uddin LQ, Heller AS. Moment-to-moment BOLD signal variability reflects regional changes in neural flexibility across the lifespan. *J Neurosci.* (2017) 37:5539–48. doi: 10.1523/JNEUROSCI.3408-16.2017

51. Baum SH, Beauchamp MS. Greater BOLD Variability in older compared with younger adults during audiovisual speech perception. *PLoS ONE.* (2014) 9:e111121. doi: 10.1371/journal.pone.0111121

52. Scarapicchia V, Mazerolle EL, Fisk JD, Ritchie LJ, Gawryluk JR. Resting state BOLD variability in Alzheimer's disease: a marker of cognitive decline or cerebrovascular status? *Front Aging Neurosci.* (2018) 10:1–13. doi: 10.3389/fnagi.2018.00039

53. Ma X, Jiang G, Fu S, Fang J, Wu Y, Liu M, et al. Enhanced network efficiency of functional brain networks in primary insomnia patients. *Front Psychiatry.* (2018) 9:46. doi: 10.3389/fpsyt.2018.00046

54. Yuan W, Holland SK, Shimony JS, Altaye M, Mangano FT, Limbrick DD, et al. Abnormal structural connectivity in the brain networks of children with hydrocephalus. *NeuroImage Clin.* (2015) 8:483–92. doi: 10.1016/j.nicl.2015.04.015

55. Siegel JS, Seitzman BA, Ramsey LE, Ortega M, Gordon EM, Dosenbach NUF, et al. Re-emergence of modular brain networks in stroke recovery. *Cortex.* (2018) 101:44–59. doi: 10.1016/j.cortex.2017.12.019

56. Tosh CR, McNally L. The relative efficiency of modular and non-modular networks of different size. *Proc R Soc B Biol Sci.* (2015) 282:20142568. doi: 10.1098/rspb.2014.2568

57. Payne JM, Hearps SJC, Walsh KS, Paltin I, Barton B, Ullrich NJ, et al. Reproducibility of cognitive endpoints in clinical trials: lessons from neurofibromatosis type 1. *Ann Clin Transl Neurol.* (2019) 6:2555–65. doi: 10.1002/acn3.50952

58. West R, Murphy KJ, Armilio ML, Craik FIM, Stuss DT. Effects of time of day on age differences in working memory. *J Gerontol Ser B Psychol Sci Soc Sci.* (2002) 57:P3–P10. doi: 10.1093/geronb/57.1.P3

59. Noble S, Scheinost D, Constable RT. A decade of test-retest reliability of functional connectivity: a systematic review and meta-analysis. *Neuroimage.* (2019) 203:116157. doi: 10.1016/j.neuroimage.2019.116157

frontiers | Frontiers in Neurology

TYPE Original Research
PUBLISHED 13 October 2022
DOI 10.3389/fneur.2022.990208

OPEN ACCESS

EDITED BY
Jan Kassubek,
University of Ulm, Germany

REVIEWED BY
Nico Sollmann,
University of California, San Francisco, United States
Kornelia Kreiser,
Technical University of Munich, Germany

*CORRESPONDENCE
Martin Kenda
martin.kenda@charite.de

SPECIALTY SECTION
This article was submitted to Applied Neuroimaging, a section of the journal Frontiers in Neurology

RECEIVED 09 July 2022
ACCEPTED 12 August 2022
PUBLISHED 13 October 2022

CITATION
Kenda M, Cheng Z, Guettler C, Storm C, Ploner CJ, Leithner C and Scheel M (2022) Inter-rater agreement between humans and computer in quantitative assessment of computed tomography after cardiac arrest. *Front. Neurol.* 13:990208. doi: 10.3389/fneur.2022.990208

Inter-rater agreement between humans and computer in quantitative assessment of computed tomography after cardiac arrest

Martin Kenda[1,2]*, Zhuo Cheng[3], Christopher Guettler[3], Christian Storm[4], Christoph J. Ploner[1], Christoph Leithner[1] and Michael Scheel[3]

[1]Department of Neurology With Experimental Neurology, Freie Universität Berlin and Humboldt-Universität zu Berlin, Charité—Universitätsmedizin Berlin, Berlin, Germany, [2]BIH Charité Junior Digital Clinician Scientist Program, Berlin Institute of Health at Charité—Universitätsmedizin Berlin, BIH Biomedical Innovation Academy, Berlin, Germany, [3]Department of Neuroradiology, Freie Universität Berlin and Humboldt-Universität zu Berlin, Charité—Universitätsmedizin Berlin, Berlin, Germany, [4]Department of Nephrology and Intensive Care Medicine—Circulatory Arrest Center Berlin, Corporate Member of Freie Universität Berlin and Humboldt-Universität zu Berlin, Charité—Universitätsmedizin Berlin, Berlin, Germany

Background: Head computed tomography (CT) is used to predict neurological outcome after cardiac arrest (CA). The current reference standard includes quantitative image analysis by a neuroradiologist to determine the Gray-White-Matter Ratio (GWR) which is calculated *via* the manual measurement of radiodensity in different brain regions. Recently, automated analysis methods have been introduced. There is limited data on the Inter-rater agreement of both methods.

Methods: Three blinded human raters (neuroradiologist, neurologist, student) with different levels of clinical experience retrospectively assessed the Gray-White-Matter Ratio (GWR) in head CTs of 95 CA patients. GWR was also quantified by a recently published computer algorithm that uses coregistration with standardized brain spaces to identify regions of interest (ROIs). We calculated intraclass correlation (ICC) for inter-rater agreement between human and computer raters as well as area under the curve (AUC) and sensitivity/specificity for poor outcome prognostication.

Results: Inter-rater agreement on GWR was very good (ICC 0.82–0.84) between all three human raters across different levels of expertise and between the computer algorithm and neuroradiologist (ICC 0.83; 95% CI 0.78–0.88). Despite high overall agreement, we observed considerable, clinically relevant deviations of GWR measurements (up to 0.24) in individual patients. In our cohort, at a GWR threshold of 1.10, this did not lead to any false poor neurological outcome prediction.

Conclusion: Human and computer raters demonstrated high overall agreement in GWR determination in head CTs after CA. The clinically

relevant deviations of GWR measurement in individual patients underscore the necessity of additional qualitative evaluation and integration of head CT findings into a multimodal approach to prognostication of neurological outcome after CA.

KEYWORDS

cardiac arrest (CA), neuroprognostication, computed tomography, automated image analysis, resuscitation, inter-rater agreement, brain imaging

Introduction

Hypoxic-ischemic encephalopathy (HIE) remains a major cause of death and disability following cardiac arrest (1). Many CA survivors remain with disabling neurological symptoms ranging from cognitive and movement disorders to severe impairments of consciousness (2). Reliable neurological outcome prediction after CA is a challenging task. When deciding on continuation or withdrawal of life sustaining therapies, an accurate prognosis is crucial. Currently, a combination of several prognostic investigations is recommended: repeated neurological examination, electroencephalography (EEG), somatosensory evoked potentials (SSEP), serum neuron-specific enolase (NSE) and brain imaging (3).

Despite efforts for standardization, there is heterogeneity in prognostic performance between raters and centers for most of the tests used. Inter-rater agreement on EEG interpretation is fair to substantial (4) and good on SSEP interpretation for the prediction of poor outcome in comatose patients early after CA (5).

Head CTs are obtained early after CA to rule out intracranial causes for the arrest and later after CA (typically within 3–5 days) to assess the degree of HIE. The current reference standard for assessing head CT imaging is interpretation by a neuroradiologist ("qualitative analysis"). Typical characteristics of HIE include global brain edema frequently visible as sulcal effacement, loss of discrimination between gray and white matter, pseudo-subarachnoid hemorrhage or hypodense cortex and gray matter basal ganglia structures ("reversal sign") (6). International guidelines recommend using imaging findings of "diffuse and extensive anoxic injury" for prediction of poor neurological outcome without providing a clear definition of this finding (3, 7, 8). Studies on the inter-rater reliability of qualitative assessment of head CT have consequently found poor to moderate agreement on the presence and/or severity of HIE between different raters, sites, and specialties (9, 10).

Quantitative analysis could aid in reducing Inter-rater variability. Determination of the gray-white matter ratio (GWR) by manual placement of small regions of interest (ROI) in different gray and white matter target regions has been evaluated in many mostly retrospective, single center studies (11, 12). Protocols for GWR determination are not fully standardized and differ relevantly between centers (13). Our group recently developed and successfully tested an algorithm for automated GWR assessment that uses linear and non-linear co-registration with MRI-based standard atlases to determine ROIs (14).

Limited data is available on the Inter-rater agreement in GWR determination, especially with respect to different levels of expertise. Moreover, there are no studies that investigate the agreement between conventional human raters and automated assessment by a computer algorithm.

Therefore, this study aims at the following:

1. To assess inter-rater agreement of GWR assessment between 3 human raters with different levels of expertise.
2. To assess the agreement between human raters and automated computer GWR assessment.
3. To identify potential sources of Inter-rater variability.
4. To evaluate the impact of Inter-rater variability on prognostic performance.

Methods

Patients

The study was approved by the local ethics committee. We retrospectively included 353 patients from a previously published cohort of our CA database from the circulatory arrest center of a large academic hospital (15). One hundred eleven patients received native head CTs within the first 7 days after CA. Three patients had technically compromised data files and could not be reanalyzed. Thirteen patients with additional cerebral pathologies such as older ischemic lesions, hemorrhage or severe motion artifacts in imaging were excluded (Supplementary Figure 1). Patients were treated with targeted temperature management (TTM, 33°C for 24 h) according to the guidelines (16). Clinicians were blinded to the results of quantitative CT analysis but had access to the radiologic report. Neurological outcome was assessed by the treating physicians at hospital discharge using the cerebral performance category

(CPC) scale and dichotomized in "good" (CPC 1–3) and "poor" outcome (CPC 4–5) for statistical analysis (17).

GWR determination

All raters were blinded to clinical information except for the overall context of CA and blinded to each other's results. Images were rated by a board-certified neuroradiologist with 13 years of clinical expertise, a resident neurologist with 3 years of experience in post-cardiac arrest care and a final year medical student who underwent a short, 3-h training session to assess GWR beforehand but had no clinical experience in the field. Using Horos (Version 3.1.2, The Horos Project, https://horosproject.org), each rater was asked to bilaterally place 10 mm^2 ROIs into the putamen and posterior limb of the internal capsule (PLIC).

For automated analysis, we used a previously published algorithm, modified to use circular ROIs instead of atlas maps (14). In summary, CTs are first co-registered in a linear and non-linear mode to a standardized CT template in an MRI-based standard space using the *FNIRT* and *FLIRT* functions from FSL (Version 5.0.9, Analysis Group, FMRIB, Oxford, United Kingdom) (18). The reverse transformation fields are then used to automatically place predefined standardized 10 mm^2 circular ROIs into the center of target regions in the individual CT spaces. Mean hounsfield units (HU) in the ROIs were measured and GWR was calculated as $\frac{HU\ Putamen}{HU\ PLIC}$.

Statistical analyses

For statistical analysis, we used RStudio (Version 1.4.1653, RStudio, Boston, MA) with the *pROC*-package (19) for receiver operating characteristics (ROC), the *ggpubr*-package for data visualization and the *psych*-package (20) for ICC calculation. Intraclass correlation (ICC) (ICC 3, two-way mixed, single measure model) was conducted to measure overall and pairwise Inter-rater agreement on the radiodensity (HU) and GWR between the reference standard neuroradiologist and the other three raters. We also calculated ICC (ICC3k, Two-way mixed, average measure) between a mean of three human raters and the computer.

Intraclass correlation values < 0.2 were considered as *poor* agreement, between 0.21 and 0.4 as *fair* agreement, between 0.41 and 0.6 as *moderate* agreement, 0.61 and 0.80 as *good* agreement, and values > 0.80 as *very good* agreement (21). For comparison between the raters, we used the Wilcoxon test for the rating results and the DeLong's test for the AUCs. "Severe HIE", was assumed if GWR was <1.10 (22). Statistical significance was defined as $p<0.05$. Confidence intervals (*CIs*) for neurological outcome prediction were calculated with 95% CIs using the Wilson score method.

TABLE 1 Baseline data of 95 CA patients.

Parameter	Overall
n	*95*
Age (years)	61 [48–73]
Sex	
Male	63 (66.3%)
Out-of-hospital Cardiac Arrest	79 (83.2%)
Shockable Rhythm	29 (30.5%)
Primary cause of arrest	
Cardiac	47 (49.5%)
Respiratory	35 (37.2%)
Other	13 (13.6%)
Time to ROSC (min)	16 [12–24]
Total Adrenalin Dose (mg)	2 [1–5]
APACHE Score	30 [23–35]
Length of ICU stay (days)	9 [4–23]
Time on Ventilator (hours)	204 [108–512]
CT acquisition (hours after CA)	4 [1–19.5]
Neurological Outcome at ICU Discharge	
CPC 1	23 (24.2%)
CPC 2	14 (14.7%)
CPC 3	2 (2.1%)
CPC 4	9 (9.5%)
CPC 5	47 (49.5%)

Median [IQR] for continuous and numbers (%) for categorical data.

Results

Patients

Ninety five patients with native head CTs were eligible for analysis. In the predominantly male (66.3%) study cohort (Table 1), the majority had an OHCA (83.2%) and a non-shockable rhythm (69.5%). Half of the patients had a primary cardiac cause of arrest, the other half either a respiratory (35%) or other cause (intoxication, metabolic, and unknown). Median length of ICU stay was 9 days [IQR 4–23]. At ICU discharge, 56 (59%) patients had a poor neurological outcome (CPC 4–5), 9 of which in unresponsive wakefulness syndrome (UWS; CPC 4), the other 47 dead (CPC 5). CTs were acquired at a median of 4 h (IQR, 1–19.5) after cardiac arrest.

Inter-rater agreement in GWR determination

Figure 1 illustrates ROI placement in 3 patients with different extent of post hypoxic brain damage. For the measurement of putamen radiodensity, ICC for agreement with the study neuroradiologist (reference standard) was *very good*

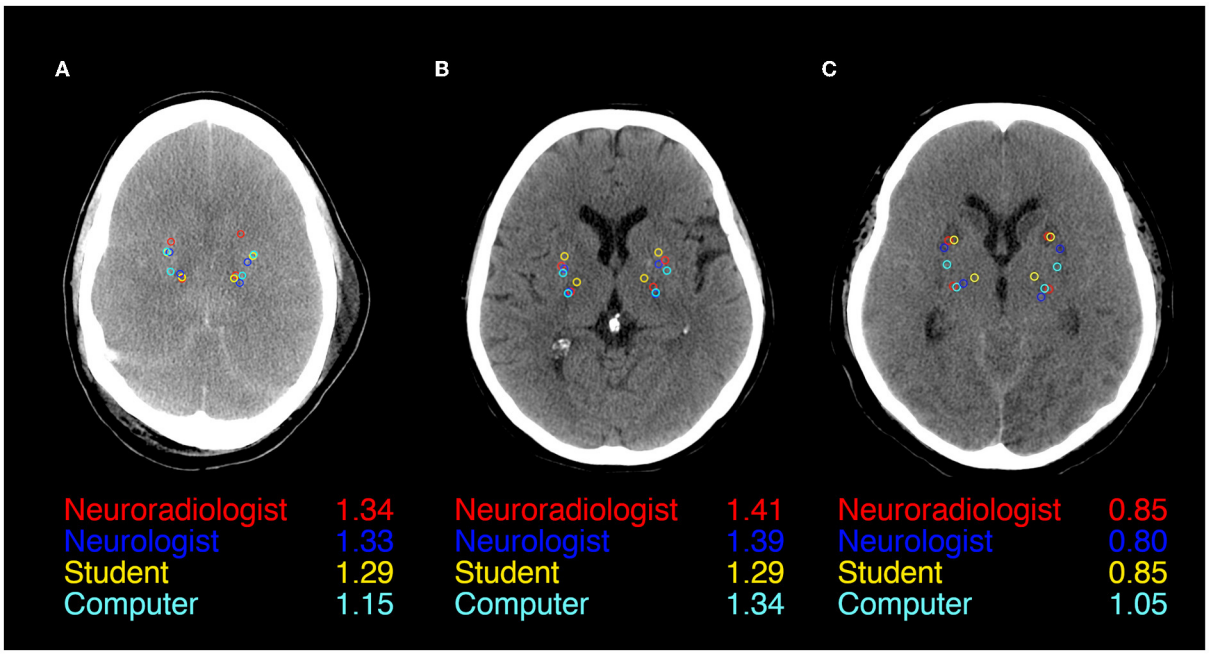

FIGURE 1
ROI Placement during GWR assessment in Putamen and Posterior Limb of the internal Capsule (PLIC) in CTs of three patients after cardiac arrest **(A–C)**. All four raters (Neuroradiologist in red, Neurologist in blue, Student in yellow, and Computer in cyan) and GWRs displayed.

for all three raters (student 0.83, neurologist 0.92, computer 0.92). The agreement for PLIC was lower, although still at *good* levels (student 0.66, neurologist 0.71, computer 0.72; Figure 2). The student had the lowest correlation with the neuroradiologist in both regions (Putamen ICC 0.84, CI 0.78–0.88; PLIC 0.66 0.56–0.75) with differences ranging up to a maximum of 4.4 HU for PLIC. Moreover, the computers' agreement with the average of all human raters was *very good* (ICC Putamen 0.96, CI 0.95–0.97; PLIC 0.98, CI 0.84–0.92; Figure 3).

The raters' overall agreement with the study neuroradiologist on the GWR was *very good* (overall ICC 0.83; CIs 0.78–0.87), with 95%-CIs ranging into *good* agreement (Figure 2). Furthermore, the agreement between the computer and the average of all three human raters was *very good* (0.93; CI 0.91–0.96, Figure 3). However, when comparing individual GWR values between computer and neuroradiologist (ICC 0.84; CI 0.78–0.88), differences ranged from a minimum of 0.003 to a maximum of 0.24 with disagreement across the pre-defined cut-off for severe HIE (GWR $<$ 1.10) in eight poor neurological outcome patients (Figure 4, CT image examples in Supplementary material). Similarly, the neurologist disagreed in six poor neurological outcome cases and the student nine cases with the neuroradiologist (Supplementary Figure 2). No disagreement with the neuroradiologist across the cutoff was observed in any good neurological outcome patient for any rater.

Prognostic variability

Median GWRs were significantly lower in patients with poor neurological outcome than in patients with good neurological outcome, regardless of the rater (Supplementary Table 1). Predictive performance for poor neurological outcome prediction by GWR, quantified by the area under the ROC curve (AUC) was equally good for neuroradiologist and computer (AUC 0.80; CI 0.71–0.89) and lower for the neurologist (0.74; CI 0.65–0.84) and student (0.78; CI 0.69–0.87) (Figure 5). The differences in AUC between all raters were not statistically significant. Sensitivity at GWR $<$ 1.10, a 100% specificity cutoff for all raters ranged between 18% for the computer and was highest at 29% for the neuroradiologist (Supplementary Table 2).

Discussion

Our main findings are:

1. The Inter-rater agreement on the Gray-White Matter Ratio measured in head CTs after CA was very good between 3 human raters across different levels of expertise.
2. The Inter-rater agreement on GWR measured in head CTs was very good between human raters and a computer algorithm.

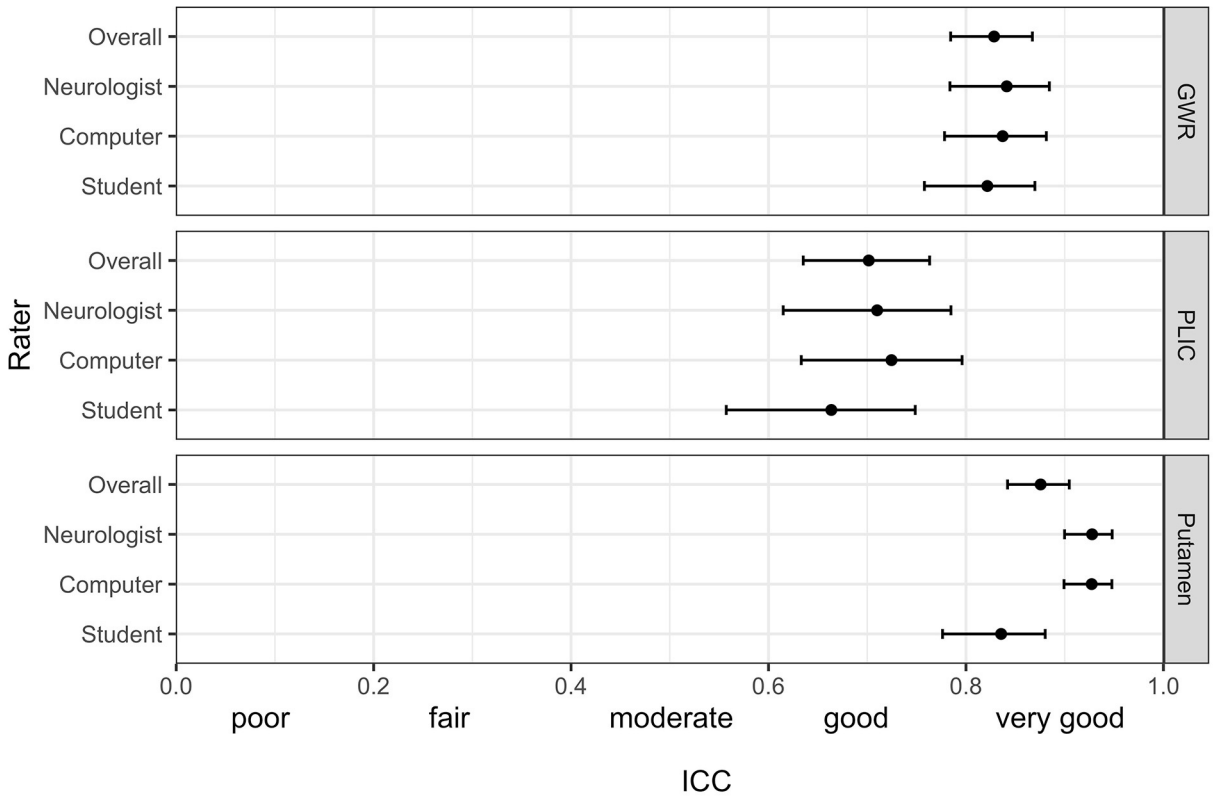

FIGURE 2
Intraclass correlation (ICC) (95% CI) for the pairwise agreement of three different raters with the study neuroradiologist in GWR and ROI assessment (Putamen and PLIC) in Hounsfield Units (HU) in CTs after cardiac arrest.

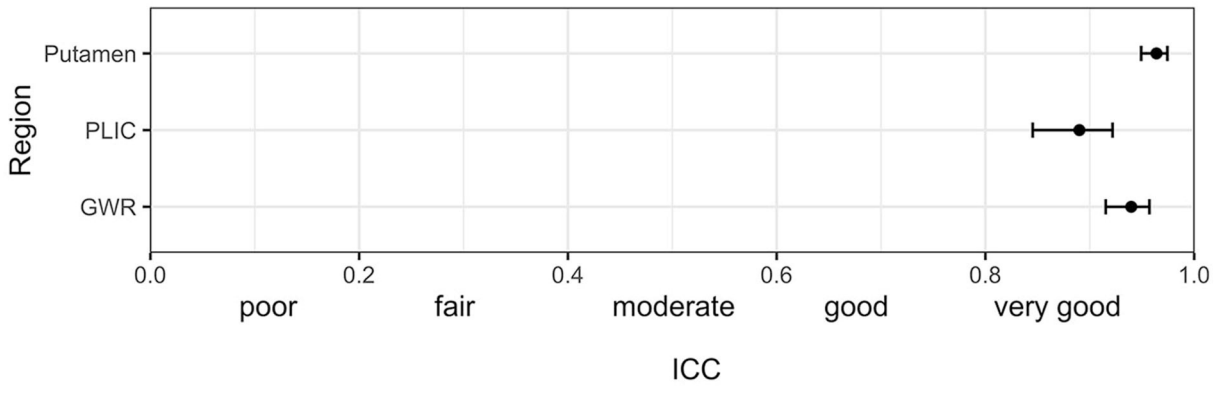

FIGURE 3
Intraclass correlation (ICC) (95%-CI) for the combined agreement of three human raters (mean of student, neurologist and neuroradiologist) with the computer algorithm in GWR and ROI assessment (Putamen and PLIC) in Hounsfield Units (HU) in CTs after cardiac arrest.

3. Inter-rater agreement was lower for ROIs placed in the posterior limb of the internal capsule than for those placed in the putamen.
4. Despite high overall agreement, considerable deviations in GWR between raters were observed in individual patients. In our cohort, at a GWR threshold of 1.10, this did not lead to any false poor neurological outcome predictions.

In this study investigating the Inter-rater variability of quantitative head CT assessment in patients after cardiac arrest, Inter-rater agreement was considerably better than in studies

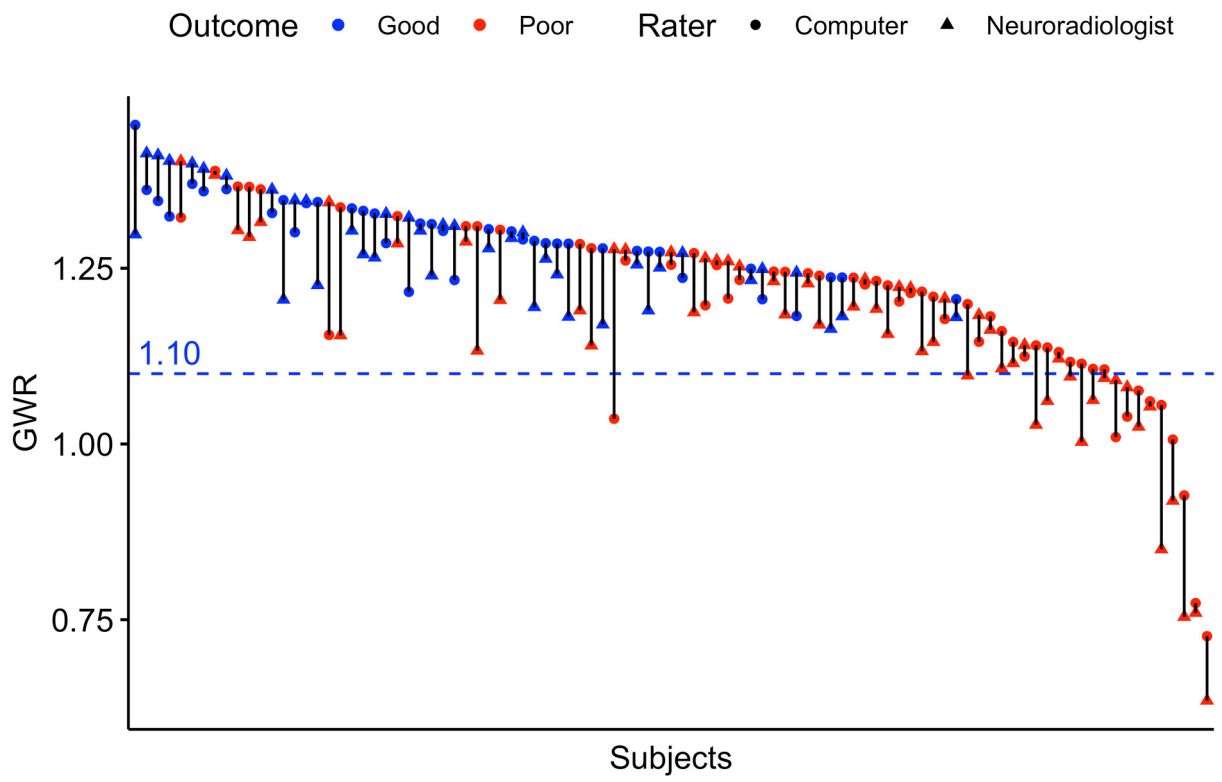

FIGURE 4
Pairwise GWR values for $n = 95$ patients rated by computer and neuroradiologist. Blue pairs representing patients with good outcome (CPC 1–3), red pairs poor outcome (CPC 4–5). Triangles for manual rater (neuroradiologist), dots for computer. Blue dotted line at GWR-cutoff = 1.10.

investigating descriptive, qualitative assessment (9, 10). Previous evidence on the subject had been inconclusive with one study reporting moderate agreement between three human raters and another study reporting good agreement between four human raters (23, 24). We provide the first data for the Inter-rater agreement between human raters and an atlas-based computer algorithm.

We observed the highest variability in the HU measurements of the PLIC-ROI, which mainly accounted for the variability of GWR values. ROI-placement in the Putamen was more consistent. This is illustrated in our visual examples and might be due to a less evident visual delineation of internal capsule in contrast to a clear structural border of the basal ganglia (Figure 1). Another reason could be the increasing difficulty with visually identifying anatomical regions when gray-white matter differentiation is lost due to brain edema (Figure 1A). We also provide evidence that this effect could partly be solved by automated delineation: we observed the highest agreement for the PLIC-ROI between the computer and the neuroradiologist. Considerable GWR deviations or disagreements across the cutoff for HIE occurred both in CTs with extensive as well as subtle pathological changes (Supplementary Figures 3, 4). Three main sources for variability can be observed in these images: First, raters seem to have a preference as to where to place ROIs within the target structures. Future studies with manual placement should therefore standardize ROI placement i.e., by defining the position within the anatomical region and the ROIs relation to other adjacent landmarks. Second, due to small structural focal hypo- or hyperdensitites (e.g., vessels and small lacunar defects) HU values can also vary if ROIs are placed correctly within the anatomic region. We therefore suggest that raters consider the HU value during ROI placement to be in an area representative of the regions radiodensity. Both problems can be solved if instead of circular ROIs, the whole anatomical region is delineated and its radiodensity averaged, an approach that has been successfully used in automated CT quantification by our group an others (14, 25, 26). Third, there are cases where ROIs are misplaced by the rater. Therefore, the results of manual and/or automated ROI placements should be visually re-inspected after qualitative and quantitative analysis are completed to identify cases of misplacement.

Although overall agreement on the GWR values as measure of the degree of edema was very good, we observed considerable variability in individual patients in both neurological outcome groups, the extent of which has not been previously reported. In some cases, this also affected whether a patient was above or below our predefined cut-off for "severe HIE" (GWR < 1.10). In our cohort this exclusively occurred in poor neurological outcome patients, no good neurological outcome patient was misclassified as below the cut-off. Thus, it influenced

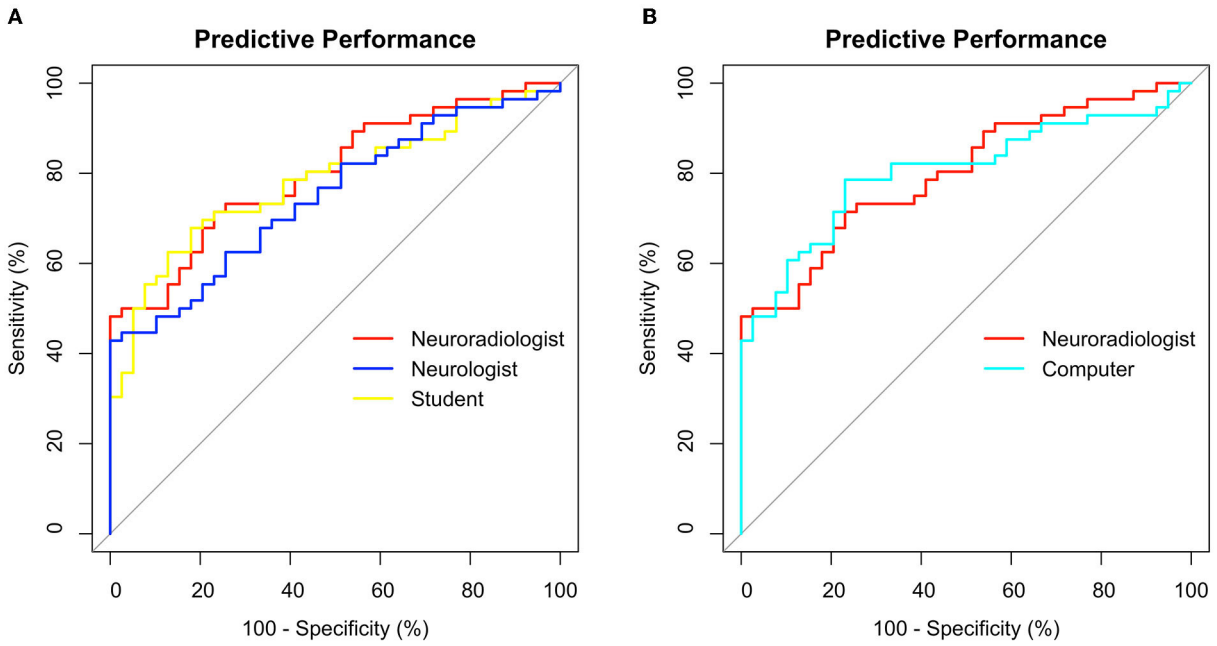

FIGURE 5
Receiver operating characteristics (ROC) for poor outcome prediction after CA using GWR rated by **(A)** 3 different human raters **(B)** Neuroradiologist vs. Computer. Sensitivity and Specificity in %.

the sensitivity while retaining the high specificity for poor neurological outcome prediction. It is still possible, however, that the degree of variability observed in some patients of our study might occur in good neurological outcome patients in another cohort. We therefore advise caution for solely relying on the GWR values as prognostic information derived from CT after CA, especially when the values are close to the cut-off. We suggest that CT interpretation should be based on an SOP that integrates both qualitative and quantitative analysis before concluding on the absence or presence of HIE. This information should then always be put into the context of the results of other diagnostic modalities (EEG, SEP, and serum biomarkers).

Despite a tendency toward more consistent ROI placement in experienced human raters, we observed no significant difference in overall prognostic performance between all 4 raters, even though a clinically unexperienced graduate student who was pre-trained for the task was included. The results contrast with the considerable Inter-rater variability of experienced clinicians in qualitative assessment (9) and underscores that CT quantification reduces Inter-rater variability. We therefore recommend a protocol-based training for physicians doing GWR-assessment in future studies and in the clinical routine. Using a standardized automated method could eliminate the problem of Inter-rater variability overall by assisting the rating physician through visually delineating structures or recommending ROIs.

In this study, GWR performed similar in poor neurological outcome prediction as compared to previous studies by our group and others (13, 14, 22). We account the lower sensitivity of 18–28% in this study to the design that did not stratify between early CTs obtained within 24 h and late CTs performed later than 24 h after CA. The majority of CTs included in our study were early CTs. In our cohort, GWR < 1.10 was a safe and reliable cutoff for poor neurological outcome prediction at 100% specificity, regardless of the rater. Using a higher cutoff in our cohort improved sensitivity considerably for some raters without trade-offs in specificity, for instance up to 48% for the neuroradiologist or 42% for the computer (Figure 5) but would have further increased the risk of misclassification of patients when applying to another cohort (Supplementary Figure 2).

Limitations

There are potential additional sources of rater-independent variability such as the type of CT scanner, acquisition parameters or post-processing software (27). We did not examine intra-rater agreement as additional source of variability. Because of the low number of raters, the three human raters' performance is not representative of that of their group (neuroradiologist, neurologist, and student). CT images were used as part of a multimodal approach to decide on continuation or withdrawal of life-sustaining therapy (WLST). Thus, we cannot exclude self-fulfilling prophecy (28). Prognostication was always based on careful consideration of multimodal diagnostics and a considerable observation period. Because

neurological outcome was assessed at hospital discharge, we cannot exclude later improvement in patients assigned to the poor neurological outcome group. We therefore assigned CPC 3 (severe neurological deficit) to the good neurological outcome group to prevent overly pessimistic prognosis. As this was a single-center study, the subject should be further studied on larger, prospective cohorts in different clinical settings.

Conclusion

Inter-rater agreement on quantitative head CT analysis after CA was very good in between human raters with different levels of expertise and a computer algorithm. As we observed considerable Inter-rater variability in a few individual patients, we advise caution for solely relying on GWR values as prognostic information derived from CT after CA. The results underscore the need for strategies to further standardize quantitative head CT analysis and for multimodal prognostication in general. Inter-rater variability should be investigated and considered in all future studies of CT quantification.

Data availability statement

The datasets presented in this article are not readily available because of ethical and privacy restrictions. Requests to access the datasets should be directed to the corresponding author.

Ethics statement

The studies involving human participants were reviewed and approved by Ethikkommission der Charité—Universitätsmedizin Berlin. Written informed consent for participation was not required for this study in accordance with the national legislation and the institutional requirements.

Author contributions

MK undertook literature research, data collection, manual and automated image analysis, statistical analysis, and drafted the manuscript. ZC rated images and performed statistical analysis. MS rated images. CP, MS, CS, CG, and CL critically reviewed the manuscript. All authors contributed to the article and approved the submitted version.

Funding

MK is participant in the BIH Charité Junior Digital Clinician Scientist Program funded by the Charité—Universitätsmedizin Berlin, and the Berlin Institute of Health at Charité (BIH). CL is participant in the BIH Clinical Fellow Program funded by the Charité—Universitätsmedizin Berlin, and the Berlin Institute of Health at Charité (BIH). Both received a grant from the Laerdal Foundation for research in post cardiac care.

Conflict of interest

Author CL reported institutional fees for lecturing from BD Bard, Zoll, and Bristol Meyer Squibb outside the submitted work. Author CS reported receiving personal fees for consultancy from Philips, BD Bard, Zoll, Rhinocill, and Sedana Medical outside the submitted work.

The remaining authors declare that the research was conducted in the absence of any commercial or financial relationships that could be construed as a potential conflict of interest.

Publisher's note

Supplementary material

The Supplementary Material for this article can be found online at: https://www.frontiersin.org/articles/10.3389/fneur.2022.990208/full#supplementary-material

References

1. Virani SS, Alonso A, Benjamin EJ, Bittencourt MS, Callaway CW, Carson AP, et al. Heart disease and stroke statistics-2020 update: A report from the american heart association. *Circulation.* (2020) 141:e139–596. doi: 10.1161/CIR.0000000000000746

2. Sandroni C, Cronberg T, Sekhon M. Brain injury after cardiac arrest: pathophysiology, treatment, and prognosis. *Intensive Care Med.* (2021) 47:1393–414. doi: 10.1007/s00134-021-06548-2

3. Nolan JP, Sandroni C, Bottiger BW, Cariou A, Cronberg T, Friberg H, et al. European Resuscitation Council and European Society of Intensive Care

Medicine guidelines 2021: post-resuscitation care. *Intensive Care Med.* (2021) 47:369–421. doi: 10.1007/s00134-021-06368-4

4. Westhall E, Rosen I, Rossetti AO, van Rootselaar AF, Wesenberg Kjaer T, Friberg H, et al. Inter-rater variability of EEG interpretation in comatose cardiac arrest patients. *Clin Neurophysiol.* (2015) 126:2397–404. doi: 10.1016/j.clinph.2015.03.017

5. Pfeifer R, Weitzel S, Gunther A, Berrouschot J, Fischer M, Isenmann S, et al. Investigation of the inter-observer variability effect on the prognostic value of somatosensory evoked potentials of the median nerve (SSEP) in cardiac arrest survivors using an SSEP classification. *Resuscitation.* (2013) 84:1375–81. doi: 10.1016/j.resuscitation.2013.05.016

6. Greer DM, Wu O. Neuroimaging in Cardiac Arrest Prognostication. *Semin Neurol.* (2017) 37:66–74. doi: 10.1055/s-0036-1594253

7. Bender A. S1-Leitlinie Hypoxisch-ischämische Enzephalopathie im Erwachsenenalter. Deutsche Gesellschaft für Neurologie. In: *Leitlinien für Diagnostik und Therapie in der Neurologie.* (2018)

8. Panchal AR, Bartos JA, Cabanas JG, Donnino MW, Drennan IR, Hirsch KG, et al. Part 3: Adult basic and advanced life support: 2020 american heart association guidelines for cardiopulmonary resuscitation and emergency cardiovascular care. *Circulation.* (2020) 142:S366–S468. doi: 10.1161/CIR.0000000000000918

9. Caraganis A, Mulder M, Kempainen RR, Brown RZ, Oswood M, Hoffman B, et al. Interobserver variability in the recognition of hypoxic-ischemic brain injury on computed tomography soon after out-of-hospital cardiac arrest. *Neurocrit Care.* (2020) 33:414–21. doi: 10.1007/s12028-019-00900-7

10. Beekman R, Maciel CB, Ormseth CH, Zhou SE, Galluzzo D, Miyares LC, et al. Early head CT in post-cardiac arrest patients: A helpful tool or contributor to self-fulfilling prophecy? *Resuscitation.* (2021) 165:68–76. doi: 10.1016/j.resuscitation.2021.06.004

11. Lopez Soto C, Dragoi L, Heyn CC, Kramer A, Pinto R, Adhikari NKJ, et al. Imaging for neuroprognostication after cardiac arrest: systematic review and meta-analysis. *Neurocrit Care.* (2019) 32:206–216. doi: 10.1007/s12028-019-00842-0

12. Zhou F, Wang H, Jian M, Wang Z, He Y, Duan H, et al. Gray-white matter ratio at the level of the basal ganglia as a predictor of neurologic outcomes in cardiac arrest survivors: a literature review. *Front Med.* (2022) 9:847089. doi: 10.3389/fmed.2022.847089

13. Na MK, Kim W, Lim TH, Jang B, Cho Y, Choi KS, et al. Gray matter to white matter ratio for predicting neurological outcomes in patients treated with target temperature management after cardiac arrest: A systematic review and meta-analysis. *Resuscitation.* (2018) 132:21–8. doi: 10.1016/j.resuscitation.2018.08.024

14. Kenda M, Scheel M, Kemmling A, Aalberts N, Guettler C, Streitberger KJ, et al. Automated assessment of brain CT after cardiac arrest-an observational derivation/validation cohort study. *Crit Care Med.* (2021) 49:e1212–22. doi: 10.1097/CCM.0000000000005198

15. Scheel M, Storm C, Gentsch A, Nee J, Luckenbach F, Ploner CJ, et al. The prognostic value of gray-white-matter ratio in cardiac arrest patients treated with hypothermia. *Scand J Trauma Resusc Emerg Med.* (2013) 21:23. doi: 10.1186/1757-7241-21-23

16. Nolan JP, Soar J, Cariou A, Cronberg T, Moulaert VR, Deakin CD, et al. European Resuscitation Council and European Society of Intensive Care Medicine Guidelines for Post-resuscitation Care 2015: Section 5 of the European Resuscitation Council Guidelines for Resuscitation 2015. *Resuscitation.* (2015) 95:202–22. doi: 10.1016/j.resuscitation.2015.07.018

17. Phelps R, Dumas F, Maynard C, Silver J, Rea T. Cerebral Performance Category and long-term prognosis following out-of-hospital cardiac arrest. *Crit Care Med.* (2013) 41:1252–7. doi: 10.1097/CCM.0b013e31827ca975

18. Jenkinson M, Beckmann CF, Behrens TE, Woolrich MW, Smith SM. Fsl. *Neuroimage.* (2012) 62:782–90. doi: 10.1016/j.neuroimage.2011.09.015

19. Robin X, Turck N, Hainard A, Tiberti N, Lisacek F, Sanchez JC, et al. pROC: an open-source package for R and S+ to analyze and compare ROC curves. *BMC Bioinformatics.* (2011) 12:77. doi: 10.1186/1471-2105-12-77

20. Revelle W. *Psych: Procedures for Psychological, Psychometric, and Personality Research.* Evanston, Illinois: Northwestern University. R package version 2.1.9(R package version 2.1.9). (2021).

21. Altman DG. *Practical Statistics for Medical Research.* 1st ed ed. London, New York: Chapman and Hall. (1991). p. 611.

22. Streitberger KJ, Endisch C, Ploner CJ, Stevens R, Scheel M, Kenda M, et al. Timing of brain computed tomography and accuracy of outcome prediction after cardiac arrest. *Resuscitation.* (2019) 145:8–14. doi: 10.1016/j.resuscitation.2019.09.025

23. Kirsch K, Heymel S, Gunther A, Vahl K, Schmidt T, Michalski D, et al. Prognostication of neurologic outcome using gray-white-matter-ratio in comatose patients after cardiac arrest. *BMC Neurol.* (2021) 21:456. doi: 10.1186/s12883-021-02480-6

24. Cristia C, Ho ML, Levy S, Andersen LW, Perman SM, Giberson T, et al. The association between a quantitative computed tomography (CT) measurement of cerebral edema and outcomes in post-cardiac arrest-a validation study. *Resuscitation.* (2014) 85:1348–53. doi: 10.1016/j.resuscitation.2014.05.022

25. Wu O, Batista LM, Lima FO, Vangel MG, Furie KL, Greer DM. Predicting clinical outcome in comatose cardiac arrest patients using early noncontrast computed tomography. *Stroke.* (2011) 42:985–92. doi: 10.1161/STROKEAHA.110.594879

26. Hanning U, Bernhard Sporns P, Lebiedz P, Niederstadt T, Zoubi T, Schmidt R, et al. Automated assessment of early hypoxic brain edema in non-enhanced CT predicts outcome in patients after cardiac arrest. *Resuscitation.* (2016) 104:91–4. doi: 10.1016/j.resuscitation.2016.03.018

27. Oh JH, Choi SP, Wee JH, Park JH. Inter-scanner variability in Hounsfield unit measured by CT of the brain and effect on gray-to-white matter ratio. *Am J Emerg Med.* (2019) 37:680–4. doi: 10.1016/j.ajem.2018.07.016

28. Geocadin RG, Peberdy MA, Lazar RM. Poor survival after cardiac arrest resuscitation: a self-fulfilling prophecy or biologic destiny? * *Crit Care Med.* (2012) 40:979–80. doi: 10.1097/CCM.0b013e3182410146

Advantages of publishing in Frontiers

OPEN ACCESS
Articles are free to read for greatest visibility and readership

FAST PUBLICATION
Around 90 days from submission to decision

HIGH QUALITY PEER-REVIEW
Rigorous, collaborative, and constructive peer-review

TRANSPARENT PEER-REVIEW
Editors and reviewers acknowledged by name on published articles

Frontiers
Avenue du Tribunal-Fédéral 34
1005 Lausanne | Switzerland

Visit us: www.frontiersin.org
Contact us: frontiersin.org/about/contact

REPRODUCIBILITY OF RESEARCH
Support open data and methods to enhance research reproducibility

DIGITAL PUBLISHING
Articles designed for optimal readership across devices

FOLLOW US
@frontiersin

IMPACT METRICS
Advanced article metrics track visibility across digital media

EXTENSIVE PROMOTION
Marketing and promotion of impactful research

LOOP RESEARCH NETWORK
Our network increases your article's readership